The role of Scara5 in adipogenesis and breast cancer pathogenesis

Caterina Maddalena Suelzu

A thesis submitted for the degree of Doctor of Philosophy

University of East Anglia

Norwich Medical School

September 2023



© This copy of the thesis has been supplied on condition that anyone who consults it is understood to recognise that its copyright rests with the author and that use of any information derived there from must be in accordance with current UK Copyright Law. In addition, any quotation or extract must include full attribution.

Declaration

I declare that the content of this thesis entitled “The role of Scara5 in adipogenesis and breast cancer pathogenesis” was completed by myself unless otherwise acknowledged. The present thesis has been submitted to the University of East Anglia for the degree of Doctor of Philosophy and has not been submitted in support of an application for another degree or qualification in this or any other university or institution.

This thesis is approximately 53,000 words in length.



Caterina Maddalena Suelzu

“Sometimes fate is like a small sandstorm that keeps changing directions. You change direction but the sandstorm chases you. You turn again, but the storm adjusts. Over and over you play this out, like some ominous dance with death just before dawn. Why? Because this storm isn't something that blew in from far away, something that has nothing to do with you. This storm is you. Something inside of you. So all you can do is give in to it, step right inside the storm, closing your eyes and plugging up your ears so the sand doesn't get in, and walk through it, step by step. There's no sun there, no moon, no direction, no sense of time. Just fine white sand swirling up into the sky like pulverized bones. That's the kind of sandstorm you need to imagine.

And you really will have to make it through that violent, metaphysical, symbolic storm. No matter how metaphysical or symbolic it might be, make no mistake about it: it will cut through flesh like a thousand razor blades. People will bleed there, and you will bleed too. Hot, red blood. You'll catch that blood in your hands, your own blood and the blood of others.

And once the storm is over you won't remember how you made it through, how you managed to survive. You won't even be sure, in fact, whether the storm is really over. But one thing is certain. When you come out of the storm you won't be the same person who walked in. That's what this storm's all about.”

Haruki Murakami, *Kafka on the Shore*

Acknowledgments

First and foremost, I would like to express my heartfelt gratitude to my supervisors, Professors Nicole Horwood and Jeremy Turner, for their guidance, support, and faith in my abilities. This PhD journey would have been drastically different if I had not been given the freedom to become the scientist I aspired to be.

I am indebted to the BCRE technical team, Jasmine, Catherine, and Chris. Their patience in listening to all my doubts and my concerns about chemicals is admirable; their assistance and kindness are etched in my memory. I also extend my gratitude to the DMU staff for their exceptional teaching. A special acknowledgment goes to Rich and Jon, whose guidance proved invaluable.

Thanks to Dr Adel Ersek for her tremendous assistance in conducting the osteoporosis and diabetes experiments *in vivo*, and to Dr Stephen Robinson for his help with breast cancer animal models. Additionally, I want to express my appreciation to Dr Justin Bradley and Professor Nick Le Brun for their indispensable support in performing the quantification of murine organs' iron levels.

To my family and friends, a constant anchor and guiding light in my life.

No one feels offended if my deepest gratitude goes to Gabriele, my better half. I am fully aware that the word 'thanks' will never repay him for his boundless patience and unwavering belief in me. The privilege of pursuing our PhDs together was an incredible stroke of luck and I am immensely grateful for his help and constant support, without which none of this would have been achievable.

Four years ago, I embarked on this journey as an entirely different person. For a long time I was my own worst enemy, undermining every accomplishment and questioning my own worth. I owe myself an apology for harbouring those negative thoughts, and I owe Maria my gratitude for providing the spark that made me realise the urgency of not squandering time. Every stride I take is dedicated to my childhood best friend, who will forever hold a special place in my heart.

Abstract

Affecting millions of people around the world, osteoporosis and bone fragility represent a serious health concern and one of the major threats for elderly people, since the risk of fracture tends to increase with ageing. Similarly, metabolic disorders such as diabetes and obesity stand as major public health problems worldwide. Both bone loss-related diseases and metabolic disorders impact on mesenchymal stromal cells (MSCs) differentiation fate, with adipogenesis favoured at the expense of osteogenesis and resulting in increased adiposity and decreased bone mass. A plethora of factors have been identified as crucial for MSCs lineage differentiation; scavenger receptor class A member 5 (Scara5) recently emerged as a regulator of adipogenesis *in vitro*. Among its many functions, Scara5 is a ferritin receptor and is reportedly downregulated in human breast cancer (BrCa) cell lines.

Studies conducted on Scara5 -knock out (KO) mice revealed an increased bone mass and a reduced fat deposition. However, bone/fat-related pathologies (i.e. osteoporosis, diabetes) were not influenced by the genetic deletion. In line with these results, Scara5-KO bone marrow MSCs (BMSCs) showed a propensity to become osteoblasts and a reduced ability to differentiate into adipocytes. Mechanistic studies proved that Scara5 deficiency impinged on BMSCs mitochondrial activity during adipogenic differentiation, as well as on murine kidney iron levels. The reduced iron content and adipose tissue deposition also impacted on BrCa development; indeed, Scara5-KO mice developed smaller tumours upon cancer cell injection into the mammary fat pad, as a result of an iron homeostasis perturbation and the consequent reduced fat deposition.

This thesis presents Scara5 as a central regulator of iron homeostasis, MSCs adipogenesis, and breast cancer pathogenesis. Although a reduction in Scara5 has been associated with health problems (i.e. cancer), these findings propose that targeting Scara5 may be useful for developing new therapies to counteract obesity and BrCa pathogenesis.

Access Condition and Agreement

Each deposit in UEA Digital Repository is protected by copyright and other intellectual property rights, and duplication or sale of all or part of any of the Data Collections is not permitted, except that material may be duplicated by you for your research use or for educational purposes in electronic or print form. You must obtain permission from the copyright holder, usually the author, for any other use. Exceptions only apply where a deposit may be explicitly provided under a stated licence, such as a Creative Commons licence or Open Government licence.

Electronic or print copies may not be offered, whether for sale or otherwise to anyone, unless explicitly stated under a Creative Commons or Open Government license. Unauthorised reproduction, editing or reformatting for resale purposes is explicitly prohibited (except where approved by the copyright holder themselves) and UEA reserves the right to take immediate 'take down' action on behalf of the copyright and/or rights holder if this Access condition of the UEA Digital Repository is breached. Any material in this database has been supplied on the understanding that it is copyright material and that no quotation from the material may be published without proper acknowledgement.

Table of Contents

Declaration ..... **I**

Acknowledgments ..... **III**

Abstract ..... **IV**

Table of Contents ..... **VI**

List of Figures ..... **XIII**

List of Tables ..... **XVII**

List of Abbreviations ..... **XVIII**

Chapter 1: Introduction **23**

1.1 Bone **23**

1.1.1 Bone forming osteoblasts 24

1.1.2 Regulation of osteoblast differentiation 26

1.1.3 Osteoblast-osteoclast coupling 29

1.1.4 Bone loss-related pathologies: osteoporosis and diabetes 32

1.2 Adipose tissue **34**

1.2.1 Features and functions of adipocytes 35

1.2.1.1 Adipose tissue as an endocrine organ 39

1.2.2 Regulation of adipocyte differentiation 40

1.3 Mesenchymal stromal cells as common precursors of osteoblasts and adipocytes **44**

1.3.1 Origin and lineage differentiation of MSCs 45

1.3.2 Regulation of MSCs differentiation into osteoblasts and adipocytes 47

1.3.3 Metabolic requirements of differentiating MSCs 50

1.4 Scavenger receptor class A member 5 (Scara5) as a multifaceted biomolecule **53**

1.4.1 Scavenger receptor class A members 53

1.4.2 Scara5 in human diseases: GWAS catalog 55

1.4.3 Scara5 expression in human and mice 59

1.4.4 Scara5 as a ferritin receptor 61

1.4.5 Scara5, adipogenesis, and breast cancer 64

1.5 Hypothesis, aims and objectives 67

Chapter 2: Materials and methods 69

2.1 Materials, reagents, and chemicals 69

2.2 Experimental mice 69

2.3 Backcrossing programme and genotyping 70

2.4 Primary cells and cell line culture 73

2.4.1 Murine bone marrow mesenchymal stem cells (BMSCs) 73

2.4.2 Murine breast cancer cells 74

2.4.3 Human fetal osteoblasts (hFOB) 1.19 75

2.5 Osteogenic and adipogenic differentiation 75

2.6 Alkaline phosphatase (ALP) assay 76

2.7 Alizarin Red S and Oil Red O staining 77

2.8 RNA extraction, Reverse Transcription, and Reverse Transcription-quantitative Polymerase Chain Reaction (RT-qPCR) 77

2.9 Scara5 Plasmid amplification and purification 80

2.10 GapmeRs 82

2.11 Cell transfection 83

2.12 Cell proliferation assay (MTT assay) 84

2.13 Cell adhesion assay 84

2.14 Murine samples harvest and processing 85

2.14.1 Murine tissue harvest 85

2.14.2 Inguinal fat supernatant production 85

2.15 Microcomputed tomography (μCT) 86

2.15.1 Bone microarchitecture analysis 86

2.15.2 Bone marrow adipose tissue evaluation by Osmium tetroxide (OsO_4) staining 86

2.16 Murine samples histology 87

2.16.1 Hematoxylin and Eosin (H&E) staining 87

2.16.2 Iron staining (Potassium Ferrocyanide) 88
2.16.3 Inguinal fat histology analysis 88
2.17 Calcein injection assay (*in vivo* bone formation assay) 89
2.17.1 PBS, LPS and Calcein injection protocol (experimental design) 89
2.17.2 Calvaria plastic embedding, sectioning, and analysis 89
2.18 Oestrogen deficiency-induced osteoporosis animal model (ovariectomy-induced osteoporosis) 90
2.19 Streptozotocin-induced diabetes animal model 90
2.20 Breast cancer animal models 91
2.21 Western Blot (WB) 92
2.21.1 Protein extraction and quantification 92
2.21.2 Protein separation: sodium dodecyl-sulfate (SDS)-page electrophoresis 92
2.21.3 Protein transfer and immunoblotting 92
2.22 AKT phosphorylation array 93
2.23 Seahorse cell metabolic analysis (mitochondrial function analysis) 94
2.24 Iron quantification (ferene-based iron assay) 95
2.25 Data analysis and statistics 96
Chapter 3: Scara5 controls osteogenesis and adipogenesis 98
3.1 Introduction 98
3.2 Scara5-WT and -KO BMSCs respond differently to osteogenic stimuli 99
3.2.1 Passage 1 bone flushed BMSCs show the utmost potential as a primary cell model 99
3.2.1.1 Bone washed cells vs bone chips: different ways to isolate and grow BMSCs 99
3.2.1.2 Passage 1 BMSCs display the highest ALP activity when OM-treated 100
3.2.2 Scara5 gene expression is not triggered by OM treatment 102
3.2.3 Scara5-KO BMSCs are more prone to differentiate to osteoblast than WT cells. 102
3.2.4 Osteogenic marker expression does not differ between Scara5-WT and -KO BMSCs 104

3.3 Scara5-WT and -KO BMSCs respond differently to adipogenic stimuli 105
3.3.1 Scara5 gene expression is triggered by AM treatment 106
3.3.2 Scara5 deficient BMSCs differentiate less to adipocytes than WT cells.....107
3.3.3 Adipogenic gene expression is impaired in Scara5-null BMSCs 108
3.4 Osteoblast cell line hFOB 1.19 can be used to study MSCs commitment to osteoblasts and adipocytes 110
3.4.1 hFOB culture differs from the canonical osteoblast cell lines.....110
3.4.2 hFOB can differentiate both towards osteoblasts and adipocytes 111
3.4.3 Osteogenic and adipogenic marker expression increases in response to OM and AM.....113
3.4.4 Scara5 expression is sparked by AM, but not by OM, at different time points ...114
3.4.5 pmaxGFP and Scara5 plasmids can be easily lipo-transfected within hFOB 115
3.4.5.1 Both Lipofectamine 2000® and Viafect™ can be exploited to perform hFOB lipofection 115
3.4.5.2 Scara5 plasmid transfection does not have detrimental effect on hFOB proliferation 116
3.4.6 Scara5 overexpression, but not silencing, is achievable in hFOB cell line.....117
3.4.7 Scara5 plasmid over-expression influences ALP activity of OM-treated hFOB....119
3.5 Discussion 120
Chapter 4: Scara5 controls bone and fat deposition *in vivo*.....126
4.1 Introduction 126
4.2 Scara5 deficiency increases bone mass and decreases fat deposition *in vivo*.....127
4.2.1 C57BL/6J mice backcrossing to generate Scara5-WT and -KO colonies.....127
4.2.2 μCT analysis displays increased bone mass in female but not in male mice 128
4.2.3 Inguinal fat measurements show a difference between WT and Scara5-KO mice 130
4.3 *In vivo* bone formation differs between WT and Scara5-KO mice.....133
4.3.1 LPS at 0.25 mg/kg represents the optimal dose to generate a bone formation model 133

4.3.2 Calvarial assay shows that Scara5-KO mice make more bone than WT counterparts 135

4.4 Ovariectomy-induced osteoporosis causes bone mass reduction in both WT and Scara5 null female mice 136

4.4.1 Tibiae μCT reveals bone mass reduction in both WT and Scara5-KO mice 136

4.4.2 Osmium tetroxide staining shows no difference in bone marrow adipose tissue 138

4.5 Streptozotocin-induced diabetes impacted on bone/fat deposition of WT and Scara5 deficient mice 139

4.5.1 WT and Scara5-KO mice blood glucose equally increases in response to Stz treatment 140

4.5.2 Tibiae μCT shows bone mass reduction following Stz injection in both WT and Scara5 null mice 141

4.5.3 Stz-induced diabetes suppresses the fat deposition difference between WT and Scara5-KO mice 144

4.6 Discussion 145

Chapter 5: Mechanistic investigation of Scara5 in MSCs commitment 152

5.1 Introduction 152

5.2 Scara5 deficiency has minimal impact on Wnt signalling pathway 153

5.2.1 Lithium Chloride does not stimulate BMSCs osteogenesis 153

5.2.2 Wnt3a, but not Wnt5a nor Wnt10b, promotes osteogenesis of Scara5-null BMSCs more than WT counterparts 154

5.2.3 OM treatment does not stimulates Wnt signalling-related genes' expression in Scara5-WT and -KO BMSCs 156

5.2.4 Wnt3a treatment increases Wnt signalling-related genes' expression in Scara5-WT and -KO BMSCs 157

5.2.5 β-catenin expression does not change in Wnt3a-treated Scara5-WT and -KO BMSCs 158

5.3 Scara5 deficiency does not influence AKT-related pathways' function 159

5.3.1 AKT-related proteins are differentially phosphorylated in WT and Scara5-KO BMSCs treated with osteogenic and adipogenic media 160
5.3.2 Scara5 does not play a role in AKT-related pathways, as confirmed by WB analysis 162
5.4 Scara5 deficiency impacts on cell metabolism 163
5.4.1 Scara5-KO murine kidneys display reduced iron content 164
5.4.2 Metabolic gene expression differs between AM-treated WT and Scara5-KO BMSCs 165
5.4.3 Oxygen consumption rate differs between AM-treated WT and Scara5-KO BMSCs 166
5.5 Discussion 168
Chapter 6: Scara5 deficiency influences breast cancer pathogenesis 175
6.1 Introduction 175
6.2 BRPKp110-based BrCa develops similarly between WT and Scara5-KO mice 176
6.2.1 Tumour volume does not differ between Scara5-WT and -KO mice after 21 days 176
6.2.2 Tumour cell morphology, but not inflammatory marker expression, show a different pattern between WT and Scara5-null mice 178
6.3 Scara5 expression is downregulated in murine BrCa cell lines 179
6.4 PyMT-BO5-based BrCa develops differently between WT and Scara5-KO mice 180
6.4.1 Scara5-KO mice develop smaller tumours than WT mice after 15 days 180
6.4.2 Tumour cell morphology and inflammatory marker expression exhibit similar patterns between WT and Scara5-null mice 182
6.5 Scara5 deficiency impacts on adipose tissue-BO5 cells crosstalk 183
6.5.1 WT and Scara5-KO iFAT supernatants equally influence BO5 cell adhesion 183
6.5.2 WT and Scara5-KO iFAT supernatants differently stimulate BO5 cell proliferation 184
6.6 Iron as a key factor for Scara5-WT/-KO BrCa pathogenesis 185

6.6.1 DFO impairs the effect of WT more than Scara5-KO iFAT supernatant on BO5 cell proliferation 186
6.6.2 WT and Scara5-KO tumours display different iron content 187
6.7. Discussion 189
Chapter 7: Concluding Discussion 194
7.1 Discussion 194
7.1.1 Scara5 determines MSCs fate towards adipocytes at the expenses of osteoblasts 195
7.1.2 Scara5 deficiency impinges on iron homeostasis 197
7.1.3 Scara5 deficiency impacts on adipose tissue-breast cancer crosstalk 199
7.2 Future Directions 202
Chapter 8: Bibliography 205

List of Figures

Figure 1.1 Cell fate of bone forming-osteoblasts 25
Figure 1.2 RUNX2 and Osterix expression during osteoblast differentiation 26
Figure 1.3 Wnt/β-catenin signalling pathway 28
Figure 1.4 RANKL/RANK/OPG signalling pathway 31
Figure 1.5 Different types and functions of adipocytes 36
Figure 1.6 PI3K-AKT and RAS/MAPK signalling pathways induce PPARγ/CEBPα expression 43
Figure 1.7 BMSCs commitment and differentiation into adipocytes and osteoblasts 46
Figure 1.8 Osteo-adipogenic differentiation of MSCs and related signalling pathways 48
Figure 1.9 Glycolysis, TCA cycle, and OXPHOS 50
Figure 1.10 Metabolic shift through MSCs differentiation 52
Figure 1.11 Scavenger receptor class A members 54
Figure 1.12 Scara5 expression in humans 60
Figure 1.13 Scara5 expression in mice 61
Figure 1.14 H- and L-ferritin receptors 63
Figure 1.15 BrCa-adipose tissue crosstalk 67

Figure 2.1 Backcrossing scheme (designed and adapted from Sul *et al*. [230]) 71
Figure 2.2 Generation of Scara5-WT (+/+) and -KO (-/-) mice 71
Figure 2.3 BMSCs extraction methods 74
Figure 2.4 pNPP hydrolysis reaction in the presence of ALP 76
Figure 2.5 Scara5 pEGFP-N2 plasmid structure 81
Figure 2.6 GapmeRs' mechanism of action 82
Figure 2.7 *Adiposoft* macro for adipocyte size and number analysis 89
Figure 2.8 Agilent Seahorse XF Cell Mito Stress Test profile 95

Figure 3.1 Bone flushed-BMSCs and bone chips derived-BMSCs show distinct ALP activity patterns 100
Figure 3.2 Passage 1 (P1) BMSCs exhibit the highest ALP activity 101
Figure 3.3 OM treatment does not trigger Scara5 gene expression 102
Figure 3.4 Scara5 deficient BMSCs have a higher osteogenic potential than WT BMSCs 103

Figure 3.5 Alpl and OCN expression does not differ between Scara5-WT and -KO BMSCs.. 105
Figure 3.6 AM treatment triggers Scara5 gene expression 106
Figure 3.7 Oil Red O-stained lipids are less abundant in Scara5-KO BMSCs 107
Figure 3.8 Adipoq and LEP expression differs between WT and Scara5-KO BMSCs 109
Figure 3.9 hFOB cultured at 37 °C and OM-treated display the highest ALP activity 111
Figure 3.10 hFOB differentiate to osteoblasts and adipocytes under specific stimuli 112
Figure 3.11 Osteogenic and adipogenic marker expression increases after OM or AM treatment 113
Figure 3.12 AM, but not OM, triggers Scara5 gene expression 114
Figure 3.13 hFOB are GFP transfectable both using Lipofectamine 2000® and Viafect™.... 115
Figure 3.14 Scara5 plasmid is transfectable via Lipofectamine 2000® 116
Figure 3.15 Scara5 is overexpressed, but not knocked down, in hFOB cell line 118
Figure 3.16 Both Scara5 overexpression and the use of GapmeRs influence ALP activity. .. 119
Figure 3.17 Scara5 is a key factor in BMSCs fate 125

Figure 4.1 Mice backcrossing and genotyping allows to generate Scara5-WT and -KO offspring 128
Figure 4.2 Scara5 deficient females, but not males, show increased tibiae bone mass 129
Figure 4.3 Inguinal fat pad weight is higher in WT than in Scara5-KO mice 131
Figure 4.4 Inguinal fat pad histology shows no difference between Scara5-WT and -KO mice adipocyte size and number 132
Figure 4.5 0.25 mg/kg LPS calvarial injection does not have harmful effects on mice health status 134
Figure 4.6 Plastic embedded calvaria display distinct bone growth between Scara5-WT and -KO mice 135
Figure 4.7 Tibiae bone mass decreases in response to ovariectomy-induced osteoporosis 137
Figure 4.8 BMAT deposition does not change in response to Scara5 deficiency 139
Figure 4.9 Mice blood glucose increases and decreases in response to Stz and Linbit®, respectively 141
Figure 4.10 Stz-induced diabetes causes bone mass reduction 143
Figure 4.11 Fat deposition is no longer different when WT and Scara5-KO mice develop diabetes 145

Figure 4.12 Scara5 absence increases bone and decreases fat deposition *in vivo* 151

Figure 5.1 LiCl suppresses ALP activity of WT and Scara5-KO BMSCs.....154
Figure 5.2 Wnt3a, but not Wnt5a nor Wnt10b, increases BMSCs' ALP activity 155
Figure 5.3 OM does not increase the expression of Wnt signalling related genes.....157
Figure 5.4 Wnt3a stimulates the expression of Wnt signalling genes equally between WT and Scara5-null BMSCs 158
Figure 5.5 WT and Scara5-KO BMSCs respond similarly to Wnt3a treatment in terms of β-catenin expression 159
Figure 5.6 AKT phosphorylation array map.....160
Figure 5.7 OM treatment induces AKT-related proteins upregulation more in Scara5-KO than in WT BMSCs.....161
Figure 5.8 AM treatment induces AKT-related proteins upregulation more in WT than in Scara5-KO BMSCs.....162
Figure 5.9 WT and Scara5-KO BMSCs express similar levels of phosphorylated RPS6 and RSK1 once treated with AM.....163
Figure 5.10 Iron content differs between Scara5-WT and -KO mice's kidneys, but not testis 164
Figure 5.11 OM does not induce the expression of glycolysis-associated genes HK2 and PKM 165
Figure 5.12 Metabolic genes are more expressed by AM-treated WT than Scara5-KO BMSCs 166
Figure 5.13 Scara5-null BMSCs exhibit a decreased OCR once AM-treated.....167
Figure 5.14 Mild iron deficiency hypothesis.....172
Figure 5.15 Scara5 hypothetic mechanism of action 173

Figure 6.1 BRPKp110-based BrCa growth does not differ between WT and Scara5-KO mice 177
Figure 6.2 H&E staining, but not inflammatory genes' expression, reveals slight differences between WT and Scara5-KO tumours 178
Figure 6.3 BrCa cell lines express low levels of Scara5.....179
Figure 6.4 PyMT-BO5-based BrCa growth differs between WT and Scara5-KO mice.....181

Figure 6.5 Scara5-WT and -KO tumours display similar H&E staining and inflammatory markers' expression 182
Figure 6.6 WT and Scara5-KO iFAT pads are processed to obtain supernatant 183
Figure 6.7 BO5 cell adhesion is not influenced by WT/Scara5-KO iFAT supernatants 184
Figure 6.8 BO5 cell proliferation is stimulated more by WT than Scara5-KO iFAT/iFAT and BO5 supernatants 185
Figure 6.9 DFO undermines BO5 cells' proliferation once added to iFAT supernatants 187
Figure 6.10 Scara5-KO mice's tumours display low levels of iron 188
Figure 6.11 Scara5 deficiency impinges on the fat-BrCa crosstalk 193

Figure 7.1 Hypothetic mechanism of Scara5 role in adipogenesis and BrCa-fat crosstalk ... 202

List of Tables

Table 1.1 Scara5 variants and associated traits in the GWAS catalog 56

Table 2.1 Endpoint PCR primers for genotyping 72
Table 2.2 Endpoint PCR thermocycler program 72
Table 2.3 Reverse transcription thermocycler program 78
Table 2.4 SYBR Green I-based primers 78
Table 2.5 Taqman™-based RT-qPCR primers.....80
Table 2.6 RT-qPCR programs 80
Table 2.7 Antisense Scara5 LNA GapmeRs sequences 83
Table 2.8 Antibodies used for Western Blot 93

Table 4.1 Bone parameters of WT and Scara5-KO 11-weeks old mice 130
Table 4.2 Bone parameters of SHAM and OVX WT and Scara5-KO female mice 138
Table 4.3 Additional bone parameters of control and diabetic Scara5-WT/-KO male mice.144

List of Abbreviations

2T3	Murine osteoblast-like ‘BMP-2 T-Ag-3’ cell line
Ad	Adipocyte
Adipoq	Adiponectin (gene name)
AdMSCs	Adipose tissue-derived mesenchymal stromal cells
AKT	Protein kinase B
ALP	Alkaline phosphatase (protein name)
Alpl	Alkaline phosphatase (gene name)
AM	Adipogenic medium
ARS	Alizarin Red S
ATP	Adenosine triphosphate
BAT	Brown adipose tissue
BgAT	Beige adipose tissue
BMAT	Bone marrow adipose tissue
BMD	Bone mineral density
BMI	Body mass index
BMP-	Bone morphogenic protein-
BMSCs	Bone marrow mesenchymal stromal cells
BMU	Basic multicellular unit
BrCa	Breast cancer
BS	Bone surface
BV	Bone volume
cBMAT	Constitutive BMAT
CEBP-	CCAAT-enhancer-binding protein-
CM	Complete (maintenance) medium
CoA	Coenzyme A
Col1a1	Type I collagen (gene name)
Ctrl	Control
CXCL12	C-X-C motif chemokine ligand 12

Dex	Dexamethasone
DFO	Desferrioxamine
DKK-1/2	Dickkopf-1/2
DVL	Dishevelled (protein name)
Dvl3	Dishevelled 3 (gene name)
ECM	Extracellular matrix
EGFP	Engineered GFP
ER	Oestrogen receptor
ERK	Extracellular signal-regulated kinase
ESCC	Oesophageal squamous cell carcinomas cell line
FAK	Focal adhesion kinase
FBS	Fetal bovine serum
FCCP	Carbonyl cyanide-p-trifluoromethoxyphenylhydrazone
Fe	Iron
FFAs	Free fatty acids
FoxO1	Forkhead Box O1
Fsp27	Fat specific protein 27
GAPDH	Glyceraldehyde 3-phosphate dehydrogenase
GFP	Green fluorescent protein
Glut4	Glucose transporter 4
GSK3β	Glycogen synthetase kinase 3β
GWAS	Genome wide association studies
H&E	Hematoxylin and Eosin
hCM	hFOB complete maintenance medium
HER	Human epidermal growth factor receptor
HET (+/-)	Heterozygous
hFOB (1.19)	Human fetal osteoblasts 1.19 cell line
Hh	Hedgehog
hOM	hCM supplemented with osteogenic reagents
Hsl	Hormone-sensitive lipase

iFAT	Inguinal fat
IFNγ	Interferon gamma
IGF-1	Insulin-like growth factor-1
IL-	Interleukin-
KO (-/-)	Knockout
LDL	Low-density lipoprotein
LEF	Lymphoid enhancer factor (protein name)
Lef1	Lymphoid enhancer factor 1 (gene name)
LEP	Leptin
LiCl	Lithium Chloride
LPS	Lipopolysaccharide
LRP5/6	Lipoprotein receptor-related protein 5/6
MAPK	Mitogen-activated protein kinase
MAR	Mineral apposition rate
MARCO	Macrophage receptor with collagenous domain
MEK	MAPK kinase
MSCs	Mesenchymal stromal cells
MSR1	Macrophage scavenger receptor 1
mTOR	Mammalian target of rapamycin
MTT	3-(4,5-dimethylthiazol-2-yl)-2,5-diphenyl-2H-tetrazolium bromide
Myf5	Mesodermal myogenic factor 5
NaCl	Sodium Chloride
Ob	Osteoblast
OCN	Osteocalcin
OD	Optical density
OM	Osteogenic medium
OPG	Osteoprotegerin
OPN	Osteopontin
ORO	Oil Red O
OVX	Ovariectomy

OXPHOS	Oxidative phosphorylation
P70S6K	p70 ribosomal S6 kinase
PAT	Pink adipose tissue
PBS	Phosphate buffered saline
PCR	Polymerase chain reaction
PI3K	Phosphatidylinositol-3-kinase
pNP	p-Nitrophenol
pNPP	p-Nitrophenylphosphate
PPAR-	Proliferator activated receptor-
PR	Progesterone receptor
PTEN	Phosphatase and Tensin Homolog
RAF	Rapidly accelerated fibrosarcoma
RANK	Receptor activator of nuclear factor kappa beta
RANKL	RANK ligand
RAS	Rat sarcoma virus
rBMAT	Regulated bone marrow adipose tissue
ROS	Reactive oxygen species
RPS6	Ribosomal protein S6
RSK	Ribosomal S6 Kinase
RT	Room temperature
RT-qPCR	Reverse Transcription-quantitative Polymerase Chain Reaction
RUNX2	Runt-related transcription factor 2
Scara3	Scavenger receptor class A member 3
Scara4	Scavenger receptor class A member 4
Scara5	Scavenger receptor class A member 5
SD	Standard deviation
SEM	Standard error of the mean
sFRPs	Secreted frizzled-related proteins
Sn	Supernatant
SRCR	Scavenger receptor cysteine-rich

SRs	Scavenger receptors
Stz	Streptozotocin
T0	Time zero
T1D	Type 1 diabetes
T2D	Type 2 diabetes
TAGs	Triacylglycerol
TAMs	Tumour-associated macrophages
Tb.N	Trabecular number
Tb.Sp	Trabecular separation
Tb.Th	Trabecular thickness
TCA	Tricarboxylic acid cycle
TCF	T-cell factor
Tf	Transferrin
TFGβ	Transforming growth factor beta
TfR	Transferrin receptor
TME	Tumour microenvironment
TNFα	Tumour necrosis factor alpha
TV	Total volume
Ucp-	Uncoupling protein-
vWF	von Willebrand factor
WAT	White adipose tissue
WB	Western blot
Wnt	Wingless-related integration site
WT (+/+)	Wild type
µCT	Microcomputed tomography

Chapter 1: Introduction

1.1 Bone

Bone is a mineralised connective tissue consisting of cells, blood vessels, and extracellular matrix (ECM) made up of type 1 collagen triple helices and crystals of calcium phosphate rich mineral in form of hydroxyapatite [1, 2]. It exerts several mechanical functions, providing rigidity, shape, protection, and support for body structures, as well as aiding locomotion and regulating mineral homeostasis by acting as a large reservoir for calcium, phosphate, and magnesium [1]. The bone formation process is called either bone ossification or osteogenesis. Bone ossification begins during the sixth/seventh week of embryonic development and terminates around the age of twenty-five years; it can be described as intramembranous and endochondral, depending on how precursor cells transform into bone [3].

During intramembranous ossification, osteogenic precursors mesenchymal stromal cells (MSCs) directly differentiate into bone forming osteoblasts, that produce an unmineralised matrix called osteoid. Once osteoid binds calcium, the mineralisation and subsequent hardening of the matrix results in some osteoblasts being trapped and differentiating into osteocytes [3]. Osteoblasts continuous secretion of osteoid culminates in the formation of trabecular/spongy bone, whereas MSCs lying on the trabecular bone surface will form the periosteum. The differentiation of periosteal MSCs into osteoblasts, and the consequent production and mineralisation of osteoid, will then form multiple layers that represent the cortical/compact bone [3, 4]. Flat bones of the cranial vault, part of facial bones, and clavicle all develop intramembranously [3, 5].

On the other hand, most of the appendicular and axial skeleton is formed through endochondral ossification, the process by which hyaline cartilage is replaced by bone [6]. MSCs differentiate into chondrocytes, which secretion of an extracellular matrix (ECM) form a bony model called cartilage model. The chondrocytes near the core of the cartilage model become hypertrophic and secrete collagen X and fibronectin, enabling the mineralisation of the ECM. The ECM mineralisation diminishes the nutrients availability for the other chondrocytes, which undergo apoptosis and create a void invaded by chondrocyte-differentiated osteoblasts and blood vessels [2, 6-9]. Whilst the blood vessels enlarge the space and create the

medullary cavity, the osteoblasts transform the perichondrium (membrane that surround the cartilage model) into periosteum, creating a region of cortical bone in its diaphyseal region. This action culminates with the formation of the primary ossification centre [2]. Cartilage proliferates longitudinally towards both ends of the bone creating growth areas, also known as epiphyseal plates. After birth, cartilage is replaced by bone in the epiphyseal region, where the secondary ossification centre developed [2, 6].

Opposite to the widely mistaken belief, bone is a dynamic organ characterised by a constant remodelling [1]. Bone remodelling is the results of the coupled action of bone forming and bone resorbing cells, osteoblasts and osteoclasts, respectively. In addition, osteoblast-derived osteocytes serve as mechano-sensors transducing extracellular signals to initiate the bone remodelling [10]. Bone cells' activity is tightly regulated by hormones, growth factors, and cytokines [2]; derailed bone remodelling can indeed result in the development of skeletal disorders such as osteoporosis, renal osteodystrophy, osteopetrosis and diabetic bone disease [2, 10, 11].

1.1.1 Bone forming osteoblasts

Osteoblasts, from Greek ὀστέο (osteo) "bone" and βλαστάνω (blastano) "germinate", state as the sole mononucleated cells able to generate bone in vertebrates [12]. Osteoblasts originate from MSCs upon specific genes expression. MSCs commit to osteoprogenitor cells following the expression of Runt-related transcription factor 2 (RUNX2) and Osterix. These pre-osteoblasts further differentiate into immature and then mature osteoblasts that secrete an organic matrix primarily composed of type I collagen, which forms dense, parallel, and cross-linked layers that accommodate calcium phosphate in the form of hydroxyapatite crystals [13]. When unmineralised, the bone matrix is referred to as osteoid [3].

Osteoblasts present with a cuboidal shape, nuclei rich in euchromatin (genetically active form of chromatin), and abundant rough endoplasmic reticulum and mitochondria; these morphological characteristics reflect the activity of osteoblasts as protein synthesising cells [12, 14]. In the bone matrix context, osteoblasts secrete alkaline phosphatase (ALP) to elevate phosphate concentrations for bone mineralisation [15]. ALP is a key indicator of bone formation and is frequently used as a marker for MSCs osteogenic activity *in vitro* [16]. In addition to ALP, osteoblasts secrete other non-collagenous proteins, crucial for the bone matrix organisation,

e.g. osteonectin, osteocalcin (OCN), and osteopontin (OPN). Osteonectin binds to both collagen and hydroxyapatite crystals initiating bone mineralisation in skeletal tissues [17, 18], whilst OCN works as an indicator of osteoblast activity and as a signalling molecule, with minor effects on bone mineralisation [10, 19]. OPN regulates hydroxyapatite crystal growth and the activity of osteoclasts, stimulating bone resorption [20].

During a standard bone remodelling cycle, osteoblasts have a limited life cycle of about 3 months. After their formation, osteoblasts can (1) be embedded in the bone matrix becoming osteocytes, (2) undergo apoptosis, or (3) become inactive on the bone surface as bone lining cells [14, 21] (**Figure 1.1**). The process by which osteoblasts are entrapped into the osteoid before mineralisation is known as osteocytogenesis. The osteoid-embedded osteoblasts become osteocytes and are contained in small chambers of the calcified matrix called lacunae. Osteocytes act as mechanotransducers following the formation of dendritic processes, which enable networking with neighbouring osteoblasts and osteoclasts [21]. As discussed later, osteocytes play an active role in the bone remodelling process.

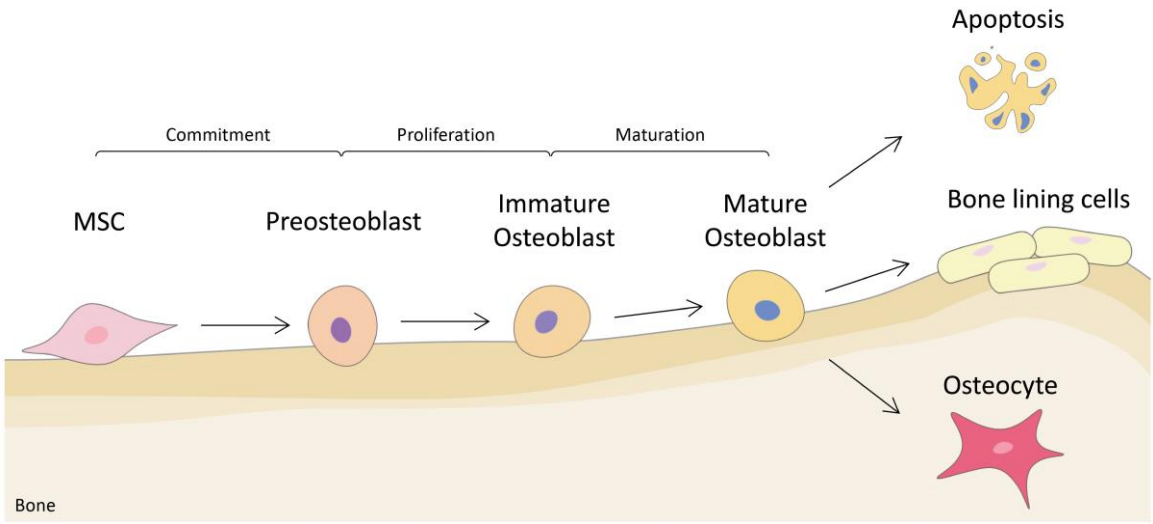


Figure 1.1 Cell fate of bone forming-osteoblasts. The process of osteoblast differentiation begins with the commitment of MSCs towards preosteoblasts, which further proliferate to immature osteoblasts before becoming mature cells. Mature osteoblasts can subsequently differentiate into bone lining cells, osteocytes (within the mineralised osteoid), or undergo programmed cell death (apoptosis).

1.1.2 Regulation of osteoblast differentiation

Throughout the years, a considerable number of morphogens, signalling pathways, and transcriptional regulators have been identified as involved in osteoblasts differentiation [1]. Among other factors, RUNX2 expression emerged as pivotal for MSCs osteogenic differentiation into osteoblasts. RUNX2 is a transcription factor, member of the Runt homology domain transcription factor family. *In vivo* experiments showed that RUNX2 mutations interfere with osteoblast activity [1, 22]. Indeed, RUNX2-null mice models lacked osteoblasts and consequently bone formation [23, 24]. RUNX2 is upregulated in differentiating MSCs, pre-osteoblasts, and immature osteoblasts, but its expression decreases in mature osteoblasts [22]. Moreover, the up-regulation of RUNX2 triggers the expression of the most important bone matrix protein genes, e.g. type I collagen (Col1a1), Osteopontin, OCN [24]. Apart from RUNX2, the RUNX family also consists of RUNX1 and RUNX3, which play a role in the maturation of chondrocytes, and thus in endochondral ossification [1]. The transcription factor Osterix is similarly upregulated in MSCs and immature osteoblasts, being equally fundamental for MSCs osteogenesis (**Figure 1.2**). In fact, osteoblasts of Osterix-deficient murine embryos did not differentiate leading to suppression of both intramembranous and endochondral ossification [1, 24, 25]. Furthermore, Osterix homozygous deletion was fatal for new-born mice, which developed breathing issues [25].

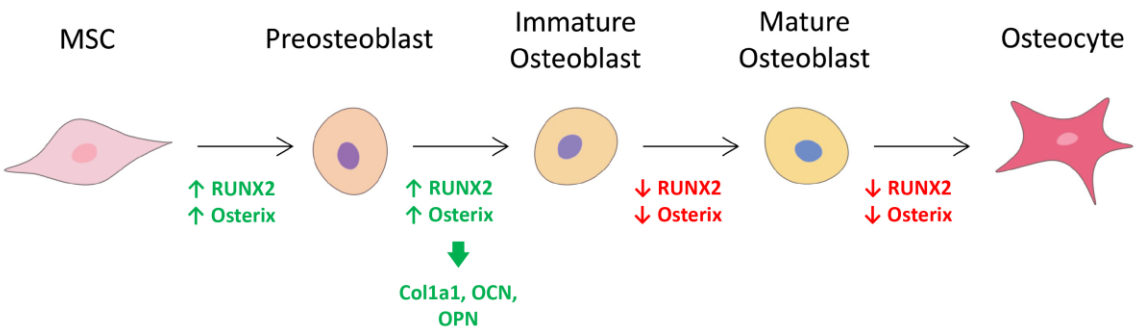


Figure 1.2 RUNX2 and Osterix expression during osteoblast differentiation. RUNX2 and Osterix expression is crucial during the early stages of osteogenic differentiation, from MSCs commitment to preosteoblasts and further differentiation into immature osteoblasts, stimulating the expression of bone matrix genes (e.g. Col1a1, OCN, OPN). By contrast, immature osteoblasts maturation and terminal differentiation are characterised by RUNX2 and Osterix downregulation.

Considering the central role of RUNX2 in osteogenesis, its expression is promoted by the activation of 2 main signalling pathways: Wingless-related integration site (Wnt)/β-catenin and bone morphogenic protein (BMP)-2 [1, 26]. Wnt/β-catenin signalling pathway, also known as canonical Wnt signalling, is highly conserved throughout different species and plays a fundamental role in regulating bone and other tissues development and homeostasis [27, 28]. This pathway promotes osteoblast proliferation, maturation, and inhibits osteoblast apoptosis [29]. Wnt proteins activate their canonical signalling pathway by binding to the ternary complex of Frizzled transmembrane receptor and lipoprotein receptor-related protein (LRP) 5/6, inhibiting glycogen synthase kinase-3 beta (GSK3β) activity and stabilising the cytoplasmic β-catenin. Non-phosphorylated β-catenin translocates to the nucleus to bind the T-cell factor (TCF)/lymphoid enhancer factor (LEF) transcription factors: this action culminates with Wnt-responsive genes transcription [28]. In the absence of Wnt ligands, canonical Wnt signalling is inactivated by GSK3β, which phosphorylates β-catenin determining its ubiquitination by E2 ligases and proteasomal degradation [26] (**Figure 1.3**). Activating mutations of LRP5 result in bone mass increase, whilst inactivating mutations lead to bone loss [1]. Similarly, β-catenin-null transgenic mice developed a severe osteopenia, with an increased osteoclast activity; on the contrary, a constitutive expression of β-catenin increased bone deposition and suppressed osteoclast functions [30]. Wnt negative regulators, such as Dickkopf (DKK)-1/2 and sclerostin, bind to LRP5/6 receptors, mimicking Wnt ligands. In contrast, secreted frizzled-related proteins (sFRPs) bind to Wnt proteins, thus preventing their binding to Frizzled and LRP5/6 receptors. Murine models with Secreted frizzled-related protein 1 (sFRP1) deletion exhibited high bone mass, thus supporting the Wnt signalling role importance in maintaining the skeleton bone mass [22]. Both *in vitro* and *in vivo* studies revealed that the activation of Wnt pathway in turn activates RUNX2 promoter and induces its gene expression in osteoprogenitor cells. Gaur *et al.* characterised RUNX2 promoter, identifying a functional TCF1 binding site. Hence, once Wnt is activated, β-catenin translocates to the nucleus to bind TCF1 on the RUNX2 promoter, inducing its expression [22].

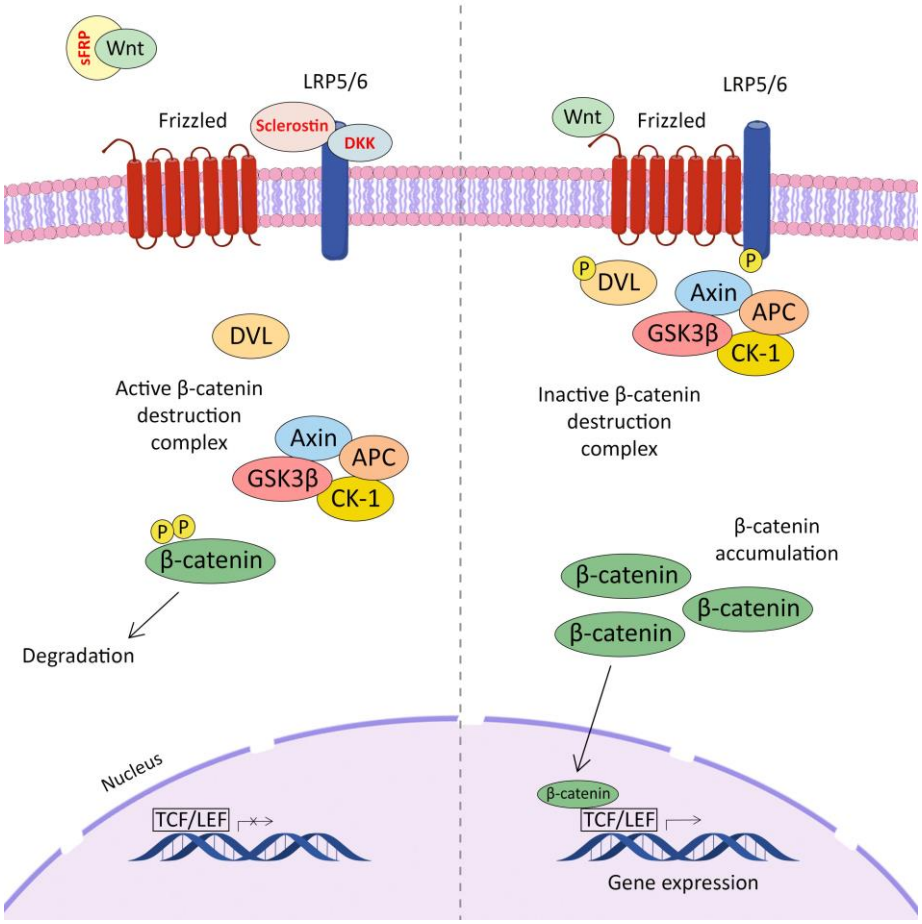


Figure 1.3 Wnt/β-catenin signalling pathway. Wnt proteins activate their canonical signalling pathway by binding the ternary complex of Frizzled transmembrane receptor and LRP5/6; dishevelled (DVL) phosphorylation inactivates the disruption complex leading to the translocation of β-catenin to the nucleus to bind the TCF/LEF transcription factors: this action culminates with Wnt-responsive genes transcription and osteogenic differentiation (right panel). When Wnt signalling is suppressed by specific inhibitors, such as Sclerostin, DKK-1/2, and sFRP, unphosphorylated DVL recruits the disruption complex: β-catenin is phosphorylated and ubiquitinated in the cytoplasm and so degraded (left panel). Abbreviations: adenomatous polyposis coli (APC), casein kinase 1 (CK-1).

As well as Wnt/β-catenin pathway, RUNX2 expression is also induced by BMP-2. BMP-2 is part of the transforming growth factor beta (TGF-β) superfamily of growth factors, which accounts for more than 30 bone morphogenic proteins (BMPs) [1, 31]. Throughout the years, BMP-2 has been described as an osteogenesis key factor that exerts its functions by binding to BMP receptor (BMPR)-2. This bond activates BMPR-1 and transmit the signal to Smad 1/5/8, the receptor substrates. Smad 1/5/8 make a complex with Smad 4 in the cytoplasm and translocates into the nucleus, where it activates RUNX2 [1, 32]. The use of BMP2 blocking

antibodies *in vitro* inhibited RUNX2-dependent osteoblast differentiation and osteogenic gene expression, therefore supporting the importance of BMP-2/Smad signalling in RUNX-2 stimulated osteogenesis [32, 33].

In summation, both β-catenin and BMP-2/Smad signalling orchestrate osteoblasts differentiation by inducing RUNX2 expression, which proved essential for osteoblast differentiation and bone formation.

1.1.3 Osteoblast-osteoclast coupling

Bone homeostasis is strictly dependent on osteoblast-osteoclast communication. Bone remodelling is a dynamic and highly regulated process, where bone formation and resorption alternate in a balanced pattern to maintain normal skeletal structure and function. This physiological process is performed by a functional and temporary structure called basic multicellular unit (BMU). The human adult skeleton accounts for 1 to 2 million active and anatomically separate BMUs, that work asynchronously to guarantee the replacement of old bone with new bone [34]. In addition to osteoblasts and osteoclasts, a BMU also benefits from the activity of osteocytes, bone lining cells, and blood vessels [14]. While osteoblasts and osteocytes, as well as bone lining cells, derive from MSCs, multinucleated osteoclasts originate from hematopoietic stem cells (HSCs) differentiation and are responsible for resorbing organic and inorganic components of bone matrix [35].

A bone remodelling cycle is characterised by three coordinated phases: resorption, reversal, and formation [2, 36]. Nonetheless, some authors refer to two more phases, considering osteoclast activation as an independent phase that precedes the resorption phase, and the formation phase as followed by the termination/mineralisation phase [37, 38]. Be that as it may, a remodelling cycle begins with the recruitment and activation of osteoclast precursors from the circulation, that start resorbing bone. This step is orchestrated by osteoclastic release of hydrochloric acid, which leads to the dissolution of inorganic matrix components (mainly hydroxyapatite crystals) [39]. Upon acidification, specialised metalloproteinases, proteases (e.g. Cathepsin K), and phosphatases, such as tartrate-resistant acid phosphatase (TRAP), degrade type I collagen-rich organic matrix. Osteoclasts finally undergo apoptosis and bone resorption switches to bone formation [37, 38]. Although the nature of this switch remains poorly understood, it certainly depends upon osteoclast-osteoblast

coupling. During bone resorption, the acid pH generated by osteoclasts is responsible for the release and activation of bone matrix growth factors, such as TGFβ, BMPs, and insulin-like growth factor (IGF)-1/2, that in turn stimulate osteoblast differentiation and osteoblastic bone formation [37, 40, 41]; hence, osteoblasts form new bone by releasing osteoid and mineralising it. Finally, as aforementioned, osteoblasts undergo apoptosis, become bone lining cells, or differentiate into osteocytes after being entrapped into the osteoid (**Figure 1.1**).

The communication between osteoblasts and osteoclasts is essential to initiate intracellular signalling. Osteoclast coupling signals regulate osteoblast differentiation and activity. As above-stated, osteoclasts stimulate osteoblastic bone formation by favouring the release of bone matrix growth factors. Together with the growth factors like TGFβ, BMPs, IGF-1/2, platelet-derived growth factor composed of two B subunits (PDGF-BB) is thought to contribute to the coupling mechanism. PDGF-BB stimulates blood vessel formation and is both released from bone matrix and secreted by osteoblasts and osteoclasts [40, 41]. In particular, preosteoclast release of PDGF-BB in bone marrow promote MSCs differentiation into osteoblasts and bone formation [42]. Osteoblast activity can also be promoted by direct cell-cell contact with proteins expressed on the osteoclast cell membrane. For example, osteoblasts secrete receptor activator of nuclear factor kappa-B ligand (RANKL) that binds to its receptor (RANK) on osteoclasts precursors, stimulating osteoclastogenesis during the resorption phase. In the formation phase, osteoblasts produce the decoy receptor osteoprotegerin (OPG) that inhibits osteoclast maturation by sequestering RANKL [36]. Osteocytes can also influence the bone remodelling process by producing Sclerostin and DKK-1/2 to negatively regulate Wnt signalling and subsequent bone formation (**Figure 1.4**). Indeed, Sclerostin and DKK-1/2 bind to LRP5, preventing Wnt ligands association [43]. On the other hand, the bone formation phase is characterised by low levels of these factors, thus promoting bone deposition [36]. Overall, different factors regulate the RANKL/RANK/OPG pathway; tumour necrosis factor alpha (TNFα), IL-1, and parathyroid hormone (PTH), for example, induce osteoblast RANKL release, therefore promoting osteoclast activation. By contrast, oestrogen and BMP2 increase OPG expression, limiting osteoclastogenesis and stimulating bone formation [37, 44].

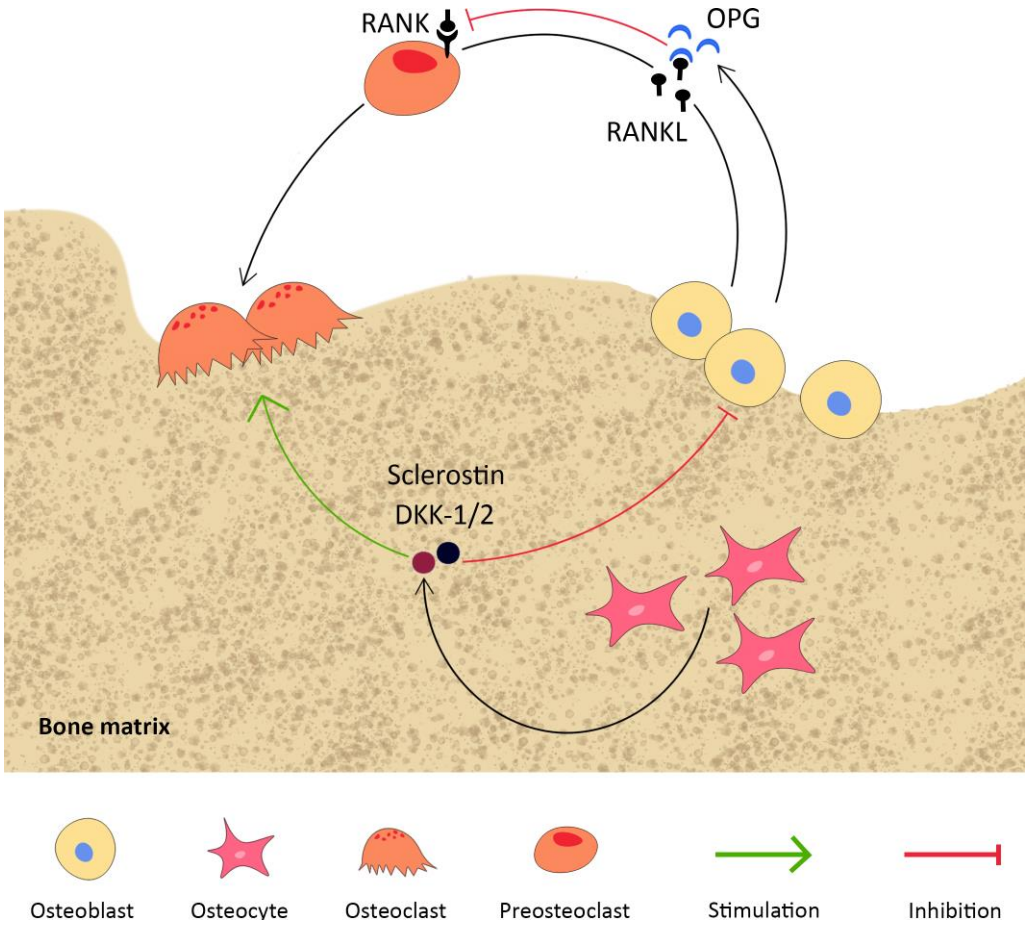


Figure 1.4 RANKL/RANK/OPG signalling pathway. Bone resorption performed by osteoclasts is followed by new bone formation in order to fill the lacunae and restore the homeostatic levels of bone. Osteoblast-produced RANKL signals through RANK-expressing preosteoclasts to induce their terminal differentiation into osteoclasts; osteoclast activity is also supported by osteocyte-released Sclerostin and DKK-1/2, which inhibit osteoblast functions (bone resorption phase). Conversely, OPG secreted by osteoblasts suppresses osteoclast activity by sequestering RANKL, thus inhibiting RANKL-RANK binding (bone formation phase).

The physiological balance of osteoblast and osteoclast activity culminates in new bone formation; impairment of this balance leads to skeletal diseases, such as osteoporosis, osteopetrosis, and Paget's disease of bone [10]. Oestrogen deficiency, the main cause of post-menopausal osteoporosis, increases IL-1 and TNF expression, which in turn upregulate IL-6 and promote osteoclastogenesis; as a result, osteoclastic bone resorption is not adequately compensated by osteoblastic bone deposition, increasing bone weakness and the fracture risk [10, 45]. In contrast, osteopetrosis affects bone remodelling as a consequence of osteoclast hypoactivation and the improper organic matrix digestion, leading to overgrowth of

abnormally organised bone, thus increasing bone fragility [10]. Paget's disease of bone is characterised by an excessive osteoclastogenesis and consequent bone resorption compensated with overactivation of osteoblasts. As a result, the new bone formed is unstructured and mechanically unstable [46]. Understanding how bone remodelling and precursor commitment is impaired in disorders that adversely affect bone mass and structure may lead to new therapeutic targets to reduce patient morbidity via the development of innovative treatments.

1.1.4 Bone loss-related pathologies: osteoporosis and diabetes

Osteoporosis, or porous bone, is a worldwide disease that affects hundreds of millions of people, especially postmenopausal women [47]. It is a skeletal disorder characterised by reduced bone strength and a consequent increase in the risk of fractures [48]. Also, the bone quality of osteoporotic patients is altered because of micro-architectural deterioration [49]. Therefore, both bone density and quality are fundamental factors in determining bone strength and their loss is crucial in osteoporosis development. Around 28 million people (22 million of whom are women) in 27 countries of the European Union (EU27) were estimated to have been diagnosed with osteoporosis [50]. The cost of fractures was estimated around 32 billion Euro per annum and, due to the ageing population, a 25% increase is expected by 2025 [50].

Bone mineral density (BMD), as assessed by dual x-ray absorptiometry (DEXA), is the gold standard for the diagnosis of osteoporosis [51]. The DEXA results reflect the differences, in standard deviations, from the peak bone density achieved in early adulthood and the patients BMD [49, 52]. DEXA results are presented in terms of T-score and the World Health Organisation (WHO) functionally defines osteoporosis as bone density T-score equal or below -2.5 [48]. Due to difficulties to obtain precise measurements because low BMD values do not always reflect a high risk of fragility fractures in people, there is a controversy among experts concerning the use of this diagnostic criterion [48, 53]. Osteoporosis can be considered as primary or secondary. Primary osteoporosis affects both males and females at all ages with a greater prevalence in postmenopausal women and older men. On the other hand, secondary osteoporosis occurrence is related to medications (e.g. glucocorticoids), or diseases (e.g. endocrine disorders, diabetes) [48]. Furthermore, several studies associate the diagnosis of

osteoporosis with risk factors including increased age, low levels of endogenous oestrogens, low body mass index (BMI), family history of osteoporosis and bone fractures, and tobacco and alcohol use [48].

Diabetes mellitus, known simply as diabetes, is a serious and chronic disease characterised by hyperglycaemia as a result of impaired insulin secretion, activity, or both [49, 54]. The destruction of β-cells in pancreatic islets, and the consequent absence of insulin production, results in the development of type 1 diabetes (T1D). Type 2 diabetes (T2D) is far more common worldwide, caused by insulin-resistance in those tissues physiologically sensitive to its action (i.e. liver, skeletal muscles, adipose tissue) [55]. The global diabetes prevalence in 2019 was estimated at 463 million people and it is predicted to rise to 700 million by 2045 [54]. T1D is an autoimmune disorder, the exact causes of which are not entirely clear, whereas the onset of T2D is largely attributable to ageing, obesity, diet, sedentary lifestyle, and genetic factors [54]. Indeed, obesity is recognised as the greatest risk factor for T2D [56].

In 1990, Bouillon introduced the term *diabetic bone disease* to indicate changes in bone remodelling, growth, mineral density and fragility fracture as a consequence of diabetes occurrence [57]. As opposed to T1D, T2D is related to an increased fracture risk and a paradox characterises this association [49]. Specifically, people with T2D frequently have higher BMD than those diagnosed with T1D or healthy, age-matched subjects, although they have a greater risk of fragility fractures [53]. For this reason, as above mentioned, BMD cannot be the only parameter to consider and the elevated risk of fracture may be related to an altered bone quality [58]. It seems that the bone microarchitecture may be negatively affected in patients diagnosed with T2D; the trabecular bone score, a non-invasive method based on DEXA image of the lumbar spine, is lower in T2D patients compared with non-diabetic controls, indicating an impaired bone structure, and thus a higher risk of fragility fracture [58, 59]. However, at present there are no validating studies for fracture risk prediction in patients diagnosed with T2D [58].

The pathogenesis of the bone quality impairment in diabetes patients is hard to understand because it depends on several factors. As a result of insulin-resistance, chronic hyperglycaemia could affect the bone integrity and quality by non-enzymatic glycosylation of several proteins with long half-life, mainly type I collagen [60]. This action leads to the formation of advanced glycation end products, found in high levels in T2D patients' serum and bone

matrix, altering bone cells homeostasis and resulting in delayed fracture healing [55, 58]. An impaired micro-vascularisation exists in diabetic patients that may impair bone strength, although comprehensive evidence supporting this statement is still lacking [58]. Metabolic diseases are often associated with a chronic inflammation and both T1D and T2D are strongly associated with high levels of pro-inflammatory cytokines (i.e. TNFα, IL-1, IL-6) that affect the differentiation and viability of osteoclasts [55, 61].

Excessive visceral adipose tissue is frequently observed in insulin-resistance states, and it is thereby associated with T2D. As previously stated, obesity is the most important risk factor in developing T2D and is also connected with a greater risk of bone fractures [56, 58]. Bone homeostasis might be negatively affected due to the secretion of cytokines from adipocytes, i.e. adipokines such as leptin and adiponectin. Their release increases bone turnover by activating osteoclasts and thus increasing bone resorption [58]. In recent years, bone marrow adipose tissue (BMAT) started to be considered as fundamental component in bone health. This type of adipose tissue is increased in people diagnosed with T2D compared with T1D and non-diabetics [55].

1.2 Adipose tissue

Due to its main function, adipose tissue or body fat is mistakenly thought as an inert depot for energy storage. In the last few decades, its role has been reconsidered and adipose tissue emerged as the largest metabolic and endocrine organ of the human body [62, 63]. Adipose tissue is a specialised connective tissue mainly composed of adipocytes or fat cells, which were firstly identified as storing energy in the form of triacylglycerol (TAGs). Adipocytes derive from the progenitors MSCs, which differentiate into pre-adipocytes first and mature adipocytes later guaranteeing the replacement of dying adipocytes [58]. Adipose progenitors were firstly identified and localised by Tang and colleagues, who demonstrated that peroxisome proliferator activated receptor gamma (PPARγ), the major regulator of adipogenesis, was expressed by a population of progenitor cells that committed to adipocytes since the pre-natal period [64]. Furthermore, Tang *et al.* isolated these cells from the adipose stroma, proving their ability to proliferate both *in vivo* and *in vitro* [64]. Similarly, Rodeheffer *et al.* characterised the adipose tissue-derived MSCs (AdMSCs) according to the cell markers they expressed and their spontaneous differentiation into adipocytes *in vivo* [65].

Adipose tissue is not merely composed of adipocytes; indeed, fat cells represent more than 90% of the adipose tissue volume, but they account for about 50% of its cellular content [66]. The non-adipocytic portion is known as stromal vascular fraction and includes preadipocytes, immune cells (e.g. macrophages, neutrophils, lymphocytes), endothelial and smooth muscle cells, and multipotent AdMSCs [67]. The process by which AdMSCs differentiate into adipocyte progenitors (or preadipocytes) and subsequently into mature adipocytes is called adipogenesis. In adult life, approximately 10% of adipocytes are renewed every year as part of the adipocytic turnover [68]. Fat turnover decreases with age as a consequence of the reduced TAGs breakdown into free fatty acids (FFAs) and glycerol, process known as lipolysis. A dysregulated fat turnover also contributes to metabolic disorders development; indeed, adipose lipid turnover diminishes in obese and dyslipidaemia-affected subjects, which will show older and dysfunctional adipocytes [69].

In summary, adipose tissue exerts different physiological functions, with a pivotal role in energy homeostasis. Different types of adipose tissue have been described so far, depending on their body location and main functions; also, a plethora of factors and signalling pathways regulate the adipocytic differentiation, therefore determining health adipose tissue expansion and renewal [70].

1.2.1 Features and functions of adipocytes

As previously stated, adipose tissue is now considered as a complex organ, with more than the mere energy storing capability. In mammals, five types of adipocytes, and hence five types of adipose tissue, can be identified: white, brown, beige, pink, and yellow (**Figure 1.5**). Each type of adipose tissue differs from the others, depending on their location, lipid content, and function [62, 71].

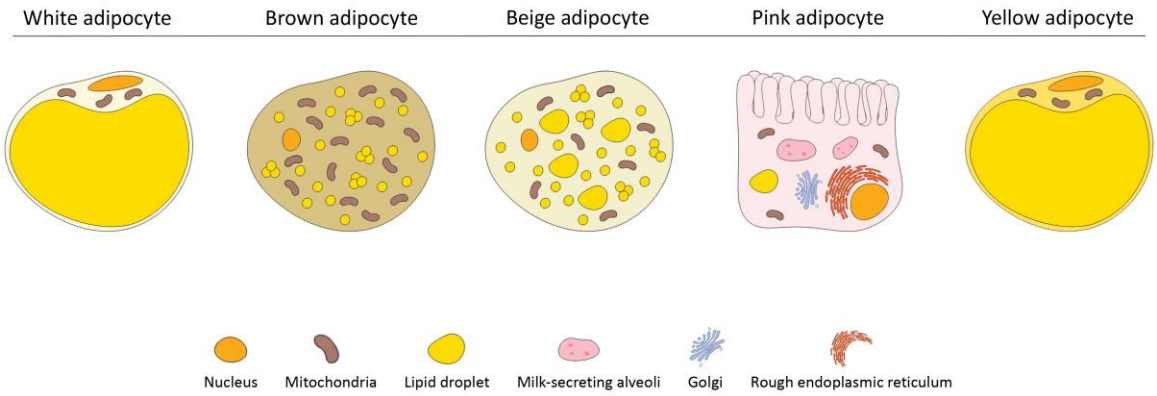


Figure 1.5 Different types and functions of adipocytes. Five types of adipocytes display different features and functions, according to their intracellular content (number of mitochondria, lipid droplets, milk secreting alveoli and organelles, i.e. Golgi and rough endoplasmic reticulum) and location (subcutaneous and scapular areas, within subcutaneous white adipose tissue, bone marrow cavity). Their functions vary from energy storage (white/beige adipocytes) to thermogenesis regulation (brown/beige adipocytes), from milk production (pink adipocytes) to osteo-adipogenesis regulation (yellow adipocytes).

White adipose tissue (WAT) is the most abundant adipose tissue, accounting for 10% of the total body weight. It is located subcutaneously in thighs, pubic regions and abdomen, as well as viscerally, thereby surrounding internal organs (e.g. liver, intestines) [67, 71]. WAT major role is to store TAGs and to release FFAs (and glycerol) for adenosine triphosphate (ATP) synthesis, thereby maintaining the energy homeostasis. White adipocytes originate from mesodermal myogenic factor 5 (Myf5)-negative MSCs [72]; WAT adipocytes present with a spheric shape and contain a single large lipid droplet that force the other cellular organelles (mitochondria and nucleus) to be packed on the side. They are between 25 and 200 μm in size, reflecting the fact that these cells can expand in response to metabolic stimuli and energy demand. The physiological expansion of WAT depends on the increase of adipocyte size (hypertrophy) and/or number (hyperplasia or adipogenesis) [67, 68, 71]. Reduced WAT plasticity has often been pointed at as a crucial determinant of metabolic dysregulations. Indeed, according to Arner and colleagues' work, hypertrophy of WAT was linked to insulin resistance and high levels of circulating insulin, whilst an increased number of small adipocytes (hyperplasia) resulted in better glycaemic profiles [73]. Dysfunctional WAT can also be observed in obese subjects, in which adipose tissue does not expand sufficiently to store the caloric excess. This condition leads to ectopic fat deposition (i.e. deposition of TAGs in non-adipose

tissue cells) and the consequent "lipotoxicity", which in turn causes insulin resistance and increases the risk of T2D [74, 75]. This state is sometimes referred to as the "lipid overflow hypothesis" [76] and the extreme exemplar state in this respect are the lipodystrophies, where there is a partial or complete absence of subcutaneous WAT leading to severe metabolic dysregulation and profound insulin resistance [77, 78].

Brown adipose tissue (BAT) is mostly present in fetal and infant life and differs from WAT for location, precursor cells, and function. It is found in scapular and subscapular areas, as well as in neck, peri-renal, and para-aortic locations [71]. BAT adipocytes derive from mesodermal Myf5-positive MSCs; it was recently demonstrated that Myf5-positive MSCs can terminally differentiate into either brown adipocytes or myocytes, according to the specific gene expression [72]. Brown adipocytes play a pivotal role in a process known as nonshivering thermogenesis: they metabolise TAGs to generate and dissipate heat. Brown adipocytes contain numerous small lipid droplets and abundant mitochondria, which contribute to the brownish colour [67, 79]. BAT adipocytes express the uncoupling protein 1 (Ucp1), a key regulator of thermogenesis localised in the mitochondrial inner membrane. Ucp1 is a proton transporter that increases the protonic conductance of the inner membrane. Upon fatty acid β-oxidation, heat will be produced at the expenses of ATP via mitochondrial respiration [62, 80]. Moreover, BAT and the related energy expenditure activity seem to exert a protective role against body weight gain [71].

Beige adipose tissue (BgAT) and pink adipose tissue (PAT) have been recently described. BgAT exhibits characteristics of both WAT and BAT and develops within subcutaneous WAT, differentiating from preadipocytes or transdifferentiating from WAT adipocytes [62]. BgAT adipocytes are characterised by numerous and small lipid droplets and many mitochondria, therefore being able to store energy and generate heat. The WAT "beiging" phenomenon can be triggered by various processes, including diet and exercise, suggesting that BgAT adipocytes may protect against metabolic dysfunction through energy expenditure [62, 81]. On the other hand, PAT has been first identified as part of the subcutaneous WAT of female mice at the end of pregnancy and during lactation. These types of fat cells originate from WAT and display a epithelial-like morphology; in fact, as epithelial cells, they contain various organelles (i.e. mitochondria, peroxisomes, Golgi, and rough endoplasmic reticulum) in addition to lipid droplets and milk-secreting alveoli [82, 83].

Another type of adipose tissue located in the bone marrow, known as yellow or bone marrow adipose tissue (BMAT), was described as involved in the regulation of bone metabolism and haematopoiesis [84]. BMAT is situated in the ribs, sternum, vertebrae and medullary cavity of long bones (i.e. tibia, femur, and humerus) and it represents more than 10% of the total fat mass in the adult body [84, 85]. At birth, bone marrow is mainly composed of hematopoietic red blood cells, for this reason called red marrow. During childhood, red marrow is gradually replaced by fat tissue, known as yellow marrow. The BMAT present in these two compartments is histologically different; the one that develops first within the yellow marrow is the constitutive BMAT (cBMAT). On the other hand, the regulated BMAT (rBMAT) arises later in the red marrow [84, 85]. BMAT accumulates centripetally in bones in a time-dependent manner: it replaces most red bone marrow from the age of 25 onwards [85]. Adipocytes are densely packed in cBMAT, accounting for around 90% of the marrow compartment, whilst they are less present in red marrow, where bone remodelling and haematopoiesis is active. While WAT and BAT originate from Myf5-negative/-positive MSCs, it seems that BMAT does not share the same precursor instead differentiating from bone marrow MSCs, even though they have broadly similar gene expression and protein secretion patterns [86]. BMAT displays different and peculiar characteristics if compared with the other types of adipose tissue. Developing within the bone marrow, BMAT impinges on hematopoietic stem cells (HSCs) differentiation into myeloid and lymphoid lineages; although several studies showed that yellow adipocytes impact negatively on haematopoiesis, others highlighted the essential role of BMAT in maintaining haematopoietic homeostasis [84]. Moreover, BMAT contributes to bone homeostasis and energy metabolism by secreting adipokines, which influences MSCs commitment towards osteoblasts/adipocytes and control the activation of osteoblasts and osteoclasts [84, 87, 88].

As such, adipose tissue is one of the most dynamic and complex endocrine organs, as well as a source of heterogeneous populations of cells. Through its extraordinary plasticity, adipose tissue regulates many biological processes including, inter alia, food intake, energy homeostasis, and body temperature [89]. Understanding how adipose tissue adaptability changes may help yielding new insights into the onset and the development of metabolic diseases.

1.2.1.1 Adipose tissue as an endocrine organ

Adipose tissue is considered an endocrine organ upon its capacity to secrete active polypeptides, generally known as adipokines. Adipokines regulate several biological functions, e.g. body weight, appetite, glucose and insulin levels, inflammation, and are released by WAT, BAT, and BMAT adipocytes and preadipocytes. To a lesser extent, adipokines can be released by other types of cells, such as osteoblasts, chondrocytes, and inflammatory cells [90]. Among others, adiponectin and leptin represent the most abundant and best described adipokines [91].

Adiponectin is involved in insulin-sensitivity regulation and has anti-inflammatory properties. Serum levels of adiponectin are used as biomarkers for insulin resistance and cardiovascular diseases, being low in obesity and other metabolic states [92]. Circulating adiponectin targets several tissues, regulating insulin sensitivity and energy metabolism by binding to its receptors adiponectin receptor 1 and 2. The main target tissue of adiponectin is the liver, where it activates AMP-activated protein kinase (AMPK) and suppresses gluconeogenesis, thereby increasing the uptake and storage of glucose [93]. Besides endocrine functions, adiponectin showed to have autocrine and paracrine activities by enhancing the physiological expansion of adipose tissue [94]. Adiponectin overexpression in preadipocytes, for example, enhanced lipid storage and increased adipogenesis [95]. Although it is mainly produced by BMAT adipocytes, its effect on bone metabolism is widely debated: if some studies correlate low serum levels of adiponectin with high BMD, others do not link these parameters together [85]. However, it is known that adiponectin inhibits osteoblasts proliferation and leads to their apoptosis by activating the phosphoinositide 3-kinase (PI3K)-Forkhead Box O1 (FoxO1)-dependent pathway, but also increases bone mass by inhibiting bone resorption due to suppression of the sympathetic nervous system via FoxO1 [84, 85]. Paradoxically, although serum levels of adiponectin decrease with obesity and other metabolic conditions, *in vitro* studies often refer to adiponectin gene (Adipoq) expression as a marker of adipogenesis. Indeed, preadipocytes differentiation was associated with an increased Adipoq mRNA expression in Körner and colleagues' work [96].

Leptin is responsible for the satiety sense in the brain and for storing energy in peripheral tissues through leptin receptor binding; WAT and BMAT of both mice and humans secrete

this adipokine [85]. Circulating levels of leptin are proportionate to the adipose tissue size, thereby reflecting the availability of energy storage. Fasting and weight loss are both associated with low levels of leptin, whilst increased levels correlate with satiety, obesity and diabetes [97]. Moreover, leptin and insulin levels seem to be closely connected, although contradictory studies have been published so far. Insulin infusions showed to maintain or increase plasma leptin concentrations [98], whereas experimental mice displayed increased expression of leptin mRNA after a single insulin injection [99]. On the other hand, leptin suppressed insulin-mediated glucose uptake in rat adipocytes and inhibited insulin gene expression and secretion of both human pancreatic islets and immortalised pancreatic β-cells [100-102]. *In vitro*, leptin inhibited adipogenesis and promote osteogenesis of human MSCs, which highly express the leptin receptor (LEPR) [35, 85]. Thomas *et al.* demonstrated that leptin treatment enhanced osteoblastic differentiation of human MSCs-like cells [103]. In contrast, leptin treatment promoted adipogenesis of LEPR-expressing preadipocytes, whilst studies by Körner *et al.* showed that leptin gene expression increased during preadipocytes differentiation *in vitro* [96].

To sum up, adipose tissue can no longer be considered as an inert tissue with the sole purpose of storing energy in form of TAGs. Indeed, as an endocrine organ and via adipokine secretion, it contributes to maintain other organ functions and metabolic homeostasis by regulating appetite, as well as glucose, insulin, and lipid metabolism [104].

1.2.2 Regulation of adipocyte differentiation

Adipogenesis is the process by which MSCs commit to preadipocytes before differentiating into mature adipocytes and requires the activation of a plethora of signalling pathways, transcriptional factors and genes [105]. The expression of the master transcription factors PPARγ and CCAAT-enhancer-binding proteins (CEBPs) is crucial for adipogenic differentiation, adipose tissue remodelling, lipid storage regulation, and energy homeostasis [105]. In addition, PPARγ expression promotes adipokine (i.e. adiponectin and leptin) secretion, which play a key role in regulating insulin sensitivity, inflammatory signalling, cell proliferation, and adipogenesis [93].

Adipogenesis is fundamental for adipose tissue development and energy homeostasis. Transcriptional regulation of adipocytes has been well investigated and the master regulators

of adipogenesis have been identified [93]. PPARγ is the most studied member of the nuclear receptor superfamily and it is found highly expressed in adipose tissue, liver, colon, and different epithelial cell types. In order to be transcriptionally active, PPARγ heterodimerises with a nuclear hormone receptor (retinoid X receptor – RXR) before binding to the DNA [106]. PPARγ expression is required in the early phases of MSCs adipogenesis [107]. Its overexpression in fibroblasts was sufficient to induce adipogenic differentiation, whilst its deficiency impaired adipogenesis *in vivo*, resulting in lipodystrophy [108, 109]. PPARγ expression was also observed in fully differentiated adipocytes; in fact, PPARγ ablation downregulated the lipid metabolism gene expression and decreased the size and lipid content of mature 3T3-L1 adipocytes [110]. Similarly, PPARγ deletion caused death of mature white and brown adipocytes in murine models [111].

PPARγ regulates adipogenesis together with members of CCAAT-enhancer-binding protein (CEBP) family. During early stages of adipogenesis, CEBP beta (CEBPβ) and CEBP delta (CEBPδ) activate the transcription of CEBP alpha (CEBPα) and PPARγ, regulating cell differentiation. WAT loss and defective BAT development were observed *in vivo* as a consequence of CEBPα deficiency, thus suggesting that CEBPα expression is crucial for adipogenesis [93]. In line with this, CEBPα proved to be important for the differentiation and the maturation of white adipocytes *in vivo* and *ex-vivo* [112]. PPARγ and CEBPα induce the expression of each other to activate the transcription of adipocytic target genes. Madsen *et al.* demonstrated the existence of a PPARγ-CEBPα crosstalk at the chromatin level. These two factors indeed facilitate each other's binding to thousands of genomic binding sites, subsequently recruiting transcriptional co-activators and increasing the transcription rate of adipogenic genes [112].

The activation of several adipogenic signalling pathway often culminates with the transcription of PPARγ and CEBPα [113]. Among them, the activation of IGF-1 signalling pathway showed to induce preadipocyte differentiation *in vitro*. Preadipocytes express IGF-1 receptors, which bind both IGF-1 and insulin; the presence of IGF-1 or insulin is in fact necessary for adipogenic differentiation *in vitro* [113, 114]. A double deletion of IGF-1 and insulin led to a decrease in mice WAT and BAT, thus suggesting that the suppression of IGF-1 signalling has a severe impact on WAT adipogenesis and BAT-related thermogenesis [115].

The peptide hormone insulin is released by pancreatic β-cells in response to blood glucose level increase. Insulin stimulates the glucose uptake by insulin responsive cells, such as mature adipocytes, by inducing the translocation of glucose transporter 4 to the plasma membrane, energy storage through lipid biogenesis (lipogenesis), and diminishing lipolysis [116, 117]. Upon feeding, these mechanisms exert a protective role for the organism; indeed, excessive glucose levels and FFAs release would be toxic and potential trigger factors for the onset of metabolic disorders [116]. In preadipocytes, once insulin binds to its receptor (insulin receptor), the insulin receptor substrate (IRS) and Src homology and collagen protein (SHC) are phosphorylated, triggering a phosphorylation cascade that activates PI3K/protein kinase B (PKB or AKT) and rat sarcoma virus (RAS)/mitogen-activated protein kinase (MAPK) signalling pathways, respectively, which independently induce PPARγ and CEBPα expression. Downstream molecules of PI3K include AKT, mammalian target of rapamycin (mTOR), p70 ribosomal S6 kinase (P70S6K), FoxO1, whilst RAS, rapidly accelerated fibrosarcoma (RAF), MAPK kinase (MEK), extracellular signal-regulated kinase (ERK)1/2 represent the main effectors of RAS/MAPK signalling (**Figure 1.6**) [117-119]. Activation of these signalling pathways culminates with the differentiation of preadipocytes. For this reason, insulin is a key element of the adipogenic cocktail, used to stimulate adipogenesis of precursor cells *in vitro* [113]. Due to its role in lipid and glucose homeostasis, abnormal PI3K-AKT pathway can lead to components of the metabolic syndromes. For example, PI3K/AKT inhibitors, clinically used as anticancer drugs, showed to induce hyperglycaemia and insulin resistance [120].

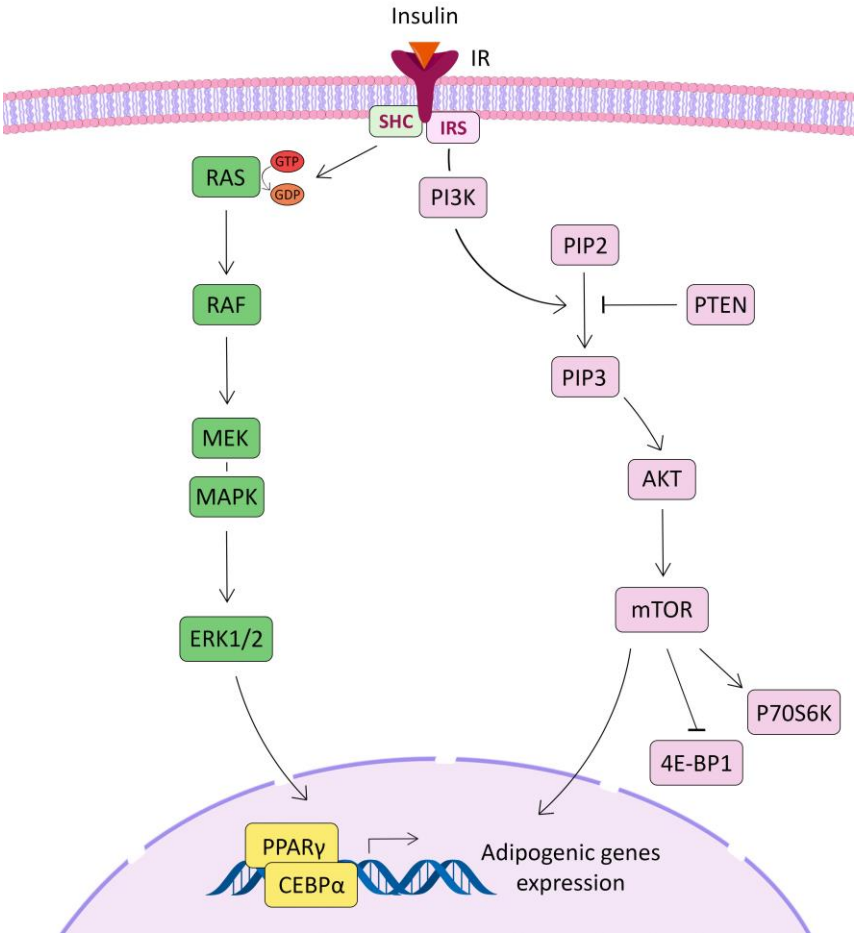


Figure 1.6 PI3K-AKT and RAS/MAPK signalling pathways induce PPARγ/CEBPα expression. Insulin binds to its tyrosine kinase receptor (IR) activating PI3K-AKT (via IRS phosphorylation) and RAS/MAPK signalling pathways (via SHC phosphorylation). Both pathways activation culminates with the expression of PPARγ and CEBPα, which in turn stimulates the expression of adipogenic genes. Abbreviations: phosphatidylinositol 4,5-bisphosphate (PIP2), Phosphatidylinositol (3,4,5)-trisphosphate (PIP3), eukaryotic translation initiation factor 4E (eIF4E)-binding protein 1 (4E-BP1).

Glucocorticoids (GCs), a class of steroid hormones, regulate transcription factors expression. Dexamethasone (Dex), a synthetic glucocorticoid, is a potent inducer of adipogenesis *in vitro*, and hence is included in most adipogenic media. Human preadipocytes express GC receptors and the GC binding promotes PPARγ and CEBPα expression during adipogenesis [113]. Moreover, preadipocyte factor 1 (Pref-1) expression is attenuated by Dex treatment, indicating a possible mechanism through which GCs induce preadipocyte differentiation. Indeed, Pref-1 is highly express by preadipocytes, and its downregulation is necessary for the terminal differentiation into adipocytes [121].

Overall, as will be discussed in the next sections, a certain number of signalling pathways regulate adipogenesis on a non-exclusive basis. As common precursors of adipocytes and osteoblasts, MSCs are highly regulated for their differentiation; their lineage commitment is indeed balanced and orchestrated by diverse pathways and related factors [122]. Nonetheless, the expression of PPARγ and CEBPs is necessary for the transcription of adipogenic genes, determining the commitment of MSCs towards preadipocytes and the final differentiation into mature adipocytes [113].

1.3 Mesenchymal stromal cells as common precursors of osteoblasts and adipocytes

Mammalian adult tissues with regenerative capacity host tissue-specific stem cells that self-renew, proliferate, and differentiate into mature cells, thus reconstituting the damaged tissue. Bone, for example, has a remarkable capacity to self-repair after injury [123]. The presence of non-haematopoietic stromal cells within bone marrow was first suggested more than 130 years ago by Cohneim, a German pathologist who proposed the bone marrow as a source of fibroblast-like cells with wound healing properties [124]. The presence of fibroblast-like cells in the rodent bone marrow was demonstrated by Friedenstein and colleagues in 1976. These cells displayed clonogenic potential *in vitro* and self-renewal ability *in vivo* [123]. Over the years, many researchers confirmed these findings and suggested that these cells also exist in the human bone marrow, from which they can be isolated, cultivated, and differentiated *in vitro*. In 1991, Caplan named them “mesenchymal stem cells”, although their nomenclature has been widely debated. Due to the heterogeneity and stromal origin of these cells, the definition “mesenchymal stromal cells” is considered more appropriate [125, 126]. “Mesenchymal stromal cells”, or “MSCs”, is therefore the nomenclature used in this thesis.

MSCs can thus be defined as adult stromal cells with differentiation and self-regenerative capacity [127]. In 2006, the International Society for Cellular Therapy provided three minimal criteria for their definition: (1) they must adhere to plastic supports, (2) express specific surface antigens (i.e. CD73, CD90, CD105) and lack the expression of others (e.g. CD34, CD45, HLA class II), (3) they must differentiate into osteoblasts, adipocytes, chondrocytes under specific conditions *in vitro* [128]. Although MSCs are commonly known to differentiate into osteoblasts, adipocytes, and chondrocytes, several studies pointed at their role in neural, wound, heart, liver, kidney regeneration, and wound repair. Hence, MSCs primary

characteristics (differentiation multipotency, immunomodulatory effect, growth factors production) make them the optimal candidates for regenerative medicine use [129].

1.3.1 Origin and lineage differentiation of MSCs

Adult MSCs are mainly found in the perivascular "niche", a microenvironment with tissue-specific functions and locations. Within the niche, the extracellular matrix (ECM), offers support to other cells (e.g. immune cells), soluble factors, neural inputs, blood vessels and adhesion molecules (e.g. integrin) [127, 130, 131]. The niches are important in maintaining MSCs homeostasis and proliferation activity; niche-MSCs display a typical asymmetric structure: after cell division, one daughter cell remains anchored to the niche whilst the others leave it to proliferate and differentiate into mature cells [127].

MSCs were initially isolated from the bone marrow, but other sources have been identified as promising for cell harvesting. Indeed, adult tissues such as adipose tissue, tendons, peripheral blood, and foetal tissues such as umbilical cord blood and Wharton's jelly can be processed in order to isolate MSCs [127]. Bone marrow MSCs (BMSCs) reside in the marrow endosteal surface and can be considered as multipotent non-hematopoietic cells able to differentiate into diverse connective tissue cell types. They account for 0.001-0.1% of bone marrow nucleated cells [122]. Due to the fact that BMSCs are collected via bone marrow aspiration, an invasive procedure, other sources of MSCs have been identified to harvest a high concentration of these cells [127, 132]. Adipose-derived MSCs (AdMSCs) are an alternative to BMSCs because adipose tissue is abundant and easy to collect. Although these two populations of cells share similar properties, they are not identical, displaying a diverse phenotype [127]. Indeed, AdMSCs exhibit a lower osteogenic differentiation ability compared to BMSCs [36]. Interestingly, low levels of circulating MSCs have been also discovered in peripheral blood, even though an efficient technique to separate these cells from the whole blood does not yet exist [127]. Circulating MSCs migrate to the injury sites, thereby increasing MSC number under pathological conditions, and share most of the characteristics of MSCs aforementioned [133].

Throughout the years, BMSCs have been widely characterised, although what will be discussed broadly applies to MSCs from other sources despite any morphology or molecular differences. BMSCs commitment is a complex process strictly regulated by different factors

(e.g. hormones, cytokines, transcription factors) that can be produced locally and/or released from peripheral tissues such as WAT/BAT, skeletal muscle, liver or central nervous system (**Figure 1.7**) [35]. Key transcription factors in the commitment of BMSCs to the adipocyte lineage are PPARγ and CEBP family members. Recently, inhibitors of Wnt signalling (Sclerostin, sFRP1, DKK-1/2) have been identified as adipogenic factors by blocking a pathway that otherwise stimulates osteoblastogenesis; all these molecules positively regulate BMSCs commitment towards adipocytes at the expense of osteoblasts, and thus increase adiposity within the bone marrow [35]. On the other hand, delta-like 1/preadipocyte factor 1 (Dlk1/Pref-1) negatively regulates BMSCs differentiation in general, suggesting a role in maintaining these cells in their undifferentiated state. Moreover, IGF-1, the most represented growth factor in the bone matrix, is involved in maintaining bone homeostasis and thus plays an important role in osteoblast differentiation. Regarding BMSCs differentiation towards osteoblasts, TGFβ superfamily members, such as TGFβ itself or BMPs, are involved in MSC self-regeneration and commitment. Furthermore, RUNX2 and Osterix are well known as osteoblast-specific transcription factors [35].

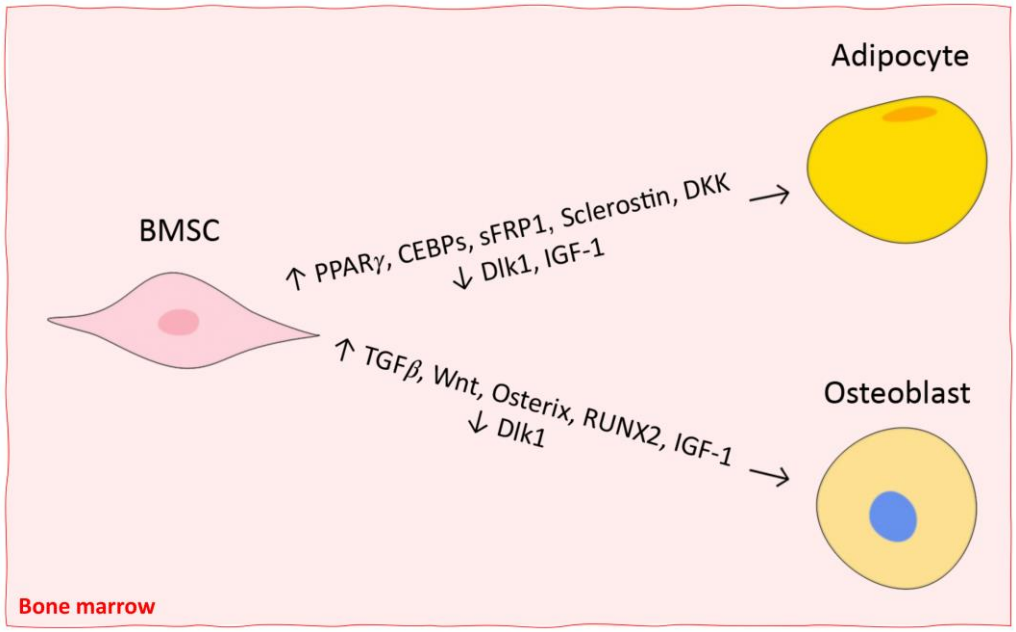


Figure 1.7 BMSCs commitment and differentiation into adipocytes and osteoblasts. Bone marrow consists of a heterogeneous cell population, with BMSCs representing a 0.001-0.1% of the total cells. BMSCs mainly differentiate into adipocytes and osteoblasts by a process regulated via a plethora of transcription factors and secreted molecules.

To sum up, the molecular mechanisms behind MSCs differentiation are intricate. In the next section, the osteo-adipogenesis balance necessary to maintain bone and fat homeostasis and to prevent bone loss-associated pathologies will be discussed.

1.3.2 Regulation of MSCs differentiation into osteoblasts and adipocytes

MSCs differentiation process can be considered as a two-step process, in which the commitment of MSCs to progenitor cells is followed by their complete maturation. During the past decade, it became more evident that MSCs osteogenesis and adipogenesis influence each other as competing events. Some signalling pathways, already mentioned in this work, proved to have a dual role in regulating both osteo- and adipogenesis of MSCs (**Figure 1.8**) [122]. BMPs, for example, exert a role in osteogenesis and adipogenesis depending on the family member considered. High doses of BMP-2 pushed MSCs-like cells (i.e. CH310T1/2) to differentiate into osteoblasts, whilst low doses promoted their adipogenic differentiation [134]. By binding to their receptor (BMPR), BMPs can either activate canonical Smad-dependent pathway (BMP/Smad signalling) or non-canonical Smad-independent pathway (p38/MAPK signalling). BMP/Smad signalling, as aforementioned, induces RUNX2 expression, while p38/MAPK signalling activates PPARγ, stimulating adipogenic differentiation of MSCs [122].

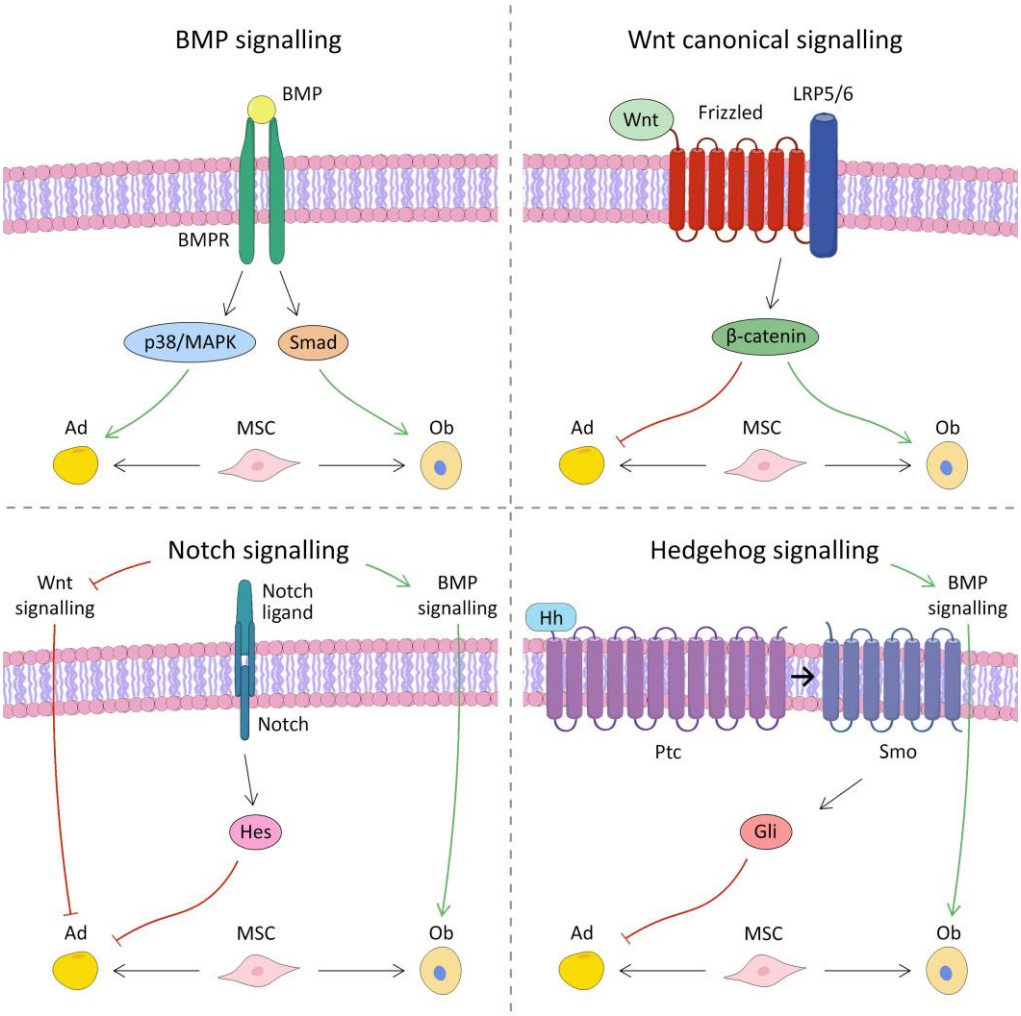


Figure 1.8 Osteo-adipogenic differentiation of MSCs and related signalling pathways. MSCs differentiation fate towards osteoblasts (Ob) and adipocytes (Ad) is critically regulated by several signalling pathways and related factors. In particular, the activation of BMP, Wnt, Notch, and Hedgehog pathways proved to determine MSCs fate by regulating the expression of pivotal transcription factors (RUNX2 and Osterix for osteogenesis, PPARγ and CEBPs for adipogenesis).

The activation of Wnt canonical signalling pathway stimulates MSCs osteogenesis whilst inhibiting adipogenic differentiation. Wnt10b overexpression increased bone mass by stimulating osteogenesis *in vivo* [135], whereas Wnt3a treatment both inhibited and stimulated MSCs osteogenic differentiation *in vitro* [136, 137]. Ross and colleagues showed that Wnt signalling inhibited the expression of PPARγ and CEBPα during preadipocyte adipogenesis [138]. It seems that Axin2 directly inhibits CEBPβ expression, therefore blocking PPARγ and CEBPα transcriptional activity. Consistently, the disruption of Wnt pathway leads to CEBPβ activation [139].

Notch signalling pathway regulates several biological processes, such as cell proliferation, differentiation, and cell death [140]. Notch ligands and notch receptors are single transmembrane proteins associated with adipogenesis; in particular, studies carried out on preadipocytes revealed that Notch signalling both inhibits and stimulates adipogenic differentiation [122, 141]. Hes-1 (i.e. Notch target gene) overexpression in preadipocytes inhibited the expression of both CEBPα and PPARγ, indicating that the activation of Notch signalling impinges on adipogenic differentiation [142]. Similarly, Song *et al.* showed that the inhibition of this pathway promoted MSCs differentiation towards adipocytes by activating PI3K/AKT signalling [143]. Notch activation also inhibited osteogenic differentiation by suppressing Wnt signalling. On the other hand, the crosstalk between Notch and BMP2 signalling promoted MSCs-like cells osteogenic differentiation, thereby confirming that Notch pathway plays a role in both MSCs adipogenesis and osteogenesis [144].

Hedgehog (Hh) signalling pathway has often been associated with MSCs differentiation. Secreted Hh fragments regulate cell activity by binding to two transmembrane proteins, Patched (Ptc) and Smoothened (Smo). Hh ligands bind to Ptc releasing Smo, which activates Cubitus Interuptus transcription factor, known as Gli. Subsequently, Hh target genes are expressed [145]. Hh signalling resulted downregulated during MSCs adipogenic differentiation because of Gli reduced expression. In line with this, Fontaine and colleagues demonstrated that Hh pathway activation negatively affected preadipocytes and MSCs-like cells adipogenic differentiation, as supported by PPARγ and CEBPα downregulation and diminished lipid accumulation [122, 146]. Conversely, Hh signalling promoted MSCs osteogenesis by activating BMP/Smad signalling [147].

Overall, MSCs differentiation to osteoblasts and adipocytes is a finely regulated process. Beside the signalling pathways, MSCs osteo-adipogenic balance can be affected by several biological and biochemical processes. During aging, for example, the reduced osteogenic ability of MSCs increases bone marrow adiposity. Moreover, aged cells display increased levels of reactive oxygen species (ROS) and oxidative stress, which contribute to age-related bone loss and stimulate the adipogenic differentiation via PPARγ expression [122]. MSCs osteo-adipogenesis is also regulated by mitochondrial function and energy metabolism, as will be expanded upon below.

1.3.3 Metabolic requirements of differentiating MSCs

Cell survival, proliferation, and differentiation are energy-dependent processes, thus requiring the oxidation of macromolecules to obtain adequate adenosine triphosphate (ATP) supply. Glycolysis, tricarboxylic acid (TCA) or Krebs cycle, and oxidative phosphorylation (OXPHOS) represent the biochemical pathways that orchestrate cellular metabolism (**Figure 1.9**) [148]. Different substrates can be used to produce energy in form of ATP; however, the amount of ATP molecules produced varies upon the pathway activated [148]. Glucose degradation, for example, produces two molecules of ATP and pyruvate per molecule of glucose, which is later converted into lactate in the cytosol (anaerobic glycolysis). Pyruvate can also enter the mitochondrial TCA cycle after being decarboxylated to acetyl coenzyme A (CoA); TCA cycle generates 2 molecules of ATP per molecule of pyruvate and provides NADH and $FADH_2$ to the electron transport chain for OXPHOS, which finally produces 34 molecules of ATP per molecule of pyruvate (aerobic glycolysis) [148-150]. Beside glucose, Acetyl-CoA can be generated from lipids via β-oxidation and amino acid catabolism [149].

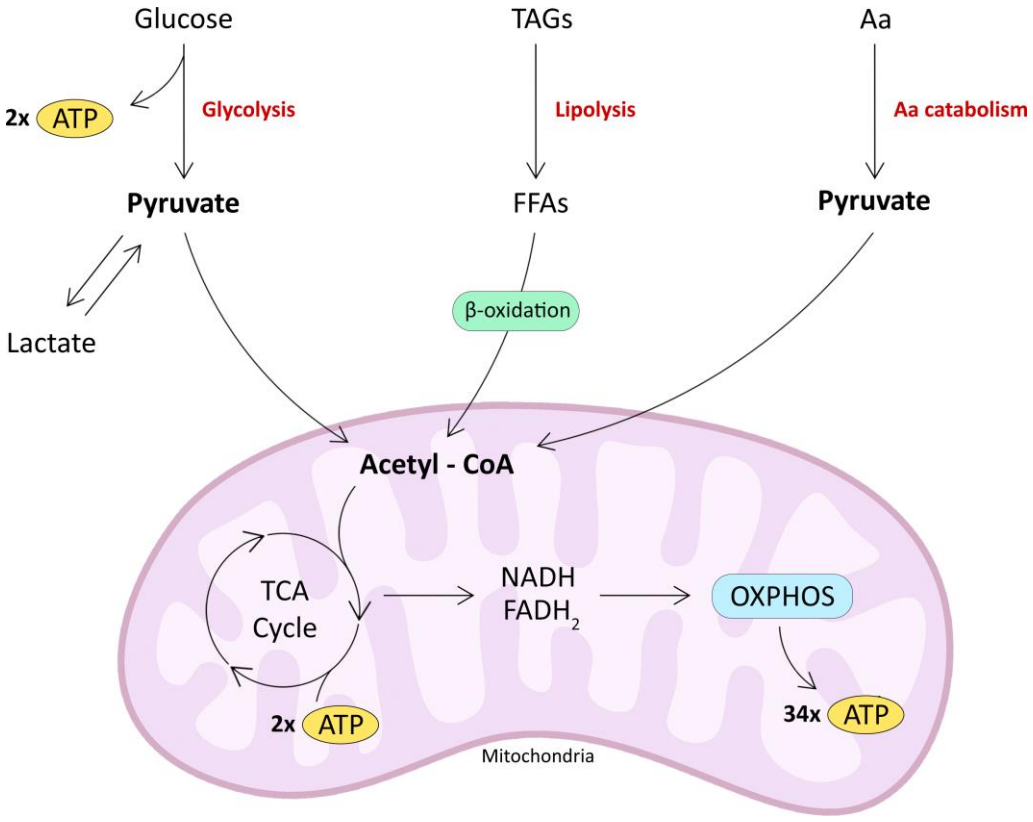


Figure 1.9 Glycolysis, TCA cycle, and OXPHOS. Diverse substrates (i.e. glucose, TAGs, amino acids – Aa) can be degraded to generate Pyruvate and Acetyl-CoA, which enters the mitochondrial TCA cycle

to provide NADH and $FADH_2$ to the ETC for OXPHOS. Via anaerobic glycolysis, pyruvate, lactate, and 2 molecules of ATP are generated; on the other hand, OXPHOS produces 34 molecules of ATP. While pyruvate is released in the cytosol upon glycolysis and Aa catabolism, TAGs degradation releases FFAs that need to be oxidised via β-oxidation to generate Acetyl-CoA.

It recently emerged that mitochondrial function and energy metabolism regulate MSCs self-renewal, osteo-adipogenic differentiation, as well as apoptosis and immunomodulatory properties [151]. Uncommitted MSCs mainly rely on anaerobic glycolysis for ATP generation, which proved sufficient for their "stemness" maintenance [152]. On the other hand, differentiating progenitor cells are characterised by mitochondrial biogenesis, accompanied by reduced glycolysis and increased OXPHOS. The number of mitochondria and the expression of mitochondrial proteins increase to meet the high energy demand of differentiating cells [153, 154]. As aforementioned, OXPHOS-related ATP production is much higher than the anaerobic glycolysis counterpart. Regarding the differentiated cells, BMAT adipocytes and osteogenic cells showed to have different metabolic needs; whilst osteogenic cells use glucose metabolism for energy production, BMAT adipocytes mostly rely on fatty acid metabolism. Adipocytes depend on lipolysis to generate FFAs, which undergo β-oxidation before entering the TCA cycle and producing ATP via OXPHOS (**Figure 1.9**). Although FFAs represent a source of energy, excessive levels exert detrimental effects on osteoblast functions and lifespan [155].

Be that as it may, MSCs lineage-differentiation demonstrated to depend on specific metabolic programming. Tencerova and colleagues used murine BMSCs to determine the metabolic profile and the molecular mechanisms underlying their osteo-adipogenic differentiation [156]. In line with previous studies [157, 158], adipogenic BMSCs mainly relied on OXPHOS for energy production, whereas osteogenic progenitors employed OXPHOS to a lesser extent, preferring glycolysis to generate ATP (**Figure 1.10**). In addition, adipogenic BMSCs displayed an increased expression of insulin signalling genes, as well as lipid metabolism genes (fat specific protein 27 – Fsp27, hormone sensitive lipase – HSL), glucose transporter 4 (Glut4) gene, and bioenergetic genes (uncoupling proteins – Ucp, peroxisome proliferator-activated receptor alpha - PPARα) if compared with the osteogenic BMSCs [156]. It is hypothesised that the higher glycolytic profile of osteogenic BMSCs reflects the needs of these cells to rapidly regenerate bone after fractures or bone remodelling. In fact, anaerobic

glycolysis is a rapid source of energy [156, 159]. On the other hand, BMSCs respond to adipogenic stimuli by increasing mitochondria number and oxygen consumption rate, suggesting that this lineage differentiation requires high levels of energy to proceed [160]. Moreover, mitochondria are the main source of ROS, production of which proved essential for adipogenic commitment, influencing adipogenic genes expression and suppressing osteogenic pathways activation [160].

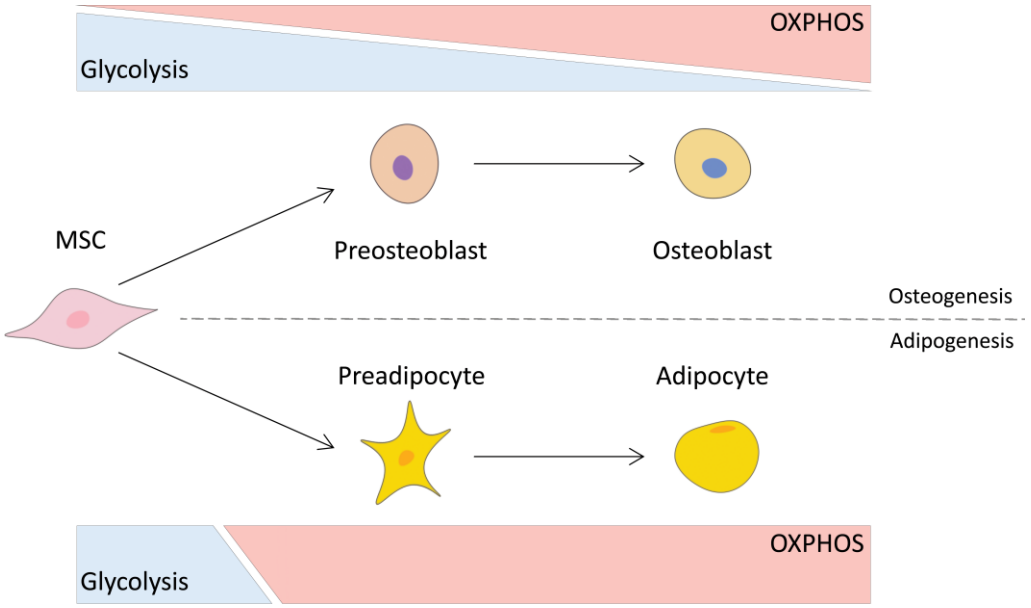


Figure 1.10 Metabolic shift through MSCs differentiation. MSCs differentiation is orchestrated by metabolic changes. During osteogenesis, MSCs rely on glycolysis for energy production, shifting to OXPHOS at the end of the osteogenic differentiation. By contrast, MSCs adipogenesis mostly relies on OXPHOS, thus requiring higher levels of energy to occur.

Conditions such as hypoxia and iron deficiency impact on the metabolic state of differentiating MSCs. Hypoxia is an important characteristic of MSCs niche, where MSCs are maintained in the undifferentiated state, with self-renew capacity and multipotency preserved. In these conditions, MSCs mitochondrial activity is reduced, which is why uncommitted MSCs mostly rely on anaerobic glycolysis. However, under hypoxia and differentiating stimuli, MSCs are more prone to become osteoblasts then adipocytes, as confirmed by increased expression of Alpl, OCN, Col1a1 and reduced expression of PPARγ [161]. Similarly, iron deficiency induced by desferrioxamine (DFO), a hypoxia-mimetic reagent, impinged on the mitochondrial oxygen consumption of MSCs, forcing them to employ

glycolysis for ATP generation when iron levels are reduced [162]. Accordingly, MSCs-like cellular differentiation towards osteoblasts increased, supporting the general idea of osteoblasts-dependency on glycolysis [163]. In contrast, adipogenic differentiation of preadipocytes was suppressed by DFO treatment [164].

1.4 Scavenger receptor class A member 5 (Scara5) as a multifaceted biomolecule

Throughout the years, a plethora of factors involved in the commitment of MSCs has been identified. Scavenger receptor class A, member 5 (Scara5 or SR-A5) emerged as a novel and potential mediator of adipocyte commitment [165]. As its name suggests, it belongs to the scavenger receptor (SR) family of pattern recognition receptors, known as mediators of the innate immune response via recognition of pathogen-associated molecular patterns (PAMPs). In addition, SRs detect and internalise modified lipoproteins, such as acetylated and oxidised low-density lipoproteins (LDL) [166]. Scara5 was identified as ferritin receptor, being able to internalise both H- and L-ferritin [167]. It is therefore conceivable that it plays a role in iron homeostasis. A search on Pubmed.ncbi.nlm.nih.gov made on 18th August 2023 generated a list of 104 papers, half of which correlate Scara5 with cancer. Several types of cancer have been associated with Scara5 downregulation (e.g. colorectal cancer, oral squamous cell carcinoma, breast cancer – BrCa), thus suggesting that its overexpression was sufficient to suppress cancer cell proliferation, migration, invasion [168-170]. Hence, among the other members of its family, Scara5 is a multifaceted receptor with various roles.

1.4.1 Scavenger receptor class A members

Due to their structural differences and diverse specificity in ligand-binding, SRs have been divided into 11 classes (A-L) [171]. The class A includes Scara5 and another 4 members, all type II trimeric glycoproteins with intracellular N-terminal and extracellular C-terminal domains: macrophage scavenger receptor 1 (MSR1 or SR-A1), macrophage receptor with collagenous domain (MARCO or SR-A6), scavenger receptor class A member 3 (Scara3 or SR-A3) and scavenger receptor class A member 4 (Scara4 or SR-A4) [166, 171] (**Figure 1.11**). Proteins with a scavenger receptor cysteine rich (SRCR) domain were found involved in pathogen recognition, as well as endocytosis and immune response, although its role in class A SRs is not fully understood. The cellular expression of class A SRs differs among members: MSR1 and MARCO

are mainly expressed on macrophages whilst Scara3, Scara4, and Scara5 on the membrane of epithelial cells of different organs (e.g. testis, trachea, lung, bladder, small intestine) [166, 172]. MSR1 and MARCO are found expressed on human and murine immune cells (i.e. monocytes, macrophages, mast cells, dendritic cells), exerting a role in binding to surface molecules of Gram-positive and Gram-negative bacteria (e.g. lipopolysaccharide, lipoteichoic acid) [171, 173]. Coherently, MSR1- and MARCO-deficient mice present with low levels of circulating antibodies against bacterial polysaccharides [174]. Scara3 exerts a protective role from ROS being expressed in response to oxidative stress, whilst Scara4 and Scara5 bind to bacteria *in vitro* [166].

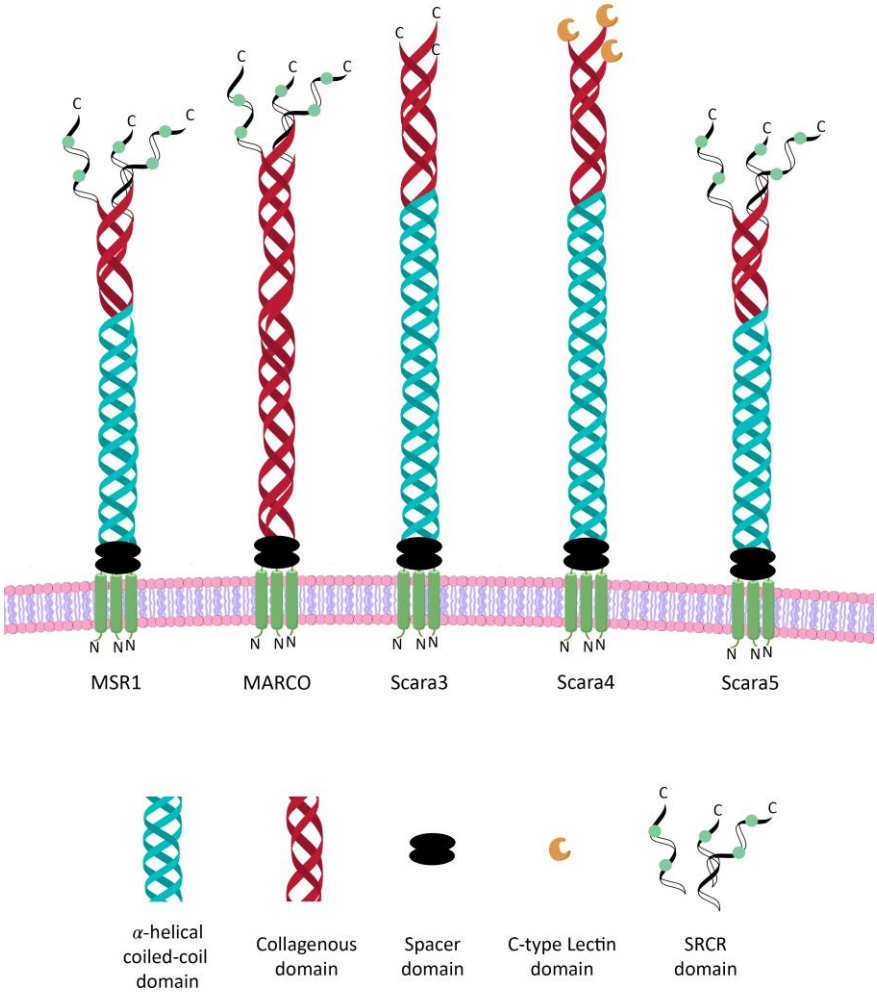


Figure 1.11 Scavenger receptor class A members. SR class A members mainly differ for their C-terminal domain; MSR1, MARCO and Scara5 share a highly conserved terminal SRCR domain, while Scara3 and Scara4 possess a collagenous domain and a C-type lectin domain, respectively. MARCO is the only member that presents a long extracellular collagenous domain.

Different roles have been attributed to Scara5 so far. As with the other proteins of class A SRs, Scara5 has been found to bind to Gram-positive and Gram-negative bacteria *in vitro*, even though this capacity has not been demonstrated *in vivo* [172]. Scara5 recognises polyanionic motifs in general, and it was thought to be unable to bind and internalise modified LDL as the other members of SRs class A [172]. However, Cheng and colleagues recently discovered that MSR1, MARCO, and Scara5 can recognise acetylated and oxidised LDL via their SRCR domain in a calcium-dependent manner [175]. Some members of SRs family are therefore considered potential proatherogenic molecules, promoting cellular cholesterol accumulation and the development of atherosclerotic lesions [176]. However, there are not studies that prove a direct impact of SRs on atherogenesis *in vivo*. Scara5 has been found abundantly expressed by epithelial cells and fibroblasts of diverse organs, but not by macrophages [172, 177, 178]. Nonetheless, Scara5 emerged as a singular member of SRs class A because of its roles as ferritin receptor, cancer suppressor gene, and as a novel adipogenic marker.

1.4.2 Scara5 in human diseases: GWAS catalog

Genome wide association studies (GWAS) aim to screen the entire genome of large numbers of individuals in order to associate human genomic variants (e.g. single nucleotide polymorphisms – SNPs, copy number variants, sequence variations) to specific traits and diseases [179]. GWAS results have been incorporated in the NHGRI-EBI GWAS catalog, which presents genetic variants that exhibit statistically significant associations with the trait/s of interest.

According to GWAS catalog, Scara5 variants have been associated with 29 different traits, 20 of each have been linked to various blood protein measurements (**Table 1.1**). Notably, 10 of the Scara5 variants have been reportedly associated with changes of protein measurement (i.e. Tenascin and Chymotrypsin-like elastase family member 1), and a further 12 variants with blood-clotting protein measurement (i.e. factor VIII and von Willebrand factor – vWF). Scara5 variants have also been associated with non-disease traits, such as body height. To date, there have been no studies investigating the nature and impact of these variants on biological aspects. In 2019, Swystun and colleagues confirmed that Scara5 is an endocytic receptor for vWF, although they concluded that it might only have a modest effect on vWF clearance in humans [177].

Table 1.1 Scara5 variants and associated traits in the GWAS catalog

Variant and risk allele	P-value	Risk allele frequency	Trait(s)	Study accession	Location	Author
rs17481534-?	$4x10^{-9}$	/	Alzheimer disease, polygenic risk score	GCST90132260	8:27885545	[180]
rs200343341-?	$8x10^{-7}$	0.9698	Behavioural disinhibition measurement	GCST007623	8:27933329	[181]
rs2727013-A	$3x10^{-10}$	0.66984375	Blood protein measurement	GCST006585	8:27930467	[182]
rs2727013-A	$2x10^{-13}$	0.66984375	Blood protein measurement	GCST006585	8:27930467	[182]
rs2727013-A	$1x10^{-14}$	0.66984375	Blood protein measurement	GCST006585	8:27930467	[182]
rs2727013-A	$1x10^{-16}$	0.66984375	Blood protein measurement	GCST006585	8:27930467	[182]
rs2727013-A	$1x10^{-17}$	0.66984375	Blood protein measurement	GCST006585	8:27930467	[182]
rs2727013-A	$7x10^{-18}$	0.66984375	Blood protein measurement	GCST006585	8:27930467	[182]
rs2727013-A	$1x10^{-22}$	0.66984375	Blood protein measurement	GCST006585	8:27930467	[182]
rs2685422-A	$3x10^{-37}$	0.3205	Blood protein measurement	GCST90086257	8:27947867	[183]
rs17058204-A	$8x10^{-21}$	0.09477	Blood protein measurement	GCST90088611	8:27909549	[183]
rs2685417-C	$4x10^{-32}$	0.2919	Blood protein measurement	GCST90088611	8:27949917	[183]
rs58646328-A	$6x10^{-09}$	0.09415	Blood protein measurement	GCST90089139	8:27909759	[183]
rs2726951-T	$1x10^{-32}$	0.2916	Blood protein measurement	GCST90089139	8:27948266	[183]
rs28588017-G	$2x10^{-18}$	0.09494	Blood protein measurement	GCST90089183	8:27911850	[183]
rs2685417-C	$2x10^{-42}$	0.2919	Blood protein measurement	GCST90089183	8:27949917	[183]
rs4276643-C	$2x10^{-13}$	0.352	Blood protein measurement	GCST90089266	8:27946082	[183]
rs2726948-A	$2x10^{-15}$	0.2961	Blood protein measurement	GCST90089284	8:27951870	[183]
rs28588017-G	$1x10^{-17}$	0.09494	Blood protein measurement	GCST90089326	8:27911850	[183]

Variant and risk allele	P-value	Risk allele frequency	Trait(s)	Study accession	Location	Author
rs2726951-T	$2x10^{-39}$	0.2916	Blood protein measurement	GCST90089326	8:27948266	[183]
rs28588017-G	$3x10^{-08}$	0.09494	Blood protein measurement	GCST90089616	8:27911850	[183]
rs2685417-C	$3x10^{-23}$	0.2919	Blood protein measurement	GCST90089616	8:27949917	[183]
rs184024600-?	$4x10^{-08}$	/	Body height	GCST007841	8:27875920	[184]
rs2726955-C	$1x10^{-08}$	0.3496	Body height	GCST90245848	8:27939857	[185]
rs898463-C	$8x10^{-19}$	0.0658	Body height	GCST90245848	8:27872346	[185]
rs28588017-G	$3x10^{-10}$	0.09494	Cholesteryl ester transfer protein measurement	GCST90089679	8:27911850	[183]
rs2726951-T	$2x10^{-41}$	0.2916	Cholesteryl ester transfer protein measurement	GCST90089679	8:27948266	[183]
rs17058252-C	$4x10^{-08}$	/	Chronic obstructive pulmonary disease	GCST90244098	8:27917421	[186]
rs10088319-A	$9x10^{-06}$	0.986	Color vision disorder	GCST90301671	8:28015686	[187]
rs1551720-?	$3x10^{-08}$	/	DNA methylation	GCST006660	8:27840720	[188]
rs11136012-?	$1x10^{-07}$	/	Erythrocyte count	GCST007069	8:27842198	[184]
rs11136012-C	$2x10^{-08}$	/	Erythrocyte count	GCST90018971	8:27842198	[189]
rs55829013-?	$6x10^{-10}$	/	Factor VIII measurement	GCST007445	8:27920631	[190]
rs55829013-?	$3x10^{-10}$	/	Factor VIII measurement	GCST007445	8:27920631	[190]
rs7816579-A	$5x10^{-16}$	0.32	Factor VIII measurement	GCST007445	8:27948298	[190]
rs11780263-?	$3x10^{-17}$	/	Factor VIII measurement	GCST007445	8:27966315	[190]
rs4276643-T	$1x10^{-19}$	0.66	Factor VIII measurement	GCST007445	8:27946082	[190]
rs11780263-?	$1x10^{-19}$	/	Factor VIII measurement	GCST007445	8:27966315	[190]
rs7816579-A	$7x10^{-21}$	0.35	Factor VIII measurement	GCST007445	8:27948298	[190]
rs7816579-?	$4x10^{-20}$	/	Factor VIII measurement, coronary artery disease	GCST90129543	8:27948298	[191]

Variant and risk allele	P-value	Risk allele frequency	Trait(s)	Study accession	Location	Author
rs7816579-?	$2x10^{-22}$	/	Factor VIII measurement, ischemic stroke	GCST90129550	8:27948298	[191]
rs73568968-?	$1x10^{-24}$	/	Factor VIII measurement, venous thromboembolism	GCST90129536	8:27953196	[191]
rs7816579-?	$2x10^{-35}$	/	Factor VIII measurement, vWF measurement	GCST90129556	8:27948298	[191]
rs4395853-T	$2x10^{-21}$	0.723	GDP-fucose protein O-fucosyltransferase 2 measurement	GCST90241251	8:27951253	[192]
rs4276643-?	$5x10^{-29}$	/	Ischemic stroke, vWF measurement	GCST90129551	8:27946082	[191]
rs61737292-A	$7x10^{-35}$	0.1	Level of scavenger receptor class A member 5 in blood serum	GCST90232861	8:27922095	[193]
rs4395853-T	$3x10^{-43}$	0.723	Prolargin measurement	GCST90242391	8:27951253	[192]
rs939715-T	$8x10^{-39}$	0.72	Protein eva-1 homolog C measurement	GCST90242442	8:27953109	[192]
rs2685416-A	$1x10^{-49}$	0.263	Protein FAM163A measurement	GCST90242451	8:27950972	[192]
rs58646328-A	$9x10^{-11}$	0.1	Protein measurement	GCST90247434	8:27909759	[194]
rs8180975-T	$3x10^{-07}$	0.11	Protein measurement	GCST90249798	8:27851410	[194]
rs58646328-A	$2x10^{-14}$	0.1	Protein measurement	GCST90249798	8:27909759	[194]
rs28588017-T	$1x10^{-16}$	0.9	Protein measurement	GCST90249798	8:27911850	[194]
rs28588017-T	$5x10^{-22}$	0.9	Protein measurement	GCST90249798	8:27911850	[194]
rs28588017-T	$5x10^{-23}$	0.9	Protein measurement	GCST90249798	8:27911850	[194]
rs2685414-T	$5x10^{-44}$	0.26	Protein measurement	GCST90249798	8:27952867	[194]
rs2685412-C	$3x10^{-98}$	0.74	Protein measurement	GCST90249798	8:27953086	[194]
rs2685417-C	$5x10^{-158}$	0.26	Protein measurement	GCST90249798	8:27949917	[194]

Variant and risk allele	P-value	Risk allele frequency	Trait(s)	Study accession	Location	Author
rs4395853-T	$8x10^{-172}$	0.72	Protein measurement	GCST90249798	8:27951253	[194]
rs35039172-T	$4x10^{-51}$	0.721	Pulmonary surfactant-associated protein C measurement	GCST90242557	8:27950414	[192]
rs11774576-A	$3x10^{-06}$	0.581	Response to cisplatin, response to antineoplastic agent	GCST002007	8:27882900	[195]
rs566279589-?	$2x10^{-50}$	0.71	Scavenger receptor class A member 5 measurement	GCST90249438	8:27946933	[194]
rs10866867-G	$8x10^{-21}$	0.722	Scavenger receptor class A member 5 measurement	GCST90242718	8:27951477	[192]
rs11994699-A	$2x10^{-39}$	0.723	Tenascin measurement	GCST90242977	8:27950722	[192]
rs2685413-G	$1x10^{-25}$	0.150085	Tenascin measurement	GCST90161997	8:27953060	[196]
rs2726959-T	$8x10^{-06}$	/	Tinnitus	GCST90267564	8:27891827	[197]
rs28810390-A	$4x10^{-06}$	/	Tinnitus	GCST90267564	8:27880511	[197]
rs28810390-A	$5x10^{-07}$	/	Tinnitus	GCST011540	8:27880511	[198]
rs2685421-?	$7x10^{-31}$	/	Venous thrombo embolism, vWF measurement	GCST90129537	8:27947981	[191]
rs62496810-?	$5x10^{-08}$	/	vWF measurement	GCST007446	8:27957964	[190]
rs62496810-?	$4x10^{-08}$	/	vWF measurement	GCST007446	8:27957964	[190]
rs4276643-T	$6x10^{-27}$	0.68	vWF measurement	GCST007446	8:27946082	[190]
rs4276643-T	$9x10^{-28}$	0.67	vWF measurement	GCST007446	8:27946082	[190]
rs4276643-?	$3x10^{-07}$	/	vWF measurement	GCST003210	8:27946082	[199]
rs4276643-?	$7x10^{-27}$	/	vWF measurement, coronary artery disease	GCST90129544	8:27946082	[191]

1.4.3 Scara5 expression in human and mice

Expression Atlas (European Bioinformatics Institute) is a publicly available resource that gives insights on gene and protein expression by combining transcriptomic and proteomic studies. Data are presented as heatmaps, showing gene and protein expression levels over different species, organs, experiments, and biological conditions [200].

As depicted in **Figure 1.12**, Scara5 transcript is expressed in most organs, exhibiting elevated expression in testis (in 7 out of 10 studies) and heart (in 5 out of 10 studies). Similarly, Scara5 mRNA expression is classified as "medium" in colon, stomach, and adipose tissue. On the other hand, the Wang *et al.* study indicates that Scara5 protein is expressed in nearly all organs listed in **Figure 1.12** [201]. Conversely, the Human Proteome Map study reports low Scara5 protein expression exclusively in testis, with no detection in other organs.

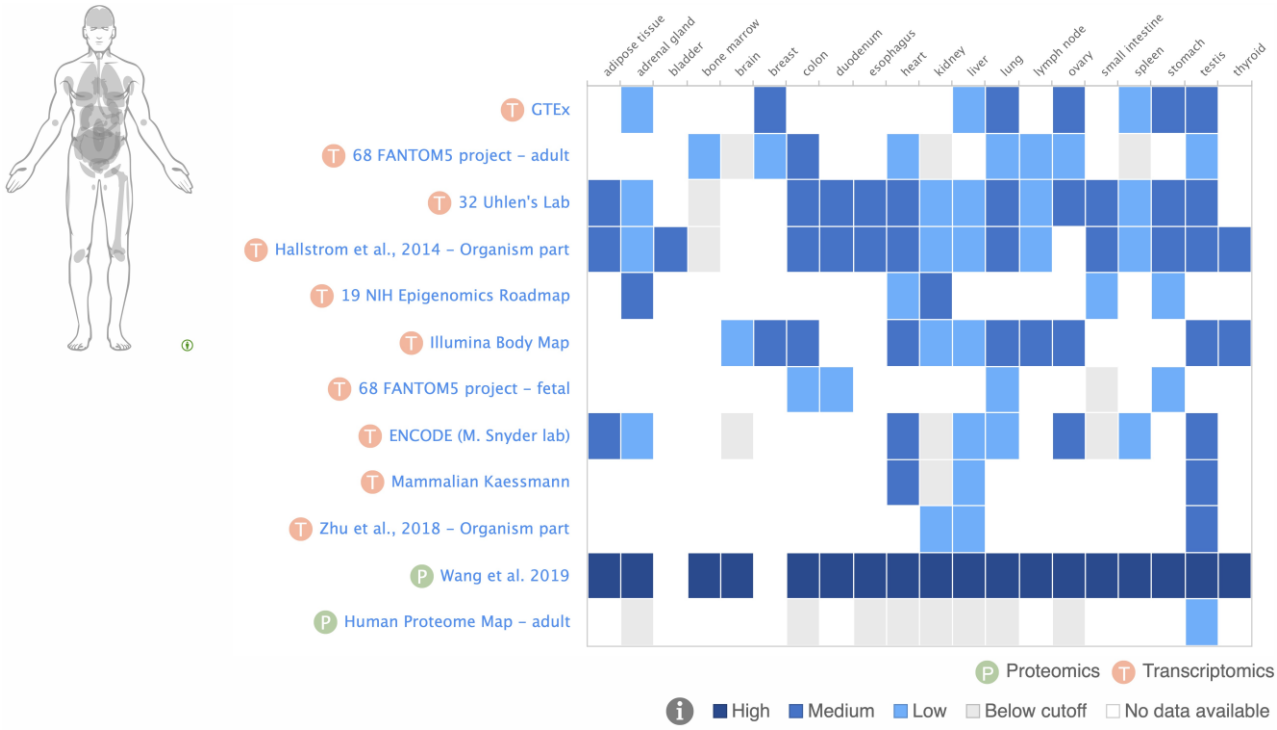


Figure 1.12 Scara5 expression in humans. Transcriptomic and proteomics analyses highlighted Scara5 expression over different human organs. Most relevant data are shown as heat map. Complete dataset is available online [202].

The expression of Scara5 in mice contrasts with that observed in humans. Indeed, the overall Scara5 mRNA expression is low in most organs, as shown in **Figure 1.13**. However, similarly to Scara5 mRNA expression in humans, Scara5 transcript has been found moderately abundant in murine testis (in 10 studies out of 25) and heart (in 6 studies out of 25). Proteomics analyses by Huttlin and colleagues reveal abundant expression of Scara5 protein uniquely in testis [203].

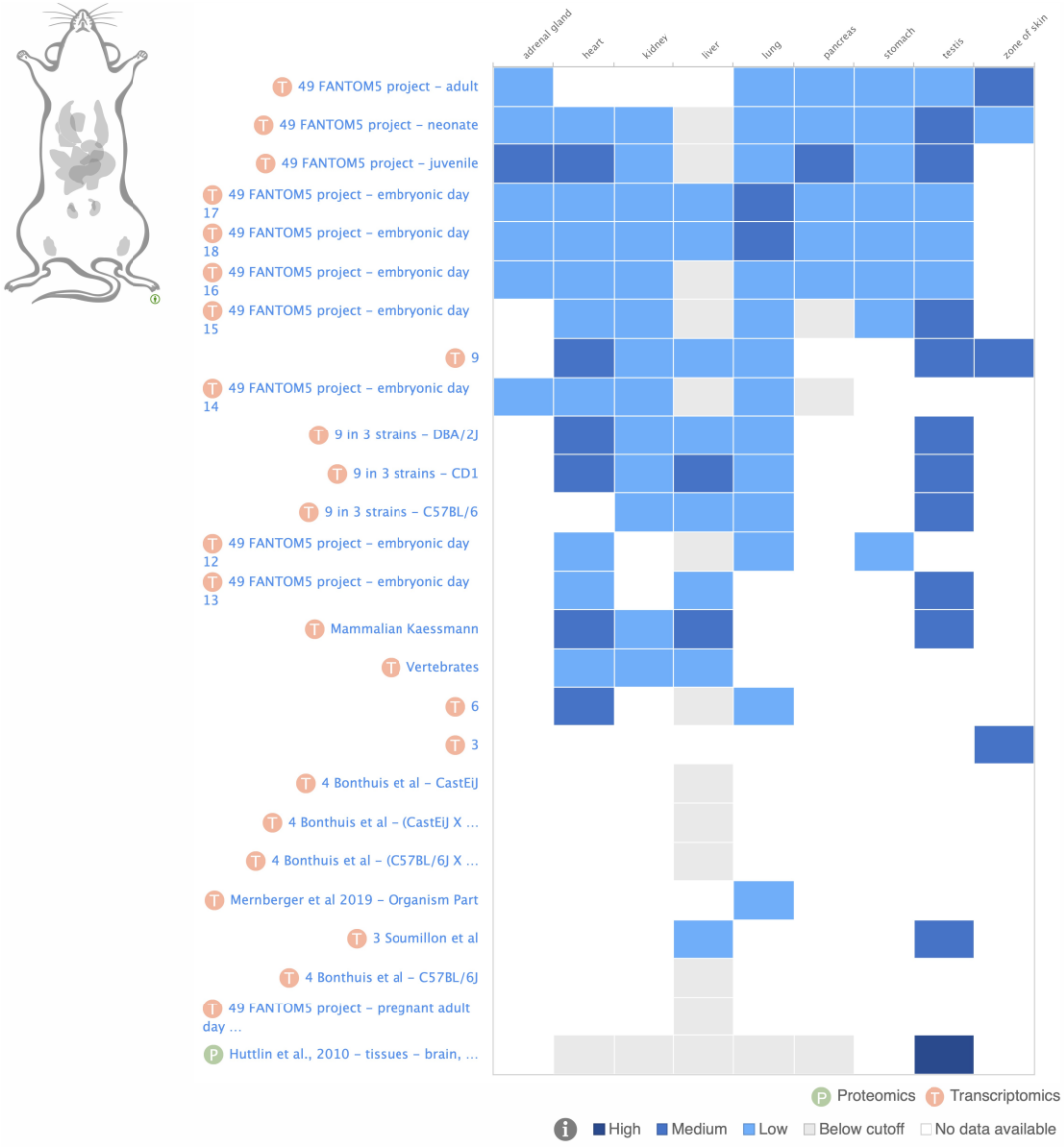


Figure 1.13 Scara5 expression in mice. Transcriptomic and proteomics analyses highlighted Scara5 expression over different murine organs. Most relevant data are shown as heat map. Complete dataset are available online [204].

In summary, based on Expression Atlas data, both human and murine Scara5 is abundantly expressed in testis and heart as mRNA, while Scara5 protein is expressed in various organs in humans [201] and solely in testis in mice [203].

1.4.4 Scara5 as a ferritin receptor

Iron is a crucial element for nearly all living organisms, representing the core of oxygen-carrying proteins (i.e. haemoglobin, myoglobin) electron transporting chain proteins (i.e. cytochromes), as well as several enzymes required for ATP production. Iron homeostasis must

be tightly preserved; in fact, both iron deficiency-related anaemia and iron overload-ROS production showed has been shown to have detrimental effects on tissues and organs [205]. The major regulator of iron homeostasis is a peptide hormone mainly secreted by hepatocytes, known as hepcidin. Hepcidin uniquely targets ferroportin, the iron exporter; the binding of hepcidin-ferroportin on the cell membrane results in the endocytosis and proteolysis of ferroportin, thus reducing the levels of iron exported to plasma [206].

Almost all plasma iron is bound by transferrin (Tf) and ferritin; Tf represents the main source of iron and binds to its ubiquitously expressed receptor, Tf receptor 1 (TfR1). Once delivered within the cytoplasm, free iron is used according to the cellular needs. It can, for example, be used by mitochondria for heme (haemoglobin core) synthesis or be captured by ferritin for storage. Empty Tf is subsequently released in plasma to bind new iron [207]. Beside Tf, iron can be bound by circulating ferritin. Ferritin is the iron storage molecule, and its structure combines 24 subunits of light (L) and heavy (H) chains, forming a nano-cage able to contain up to 4500 iron atoms. The ratio H:L subunits depends on the type of tissue considered; for example, H subunit-rich ferritin (simplified as H-ferritin) can be found in the heart, whereas liver ferritin is rich in L subunit (L-ferritin) [208]. Intracellular ferritin holds iron intracellularly and release it upon deficiency conditions or increased demand [209]. Circulating ferritin levels reflect the intracellular iron storage, which is why ferritin is used clinically as a serum marker of total body iron [210]. Serum ferritin is mainly composed by L subunits, and it usually carries much less than 4500 iron atoms. Nevertheless, it plays a significant role in iron delivery, also considering that Tf binds maximum two iron atoms [208]. Ferritin can be secreted by different cell types (e.g. hepatocytes, Kupffer cells, macrophages) and it is internalised via different receptors (i.e. TfR1, Scara5, T cell immunoglobulin-domain and mucin-domain 2 – TIM-2) based on its subunit structure (**Figure 1.14**). Chen *et al.* demonstrated that TIM-2 binds H-ferritin but not L-ferritin [211]. Similarly, Li *et al.* described TfR1 as a H-ferritin receptor [212].

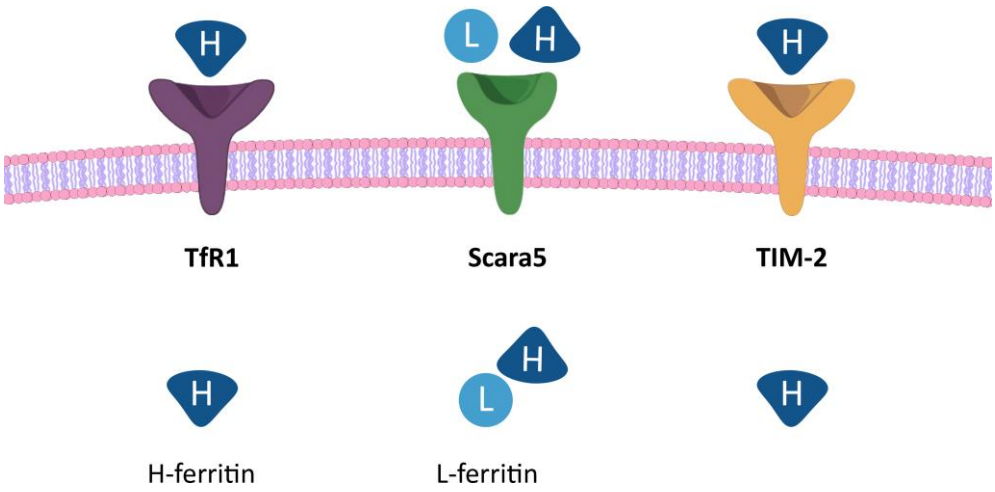


Figure 1.14 H- and L-ferritin receptors. H subunit-rich ferritin can bind to both TfR1 and TIM-2, whilst Scara5 has been shown to bind and internalise both H and L subunit-rich ferritin.

In 2009, Li and colleagues showed that Scara5 plays a role in iron delivery being a renal receptor of ferritin; during kidney development, the renal capsule internalised ferritin via Scara5. Ferritin possesses repeating polyanionic monomers and for this reason can be bound by Scara5 [213]. Scara5 demonstrated to bind both L- and H-ferritin, although it preferentially binds L-ferritin [167, 213, 214] (**Figure 1.14**). Yu *et al.* revealed that Scara5 binds to ferritin via the SRCR domain in a calcium-dependent manner. Furthermore, MRC1 and MARCO proved to bind ferritin via SRCR domain *in vitro*, whereas Scara3 and Scara4 did not bind ferritin as they lack the SRCR domain [167]. Although it was originally identified as a renal receptor of ferritin, Scara5 was found expressed in the eye throughout the retinal cells, where it bound to L-ferritin [214]. It can be therefore speculated that Scara5 works as ferritin receptor in the tissues in which it is expressed, even though it remains unknown whether Scara5 internalises ferritin independently of the cell type/tissue considered. As a ferritin receptor, Scara5 could regulate iron homeostasis. Liu *et al.* recently demonstrated that Scara5 overexpression increased iron levels in oesophageal squamous cell carcinoma (ESCC) cells, thus determining cell death by ferroptosis, a form of programmed cell death driven by elevated iron levels and ROS accumulation [215].

To sum up, Scara5 binds ferritin via its SRCR domain, thus delivering iron to the cells in a Tf-independent way. It remains unknown whether any Scara5-expressing cell internalises ferritin or this function is limited to specific tissues. Be that as it may, Scara5 role in iron homeostasis deserves to be explored, as it could result critical for cellular metabolism.

1.4.5 Scara5, adipogenesis, and breast cancer

SRs were originally observed as expressed on macrophages' surface; however, some of class A members proved to have unexpected roles. MSR1, for example, plays a role in bone biology. Deletion of MSR1 negatively affected osteoclast differentiation *in vivo*, resulting in increased bone deposition and overall growth of mice models [216]. It is not surprising that MSR1 is largely expressed on macrophages and contributes to bone development. Indeed, macrophages and osteoclasts derive from the same myeloid progenitors, which become osteoclasts upon macrophage colony-stimulating factor (M-CSF) and RANKL stimulation [217]. Similarly, Scara3 overexpression increased BMSCs osteogenesis at the expense of adipogenesis *in vitro*, also reducing bone loss and BMAT accumulation in OVX and aged murine models [218].

Scara5 is highly expressed in WAT with potentially entirely different roles to those previously recognised in other tissues. Lee *et al.* highlighted the expression of Scara5 in the WAT suggesting its involvement in adipogenesis. A33 and C3H10T1/2 cell lines were utilised, in order to study the expression of Scara5 in preadipocytes and MSCs-like cells, respectively. Scara5 expression was non-significantly expressed in uncommitted cells, whilst was greater in preadipocytes and in the heterogeneous stromal vascular fraction of adipose tissue than in adipocytes [165]. In particular, Scara5 gene knockdown in A33 cells considerably impaired adipogenic differentiation, as demonstrated by lower levels of adipogenic factors (e.g. CEBPs and PPARγ); whereas, the overexpression of Scara5 within the multipotent cell line showed that adipogenic factors' expression increase, implying Scara5's potential to promote adipogenesis. Hence, Scara5 can induce the commitment of MSCs towards adipocyte at the expense of osteoblasts, and the differentiation of preadipocytes into mature cells [165]. As adipogenesis is the counterpart of osteogenesis, Lee and colleagues also considered the effect of Scara5 overexpression on C3H10T1/2 cells. According to the published data, osteogenic gene expression (i.e. Alpl, OCN) decreased in response to osteogenic stimuli. Nonetheless, Scara5 effect on osteogenesis is yet unknown.

Lee *et al.* demonstrated that a knockdown of Scara5 increased focal adhesion kinase (FAK) phosphorylation levels, along with extracellular signal-regulated kinase (ERK) phosphorylation. On the other hand, Scara5 overexpression was linked to decreased levels of these signalling molecules, suggesting that Scara5, by suppressing FAK pathway, may be

needed for MSCs differentiation towards adipocytes instead of osteoblasts. FAK, a cytoplasmic tyrosine kinase, plays a crucial role in regulating focal adhesion dynamics and was observed overactivated in several tumour cell lines. Activated FAK forms a complex with the associated proteins proto-oncogene tyrosine-protein kinase Src and BrCa anti-oestrogen resistance 1 (p130Cas), and tyrosine phosphorylation is required for focal adhesion formation, leading to tumour growth and metastasis by promoting cell migration [219]. Overexpression of Scara5 seems to inhibit tyrosine phosphorylation and pathway activation, also suppressing tumour proliferation and invasion [219]. Moreover, FAK-ERK signalling promotes the osteogenic differentiation of MSCs throughout matrix production and osteogenesis. It has been demonstrated that the contact between MSCs and ECM proteins stimulates the activation of ERK, with FAK acting as a bridge [220]. Subsequently, ERK phosphorylates osteogenic transcription factors such as RUNX2 and Osterix. Osteoblasts in osteoporosis patients are reported to have reduced FAK activity and this supports FAK-ERK signalling pathway involvement in osteoblastic MSC differentiation [220]. In summary, through FAK inactivation Scara5 influences MSCs differentiation to the adipogenic lineage, thus unbalancing their fate. Further investigations are necessary to clarify how Scara5 expression is regulated and which factors are involved.

Interestingly, Scara5 expression is downregulated in diverse tumour cell lines/samples. Yan *et al.* showed that the therapeutic upregulation of Scara5 suppressed tumour growth and metastasis of human glioma cells via inactivation of signal transducer and activation of transcription 3 (STAT3), a key modulator of the inflammatory response through the regulation of cytokine production [221]. In addition, phosphorylated FAK levels decreased upon Scara5 overexpression, together with p-AKT, Cyclin B1 and D1, indicating that Scara5 impacts on adhesion and survival of human glioma cells [221], oral squamous cell carcinoma [169], and BrCa cells [170]. Similarly, Scara5 overexpression was linked to the suppression of retinoblastoma cells proliferation and migration via PI3K-AKT pathway inhibition [222].

Scara5 has been associated with both adipogenesis and BrCa. Fat and BrCa cells intercommunicate to support cancer cells growth. BrCa is the most common cancer in women; in 2020, over 2.3 million new cases were registered worldwide, and this number is predicted to increase to over 3 million by 2040 [223]. BrCa is a heterogenous tumour and different subtypes are described based on the expression of hormone receptors, i.e.

oestrogen receptor (ER), progesterone receptor (PR), human epidermal growth factor receptor positive (HER), and so-called "triple negative" [224]. Luminal A BrCa is characterised by the immunohistochemical expression of ER, PR, and the absence of HER. Ki-67, a proliferation marker, is poorly expressed by this subtype of BrCa. Luminal B BrCa subtype shows a worse prognosis that Luminal A BrCa. Luminal B tumours are ER-positive, PR-positive or -negative, and HER-negative; Ki-67 expression is elevated, which is why these tumours grow rapidly, representing a more aggressive subtype. HER-positive subtype is HER-positive and ER/PR-negative, being more aggressive and fast-growing than the Luminal subtypes. ER-, PR-, and HER-negative tumours, known as triple negative tumours, represent 80% of BrCa tumours with an elevated expression of Ki-67 and an aggressive behaviour [224]. In You *et al.*, Scara5 was reported as down-regulated in human breast cancer tissues, while normally expressed in the para-cancerous ones. Also, Scara5 down-regulation was associated with bigger tumour size, higher histological grade, and ability to metastasise to lymph nodes [170].

Adipose tissue represents the main tumour microenvironment (TME) of BrCa; breast is indeed mainly composed of adipose tissue and fibroglandular tissues [225]. The adipose component of breast contributes to BrCa development and progression due to the role it exerts as energy storage depot. BrCa cells obtain energy from the induction of lipolysis in adipocytes, using the released FFAs to generate Acetyl-CoA via β-oxidation and ATP via OXPHOS (**Figure 1.15**) [226]. Adipocyte lipolysis leads to the release of immunomodulatory factors (e.g. cytokines, adipokines), hormones, and proteases, thereby supporting BrCa growth. Consistently, high body mass index (BMI) has been positively associated with an increased risk of developing BrCa [227]. Dysfunctional obese adipocytes release higher levels of pro-inflammatory cytokines (e.g. IL-6, IL-8, TNFα), adipokines (e.g. adiponectin and leptin), chemokines (e.g. chemokine C–C motif ligand 5 – CCL5), promoting cancer cells migration, invasion and metastasis [226, 228]. Furthermore, macrophages play a role in the fat-BrCa crosstalk. Macrophages are the most abundant immune cells of adipose tissue, described as M1 and M2 macrophages according to their phenotype; M1 macrophages release pro-inflammatory cytokines, whilst M2 macrophages release anti-inflammatory cytokines [229]. Tumour-associated macrophages (TAMs) are mostly M2 macrophages. They exhibit increased expression of anti-inflammatory cytokines (e.g. IL-4, IL-10, TGF-β), in order to suppress the anti-tumoral effect, therefore supporting breast cancer cells growth, proliferation and

migration. It is possible that the crosstalk between adipose tissue and breast cancer cells induces a change in macrophages polarisation, favouring M2 phenotype or that M1 and M2 phenotypes coexist by exerting both anti and pro-inflammatory roles [230].

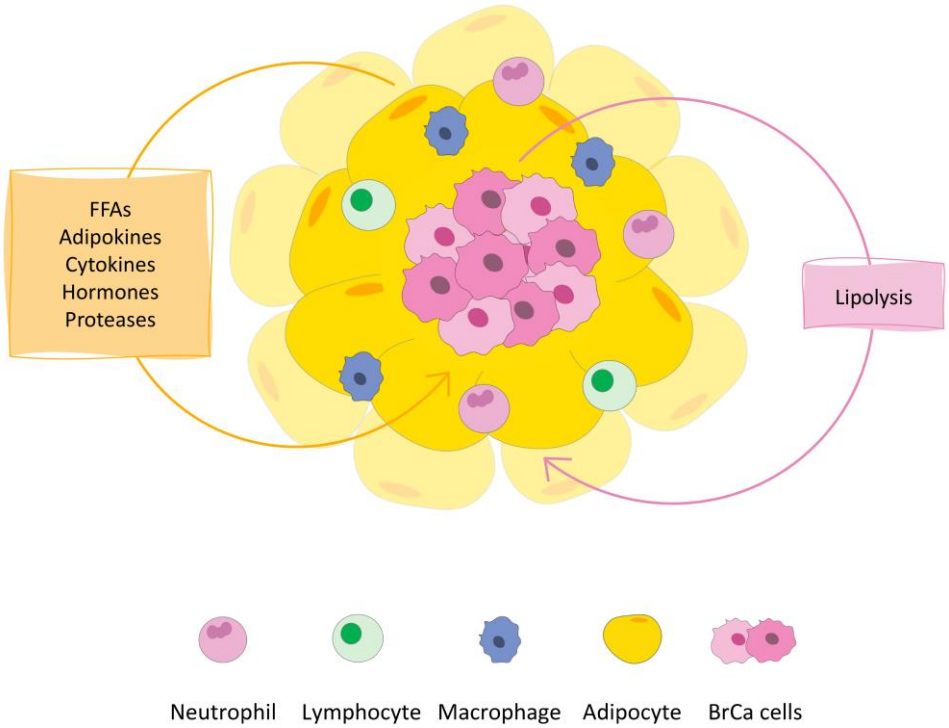


Figure 1.15 BrCa-adipose tissue crosstalk. Adipose tissue and BrCa cells crosstalk revealed fundamental to fuel cancer growth. BrCa cells induce lipolysis of adipocytes in order to release adipokines, cytokines, hormones (e.g. oestrogens), proteases, and metabolites as FFAs. FFAs can then be used by cancer cells as substrates to produce energy to survive, proliferate, and migrate.

In conclusion, in the past few decades Scara5 emerged as a class A scavenger receptor able to internalise both H- and L-ferritin and is often downregulated by cancer cell lines and human breast cancer tissues. Additionally, Scara5 was recently identified as a key adipogenic factor. To date, it remains elusive whether and how Scara5 multiple roles are interconnected, thus paving the way for new investigations that provide insights into Scara5 mechanisms of action.

1.5 Hypothesis, aims and objectives

Scara5 has been recently associated with adipogenesis, placing itself as a potential novel regulator of MSCs fate towards adipocytes [165]. Moreover, Scara5 has been associated with a variety of tumours, including BrCa [170]. It is well known that increased adiposity negatively

correlates with BrCa development [231]. It was therefore hypothesised that Scara5 plays a central role in MSCs adipogenesis at the expense of osteogenesis, thereby contributing to BrCa pathogenesis.

To validate the hypothesis, this study aims:

- To determine whether Scara5 deficiency affects murine BMSCs differentiation towards adipocytes and osteoblasts *in vitro.*
- To assess whether Scara5-deficient mice display a bone and/or fat phenotype *in vivo.*
- To investigate the molecular mechanism by which Scara5 determines BMSCs fate.
- To explore BrCa-adipose tissue crosstalk in the absence of Scara5.

Chapter 2: Materials and methods

2.1 Materials, reagents, and chemicals

Cell culture plates, culture media (α Minimum Essential Medium – αMEM, Dulbecco's Modified Eagle Medium – DMEM, DMEM/F12 1:1, OptiMEM reduced serum), media supplements (Fetal Bovine Serum – FBS, Penicillin-Streptomycin 10,000 U/ml – P/S, GlutaMAX I 200 mM) and 0.05% (w/v) Trypsin-EDTA 1X were purchased from Gibco (ThermoFisher Scientific UK Ltd, Loughborough, UK).

All chemicals, buffers, reagents, as well as SYBR Green I based reverse transcription-quantitative polymerase chain reaction (RT-qPCR) primers and Streptozotocin were purchased from Merck Life Science UK Limited (Gillingham, UK), unless differently specified.

Routinely used chemicals such as methanol, ethanol, isopropanol, Ethylenediaminetetraacetic acid (EDTA), Tris-Base, sodium chloride (NaCl), sodium hydroxide (NaOH), hydrochloric acid (HCl), glycerol, glacial acetic acid, Tween 20®, xylene substitute, and nitric acid were obtained from Fisher Scientific (ThermoFisher Scientific UK Ltd, Loughborough, UK).

2.2 Experimental mice

C57BL/6J mice were purchased by Charles River UK Ltd (Margate, UK) and the Scara5-KO mice (on agouti 129/Sv and C57BL/6J background, generation 5) were a kind gift from Dr Nick Platt, Department of Pharmacology, University of Oxford (Oxford, UK).

Mice were bred and housed under 12 hours light/12 hours dark cycle and fed ad libitum with standard chow diet in the Disease Modelling Unit (DMU), School of Biological Sciences, University of East Anglia (Norwich, UK). Their care and experimental procedures were approved by the Home Office and the University of East Anglia Local Ethical Review Committee, and conducted under Home Office Project Licences PBFB4BA22, PP5500397 and PP8873233, in accordance with the UK Home Office Animals Act of 1986. Mice with and without a constitutive Scara5 gene deletion were euthanised by CO_2 inhalation followed by

cervical dislocation after weaning (3 to 4 weeks old) or when adults (11, 13, 15, or 20 weeks old), depending on the experiment's objectives.

2.3 Backcrossing programme and genotyping

Scara5 deficient mice were originated by GenOway in 2007 (Lyon, France); the process of gene deletion involved the substitution of exons 7-9, which produce a crucial 228 bp section of the collagen domain, with an IRES-NLS-lacZ cassette using homologous recombination in embryonic stem cells derived from 129Sv/Pas mice. The modified stem cells were subsequently injected into blastocysts. By backcrossing the Scara5-heterozygous (+/- or HET) offspring for 9 generation to the C57BL/6J strain, the mice exhibited 99.99% of C57BL/6J genetic background (**Figure 2.1**). Scara5-WT and Scara5-KO mice were obtained by breeding Scara5-HET mice together followed by selective mating of mice identified to be Scara5-WT and Scara5-KO by rigorous genotyping (**Figure 2.2**). Finally, Scara5-KO mice were bred in order to obtain pure and KO animals. Similar genotyping and selective mating program was applied also in the case of Scara5-WT animals in the Scara5 colony. The deletion of exons 7-9 produced a shorter form of the collagenous domain, thus preventing Scara5 ligand binding. However, it remains unclear whether Scara5-KO mice still express a truncated form of Scara5, which might have signalling and/or dominant negative functions.

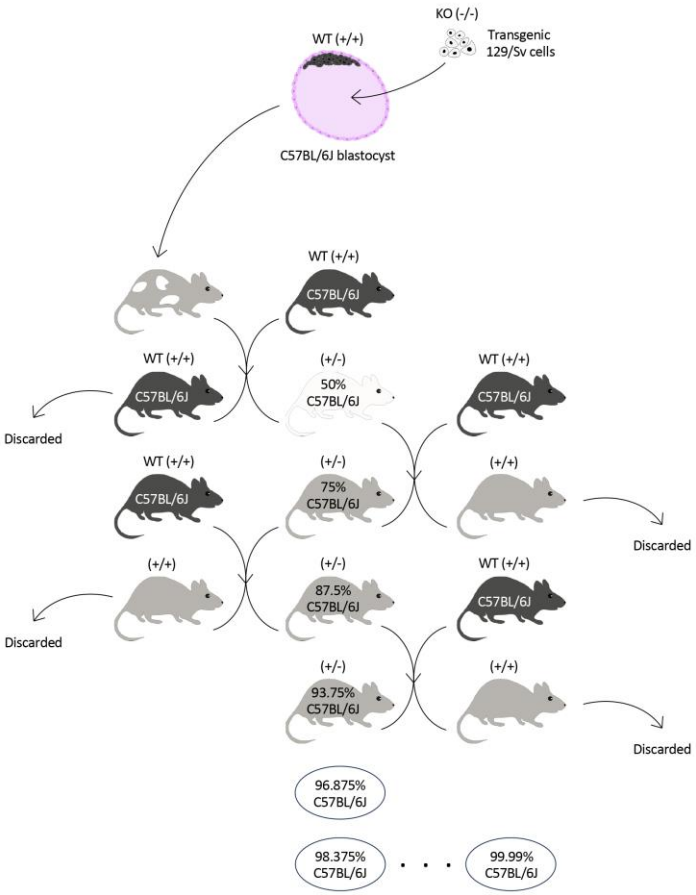


Figure 2.1 Backcrossing scheme (designed and adapted from Sul *et al*. [232]). Scara5 gene deletion was performed on 129/Sv cells, which were then transferred into C57BL/6J blastocyst. Subsequent backcrosses increased the percentage of C57BL/6J background in the offspring.

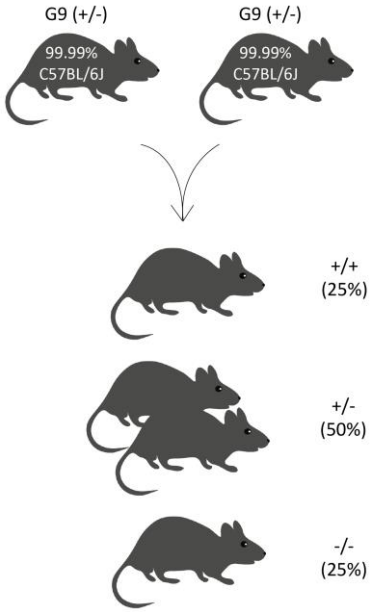


Figure 2.2 Generation of Scara5-WT (+/+) and -KO (-/-) mice. Litters of Scara5-WT (+/+), -HET (+/-),

and -KO (-/-) were obtained from generation 9 (G9) HET breeding pairs. From WT and KO mice breeding, pure WT and Scara5-KO mice were obtained.

Genotyping was performed on 2 to 3 weeks old Scara5 mice ear notches. The ear clips were digested in 50 mM NaOH for 45 minutes at 95 °C, after which a brief centrifugation allowed to obtain DNA in the supernatant. Endpoint polymerase chain reaction (PCR) was carried out utilising New England Biolabs (Hitchin, UK) reagents (10X ThermoPol Buffer, 10 mM dNTPs, Taq DNA Polymerase) and Scara5 primers (Invitrogen, ThermoFisher Scientific UK Ltd, Loughborough, UK). Amplicons were separated on a 2% (w/v) agarose gel (Invitrogen, ThermoFisher Scientific UK Ltd, Loughborough, UK) in Tris-acetate-EDTA (TAE) buffer, stained with SYBR Safe-DNA Gel Stain (10,000 X, Invitrogen, ThermoFisher Scientific UK Ltd, Loughborough, UK), and visualised under UV light with either the M-20V Benchtop Variable Transilluminator (Ultra-Violet Products Ltd, Cambridge, UK) or the G:BOX Chemi XRQ transilluminator (Syngene, Cambridge, UK). Detailed list of primers and PCR cycles are reported in **Table 2.1** and **Table 2.2**, respectively.

Table 2.1 Endpoint PCR primers for genotyping

	Primers sequences (5’ – 3’)	Product length
Scara5 WT	F: CACCCCCGCCTTTCTGTTGTC R: CTCCTCTCTCTCCTTTCTCTCCTTTTGG0	534 bp
Scara5 KO	F: AGCCCCTGATGCTCTTCGTCCAG R: TCTGATGCCGCCGTGTTCCG	400 bp

Table 2.2 Endpoint PCR thermocycler program

Step	Temperature	Time	Number of cycles
Initial denaturation	95 °C	30 seconds	1 cycle
Denaturation	95 °C	30 seconds	30 cycles
Annealing	60 °C	1 minute	
Extension	68 °C	1 minute	
Final extension	68 °C	5 minutes	1 cycle
Hold	4°C	infinite	

2.4 Primary cells and cell line culture

2.4.1 Murine bone marrow mesenchymal stem cells (BMSCs)

The current procedure was adapted from Huang *et al.* work [233]. Mice aged 3 to 4 weeks were euthanised and processed in order to isolate legs' bones. In a class II Biological Safety Cabinet, femurs and tibiae were collected and cleaned from the surrounded soft tissues. Subsequently, bones were washed twice in PBS containing 1% (v/v) P/S and transferred in a 100 mm sterile culture dish with αMEM supplemented with 15% (v/v) FBS and 1% (v/v) P/S. 6 long bones (3 tibiae and 3 femurs) collected from two mice represented a single biological sample. Bones extremities were cut and 5 ml of medium were drawn into a 5 ml syringe with a 25 g needle attached. The bone marrow was slowly flushed and the bone cavity was washed twice. Also, the cavity surface was repeatedly scaped in order to dissociate the BMSCs from the endosteum. The resulting bone shards were removed from the plate and the cells were incubated at 37 °C in 5% (v/v) CO_2 atmosphere for 5 days (**Figure 2.3 A**). At the end of this time, 80% confluent cells were washed twice with PBS and Trypsinised using 0.05% (w/v) Trypsin-EDTA at 37 °C, 5% (v/v) CO_2 for 2 minutes for detaching the BMSCs. Once Trypsin was neutralised with complete maintenance medium (CM – DMEM, 10% (v/v) FBS, 1% (v/v) P/S, 1% (v/v) GlutaMAX), the cells were centrifuged at 800 x g for 5 minutes. The cell pellet was resuspended in CM and the cells were filtered through a nylon strainer (mesh 70 µm); cells were counted using a counting chamber (Neubauer-improved bright light, Marienfeld superior, Paul Marienfeld GmbH & Co., Germany) and Trypan Blue Solution 0.4% (w/v) (Gibco, ThermoFisher Scientific UK Ltd, Loughborough, UK), which penetrated the damaged membrane of dead cells that were consequently excluded from the count. Cells were finally used for experiments as passage 1. During the optimisation of the protocol, the cells were subcultured until passage 3 and all the adherent cells that remained attached to the plate were collected by a scraper (Fisher Scientific, ThermoFisher Scientific UK Ltd, Loughborough, UK) and used for the experiment. The medium was renewed every 3 to 4 days. For every procedure here described, BMSCs were maintained at 37°C, 5% (v/v) CO_2.

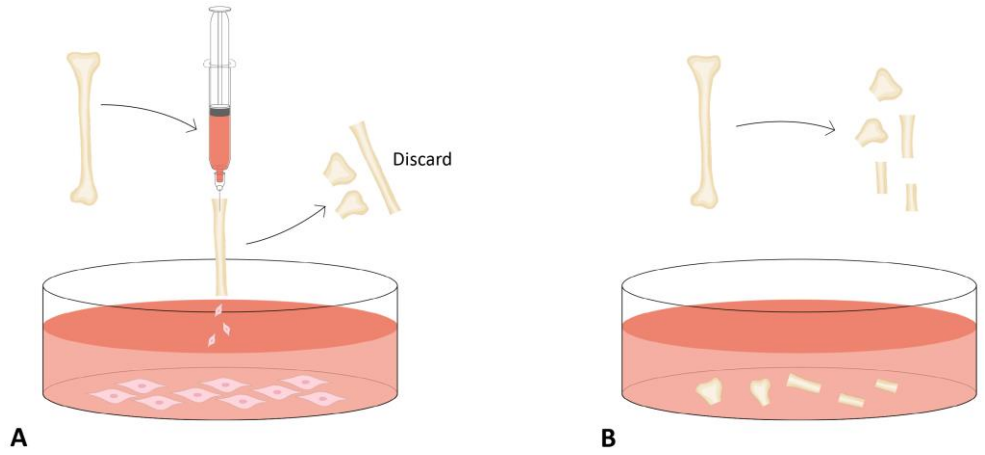


Figure 2.3 BMSCs extraction methods. Both bone flushing (**A**) and bone chips (**B**) -derived BMSCs can be cultivated and expanded *in vitro*.

During the optimisation steps, cells were also extracted by cultivating bone chips from long bones for 10 days in αMEM supplemented with 15% (v/v) FBS and 1% (v/v) P/S (**Figure 2.3 B**). Cell medium was changed after 5 days of culture and cells were trypsinised after 10 days following the procedure described above.

2.4.2 Murine breast cancer cells

Murine breast cancer (BrCa) primary cells (i.e. BRPKp110, PyMT-BO5, EO771, and 4T1) were kindly provided as cell pellets (EO771, 4T1) or frozen (BRPKp110, PyMT-BO5) by Dr Stephen Robinson (Quadram Institute, Norwich, UK). Murine osteoblast-like 'BMP-2 T-Ag-3' (2T3) cell line was used as control to assess gene expression in the BrCa cell lines, as will be described later. 2T3 cells were used as pellet for RNA extraction (**Section 2.8**) and were purchased from American Type Culture Collection, ATCC (Manassas, Virginia, USA).

BRPKp110 and PyMT-BO5 cell lines were cultured in CM, incubated at 37 °C, 5 % (v/v) CO_2, and used for 5 to 7 passages. Once 80% confluent, cells were washed twice with PBS and detached by using 0.05% (w/v) Trypsin-EDTA at 37 °C, 5% (v/v) CO_2 for 5 minutes; the solution was centrifuged at 250 x g for 5 minutes. The cell pellet was resuspended and cells were counted. The cells were used immediately or frozen in freezing medium, consisting of CM supplemented with 20% (v/v) FBS and 10% (v/v) Dimethyl sulfoxide (DMSO).

2.4.3 Human fetal osteoblasts (hFOB) 1.19

hFOB 1.19 (or simply hFOB) were purchased from Caltag-Medsystems Ltd (Buckingham, UK). This immortalised cell line was created by incorporating a temperature-sensitive mutant of SV40 large T antigen and the neomycin resistant expression vector pSV2-neo into primary fetal bone cells [234]. hFOB were cultivated in hFOB maintenance complete medium (hFOB medium or hCM), consisting of DMEM/F12 1:1, 10% (v/v) FBS, 0.3 mg/ml G418 disulfate salt solution and maintained at 34 °C, 5% (v/v) CO_2. Cells were trypsinised as previously described (**Section 2.4.2**) and Trypsin was neutralised with hCM. Cells were either used immediately or frozen in their freezing medium, which consisted of hCM supplemented with 20% (v/v) FBS and 10% (v/v) DMSO. hFOB were used until passage 15 and hCM was renewed every 3 to 4 days. Before being treated with osteogenic and adipogenic media, hFOB were moved to a 37 °C, 5% (v/v) CO_2 incubator.

2.5 Osteogenic and adipogenic differentiation

BMSCs were seeded at 5 x 10^3 - 1.5 x 10^4 cells/well in a 96 well plate for alkaline phosphatase (ALP) assay at passages 1 to 3. For Alizarin Red S staining, RNA extraction, and Western Blot, passage 1 BMSCs were seeded at densities of 3 x 10^4 cells/cm^2. Once cells were 80% confluent, osteogenic medium (OM) was added in order to induce BMSCs to differentiate into pre-osteoblasts or mature osteoblasts. OM was made by supplementing CM with 100 nM dexamethasone (Dex), 50 µg/ml ascorbic acid 2-phosphate, and 10 mM β-glycerophosphate. The osteogenic medium was changed every 3 to 4 days, depending on the length of the treatment (3, 14, 21 or 25 days).

For adipogenic differentiation, BMSCs were seeded as 3 x 10^4 cells/cm^2. Once the cells were 80% confluent, two different media were used alternatively. Adipogenic induction medium (AIM) was prepared by mixing CM, 1 µM Dex, 0.2 mM indomethacin, 1.7 µM insulin, and 0.5 mM 3-isobutyl-1-methylxanthine (IBMX); AIM was added to BMSCs for 3 days, after which was replaced by the adipogenic maintenance medium (AMM, CM supplemented with 1.7 µM insulin) for 3 day and the cycle was repeated two times. Last cycle (the third) consisted of 3 days in AIM, 1 day in AMM and the cells were left in AMM before being stained with Oil Red O.

As well as BMSCs, also hFOB were treated with osteogenic and adipogenic media for different time points (1, 3, 6, 12, and 16 days). Once 80% confluent, hFOB were moved from 34 to 37 °C. While optimising hFOB cultivation, osteogenic supplements were also added to hCM and cells were treated for 3 days before being assessed for ALP enzymatic activity, both at 37 and 34 °C, 5% (v/v) CO_2.

2.6 Alkaline phosphatase (ALP) assay

To assess ALP activity of BMSCs or hFOB, cells were treated with OM for 3 days. For Wnt signalling investigation, the following murine recombinant proteins were added to CM at different concentrations: Wnt3a (Peprotech Ltd, London, UK), Wnt5a (Stratech, Cambridge, UK), and Wnt10b (Insight Biotechnology Ltd, Wembley, UK). As well as OM treatment, also recombinant proteins were added to CM and to BMSCs for 3 days of treatment. After 3 days, media were removed and cells were washed twice with PBS. Distilled water (dH_2O) and ALP liquid substrate p-Nitrophenylphosphate (pNPP) were added to the cells, which were incubated at 37 °C, 5% (v/v) CO_2, for 15 minutes. Finally, the reaction was stopped by adding 0.2 M NaOH. This assay is designed to measure the osteoblasts' ALP hydrolysis activity of the colourless substrate pNPP into the yellow-coloured product p-Nitrophenol (pNP) and Phosphoric Acid (H_3PO_4) (**Figure 2.4**); pNP optical density (OD) was measured at 405 nm through the FLUOstar Omega plate reader (BMG Labtech Ltd, Bucks, UK). Serial dilutions of standard solution (0.5 mmol/L pNP solution, LabAssay™ ALP, Fujifilm Wako, Osaka, Japan) were used to plot a standard curve, from which data were interpolated.

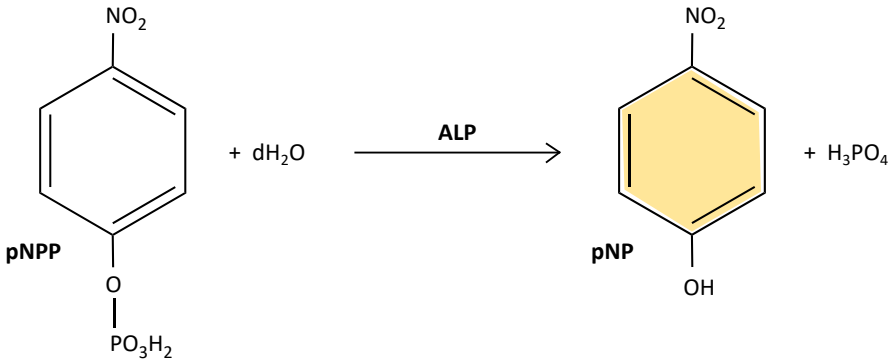


Figure 2.4 pNPP hydrolysis reaction in the presence of ALP. pNPP is hydrolysed in the presence of ALP in the sample. The resulting p-Nitrophenol product shows yellow colour, which is optically measured at 405 nm wavelength.

2.7 Alizarin Red S and Oil Red O staining

After 28 days of treatment with OM, BMSCs were stained with Alizarin Red S (ARS) staining for calcium containing bone nodules. Briefly, BMSCs were fixed in 95% (v/v) cold methanol for 10 minutes, washed twice with dH_2O and stained with 2% (w/v) ARS solution, pH 4.2, for 5 minutes. Cells were subsequently washed with dH_2O until the plate was clear. For ARS elution, BMSCs were treated with 10% (w/v) cetylpyridinium chloride buffer, and the eluted product's OD (562 nm) was measured with the FLUOstar Omega plate reader.

Adipogenic differentiation was assessed by Oil Red O (ORO) staining after 16 or 25 days of treatment with AM (for hFOB and BMSCs, respectively). Cells were washed twice with PBS and fixed in 10% (v/v) buffered formalin for 20 minutes; 0.3% (w/v) ORO stock solution was prepared by using 99% (v/v) Isopropanol (ThermoFisher Scientific UK Ltd, Loughborough, UK), while working ORO solution was prepared by mixing 3 parts of ORO stock solution and 2 parts of dH_2O. ORO working solution was prepared immediately before use and added to the cells for 5 minutes. Finally, cells were washed with dH_2O until the plate was clear.

2.8 RNA extraction, Reverse Transcription, and Reverse Transcription-quantitative Polymerase Chain Reaction (RT-qPCR)

Total RNA was extracted from cultured or pelleted cells via GenElute™ Mammalian Total RNA Miniprep Kit (Merck Life Science UK Limited, Gillingham, UK), according to the manufacturer's instructions. RNA was quantified by using the Nanodrop 2000 (ThermoFisher Scientific UK Ltd, Loughborough, UK) and 0.25-0.5 μg of it were used to synthetise cDNA by employing the High-Capacity cDNA Reverse Transcription kit (Applied Biosystems, Fisher Scientific UK Ltd, Loughborough, UK) and the T100™ Thermal Cycler (Bio-Rad Laboratories Inc, Watford, UK), following the steps listed in **Table 2.3**. Roughly 8 μg of cDNA were used for RT-qPCR, both with qPCR SyGreen Mix Lo-ROX (PCR Biosystems Ltd, London, UK) and Taqman™ Fast Advance Master Mix (Applied Biosystem, ThermoFisher Scientific UK Ltd, Loughborough, UK) master mixes. SYBR Green I-based RT-qPCR employed customised primers (**Table 2.4**), while Taqman™ RT-qPCR used Taqman™ primers (ThermoFisher Scientific UK Ltd, Loughborough, UK) (**Table 2.5**). Taqman™ primers efficiency was validated by the company (ThermoFisher Scientific UK Ltd, Loughborough, UK), whereas primers' efficiency was not tested for SYBR

Green primers. Manually designed SYBR Green primers (i.e. mouse Alpl, mouse Adipoq, mouse Axin2, mouse Dvl3, human Scara5, **Table 2.4**) were selected across exons. Melting curve analyses were run after SYBR Green I-based RT-qPCRs, to ascertain whether the fluorescence detected originated from a single or multiple amplicons. Details of RT-qPCR programs are reported in **Table 2.6**. RT-qPCR reactions were run in QuantStudio™ 5 384-Well Block (ThermoFisher Scientific UK Ltd, Loughborough, UK) and Roche LightCycler® 480 II (Roche Products Limited, Welwyn, UK) PCR systems. RT-qPCR data were analysed using the $2^{-\Delta\Delta CT}$ method, normalising gene expression to glyceraldehyde 3-phosphate dehydrogenase (GAPDH) expression.

Table 2.3 Reverse transcription thermocycler program

Step	Temperature	Time
Primer annealing	25 °C	10 minutes
DNA polymerisation	37 °C	120 minutes
Enzyme deactivation	85 °C	5 minutes
Hold	4°C	infinite

Table 2.4 SYBR Green I-based primers

Gene	Primers sequences (5' – 3')	Product length	Specie	Source
GAPDH	F: TGACCACAGTCCATGCCATC R: GACGGACACATTGGGGGTAG	203 bp	Mouse	[235]
Alpl	F: GCACCTGCCTTACCAACTCTTTTG R: GCAGCGGTTACTGTGGAGACG	178 bp	Mouse	Manually designed
OCN	F: CTTGAAGACCGCCTACAAAC R: GCTGCTGTGACATCCATAC	154 bp	Mouse	[236]
Adipoq	F: GTTCCCAATGTACCCATTCGC R: CGTAGGTGAAGAGAACGGC	187 bp	Mouse	Manually designed
LEP	F: ATGACTCCACAATGCTTGA R: GCTCTTATCTCTACTTGCTGA	154 bp	Mouse	Oligoarchitect™ Merck
Axin2	F: GTCTTTGCACCAGCCACCAGCG R: CGGAAAATGAGGTAGAGACA	192 bp	Mouse	Manually designed
Dvl3	F: TTCTGCAGCGGCCCAGCTATAAG R: GACGGGTTGTCAGCACAGAAAGG	184 bp	Mouse	Manually designed

Gene	Primers sequences (5' – 3')	Product length	Specie	Source
Lef 1	F: ATCACCTACAGCGACGAGCAC R: TGGACATGGAAGTGTCGCCTG	250 bp	Mouse	[237]
HK2	F: CCCTGTGAAGATGTTGCCCACT R: CCTTCGCTTGCCATTACGCACG	133 bp	Mouse	Origene
PKM	F: TGACACCTTCCTGGAACACA R: TTCAGCATCTCCACAGATCG	117 bp	Mouse	[238]
Fsp27	F: ATCAGAACAGCGCAAGAAGA R: CAGCTTGTACAGGTCGAAGG	97 bp	Mouse	[156]
PPARα	F: GAGCCCCATCTGTCCTCTC R: ACTGGTAGTCTGCAAAACC	152 bp	Mouse	[156]
Ucp3	F: CTGCACCGCCAGATGAGTTT R: ATCATGGCTTGAAATCGGACC	191 bp	Mouse	[156]
Glut4	F: AAAAGTGCCTGAAACCAGAG R: TCACCTCCTGCTCTAAAAGG	86 bp	Mouse	[239]
Hsl	F: CAGAAGGCACTAGGCGTGATG R: GCTTGCGTCCACTTAGTTCCA	118 bp	Mouse	[240]
MGL	F: GACACCATCCAGAAGGACTACC R: GATTGGCAAGGACCAGAGGTGA	145 bp	Mouse	Origene
GAPDH	F: ACAGTTGCCATGTAGACC R: TTGAGCACAGGGTACTTTA	88 bp	Human	KiCqStart™ Merck
Scara5	F: TCTTCATCTTAGCAGTGTCCAGGC R: TGACTGGTTCTGCAGCGCGTC	182 bp	Human	Manually designed
Adipoq	F: GGCTATGCTCTTCACCTAT R: GTCCATTACGCTCTCCTTC	131 bp	Human	Oligoarchitect™ Merck

Table 2.5 Taqman™-based RT-qPCR primers

Gene	Catalogue number	Specie
GAPDH	Mm99999915	Mouse
Scara5	Mm00512269	Mouse
TNFα	Mm00443258	Mouse
CXCL12	Mm00445553	Mouse
IFNγ	Mm01168134	Mouse
IL-1b	Mm01336189	Mouse
IL-2	Mm00434256	Mouse
IL-6	Mm60446190	Mouse
IL-10	Mm00439614	Mouse
GAPDH	Hs02758991	Human
Alpl	Hs01029144	Human
BGLAP/OCN	Hs01587814	Human

Table 2.6 RT-qPCR programs

Step	Temperature	Time	Number of cycles	RT-qPCR
Hold	50 °C	2 minutes	1 cycle	SYBR Green I based
	95 °C	10 minutes		
PCR (denaturation, annealing/extension)	95 °C	15 seconds	40 cycles	
	60 °C	1 minute		
Melt Curve	95 °C	15 seconds	1 cycle	
	60 °C	1 minute		
	95 °C	15 seconds		
Hold	50 °C	2 minutes	1 cycle	Taqman™ based
	95 °C	10 minutes		
PCR (denaturation, annealing/extension)	95 °C	15 seconds	40 cycles	
	60 °C	1 minute		

2.9 Scara5 Plasmid amplification and purification

Scara5 pEGFP-N2 (597) plasmid was purchased from Addgene (Addgene plasmid #61989; Addgene INC, Watertown, Massachusetts, USA); Scara5 plasmid was sent in bacteria as agar stab (**Figure 2.5**). By using a sterile inoculating loop, the bacteria were gathered from the stab

and spread onto a 32 g/L LB agar plate with 50 μg/ml Kanamycin A sulfate (Cayman Chemical Company, Michigan, USA). LB agar was purchased from Invitrogen (ThermoFisher Scientific UK Ltd, Loughborough, UK). After incubating the plate overnight (o/n) at 37 °C, a sterile pipette tip was used to select single colonies: the tips were dropped into the 50 ml tubes containing LB broth (Invitrogen, ThermoFisher Scientific UK Ltd, Loughborough, UK) and incubated o/n at 37 °C in a shacking incubator. Subsequently, the content of the 50 ml tubes was split into bigger volumes of LB broth and incubated o/n at 37 °C in a shacking incubator. Finally, 50 ml of LB broth and bacteria were put into 50 ml tubes and centrifuges at 2900 x g for 20 minutes at 4°C. Pellets were frozen at -20 °C and processed for plasmid purification within 2 weeks.

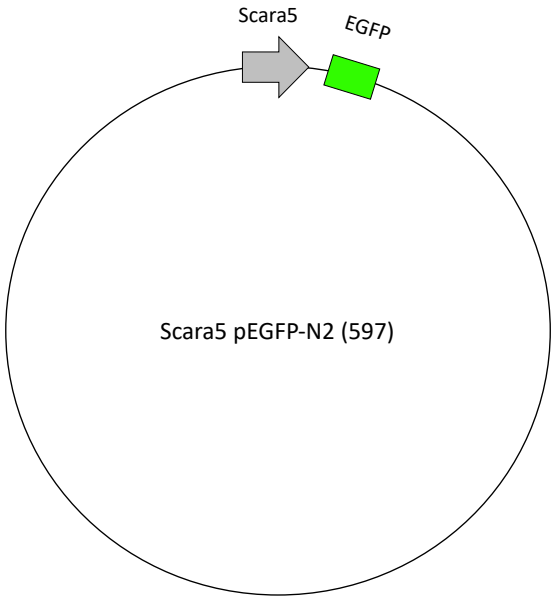


Figure 2.5 Scara5 pEGFP-N2 plasmid structure. The vector backbone used to insert Scara5 gene is the pEGFP-N2 vector, consisting of an engineered GFP (EGFP) fluorescent tag.

In order to purify Scara5 plasmid, bacterial pellets were resuspended in Buffer P1, part of EndoFree® Plasmid Maxi Kit (QIAGEN, Manchester, UK), and the purification process was completed according to the manufacturer's directions. To determine the DNA yield, DNA concentration was measured utilising the Nanodrop.

2.10 GapmeRs

To evaluate the impact of Scara5 silencing on hFOB cells, antisense GapmeRs (QIAGEN, Manchester, UK) were employed. These single-stranded oligonucleotides are 16 nucleotides long and able to trigger RNase H-mediated degradation of RNA targets that are complementary to them (**Figure 2.6**).

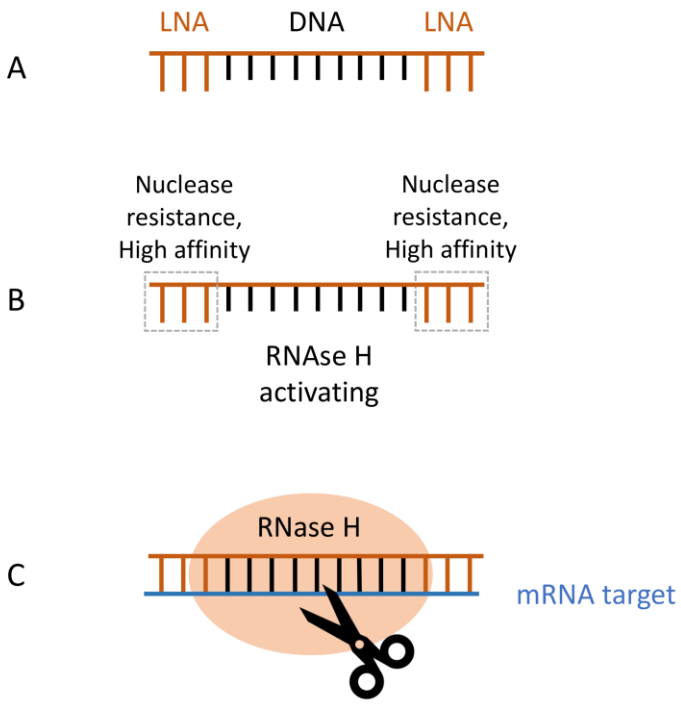


Figure 2.6 GapmeRs' mechanism of action. The GapmeRs feature a DNA fragment surrounded by locked nucleic acids (LNA) (**A**). LNA belong to a group of high affinity RNA analogues, as the ribose ring is "locked" into the optimal conformation for binding. Consequently, LNA molecules demonstrate high affinity for complementary RNA sequence, being also resistant to RNase H activity (**B**). DNA:RNA duplexes catalyse RNase H-dependent degradation of the RNA strand in the nucleus, therefore degrading the target mRNA (**C**).

2 Scara5-targeting antisense locked nucleic acids (LNA) GapmeRs (sequences reported in **Table 2.7**) and the negative control were used for hFOB transfection. All GapmeRs were resuspended in Tris-EDTA (TE) buffer at a concentration of 50 μM.

Table 2.7 Antisense Scara5 LNA GapmeRs sequences

	GapmeR sequence (3' – 5')	Target sequence (5' – 3')
Scara5 - 1	CGCATCAGGATTGAAT	ATTCAATCCTGATGCG
Scara5 - 2	CTGATTAACGGTGGAG	CTCCACCGTTAATCAG

2.11 Cell transfection

hFOB transfection was carried out at 34 °C, 5% (v/v) CO_2 for either 1 or 4 days. Scara5 plasmid, pmaxGFP plasmid (Amaxa™, Lonza, Slough, UK), and GapmeRs were used to transfect hFOB by employing OptiMEM with or without 10% (v/v) FBS and Lipofectamine 2000® (Invitrogen, ThermoFisher Scientific UK Ltd, Loughborough, UK), according to the manufacturer's instructions. Throughout transfection optimisation, also Viafect™ (Promega, Southampton, UK) was used to transfect hFOB with pmaxGFP at a ratio Transfection Reagent:DNA 4:1. Viafect™ transfection was carried out utilising OptiMEM with or without 10% (v/v) FBS.

For RNA extraction, hFOB were seeded as 1 x 10^4 cells/cm^2 and transfected once 80% confluent. 750 ng/ml of Scara5 plasmid/pmaxGFP or 50 nM of GapmeRs, together with 2.5 μl/ml of Lipofectamine 2000®, were incubated for 5 minutes before being added to the cells. 5 hours post-transfection, plasmid/GapmeRs containing OptiMEM was replaced with 10% (v/v) FBS OptiMEM. RNA was extracted 1 or 4 days after transfection, in order to synthetise cDNA and perform a RT-qPCR to assess Scara5 expression.

For ALP assay, 5 x 10^3 cells/well were seeded in a 96-well plate. For Scara5 plasmid/pmaxGFP transfection, 1 ng/ml of plasmid was mixed to 2 μl/ml of Lipofectamine 2000® in OptiMEM. hFOB were grown at 34 °C, 5% (v/v) CO_2, transfected once 80% confluent, and moved in a 37 °C, 5% (v/v) CO_2 incubator to be treated with antibiotic-free OM for 3 days. Regarding GapmeRs transfection, the only difference relies on the cell confluence before transfection: the antisense oligonucleotides (50 nM) were indeed used to transfect hFOB once cells were 50/60% confluent.

All transfection's pictures were obtained by using the EVOS M5000 Imaging System (ThermoFisher Scientific UK Ltd, Loughborough, UK) (470/525 nm light filter).

2.12 Cell proliferation assay (MTT assay)

For cell proliferation measurement, 5 mg/ml 3-(4,5-dimethylthiazol-2-yl)-2,5-diphenyl-2H-tetrazolium bromide (MTT) assay was used. This assay relies on the fact that MTT, a yellow tetrazolium salt substrate, can be reduced to purple formazan only by metabolically active cells. hFOB and PyMT-BO5 cells were seeded as 5 x 10^3 and 8 x 10^3 cells/well, respectively, within a 96-well plate. Cells were treated once 70% confluent; after specific time points (24 and 72 hours), 100 μl of 10% (v/v) MTT (ThermoFisher Scientific UK Ltd, Loughborough, UK) in CM with or without serum were added to each well and incubated at 34 or 37 °C, 5% (v/v) CO_2 for 2 hours. The MTT solution was removed and the formazan crystals formed were dissolved in 50 μl of DMSO/well. The OD of the resulting purple colour was determined at 550 and 630 nm using the FLUOstar Omega plate reader. For the final OD results, the 630 nm reading represented the background and it was therefore subtracted to the 550 nm one (test). The percentage of cell proliferation was calculated as follows:

$$\% \text{ Cell proliferation} = \frac{\text{Test}_{\text{OD 550-630 nm}}}{\text{Control}_{\text{OD 550-630 nm}}} \times 100$$

2.13 Cell adhesion assay

To determine PyMT-BO5 cells adhesion to the plastic support, a cell adhesion assay was used. 96-well plates were coated by using 50 μl/well of 2% (v/v) Matrigel® (10 mg/ml, Corning Life Sciences, Corning, New York, USA) in FBS-free CM for 30 minutes at 37 °C, 5% (v/v) CO_2. Subsequently, the solution was removed and wells were washed once with PBS. 2 x 10^4 BO5 cells/well were resuspended in inguinal fat supernatant (Sn) and inguinal fat and BO5 Sn before being seeded (**Section 2.14.2**). After 45 minutes, the Sn was removed and the cells were washed three times with PBS before being fixed with 10% (v/v) buffered formalin for 15 minutes. Wells were then washed once with PBS and 0.1% (v/v) crystal violet solution was added for 20 minutes. Finally, purple-stained cells were washed three times with dH_2O and the wells were left to air dry o/n. Images of single wells were acquired using Leica DMI3000 B microscope; 3 random fields of view (10x magnification) were analysed by ImageJ, thus determining the percentage of adhesion area occupied by BO5 cells.

2.14 Murine samples harvest and processing

Mice were humanly euthanised by CO_2 inhalation followed by cervical dislocation at different ages as previously mentioned. Total body weight was measured within two hours after euthanasia, whilst inguinal fat (iFAT) pads weight was assessed immediately after removal.

2.14.1 Murine tissue harvest

Within two hours from young (3 to 4 weeks old) or adult (≥ 11 weeks old) mice sacrifice, murine organs were collected under clean but not sterile conditions. iFAT pads, kidneys, testis, and tumours were snap-frozen in liquid Nitrogen and stored at -80 °C for subsequent experiments. For histology processing, murine organs (i.e. iFAT pads, long bones) and tumours were fixed in 10% (v/v) buffered formalin for 1 to 3 days at 4 °C, at the end of which they were washed in PBS and stored in 70% (v/v) Ethanol at 4 °C.

2.14.2 Inguinal fat supernatant production

Under sterile conditions, inguinal fat pads from 15 weeks old mice (females) were collected, washed in 1% (v/v) P/S PBS, cut into small fragments by scalpels, and added to FBS-free CM within Petri dishes (100 mm). After 24 hours, the adipose tissue fragments were removed and the supernatant (Sn) was collected and centrifuged at 250 x g for 5 minutes; the Sn was filtered through a 0.45 μm filter and aliquoted in 1.5 ml tubes, which were stored at -80 °C. Adipose tissue fragments were also added to PyMT-BO5 BrCa cells once 80% confluent. The Sn from co-cultured inguinal fat and PyMT-BO5 cells was obtained as above-described.

iFAT Sn and iFAT and PyMT-BO5 cells Sn were used as treatments for PyMT-BO5 cells, which proliferation (**Section 2.12**) and adhesion (**Section 2.13**) were assessed after 1/3 days and 45 minutes, respectively. Moreover, different concentrations of the iron chelator Desferrioxamine (DFO) were added to iFAT Sn and iFAT and PyMT-BO5 cells Sn before being used as a treatment for BO5 cells. After 3 days, Sn and DFO effect on BO5 proliferation was assessed via MTT assay (**Section 2.12**).

2.15 Microcomputed tomography (μCT)

2.15.1 Bone microarchitecture analysis

Mouse tibiae were fixed and stored as described in **Section 2.14.1;** tibiae kept in 70% (v/v) ethanol were washed in PBS and wrapped in plastic foil before scanning with SkyScan 1174 X-ray Microtomograph (Bruker Ltd, Coventry, UK). The X-ray source was set to a current of 800 mA and a voltage of 50 kV, with a pixel resolution of 6 μm. To analyse the trabecular bone, a set of consistent criteria was used to select either 160 (for 11 weeks old mice) or 201 (for ovariectomised/diabetic mice) serial cross sections from the bone's growth plate to the diaphysis. The SkyScan NRecon package (version 1.7.1.0) was then used to reconstruct cross-sectional images from the tomography X-ray projections, and volumes and regions of interest were selected and analysed using SkyScan software products, including CT-analyser (version 1.17.7.2) and CT-volume (version 2.2.3.0), which employ volume modelling.

2.15.2 Bone marrow adipose tissue evaluation by Osmium tetroxide (OsO_4) staining

Osmium staining of bone marrow adipose tissue was performed as described before [241]. Shortly, the tibiae were fixed in 10% (v/v) buffered formalin for 1-3 days and the bone was cleaned thoroughly by all the surrounding tissue and the distal end was cut than tibiae were placed in Osteosoft®, an EDTA-based solution, in order to be decalcified at room temperature (RT). After about 11 days, the decalcifying state was verified by μCT and bones were moved into histology cassettes (Histosette®, Merck Life Science UK Limited, Gillingham, UK) and washed for several hours in running water. Subsequently, tibiae were stained individually with 4% OsO_4 (v/v) in 0.5 ml tubes at RT for 3 days and afterwards washed in running H_2O for several hours. Decalcified and osmium-stained bones were then stored in dH_2O at 4 °C for μCT scanning at a later date.

For imaging and adipose tissue evaluation of the OsO_4 stained bone marrow adipocytes, tibiae were scanned according to the previous section's method, with the only difference being that the pixel resolution was set to 21 μm instead of 6 μm. The volume of marrow adipose tissue was calculated using SkyScan software products, including CT-analyser (version 1.17.7.2) and CT-volume (version 2.2.3.0).

2.16 Murine samples histology

Murine tissues (i.e. inguinal fat, BrCa tumours) were fixed and stored as described in **Section 2.14.1**. For paraffin embedding, the fixed samples were transferred into histology cassettes and dehydrated using increasing concentrations of ethanol as follows: 80% (v/v) ethanol for 1 hour, 90% (v/v) ethanol for 1 hour, absolute ethanol for 1 hour (repeated once for a total of 2 hours), xylene substitute for 30 minutes (repeated once for a total of 1 hour). Next, the cassettes were placed in 60 °C paraffin o/n before being moved to clean paraffin for 2 hours. Finally, the samples were included in paraffin blocks and allowed to solidify for 30 minutes at RT.

Paraffin blocks were sectioned using the Leica RM225 Microtome (Leica Biosystems, Wetzlar, Germany) equipped with MX35 Ultra Disposable Microtome Blades (Epredia, ThermoFisher Scientific UK Ltd, Loughborough, UK). Glass slides (VWR International, Lutterworth, UK) were used to place sections of either 4 µm or 6 µm (tumours only) and were then moved to a 37 °C oven o/n. Following this, the tissue slides were either stored at RT for future processing or stained immediately.

2.16.1 Hematoxylin and Eosin (H&E) staining

Tissue sections were stained using Harris Hematoxylin and Eosin Y-solution 0.5% (w/v) aqueous, which mainly colour the nuclei in purple and the cytoplasm in pink. The slides were de-waxed in xylene substitute (5 minutes, repeated once for a total of 10 min), re-hydrated in decreasing concentrations of ethanol (absolute ethanol for 2 minutes, 90% (v/v) ethanol for 2 minutes, 75% (v/v) ethanol for 2 minutes, dH_2O for 2 minutes) and finally stained (Hematoxylin for 30 seconds, running water for 5 minutes, Eosin for 5 minutes, running water for 5 minutes). At the end of the procedure, slides were immersed in two different concentrations of ethanol (70% (v/v), 100% (v/v)) to remove the excess of colour, and in xylene substitute to clear them. Slides were mounted with a glass cover slip (VWR International, Lutterworth, UK) using DPX mountant and visualised with the Leica DMI3000 B microscope (Leica Biosystems, Wetzlar, Germany) after 24 hours.

2.16.2 Iron staining (Potassium Ferrocyanide)

In order to stain murine tumour slides for ferric iron (Fe^{3+}), the Epredia™ Richard-Allan Scientific™ Iron Stain was obtained from Epredia (ThermoFisher Scientific UK Ltd, Loughborough, UK). A working iron solution was prepared by combining HCl and potassium ferrocyanide solutions in a 1:1 ratio. Tissue sections were de-waxed as above described (**Section 2.16.1**), then stained in the freshly prepared working solution for 30 minutes. The slides were washed in dH_2O for 1 minute and counterstained in Nuclear Red Thiazin stain solution for 1 minute. Finally, the sections were washed in dH_2O and immersed in two different concentrations of ethanol (70% (v/v), 100% (v/v)), followed by xylene substitute, before being mounted and visualised as outlined in **Section 2.16.1**.

The stained slides displayed a pink background and a blue colour on the iron detected. This was due to the reaction of Fe^{3+} with an acidic solution and potassium ferrocyanide, which resulted in the formation of an insoluble blue pigment (Prussian Blue).

2.16.3 Inguinal fat histology analysis

Using the Leica DMI3000 B microscope, H&E-stained slides of inguinal fat were examined by imaging 3 randomly selected fields at a magnification of 20x. As both embedding and staining process of fat pads involved ethanol and clearing agent (xylene substitute) that solubilised the lipid molecules, the canonical lipid ester core staining reagents (e.g. ORO) could not be used to stain lipid-containing adipocytes. Consequently, membranes and nuclei are the only elements that can be observed by H&E-stained adipose fat, and therefore adipocytes are referred to as "ghosts."

Parameters as adipose tissue ghosts' number and diameter were measured by employing ImageJ 1.53k software (National Institutes of Health, Maryland, USA) and the *Adiposoft* macro (**Figure 2.7**) [242].

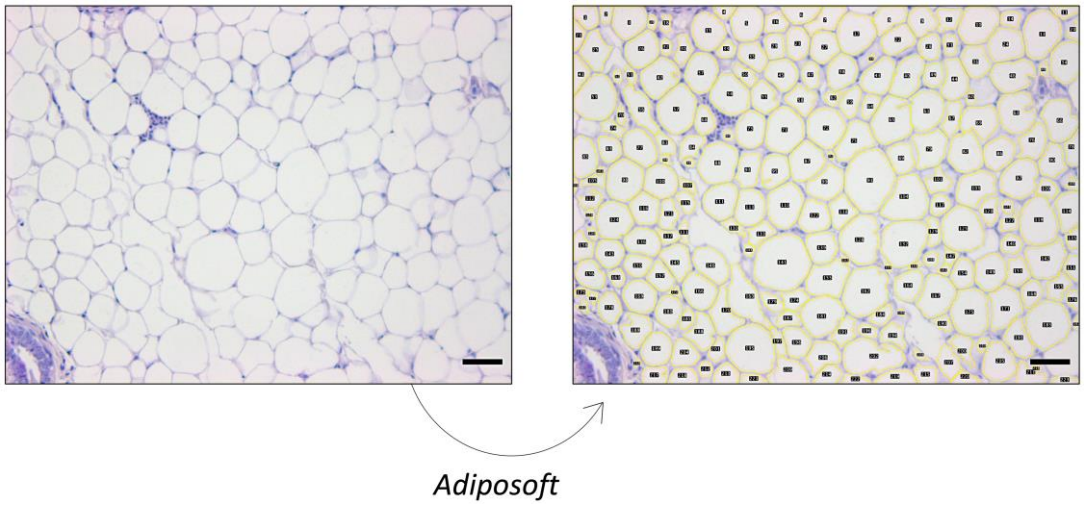


Figure 2.7 *Adiposoft* macro for adipocyte size and number analysis. H&E-stained adipocyte ghosts were processed and analysed in terms of size and number by ImageJ macro *Adiposoft* (image on the right) (20x bright field, 50 μm scale bar).

2.17 Calcein injection assay (*in vivo* bone formation assay)

Calcein injection assay is a useful experiment to study bone formation in mice models, as Calcein is a calcium chelator used to label new mineral bone deposition [243]. The aim of this experiment was to assess the effect of low dose lipopolysaccharide (LPS) on calvarial bone formation in Scara5-WT and KO mice.

2.17.1 PBS, LPS and Calcein injection protocol (experimental design)

Males of 5-7 weeks of age were subcutaneously injected on the parietal bones of the calvaria once with 50 μl of PBS or 0-25 μg/mouse of LPS Serotype R515 TLRGRADE® (Enzo Life Sciences (UK) Ltd., Exeter, UK) under general Isoflurane (Independent Vetcare Ltd, Bristol, UK) anaesthesia. 20 mg/kg Calcein (in about 200 μl/mouse) were injected intraperitoneally 7 and 14 days after PBS/LPS calvarial injection.

2.17.2 Calvaria plastic embedding, sectioning, and analysis

2 days after the last Calcein injection, mice were sacrificed and the calvaria were collected, fixed in 10% (v/v) buffered formalin for 1 day, washed in PBS, and stored at 4 °C in 70% (v/v) ethanol until ready to be processed. Bones were dehydrated in graded acetone (70% (v/v), 90% (v/v)) for 1 hour each, at RT. The last incubation in 100% (v/v) acetone was carried out

o/n. Once bones were dehydrated, they were plastic-infiltrated in the infiltrate mix, consisting of 90% (v/v) destabilised methylmethacrylate (dMMA), 10% (v/v) dibutylphtalate (DBP) and 0.05% (w/v) benzoyl peroxide (BPO) for 3 days at 4°C. Subsequently, calvaria bones were embedded in the embedding mix (85% (v/v) dMMA, 15% (v/v) DBP, 1.5% (w/v) BPO) at 37 °C for at least 1 week. Plastic blocks were placed at -20 °C for 1 h, after which they were removed from the glass vials by breaking the glass.

The blocks were then cut in half by using the IsoMet® Low Speed Saw machine (Buehler, Illinois, USA) and grinded through the Beta Grinder-Polisher (Buehler, Illinois, USA). 5 μm plastic sections were obtained by employing the the Leica RM225 Microtome. Calvaria sections were placed onto glass slides together with one drop of 95% (v/v) ethanol, covered with plastic squares, and baked o/n at 37 °C.

New bone formation was assessed by measuring the distance between the two Calcein-labelled bone's layers under the Leica DMI3000 B microscope and using the ImageJ 1.53k software.

2.18 Oestrogen deficiency-induced osteoporosis animal model (ovariectomy-induced osteoporosis)

Ovariectomy (OVX) or sham-ovariectomy (SHAM) was performed on 8 weeks old female mice under general anaesthesia (Isoflurane) and 0.3 mg/ml analgesic (Vetergesic®, Ceva Animal Health Ltd, High Wycombe, UK) administration. Body weight, as well as mice behaviour, were monitored frequently to exclude animal's suffering; mice were culled once 20 weeks old, 12 weeks after surgery, and long bones were harvested. Bones were processed and μCT-analysed as described in **Section 2.14.1** and **Section 2.15**.

2.19 Streptozotocin-induced diabetes animal model

7 weeks old male mice received a single high-dose intraperitoneal injection of Streptozotocin (Stz) (170 mg/kg) after a 6 h fasting. The high dose was likely to cause pancreatic β-cells disruption and mimic the onset of type 1 diabetes (T1D) [244]. Mice were then fed regularly and sucrose pellets were added for 3 days after the Stz injection. Blood glucose was measured weekly by using the GlucoRx Nexus blood glucometer (GlucoRx Limited, Guildford, UK), while

mice body weight was measured twice a week. Blood glucose levels above 16.7 mmol/L indicated a diabetic status in mice; in most cases, blood glucose readings were above 33.4 mmol/L, therefore above the glucometer limits. 2 weeks after the Stz injection, Linbit® pellets (LinShin Canada Inc, Toronto, Canada) were surgically implanted into mice fat pads. Linbit® pellets consist of insulin, which is sustainedly released from micro-crystallised palmitic acid (0.1U/day); 2 Linbit® pellets were implanted per 20 g of mouse body weight. Mice were sacrificed 6 weeks after the Stz injection, once 13 weeks old. Inguinal fat pads and bones were processed and analysed as described in **Section 2.14.1** and **Section 2.15.1**.

2.20 Breast cancer animal models

BRPKp110 cells (5 x 10^5) or PyMT-BO5 cells (1 x 10^5) were orthotopically injected into the left abdominal mammary fat pad of 15 weeks old female mice within 50 μl per animal of a 1:1 mixture of PBS and Matrigel®. The surgical procedure was carried out under general anaesthesia (Isoflurane), in sterile conditions, and the analgesic Vetergesic® was administered prior surgery and for 3 days after. The Grimace scale was used to determine mice suffering, as well as body weight measurements, for 10 days after surgery. Tumour growth was monitored every 2-3 days from day 10 to day 21 (BRPK-p110 model), or twice from day 10 to day 15 (PyMT-BO5 model). After 15 or 21 days, mice were sacrificed and tumours were harvested and kept in RPMI medium (Gibco, ThermoFisher Scientific UK Ltd, Loughborough, UK) for maximum 2 hours before being processed.

For both BRPK-p110 and PyMT-BO5 orthotopic models, Fisherbrand™ Traceable™ Digital Carbon Fiber Calipers (ThermoFisher Scientific UK Ltd, Loughborough, UK) were used to determine tumour volumes by employing the following formula:

$$\text{Volume } (mm^3) = \text{Length} \times \text{Width} \times 0.52$$

Tumour volumes were measured for both live and sacrificed animals, from which tumours were ultimately harvested. Tumours were halved and either fixed in 10% (v/v) buffered formalin for 1-3 days and stored in 70% (v/v) ethanol at 4 °C (for histology analysis), or snap-frozen in liquid Nitrogen and stored at -80 °C (for RT-qPCR or iron quantification).

2.21 Western Blot (WB)

2.21.1 Protein extraction and quantification

Total protein content was extracted from treated cells by means of a lysis solution, consisting of Tris-HCl (pH 8), 150 mM NaCl, 2 mM EDTA, 10% (v/v) glycerol, and 1% (v/v) Nonidet P40; for a complete lysis solution, proteinase inhibitor cocktail (Cell Signaling Technology, London, UK) and Pierce phosphatase inhibitor (ThermoFisher Scientific UK Ltd, Loughborough, UK) were added. At the end of the treatment (AM or Wnt3a), BMSCs were washed twice in ice-cold PBS, incubated with lysis solution for 30 minutes at 4 °C on a rocker, and finally harvested and centrifuged at 13,600 x g, 4 °C, for 15 minutes. The supernatant was collected and stored at -80 °C for later protein quantification analysis through Western Blot (WB).

Protein quantification was carried out by using Bradford reagent (Brilliant Blue G dye-based reagent) and bovine serum albumin as a standard. Protein concentration was ultimately assessed with the FLUOstar Omega plate reader at 595 nm.

2.21.2 Protein separation: sodium dodecyl-sulfate (SDS)-page electrophoresis

The protein samples were denatured at 95 °C for 5 minutes within a mixture consisting of 4x NuPage LDS sample buffer (Invitrogen, ThermoFisher Scientific UK Ltd, Loughborough, UK) and 1M dithiothreitol. 10 μg of denatured proteins were resolved on 8-10% (v/v) SDS polyacrylamide gels, within a Mini Protean Tetra Cell (Bio-Rad Laboratories Inc, Watford, UK) filled with running buffer (dH_2O, tris-base, glycine, SDS), in a 60-100 V run. The molecular weight was assessed by Precision Plus ProteinT Dual Color Standards (Bio-Rad Laboratories Inc, Watford, UK).

2.21.3 Protein transfer and immunoblotting

Once the electrophoresis was completed, the separated proteins were transferred to a PVDF membrane (Immobilon FL, Merck Life Science UK Limited, Gillingham, UK), using a Trans-Blot® Turbo™ Transfer System (Bio-Rad Laboratories Inc, Watford, UK). The membrane was then blocked with Intercept TBS blocking buffer (LI-COR Biosciences UK Ltd, Cambridge, UK) for 1 hour, followed by an o/n incubation with the primary antibody solution at a low rocker speed and appropriate dilution (**Table 2.8**). After 4 washes with Tris-buffered saline with 0.1% (v/v)

Tween® 20 detergent (TBST), the membrane was incubated with a secondary antibody IRDye® solution for 1 hour at RT (**Table 2.8**), followed by 4 additional washes with TBST. The membrane was rinsed with TBS and scanned immediately with the Odyssey CLx Imaging System (LI-COR Biosciences UK Ltd, Cambridge, UK). The densitometric software (Image Studio, LI-COR Biosciences UK Ltd, Cambridge, UK) was used to quantify the protein band density, which was then normalised to the signal of the housekeeping protein (β-actin).

Table 2.8 Antibodies used for Western Blot

Antibody	Molecular weight	Dilution	Source	Catalogue number	Supplier	
β-actin	43 kDa	1:2000	Mouse	sc-47778	Santa Cruz Biotechnology, Inc (Heidelberg, Germany)	Primary antibodies
β-actin	43 kDa	1:5000	Rabbit	#4970	Cell Signaling Technology	
β-catenin	90 kDa	1:2000	Rabbit	AHP2418	Bio-Rad	
Phospho-RPS6 (Ser380)	≈32 kDa	1:400	Rabbit	AF3918	Bio-Techne Ltd (Abingdon, UK)	
Phospho-RSK1 (Ser235/Ser236)	≈94 kDa	1:5000	Rabbit	MAB79671	Bio-Techne Ltd	
IRDye® 680LT	/	1:10,000	Goat anti-Mouse	926-32213	LI-COR	Secondary antibodies
IRDye® 800CW	/	1:10,000	Donkey anti-Rabbit	926-68020	LI-COR	

2.22 AKT phosphorylation array

To assess Scara5-related changes within the AKT-related pathways, the RayBio® C-Series AKT Pathway Phosphorylation Array C1 was purchased from RayBiotech (RayBiotech Life, Inc., Georgia, USA). Proteins were obtained from cell lysates of Scara5-WT and -KO BMSCs treated with CM, OM, and AM for 20 minutes. According to the manufacturer instructions, 200 μg of proteins were diluted in blocking buffer (1 ml as final volume), also used to block the provided membranes at RT for 1 h. The membranes were incubated with proteins in blocking buffer

o/n at 4 °C, under gentle rotation. Afterwards, all steps were performed at RT and under gentle rotation; membranes were washed 5 times, for 5 minutes each time, and incubated for 2 hours with the detection antibody cocktail. 5 new washes followed the last step before membranes were incubated with HRP-Anti-Rabbit IgG for 2 hours. Again, membranes were washed 5 times and the detection buffer mixture was pipetted onto the membranes for 2 minutes, after which they were visualised under the G:BOX Chemi XRQ transilluminator. 1 minute-exposure was used for each membrane and the dots density was quantified using ImageJ 1.53k software.

Once dots density was quantified, the background was subtracted and the data were normalised to the positive controls signals. OM and AM membranes were finally compared to the CM membrane (the control one).

2.23 Seahorse cell metabolic analysis (mitochondrial function analysis)

Seahorse metabolic analysis was partially performed at the Quadram Institute (Norwich, UK). Seahorse plates, cartridges, medium and supplement reagents, calibrant solution, and Mito Stress Test Kit were purchased from Agilent (Agilent Technologies, Santa Clara, USA). BMSCs P1 were seeded at a density of 7000 cells/well for CM and OM treatment and 10,000 cells/well for AM treatment within an Agilent Seahorse XFe96 cell culture microplates. After 3 days, cells were treated with OM and AM for 7 days. One day prior the cell analysis, XFe96 Flux cartridges were hydrated with XF Calibrant o/n at 37 °C. Treatment media were removed after 7 days and replaced with Seahorse DMEM medium, pH 7.4 added with XF 1 M Glucose solution, XF 100 mM Pyruvate solution, XF 200 mM Glutamine solution. Cells were then equilibrated at 37 °C in a non-CO_2 incubator for 1 hour. OM/AM-treated BMSCs mitochondrial respiration was assessed using the Seahorse XF Cell Mito Stress Test Kit, which measured the cellular oxygen consumption rate (OCR) upon the injection of Oligomycin (1.5 μM), carbonyl cyanide-4- (trifluoromethoxy) phenylhydrazone (FCCP) (1 μM), and Rotenone and Antimycin A (0.5 μM), according to the manufacturer's instructions (**Figure 2.8**). Finally, cells were ready for being analysed using the Seahorse XFe96 Analyser (Agilent Technologies, Santa Clara, USA).

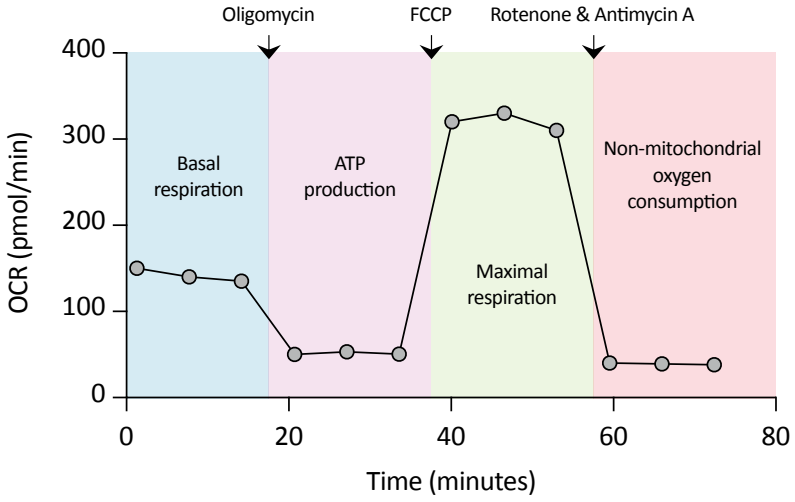


Figure 2.8 Agilent Seahorse XF Cell Mito Stress Test profile. After treatment, BMSCs were injected with Oligomycin, which determined ATP production by inhibiting ATP synthase function. FCCP injection allowed the assessment of cell maximal respiration by collapsing the proton gradient and disrupting the mitochondrial membrane potential, thus determining an uncontrolled electron flow through the electron transport chain (ETC). As a consequence, OCR reaches the maximum. Finally, non-mitochondrial oxygen consumption was measured upon the injection of Rotenone and Antimycin A, which inhibited ETC Complex I and Complex III shutting down the mitochondrial respiration. Basal and maximal respiration were subsequently measured by subtracting the non-mitochondrial oxygen consumption reading from basal and maximal respiration readings.

After the assay completion, the medium was removed and cells were fixed with 10% (v/v) buffered formalin for 15 minutes. Cells were then washed once with PBS before adding a solution of 1 mg/ml 4',6-diamidino-2-phenylindole (DAPI) (Thermo Scientific™, ThermoFisher Scientific UK Ltd, Loughborough, UK) in PBS (dilution 1:1000) for 15 minutes. Subsequently, cells were washed once with PBS and visualised using the EVOS M5000 Imaging System (420/495 nm light filter). 3 random fields of view (10x magnification) were analysed by ImageJ, thus determining the number of cells per single well. Hence, Seahorse data were normalised to the final number of cells and presented as OCR (pmol/min per 1000 cells).

2.24 Iron quantification (ferene-based iron assay)

The iron quantification was partially performed at the School of Chemistry, University of East Anglia (Norwich, UK) by Dr Justin Bradley. To determine total iron content in solid samples

(tissues, i.e. inguinal fat, testis, kidneys, tumours), a ferene-based assay was used. Briefly, ≈20 mg of tissue were digested within 68% (v/v) nitric acid and ultrapure H_2O 1:1 for 24 hours at 37 °C. Once cooled down, 80 μl of sample were mixed with 200 μl of a saturated solution of ammonium acetate (in order to neutralise the nitric acid). 40 μl of a 5% (w/v) sodium ascorbate solution were added to the sample, followed by 40 μl of 10 mM ferene solution. The samples were left to stand at RT for 30 minutes to allow the complex ferrous iron (Fe^{2+})-ferene to form. To prepare the calibration plot, iron solutions at different concentration were prepared (from zero to 50 μM). The complex optical density was measured through the VWR® Hitachi U-2900 spectrophotometer (VWR International Ltd, Lutterworth, UK); spectra were measured in a 1 cm pathlength quartz cuvette at 593 nm. This assay measured the sample total iron; although the ferene solution used is a high affinity to Fe^{2+} chelator, the addition of sodium ascorbate reduces the Fe^{3+} to Fe^{2+}, thus determining the detection of total iron.

2.25 Data analysis and statistics

Data were analysed by using the Prism 9.1.1 software (GraphPad, California, USA) and are presented as mean ± SEM (standard error of mean) or mean ± SD (standard deviation). Before analysis, data sets were submitted to the Saphiro-Wilk test, to assess if the distribution was normal. For a normal distribution and a 2 groups comparison, unpaired two-tailed Student's-t test was used, whereas for a 3 or more-group comparison, one-way ANOVA with Tukey's post hoc test was preferred. If the data distribution was not normal, Mann-Whitney U test or non-parametric Kruskal-Wallis test with Dunn's multiple comparison were used for a 2-group or a 3- or more-group comparison. When two variables were considered, a two-way ANOVA with Tukey's or Šídák's post-hoc test was performed. Due to the variability of the *in vivo* work, murine organs' and tumours' data were analysed assuming a non-normal distribution. Simple linear regression analysis was used to determine the statistical difference of *in vivo* tumour volumes by comparing the elevation of the regression lines. Each experiment was performed in replicates (2 to 6) and repeated at least 3 times, by employing 3 different biological/independent samples; sample size is indicated as "n". Statistical significance degrees are indicated as * $p \leq 0.05$, ** $p < 0.01$, *** $p < 0.001$, **** $p < 0.0001$. No significance is not showed or reported as "ns". No statistical methods were employed to predetermine sample size.

Schematic figures were originally produced, unless differently stated, employing Adobe Photoshop (version 21.1.2), Adobe Illustrator (version 24.1), Microsoft® PowerPoint (version 16.76.1), and ChemDraw® (version 16.0.1.4) software.

Chapter 3: Scara5 controls osteogenesis and adipogenesis

3.1 Introduction

Mesenchymal stromal cells (MSCs) can be defined as multipotent stromal cells present in all mesenchyme-derived tissues and easily isolatable from sources such as bone marrow and adipose tissue [245]. Throughout the years, MSCs proved to have the multipotent ability to differentiate into diverse cell types, most notably osteoblasts and adipocytes [133]. Under determinate chemical stimuli, *in vitro* MSCs commit to bone and adipose tissue precursors before being terminally differentiated into mature cells. As a confirmation of the new differentiated status, techniques such as reverse transcription-quantitative polymerase chain reaction (RT-qPCR) can be exploited to evaluate osteogenic and adipogenic markers expression (e.g. alkaline phosphatase, osteocalcin, adiponectin, leptin). Also, the compounds Alizarin Red S and Oil Red O have been widely used over the years to stain calcium and lipid droplets of MSCs-derived osteoblasts and adipocytes, respectively.

The family of Scavenger Receptor Class A consists of 5 members that are mostly expressed on macrophages, to endow them with the ability to recognise and internalise microbial pathogens [171]. MSR1, MARCO, Scara3, Scara4, and Scara5 share a similar collagenous domain, which seems crucial to confer the binding property to these receptors. Although Class A members are predominantly expressed on macrophages, in the last decades they also have been found expressed in a multitude of other tissues and cell types as, inter alia, heart, testis, placenta and epithelial cells [166]. Unlike the other members of this family, Scara5 has some unique characteristics. In 2017, Lee *et al.* firstly described Scara5 in association with adipose tissue and adipogenesis *in vitro* [165]. When Scara5 was knocked down in murine preadipocytes cells A33, adipogenic differentiation was earnestly impaired; this study pointed to Scara5 as a novel adipogenic marker [165].

MSCs commitment is controlled by a plethora of signalling pathways, many of which remains unknown. Scara5 emerged as a potential mediator of adipocyte commitment, but it has never been associated with osteogenesis. This chapter will investigate Scara5 involvement in both osteogenesis and adipogenesis using Scara5-wild type (WT) and -

knockout (KO) murine bone marrow derived MSCs (BMSCs) and human MSCs-like cells (human fetal osteoblast 1.19).

3.2 Scara5-WT and -KO BMSCs respond differently to osteogenic stimuli

3.2.1 Passage 1 bone flushed BMSCs show the utmost potential as a primary cell model

BMSCs can be isolated in different ways from bone marrow; the most common technique involves flushing long bones with medium to remove the bone marrow. In optimising the cell culture of BMSCs, also bone chips have been used to obtain the desired cells [246].

Alkaline phosphatase (ALP) assay is a gold standard technique often exploited to evaluate osteogenic potential of MSCs-like cells. The assay employs p-Nitrophenylphosphate (pNPP) substrate, which is hydrolysed into the yellow-coloured product p-Nitrophenol (pNP) by the ALP produced by differentiating BMSCs. Hence, ALP activity is represented as pNP concentration (mmol/L). In the following sections, an ALP assay was employed to select the ideal cell passage of BMSCs to be used in the majority of experiments.

3.2.1.1 Bone washed cells vs bone chips: different ways to isolate and grow BMSCs

Murine BMSCs were harvested from long bones (i.e. tibiae and femurs) of C57BL/6J mice both by flushing the bone marrow out from the cavity and by cutting up the bones to produce bone chips. While bone flushed-BMSCs were 70 to 80% confluent after 5 days of culture in complete maintenance medium (CM), it took 10 days to the bone chips derived-BMSCs to become similarly confluent (**Figure 3.1 A**). As shown in **Figure 3.1 B**, bone flushed-BMSCs displayed an elevated ALP activity in response to osteogenic medium (OM). The highest cell seeding number used (15,000) also produced the highest pNP concentration, both for CM and OM-treated cells (0.577 and 1.536 mmol/L, respectively). Regarding the bone chips derived-BMSCs, as demonstrated in **Figure 3.1 B**, pNP concentrations detected were lower than the flushed-BMSCs; the highest pNP concentration for bone chips BMSCs was, indeed, the one produced by OM-treated 15,000 cells, equal to 0.534 mmol/L. On the other hand, 5000 cells from flushed bones OM treated for 3 days produced 0.530 mmol/L of pNP. Hence, less BMSCs are required to produce a discrete amount of pNP, and this is achievable in just 5 days of bone-flushed cell culture.

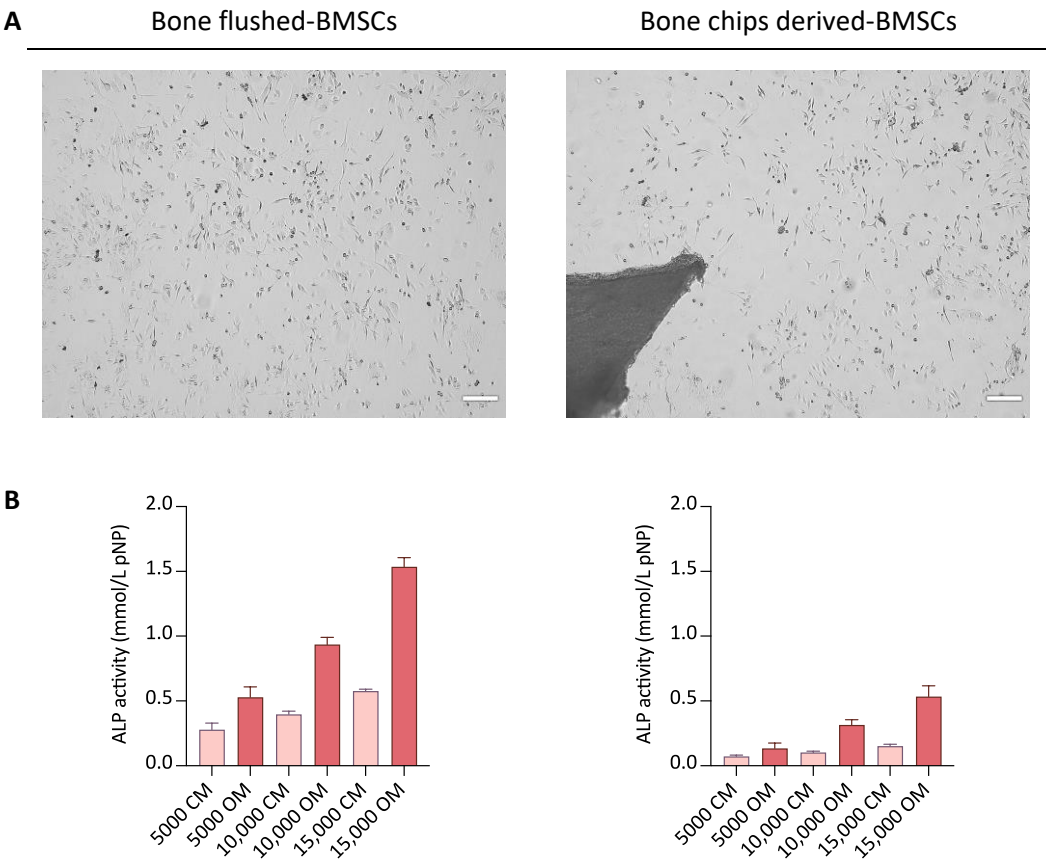


Figure 3.1 Bone flushed-BMSCs and bone chips derived-BMSCs show distinct ALP activity patterns. BMSCs bone-flushed were cultured for 5 days, whereas BMSCs from bone chips were cultured for 10 days (**A**); pictures were acquired after 5 or 10 days of culture at 10x bright field magnification (50 μm scale bar). BMSCs were then trypsinised and seeded as passage 1 at different seeding densities (from 5000 to 15,000 cells/well in a 96-well plate). Their ALP activity was assessed via ALP assay after 3 days of OM treatment (**B**). Bars represent the mean ± SD of ≥ 3 technical replicates of a single experiment.

Comparing the two different methods used to collect and cultivate BMSCs, bone flushed-BMSCs were selected as the optimal cells to be used in this work, both in terms of time of collection and ALP activity detected.

3.2.1.2 Passage 1 BMSCs display the highest ALP activity when OM-treated

Bone flushed-BMSCs were cultivated from passage (P) 1 to P3 and for each passage an ALP assay was performed. Cells were treated for 3 days with OM and the pNP concentration was determined, as depicted in **Figure 3.2 A**. P1 cells responded to osteogenic stimuli efficiently, at all three different seeding density, with 15,000 cells producing the highest concentration of pNP once treated with OM (1.526 mmol/L). P2 cells generated much higher pNP

concentrations in CM; however, OM treated cells did not respond as efficiently as P1 cells, with a fold change lower than 1.8 per seeding number used. In P3 cells, the fold changes between OM/CM were overall lower than 1.5; thus, the best fold induction in OM was in P1 cells.

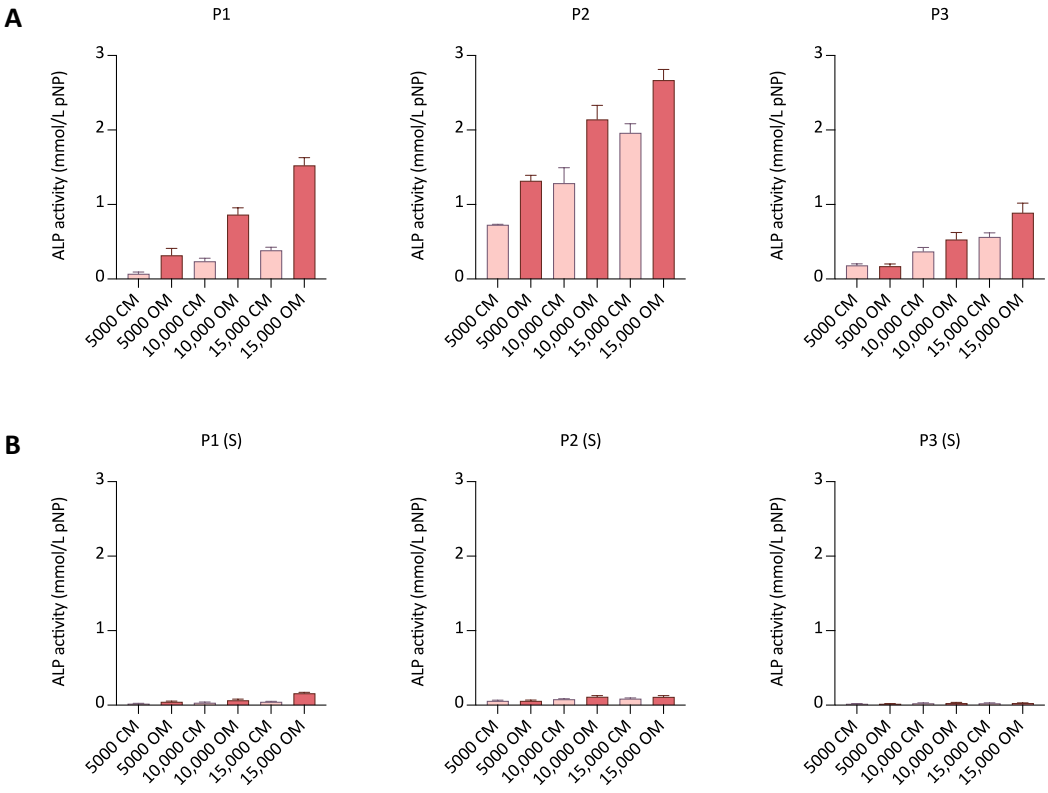


Figure 3.2 Passage 1 (P1) BMSCs exhibit the highest ALP activity. Different numbers of BMSCs passages 1-3 were seeded in a 96-well plate and treated with OM; ALP activity was assessed via ALP assay (**A**). ALP activity was also determined from scraped (S) cells, passage 1-3, after 3 days of OM treatment (**B**). Bars represent ≥ 3 technical replicates of a single experiment, shown as mean ± SD.

Due to the heterogeneous cell populations present in the bone marrow, once BMSCs are seeded some cell types (e.g. monocytes) will adhere to the plastic surface more strongly than others [233]. In order to detach the remaining cells from the Petri dishes, cell scrapers were used; the scraped cells were then subcultivated until P3 and, for each passage, treated with OM. As shown in **Figure 3.2 B**, ALP assay proved that those cells did not respond to OM, therefore lacking osteogenic potential.

Be that as it may, these results indicate that P1 cells have the greatest osteogenic potential once OM treated. Due to the scarce number of cells obtainable from bone flushing, 5000

cells/well can be experimentally used: their OM/CM fold change was 4.5, higher than the fold changes of the others seeding densities (3.6 for 10,000 cells, 3.9 for 15,000 cells) (**Figure 3.2 A,** P1).

3.2.2 Scara5 gene expression is not triggered by OM treatment

Over the last decade, Scara5 expression has been associated with several tissues, but its relation to bone is less well explored. To test whether Scara5 expression was triggered by osteogenic stimuli, BMSCs were treated with OM for 3 different time points: 7, 14, and 21 days. RNA was subsequently extracted from confluent cells and cDNA was synthesised. RT-qPCR was carried out, showing that OM did not induce Scara5 expression at any considered experimental time (**Figure 3.3**).

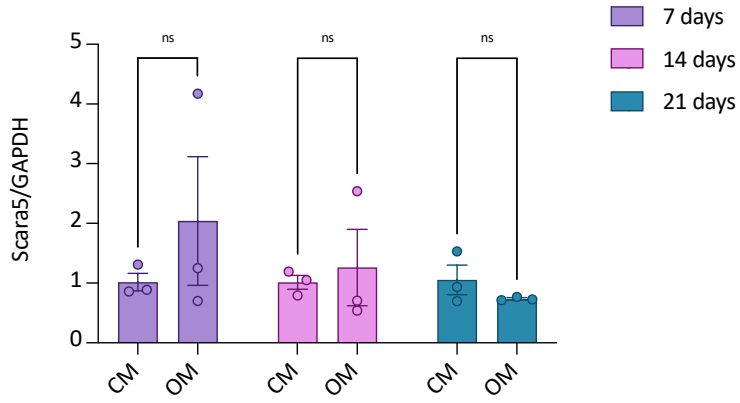


Figure 3.3 OM treatment does not trigger Scara5 gene expression. WT and Scara5-KO BMSCs were seeded as 2.88 x 10^5 cells/well in a 6 well-plate and treated with OM for 7, 14, and 21 days; qRT-PCR was performed to assess Scara5 expression. $2^{-\Delta\Delta CT}$ method was applied and Scara5 expression was normalised to GAPDH. Data are depicted as mean ± SEM and the experiment was repeated using 3 different biological samples (n=3). Two-way ANOVA with Šídák's post-hoc test was used to determine the degree of significance (^{ns} $p > 0.05$).

3.2.3 Scara5-KO BMSCs are more prone to differentiate to osteoblast than WT cells

A constitutive KO of Scara5 was performed in C57BL/6J mice models to extensively study the biological role of this gene in MSCs differentiation, as well as bone and fat homeostasis. To determine whether Scara5 genetic deletion influences cells' osteogenic potential, BMSCs were obtained from WT and Scara5-KO mice and treated with OM for 28 days, the time required to differentiate to osteoblasts. ARS was used to stain calcium-containing bone

nodules, as shown in **Figure 3.4 A**. ARS was also eluted using 10% (w/v) cetylpyridinium chloride buffer (**Figure 3.4 B**). The osteogenic differentiation process proved to be quite difficult to carry out for murine BMSCs; for this reason, the above-described results refer to a single experiment.

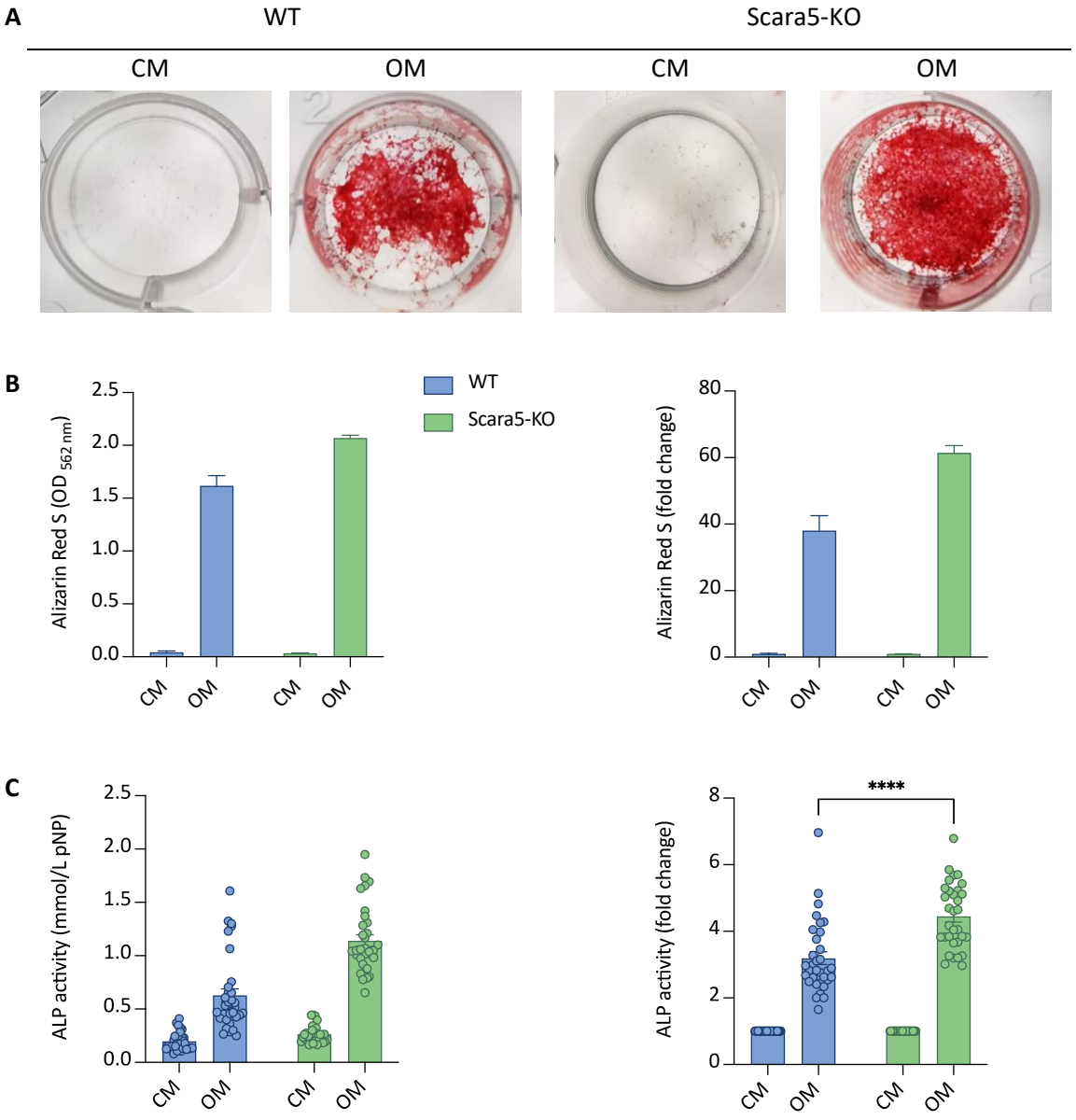


Figure 3.4 Scara5 deficient BMSCs have a higher osteogenic potential than WT BMSCs. BMSCs were seeded in a 24-well plate and treated for 28 days and the osteogenic differentiation of WT and Scara5 KO BMSCs was assessed by Alizarin Red S staining (**A**). Alizarin Red was quantified, and its quantification is presented both in terms of OD (left) and fold change (right) (**B**); graphs represent a single experiment carried out in triplicates and depicted as mean ± SD. ALP activity was evaluated by ALP assay after 3 days of treatment with OM (n=5, ≥3 technical replicates/n), presented both in terms

of pNP concentration (left) and fold change (right) (**C**). Data are shown as mean ± SEM, Mann-Whitney U test was used to determine the degree of significance (**** $p < 0.0001$).

To assess ALP activity, BMSCs WT and Scara5-KO were seeded in a 96-well plate and treated with OM for 3 days. In response to OM, Scara5-KO cells displayed a significantly higher activity of ALP than WT BMSCs (**Figure 3.4 C**). In terms of fold change, Scara5-KO OM was 1.4 higher than WT OM (mean ± SEM, 3.192 ± 0.189 vs 4.453 ± 0.173), demonstrating that the absence of Scara5 increases BMSCs osteogenesis.

3.2.4 Osteogenic marker expression does not differ between Scara5-WT and -KO BMSCs

In addition to bone nodules' staining and ALP assay, osteogenic gene expression was investigated. Alkaline phosphatase (Alpl) and osteocalcin (OCN) gene expression was assessed through RT-qPCR after BMSCs WT and Scara5-KO treatment with OM. As depicted in **Figure 3.5 A**, 7 days of treatment induced both Alpl and OCN expression, but there was no statistically significant difference between BMSCs WT and Scara5-KO. After 14 (**Figure 3.5 B**) and 21 (**Figure 3.5 C**) days of OM treatment, Alpl and OCN expression slightly decreased, but there was no statistically significant expression difference between WT and KO cells.

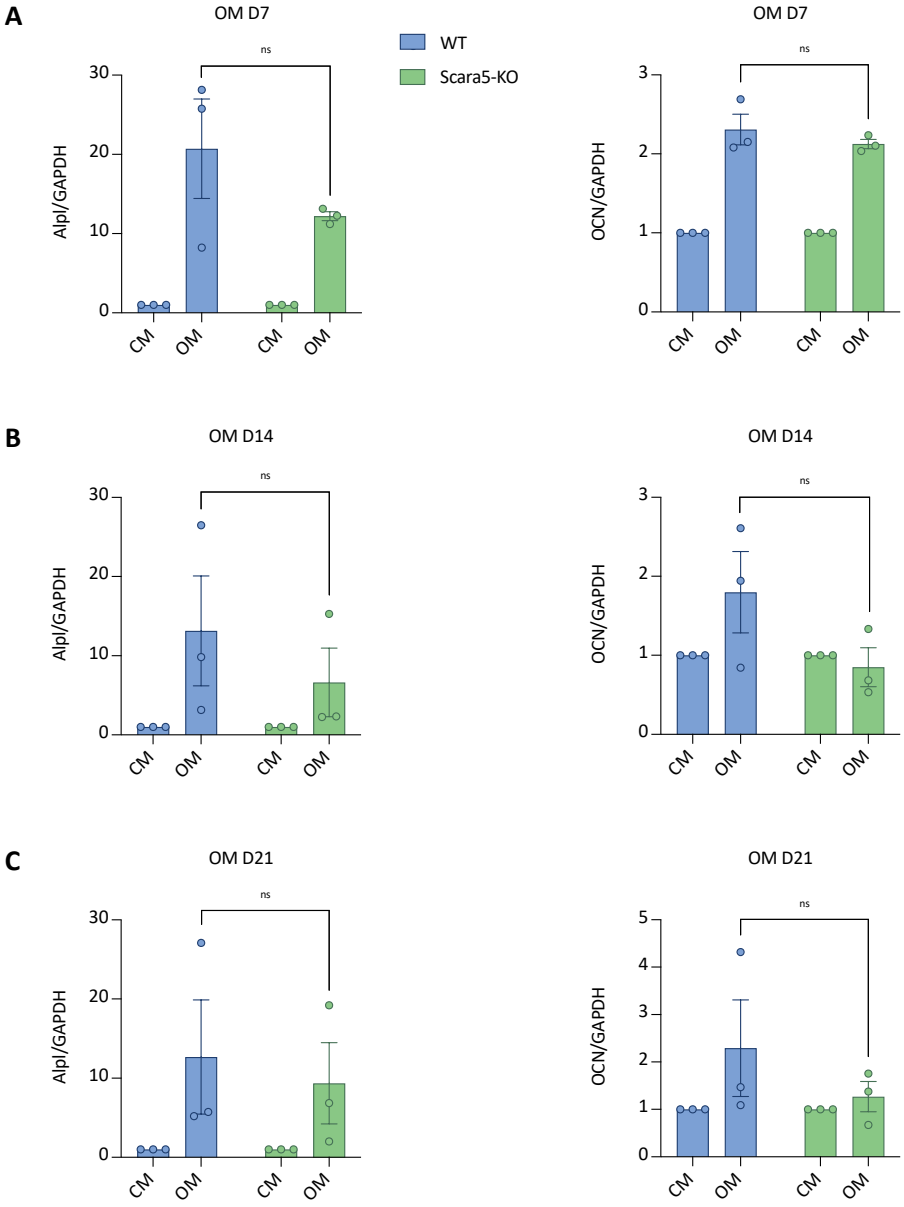


Figure 3.5 Alpl and OCN expression does not differ between Scara5-WT and -KO BMSCs. BMSCs were seeded as 2.88 x 10^5 cells/well in a 6 well-plate before being treated with OM for 7 (D7, **A**), 14 (D14, **B**), and 21 (D21, **C**) days. $2^{-\Delta\Delta CT}$ method was applied and gene expression was normalised to GAPDH; graphs of Alpl expression are shown on the right, whereas the OCN's ones on the left (n=3), and depicted as mean ± SEM. Unpaired two-tailed Student's t-test was used to determine the degree of significance (^{ns} $p > 0.05$).

3.3 Scara5-WT and -KO BMSCs respond differently to adipogenic stimuli

BMSCs differentiate towards a committed and mature cell type if appropriately stimulated; therefore, adipogenic stimuli push MSCs to differentiate to preadipocytes first, then to

adipocyte-like cells (hereafter referred to as “mature adipocytes”) if an adipogenic cocktail is used *in vitro*.

3.3.1 Scara5 gene expression is triggered by AM treatment

As Scara5 has already been associated with adipogenesis [165], murine BMSCs were treated with adipogenic medium (AM) to determine whether Scara5 expression changes after 7, 14, and 21 days of treatment. The fold change AM/CM after 7 days was equal to 13.8 ± 4.4 (mean ± SEM), and to 4 ± 2 after 21 days. Neither 14 nor 21 days of treatment stimulate Scara5 expression in BMSCs (**Figure 3.6 A**). **Figure 3.6 B** illustrates Scara5 expression in all phases of BMSCs differentiation, as follows: MSCs commitment to preadipocytes (days 0-7), MSCs differentiation into mature adipocytes (days 7-25).

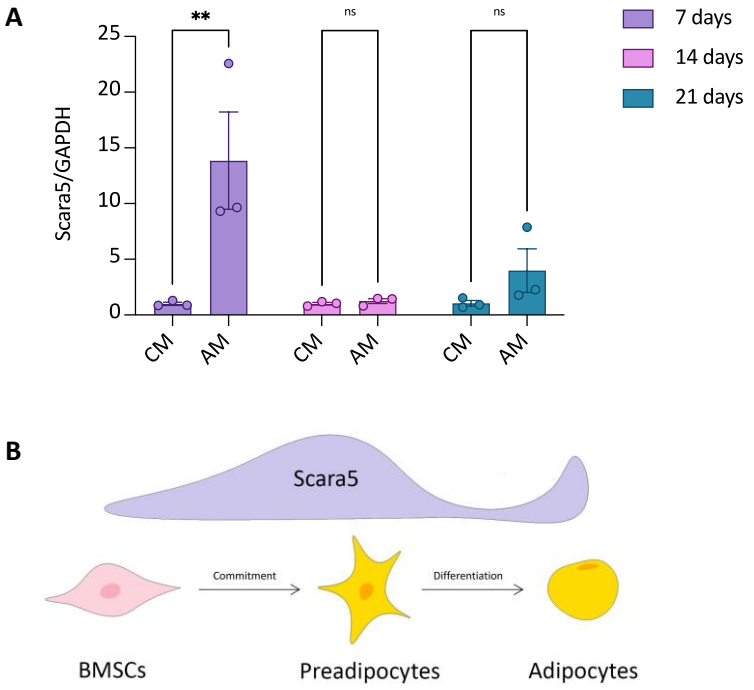


Figure 3.6 AM treatment triggers Scara5 gene expression. Scara5 expression of BMSCs WT was assessed by RT-qPCR after 7, 14, and 21 days AM treatment (n=3). $2^{-\Delta\Delta CT}$ method was applied and Scara5 expression was normalised to GAPDH; data are presented in terms of fold change and shown as mean ± SEM (**A**). Schematic representation of Scara5 expression during adipogenic differentiation of BMSCs (**B**). Two-way ANOVA with Šídák's post-hoc test was used to determine the degree of significance (^{ns} $p > 0.05$, ** $p > 0.01$).

3.3.2 Scara5 deficient BMSCs differentiate less to adipocytes than WT cells

In the presence of AM, both WT and Scara5-KO BMSCs differentiated towards adipocytes, as depicted in **Figure 3.7**. Oil Red O dye confirmed the differentiated state of BMSCs by staining cytoplasmic lipids within adipocytes. As appreciable by **Figure 3.7**, WT and Scara5-KO BMSCs did not differentiate to adipocytes equally: KO cells indeed showed less lipid-containing adipocytes after 25 days of AM treatment.

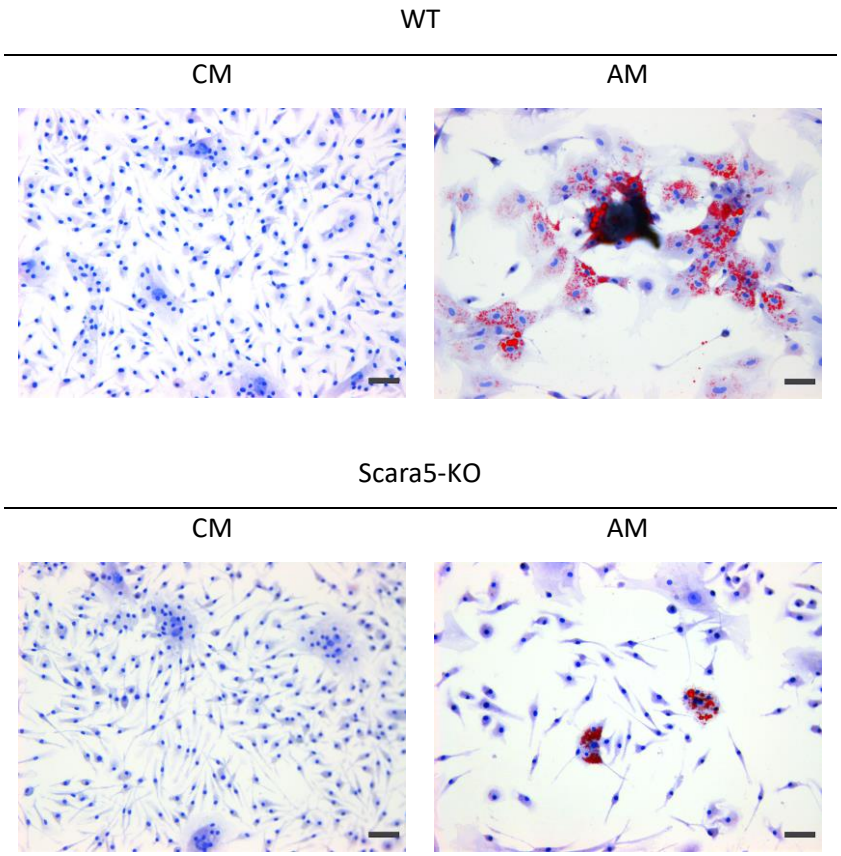


Figure 3.7 Oil Red O-stained lipids are less abundant in Scara5-KO BMSCs. BMSCs were seeded in 48-well plates and the adipogenic differentiation was assessed by Oil red O staining after 25 days of treatment with AM. Pictures are representative of a single experiment carried out in triplicates. 20x bright field magnification (50 μm scale bar).

As stated in **Section 3.2.3**, the osteogenic differentiation process was difficult to complete for primary BMSCs. The same applies to the adipogenic differentiation course: this is the reason why the results described refers to a single experiment performed in triplicates.

3.3.3 Adipogenic gene expression is impaired in Scara5-null BMSCs

Scara5 expression was strongly associated with BMSCs adipogenesis once BMSCs were treated with AM (**Section 3.3.1**). It was therefore consequential to look at adipogenic gene expression in WT and Scara5-KO BMSCs, i.e. adiponectin (Adipoq) and leptin (LEP). As shown in **Figure 3.8 A,** 7 days of AM treatment induced both Adipoq and LEP expression, although Scara5-KO BMSCs expressed both genes at lower levels; in terms of AM/CM fold change, WT BMSCs Adipoq and LEP expression were equal to 113.5 ± 21.4 (mean ± SEM) and 8.6 ± 1.6, respectively. On the other hand, Scara5-KO cells Adipoq expression was 19.5 ± 5.5, while LEP's one to 4.1 ± 0.7. WT and KO adipogenic gene expression was significantly different after 7 days of AM treatment.

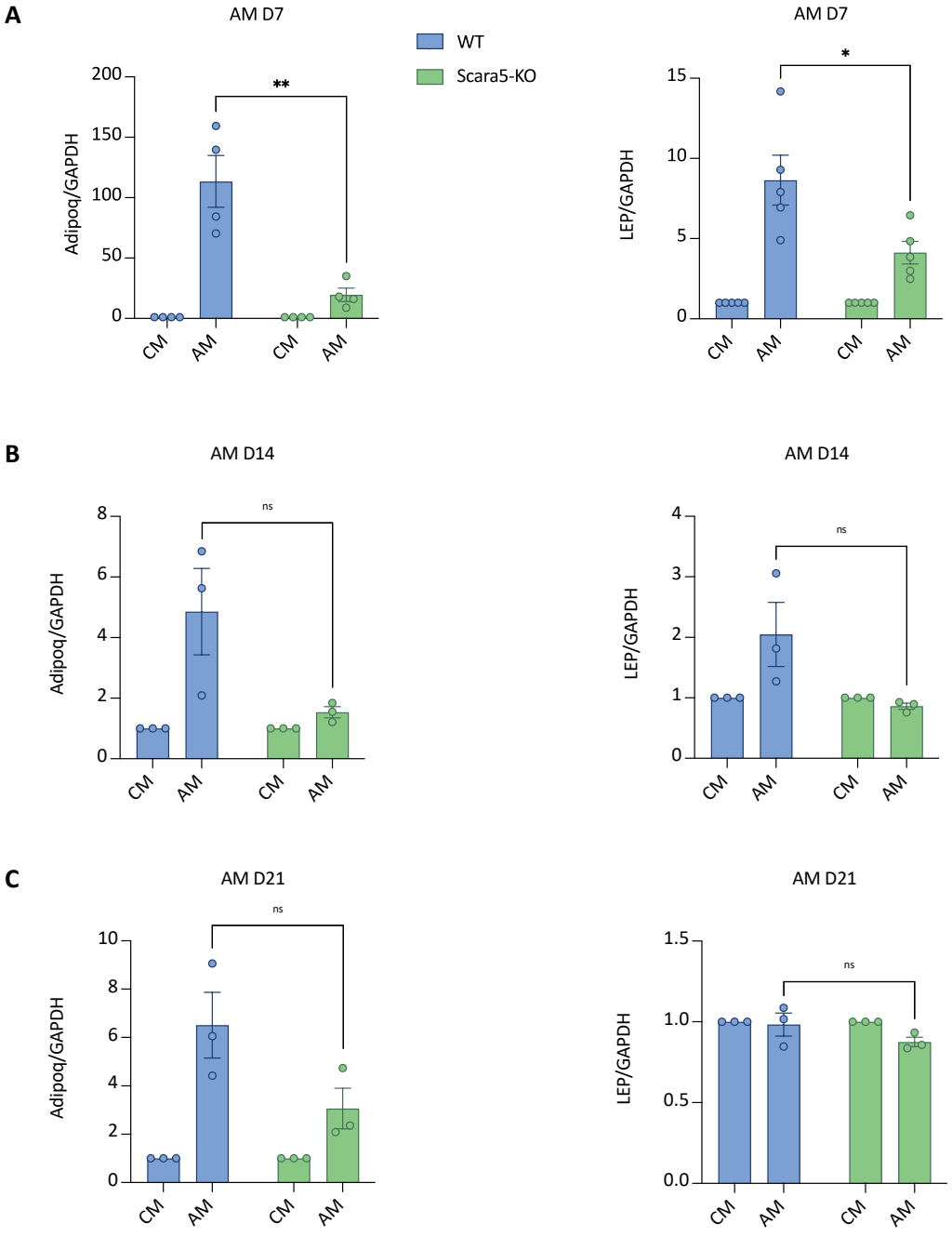


Figure 3.8 Adipoq and LEP expression differs between WT and Scara5-KO BMSCs. Adipogenic potential of BMSCs WT and Scara5-KO was assessed by RT-qPCR after 7 (**A**), 14 (**B**), and 21 (**C**) days of AM treatment (n≥3). $2^{-\Delta\Delta CT}$ method was applied and gene expression was normalised to GAPDH; data are presented as mean ± SEM and unpaired two-tailed Student's t-test was used to determine the degree of significance (^{ns} $p > 0.05$, * $p \leq 0.05$, ** $p < 0.01$).

Figure 3.8 B shows both Adipoq and LEP expression after 14 days of AM treatment. Despite a difference can be detected between Scara5-WT and -KO BMSCs in the genes' expression, this was not statistically significant ($p = 0.082$ for Adipoq, $p = 0.089$ for LEP). Furthermore, after 21 days of culture with AM (**Figure 3.8 C**), Adipoq expression remained high in WT cells (6.5 ± 1.4), but not statistically different from Scara5-KO's one (3.1 ± 0.8, $p = 0.097$). On the other hand, LEP expression did not differ between WT and KO BMSCs after 21 days of AM treatment.

3.4 Osteoblast cell line hFOB 1.19 can be used to study MSCs commitment to osteoblasts and adipocytes

Due to the difficulty in collecting and cultivating high number of cells from mouse bone marrow, an MSCs-like cell line was selected to genetically manipulate Scara5 expression and further investigate its effect on MSCs fate.

Human fetal osteoblasts (hFOB 1.19) represent an immortalised osteoprogenitor cell line, able to differentiate into mesodermal lineage cell types [247]. This section will introduce the use and the genetic manipulation of Scara5 of hFOB 1.19, as a valid but not exhaustive model to study Scara5 involvement during osteogenesis and adipogenesis.

3.4.1 hFOB culture differs from the canonical osteoblast cell lines

hFOB has a temperature-sensitive mutant of SV40 large T antigen incorporated, together with the neomycin resistant expression vector pSV2-neo [234]. These features give hFOB the ability to grow at 34 °C in the presence of neomycin (G418), which positively selects for them. To determine the culture conditions necessary to achieve the optimal osteogenic differentiation, hFOB were both cultivated at 34 and 37 °C, 5% (v/v) CO_2 with hFOB media (hFOB complete maintenance medium – hCM, and hCM supplemented with osteogenic reagents – hOM) and standard media (CM and OM) for 3 days. Specifically, hFOB were grown at 34 °C and hOM/OM treated once 80% confluent; cells then remained at 34 °C or were moved in a 37 °C incubator. **Figure 3.9 A** shows that hFOB cultivated at 34 °C did not respond greatly to hOM (hOM/hCM fold change, mean 1.6) nor to OM (OM/CM fold change, 2.1), where pNP concentration was very low and equal to 0.260 mmol/L.

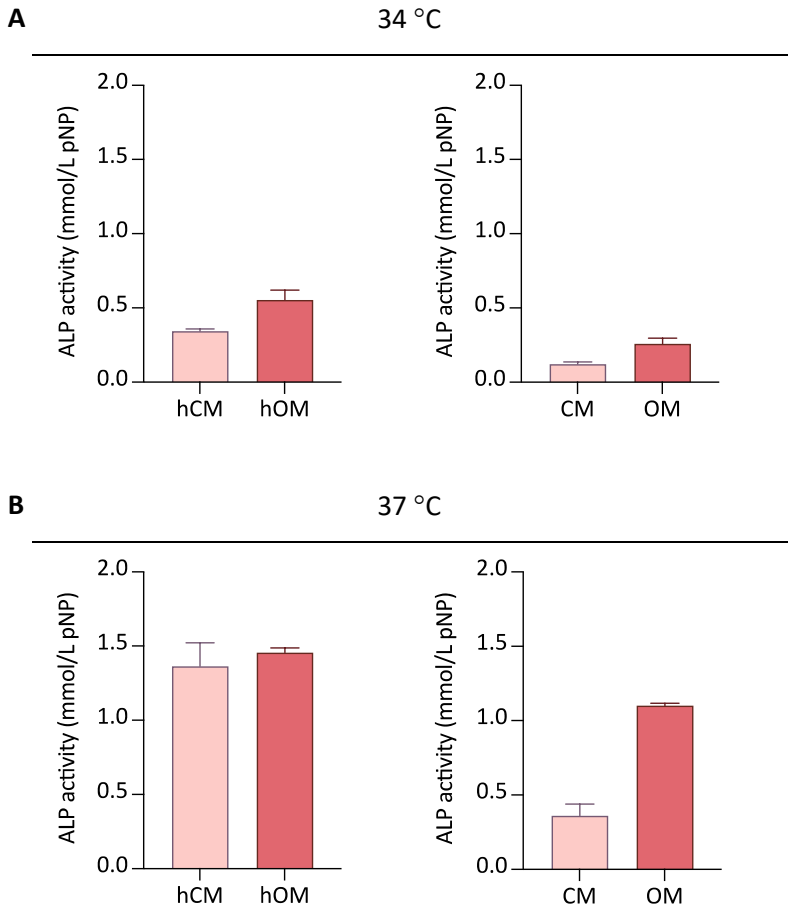


Figure 3.9 hFOB cultured at 37 °C and OM-treated display the highest ALP activity. ALP assay was performed on hFOB cultured at 34 °C both using hFOB media (hCM and hOM) and standard media (CM and OM) (**A**). At the same time, hFOB were also cultured at 37 °C with the same media conditions as above (**B**). The experiment was carried out once in triplicates, with bars represented as mean ± SD.

On the contrary, as depicted in **Figure 3.9 B**, pNP concentrations were high for hFOB treated with hFOB media at 37 °C (1.363 mmol/L for hCM, 1.456 mmol/L for hOM), but hOM treatment did not enhance ALP activity if compared to hCM. Finally, OM treatment at 37 °C increased the activity of ALP that produced 1.101 mmol/L of pNP, with an OM/CM fold change equal to 3.1. Hence, standard media and the 37 °C incubator were used to stimulate hFOB osteogenic differentiation.

3.4.2 hFOB can differentiate both towards osteoblasts and adipocytes

hFOB proved to be a useful cell line with multipotent capacity of differentiation [247]. It was therefore investigated whether the differentiation conditions above-discussed (**Section 3.4.1**) were effectively able to induce hFOB differentiation. hFOB were cultivated at 34 °C with hCM

until 80% confluent; OM was added to the cells that were moved at 37 °C for 3 days, at the end of which an ALP assay was performed (**Figure 3.10 A**). OM treatment significantly stimulated hFOB ALP activity, with a fold change OM/CM of 3.7 ± 0.1 (mean ± SEM).

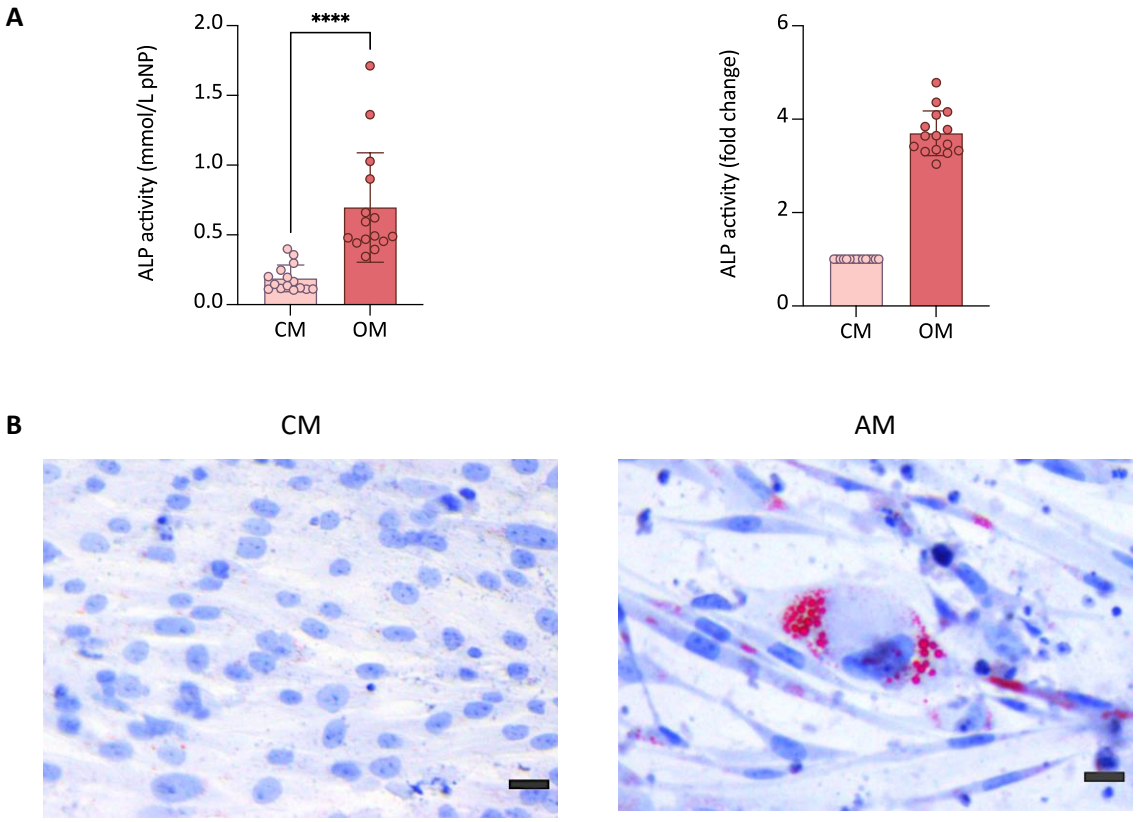


Figure 3.10 hFOB differentiate to osteoblasts and adipocytes under specific stimuli. hFOB treated with OM for 3 days produced a considerable amount of pNP, measured by ALP assay (**A**). Data are presented both in terms of pNP concentration (on the left) and fold change (on the right), as mean ± SEM (n=5, 3 technical replicates/n); unpaired two-tailed Student's t-test was used to determine the degree of significance (**** $p < 0.0001$). AM stimulated hFOB to differentiate towards adipocytes in 15 days, after which lipid droplets were stained by Oil Red O (Hematoxylin counterstaining, n=3) (**B**). Pictures acquired at a 20x magnification (50 μm scale bar).

Adipogenic potential was evaluated as well, by treating hFOB with AM for 15 days; hFOB were grown at 34 °C and were treated once 80% confluent, thereby moved at 37 °C. Oil Red O staining was carried out at the end of the treatment, showing small cytoplasmic lipid droplets within the newly differentiated cells (**Figure 3.10 B**).

3.4.3 Osteogenic and adipogenic marker expression increases in response to OM and AM

As previously shown, hFOB produced a considerable amount of pNP after 3 days of OM treatment, whilst AM promoted hFOB differentiation into adipocytes. Therefore, osteogenic and adipogenic marker expression was assessed after OM/AM treatment.

As depicted in **Figure 3.11 A**, Alpl gene expression exponentially increased from day 1 to day 6 of OM treatment, lowering again after 12 days of OM treatment. OCN expression increased after 1 day of treatment, but remained constant from day 3 until day 6, diminishing at day 12. Adipoq gene expression, on the other hand, decidedly increased from day 1 (fold change AM/CM, mean ± SEM, 2.5 ± 0.8) until day 6 (121.7 ± 30.7), and remained elevated even at day 12 of AM treatment (120.7 ± 63.9) (**Figure 3.11 B**).

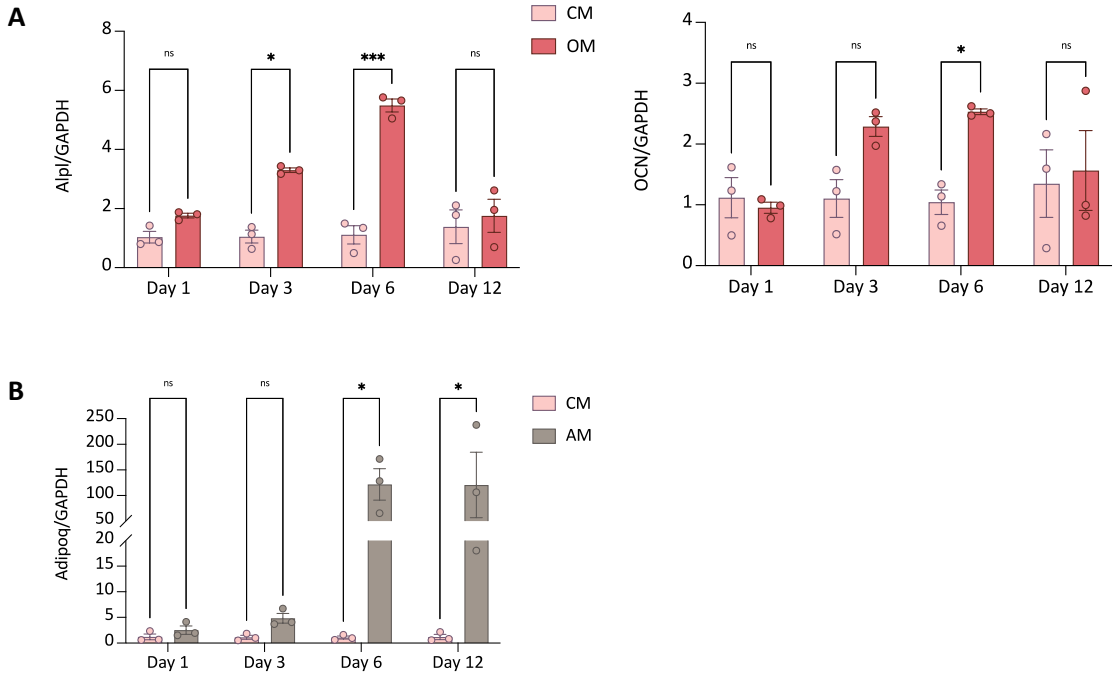


Figure 3.11 Osteogenic and adipogenic marker expression increases after OM or AM treatment. After OM treatment for different time points (1, 3, 6, 12 days), Alpl and OCN gene expression was assessed through RT-qPCR (**A**). Adipoq expression was tested in response to AM treatment at the same time points (**B**). Graphs represent 3 independent experiments, from 3 different biological samples (n=3). $2^{-\Delta\Delta CT}$ method was applied and gene expression was normalised to GAPDH; data are shown as mean ± SEM and in terms of fold change of CM. Two-way ANOVA with Šídák's post-hoc test was used to determine the degree of significance (^{ns} $p > 0.05$, * $p \leq 0.05$, *** $p < 0.001$).

3.4.4 Scara5 expression is sparked by AM, but not by OM, at different time points

To assess whether Scara5 expression was triggered by AM, but not by OM, as previously asserted for murine BMSCs (**Section 3.2.2** and **Section 3.3.1**), hFOB were treated with both differentiation cocktails for 1, 3, 6, and 12 days. As shown in **Figure 3.12 A**, Scara5 expression did not markedly increase upon OM treatment. On the other hand, **Figure 3.12 B** depicts Scara5 expression in response to AM treatment. After 1 day of culture in AM, there was an increased trend in Scara5 gene expression (fold change AM/CM, mean ± SEM, 4.7 ± 1.8) that remained stable for 3 days (4.9 ± 0.7). After 6 days of treatment, AM considerably induced Scara5 expression (78.5 ± 12.6) that continued to be elevated (but not significantly) at day 12 (26.8 ± 13.6).

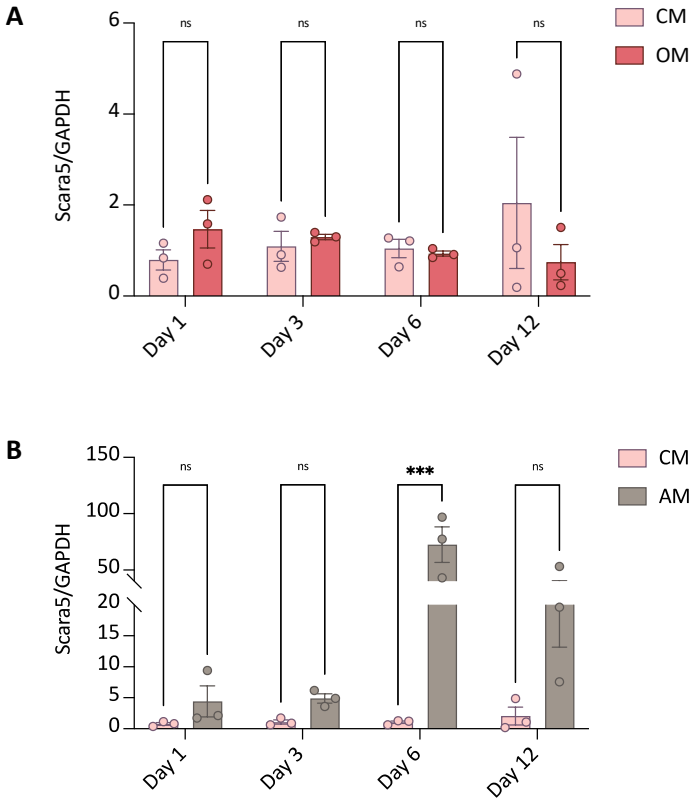


Figure 3.12 AM, but not OM, triggers Scara5 gene expression. hFOB were treated for different days (1, 3, 6, 12), with both OM (**A**) and AM (**B**), to determine Scara5 expression via RT-qPCR (n=3). $2^{-\Delta\Delta CT}$ method was applied and Scara5 expression was normalised to GAPDH; graphs are depicted as mean ± SEM and presented in terms of fold change. Two-way ANOVA with Šídák's post-hoc test was used to determine the degree of significance (^{ns} $p > 0.05$, *** $p < 0.001$).

3.4.5 pmaxGFP and Scara5 plasmids can be easily lipo-transfected within hFOB

3.4.5.1 Both Lipofectamine 2000® and Viafect™ can be exploited to perform hFOB lipofection

To transiently manipulate Scara5 expression within hFOB to study its effect on osteogenesis, hFOB transfection was optimised by using pmaxGFP. The transfections performed employed two liposome-based reagents (Lipofectamine 2000® and Viafect™) and were thereby defined as lipofections. Lipofections were carried out in the presence or absence of 10% (v/v) FBS for 4 days; as shown in **Figure 3.13**, both Lipofectamine 2000® and Viafect™ performed well, with almost overlapping results in the presence of serum. On the other hand, from 2 days post-transfection, lipofection was severely compromised by the absence of 10% (v/v) FBS using Lipofectamine 2000®, and to a lesser extent using Viafect™.

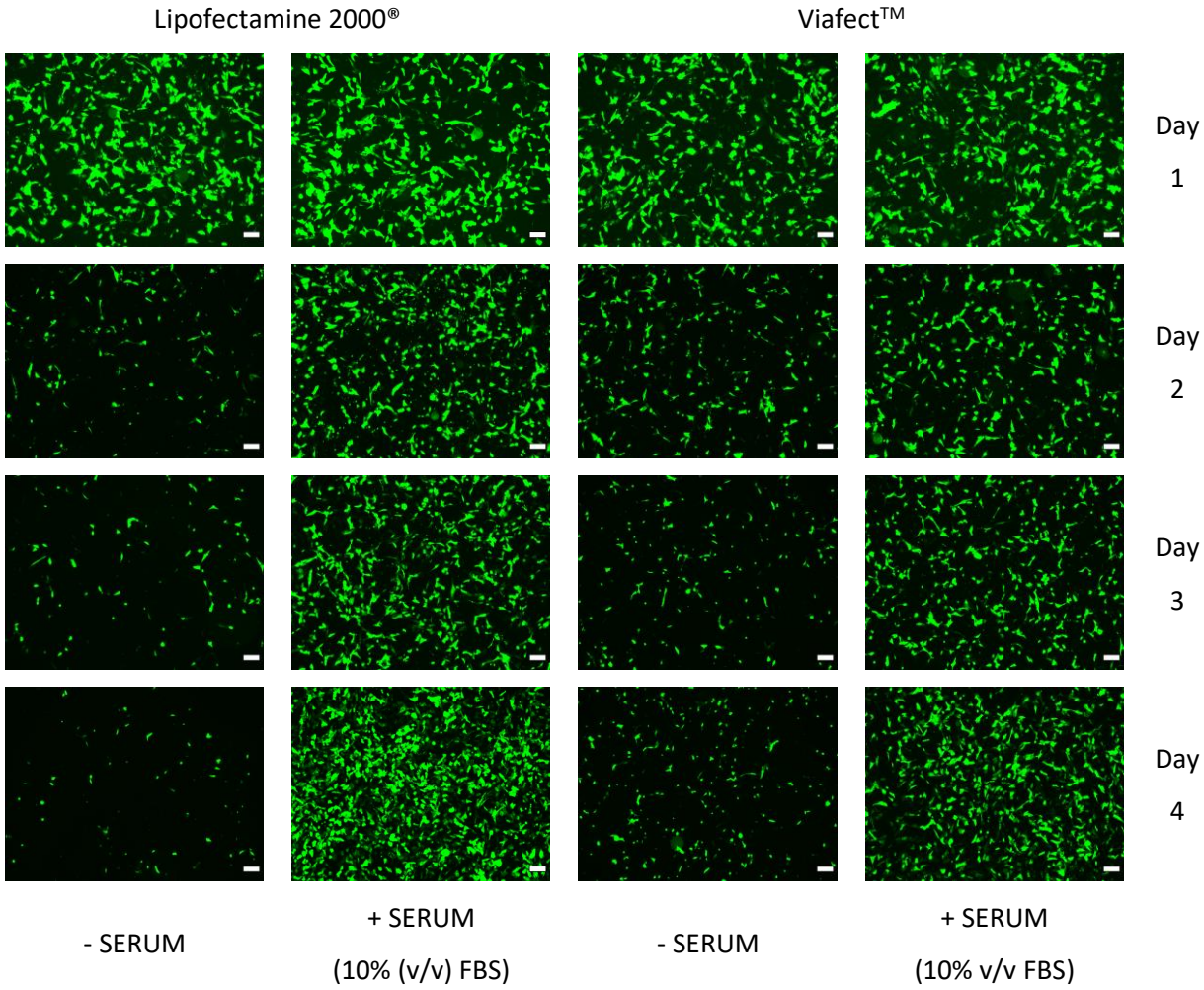


Figure 3.13 hFOB are GFP transfectable both using Lipofectamine 2000® and Viafect™. 750 ng/ml of pmaxGFP were transfected within hFOB by means of Lipofectamine 2000® (2.5 μl/ml) and Viafect™

(1:4), with or without serum. Pictures were captured every day for four days at a 4x field magnification (100 μm scale bar).

Both Lipofectamine 2000® and Viafect™ can be therefore used in transfecting hFOB, as long as 10% (v/v) FBS is added 5 hours post-transfection. Lipofectamine 2000® was selected to perform the subsequent experiments.

3.4.5.2 Scara5 plasmid transfection does not have detrimental effect on hFOB proliferation

To determine whether Scara5 overexpression has an effect on cell differentiation, hFOB were transfected with Scara5 plasmid by using Lipofectamine 2000®. The lipofection was carried out and the pmaxGFP positive cells were visualised after 1 and 4 days (**Figure 3.14 A**). Scara5-transfected hFOB did not fluoresce as brightly as pmaxGFP-transfected ones since GFP contained in Scara5 plasmid is different from pmaxGFP. However, the transfection still showed a good signal at both experimental time points.

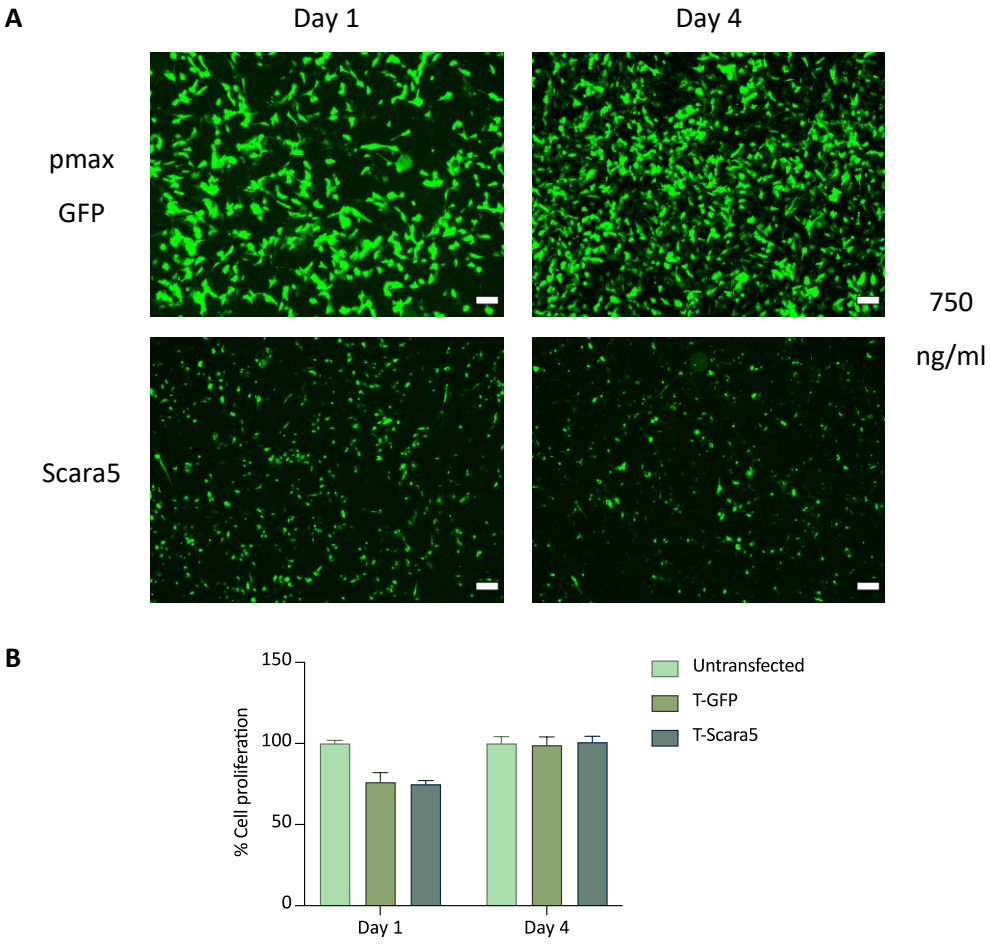


Figure 3.14 Scara5 plasmid is transfectable via Lipofectamine 2000®. Cells were transfected for 1 and

4 days with 750 ng/ml of pmaxGFP (control) or Scara5 plasmid within a 96-well plate (**A**). 4x field magnification (100 μm scale bar). MTT assay was performed at day 1 and 4 from transfection to assess lipofection effect on cell proliferation using 1 ng/ml of plasmids, according to the manufacturer instructions (**B**). Data result from a single experiment performed in triplicates and are presented as mean ± SD.

hFOB were transfected with pmaxGFP plasmid (T-GFP), as well as with Scara5 plasmid (T-Scara5), to determine the effect of the transfection on cell proliferation. As depicted in **Figure 3.14 B**, the 3-(4,5-dimethylthiazol-2-yl)-2,5-diphenyl-2H-tetrazolium bromide (MTT) assay showed a slight decrease in terms of cell proliferation, for both plasmids' transfection, after 1 day. However, 4 days post-transfection, T-GFP and T-Scara5 hFOB proliferated at the same rate of the untransfected cells.

3.4.6 Scara5 overexpression, but not silencing, is achievable in hFOB cell line

As hFOB cells easily transfected with Scara5 plasmid, the magnitude of overexpression was investigated. RT-qPCR was performed on T-GFP and T-Scara5 hFOB both 1- and 4-days post-transfection. As shown in **Figure 3.15 A**, 1-day post-transfection Scara5 expression was equal to 23.7 ± 15.3 (mean ± SEM, fold change T-GFP/Untransfected cells) for T-GFP and to 428,831.3 ± 858146.6 for T-Scara5 (fold change T-Scara5/Untransfected cells); thus, Scara5 expression was significantly higher in Scara5-transfected cells. 4-days post transfection, despite a decrease in its expression, T-Scara5 hFOB continued to express high levels of Scara5 (fold change T-Scara5/Untransfected cells, 44,062.2 ± 9753.5).

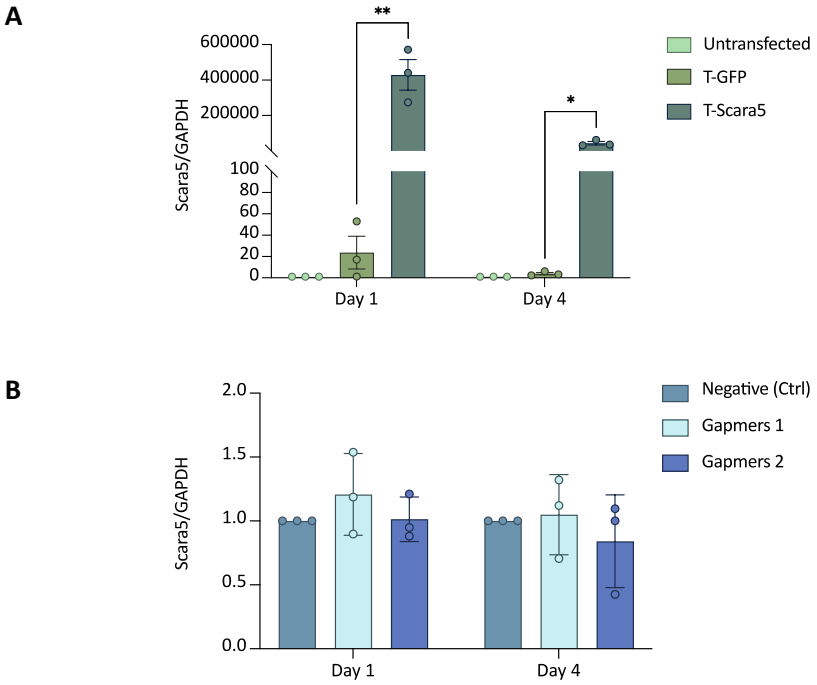


Figure 3.15 Scara5 is overexpressed, but not knocked down, in hFOB cell line. hFOB cell line was lipofected with Scara5 and its expression was assessed by RT-qPCR 1- and 4-days post-transfection (n=3) (**A**). Scara5 silencing was performed by employing 2 different sequences of Scara5 GapmeRs and gene silencing was evaluated through RT-qPCR 1- and 4-days post-transfection. 50nM of GapmerRs were used to transfect the cells for these experiments (n=3) (**B**). $2^{-\Delta\Delta CT}$ method was applied and Scara5 expression was normalised to GAPDH; graphs are depicted as mean ± SEM, with untransfected cells used as control for pmaxGFP-transfected (T-GFP) and Scara5-transfected cells (T-Scara5). Two unpaired two-tailed Student's t-tests were used to determine the degree of significance, one for each time point (* $p \leq 0.05$, ** $p < 0.01$).

Antisense GapmeRs are specifically created to bind with a specific segment of RNA, silencing the gene by triggering the cleavage of RNA by RNase H [248]. Scara5 GapmeRs were employed to genetically manipulate hFOB Scara5 expression; in particular, GapmeRs were designed to knockdown Scara5. However, as depicted in **Figure 3.15 B**, Scara5 expression was constant either by transfecting hFOB with Negative control (Ctrl), GapmeRs 1, or GapmeRs 2.

It was consequently concluded that the GapmeRs used were not capable of inducing any change in terms of Scara5 expression within hFOB, oppositely to Scara5 plasmid.

3.4.7 Scara5 plasmid over-expression influences ALP activity of OM-treated hFOB

Section 3.4.6 highlighted the possibility to increase Scara5 expression in hFOB by using Scara5 plasmid. Hence, it was worthwhile to look at ALP activity once T-Scara5 hFOB were treated with OM for 3 days. **Figure 3.16 A** shows that ALP activity of T-Scara5 OM-treated was statistically lower than the T-GFP's one (fold change OM/AM, mean ± SEM, 3.4 ± 0.2 vs 4.1 ± 0.2). These results are consistent with Scara5 "negative" effect on osteogenesis, as shown in **Section 3.2**, where Scara5-null murine BMSCs displayed a higher osteogenic potential.

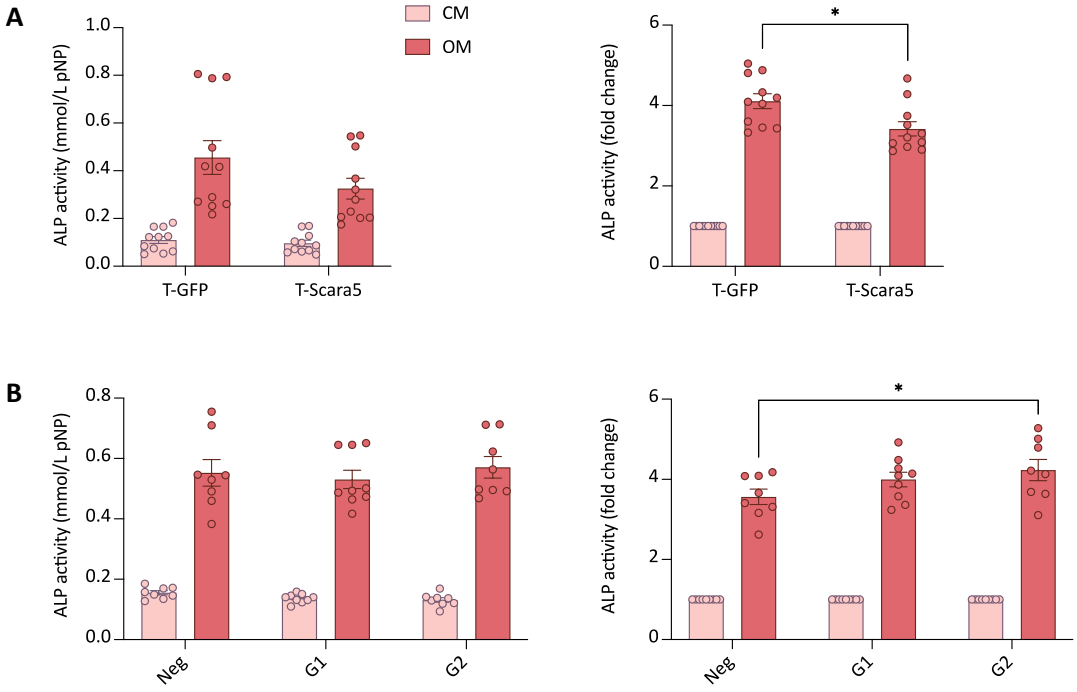


Figure 3.16 Both Scara5 overexpression and the use of GapmeRs influence ALP activity. ALP assay was performed to assess ALP activity in Scara5 transfected hFOB, after 3 days of OM treatment (n=4, ≥2 technical replicates/n). Data are presented both in terms of pNP concentration (on the left) and fold change (on the right), as mean ± SEM; Mann-Whitney U test was used for comparisons (* $p \leq 0.05$) (**A**). After GapmeRs were transfected, hFOB were treated for 3 days with OM and ALP assay was performed (n=3, ≥2 technical replicates/n). Data are presented both in terms of pNP concentration (on the left) and fold change (on the right), as mean ± SEM; one-way ANOVA test with Tukey's post hoc analysis was used to determine the degree of significance (* $p \leq 0.05$) (**B**).

50 nM GapmeRs (1 and 2) did not produce Scara5 knockdown in transfected hFOB. Nevertheless, GapmeRs-transfected hFOB underwent an ALP assay to test whether ALP activity changed in response to OM treatment. Surprisingly, OM treated hFOB responded

differently depending on the GapmeRs transfected (**Figure 3.16 B**). OM/CM fold change increase from 3.5 ± 0.2 (mean ± SEM) in Negative (Ctrl)-transfected cells to 4.4 ± 0.2 in GapmeRs 2-transfected hFOB. These data indicate that GapmeRs 2-transfection increased somehow ALP activity, although their use did not induce any change in Scara5 expression (**Figure 3.15 B**).

3.5 Discussion

MSCs can be defined, according to the *International Society for Cellular Therapy*, as cells able to adhere to the plastic surface, to express specific cell-surface antigens, and to exhibit a multipotent differentiation potential [128]. In line with the latter criterium, MSCs hold trilineage mesenchymal differentiation capacity, being therefore able to become osteoblasts, adipocytes, and chondroblasts [128]. It was then determined, throughout the years, that MSCs are capable of differentiating into other cell types, i.e. cardiac and smooth muscle cells, endothelial cells, hepatic cells, neural cells, and endocrine pancreatic cells [249, 250]. Amongst all cell types MSCs identified, MSCs differentiation into osteoblasts and adipocytes represent the most widely studied; in fact, the tug of war between these cells have been proved crucial both physiologically (related to the ageing process) and pathologically. During osteoporosis, for example, a shift of MSCs differentiation to adipocytes was pointed out as part of the cause of the reduced bone mineral density in both human and mice [251]. Also, MSCs extracted from aged mice showed a decreased ability to commit to the osteogenic lineage, thus preferring the adipogenic one [252].

Since their discovery, MSCs have been widely described and a plethora of factors involved in their differentiation have been identified. MSCs were initially isolated from the bone marrow, but over the years other sources have been identified as promising for cell harvesting. Indeed, adult tissues such as adipose tissue, tendons, peripheral blood and foetal ones can be processed to isolate MSCs [127]. The current chapter pointed out Scara5 as a new regulator of the MSCs differentiation towards adipocytes and osteoblasts. Scara5 has already been associated with adipogenesis *in vitro*. Lee *at al* indeed demonstrated that Scara5 is expressed by both white adipose tissue and adipose-derived stromal vascular fraction, being at the opposite lowly expressed by uncommitted mouse C3H10T1/2 cells (MSCs-like cell line) [165]. Nonetheless, the work above described focussed on adipogenesis, with a brief mention

to osteogenesis; when Scara5 was overexpressed in C3H10T1/2 cells, Alpl and OCN expression decreased in response to OM. It was therefore concluded that Scara5 definitely plays a role during adipogenesis and might be consequently involved in osteogenesis [165].

This work exploits murine BMSCs to investigate Scara5 role in the commitment and differentiation of these cells. As will be elucidated in the next chapter, a constitutive KO was produced in C57BL/6J mice through homologous recombination. Cells extracted from Scara5-KO mice long bones were used as Scara5-KO BMSCs, while BMSCs derived from WT C57BL/6J mice were used simultaneously to make all comparisons. BMSCs were extracted by flushing the bone marrow out from the bones and cells were used for experiments at passage 1; this method proved to be the most reliable, repeatable, time-efficient, and to produce an adequate number of cells able to respond to OM treatment successfully (**Figure 3.2 A**, P1). Furthermore, the fact that BMSCs consist of a mixed population of cells (mesenchymal stem and progenitor cells, a proportion of monocytes/macrophages, myeloid and endothelial cells [252]) is the reason why a higher ALP activity can be observed in P1 BMSCs OM treated. As stated in the literature, in fact, monocytes/macrophages are considered potent inducers of human MSCs osteogenic differentiation through oncostatin M production and STAT3 signalling activation [253, 254].

Under osteogenic stimuli, MSCs develop into osteo-precursors first and further proliferate and mature into bone forming osteoblasts [255]. Although MSCs can differentiate into osteoblasts when extracted from all identified sources, BMSCs still hold epigenetic memory for osteo-lineage, therefore possessing a superior differentiation ability [256]. Scara5 gene expression did not change/decreased in response to OM treatment, suggesting that it is not required during osteogenic differentiation of BMSCs (**Figure 3.3**). Also, Scara5 is barely expressed when BMSCs are maintained in CM. This fact supports Lee and colleagues' findings in relation to the uncommitted C3H10T1/2 cell line [165]. Although Scara5 expression was not triggered in OM-treated BMSCs, once Scara5-null BMSCs were cultivated in OM for 28 days, their ability to differentiate to osteoblasts visibly increased, thereby pointing to Scara5 as a negative regulator of osteogenesis. Scara5-KO BMSCs also produced higher levels of pNP, meaning that the absence of Scara5 increases the cells' osteogenic potential (**Figure 3.4**). Thus, Scara5 reduces BMSCs propensity to become osteoblasts.

ALP is the most studied biochemical marker for osteoblast activity. It has been shown that the osteogenic cocktail (β-glycerophosphate, ascorbic acid, and dexamethasone) makes BMSCs gradually produce ALP, which increases in parallel with the incubation time (3 to 21 days) [257]. In the present work, ALP activity was determined after 3 days of treatment as pNP concentrations were significantly higher in OM treated cells (fold changes to controls equal or above 3). Together with ALP enzymatic activity, gene expression can be examined to determine MSCs osteogenic differentiation potential. In this chapter both Alpl and OCN gene expression was investigated (**Figure 3.5**). Whilst the first gene was increasingly expressed from mature osteoprogenitors to differentiated osteoblasts, OCN was only expressed by differentiated osteoblasts [258]. Despite the results above described, Alpl and OCN expression was not significantly different between Scara5-WT and -KO BMSCs, although WT BMSCs expressed higher levels of both genes. Surprisingly, Alpl gene expression marginally decreased after 7 days of OM culture, contrary to the reported literature. On the other hand, OCN expression remained constant over all three time points instead of increasing at the latter (21 days). It can be assumed that the heterogeneous cell types that represent BMSCs express Alpl and OCN at different levels, making RT-qPCR data unclear or difficult to interpret.

Throughout the years, more evidence has accumulated towards the competition between osteoblasts and adipocytes upon MSCs commitment and differentiation [122]. Adipogenesis can therefore be defined as the osteogenesis counterpart. Being Scara5 already been found expressed in fat and pre-adipocyte cell line [165], this work also aimed to test Scara5 expression in mouse BMSCs AM-treated (**Figure 3.6**). BMSCs cultivated in AM highly expressed Scara5 after 7 and 21 days, although 14 days of treatment did not increase Scara5 expression. Thereupon, Scara5 demonstrated to play a part during adipogenic differentiation, being its expression triggered by adipogenic stimuli. The adipogenesis process foresees MSCs commitment to preadipocytes (0-7 days), the mitotic clonal expansion (7-14 days), and the terminal differentiation (14-21/25 days) [259]. Considering the time point used experimentally in this chapter, it can be concluded that BMSCs treated with AM express Scara5 during their commitment step and the terminal differentiation, while is not triggered during the cell clonal expansion (**Figure 3.6 C**). These results fit with the literature, whereby Scara5 is expressed in both murine white fat (mostly consisting of mature adipocytes) and preadipocytes [165].

In absence of Scara5, BMSCs treated with AM were no longer able to differentiate into adipocytes, as confirmed by both ORO staining and adipogenic markers expression (**Figure 3.7, Figure 3.8**). Adiponectin has been identified as a marker to determine *in vitro* differentiation of human MSCs; in particular, adiponectin was secreted proportionally to MSCs adipogenic differentiation [260]. Also, both Adipoq and LEP genes expression have been found increased by adipogenic stimuli in human preadipocytes, representing the most described and debated adipokines [96]. Consistently with the literature, both Adipoq and LEP were significantly less expressed by Scara5-KO BMSCs, corroborating the fundamental role of Scara5 in adipogenesis. RT-qPCR results for AM-treated BMSCs referred to the response of stomal cells; the medium used, indeed, caused the detachment and death of the majority of cells different from the MSCs, which were the only cells able to respond to AM and differentiate.

Primary BMSCs proved to be difficult to collect from mice and to cultivate, principally due to BMSCs heterogeneity, low numbers harvestable, and time required to grow them. Consequently, hFOB 1.19 cell line was employed to explore both osteogenic and adipogenic differentiation in relation to Scara5. This conditionally immortalised cell line was pointed out as an *in vitro* model of human mesenchymal progenitors by Yen and colleagues [234, 247]; it contains both a temperature-sensitive SV40 large T antigen and the neomycin resistance. At the temperature of 33.5/34 °C the SV40 large T antigen is active and the hFOB able proliferate, whereas they spontaneously differentiate into mature osteoblasts at 39/39.5 °C, at which the antigen is inactive. In this work, the hFOB easily grew both at 34 and 37 °C, but the osteogenic differentiation was optimal at 37 °C using the standard osteogenic cocktail (OM) (**Figure 3.9, Figure 3.10 A**). Since OM does not contain neomycin hFOB are no longer antibiotically selected, being therefore able to differentiate. Furthermore, Alpl and OCN expression increased in response to OM, confirming a differentiating status (**Figure 3.11 A**). Under the same temperature conditions, hFOB were also treated with AM, proving able to differentiate into adipocytes and to express significantly high levels of adiponectin (**Figure 3.10 B, Figure 3.11 B**). All data obtained were consistent with the literature, although the differentiation temperature used was 37 °C instead of 39 °C. Nonetheless, 37 °C showed to successfully induce both osteogenic and adipogenic differentiation.

Scara5 expression in hFOB was very similar to that described for BMSCs: it was indeed low in uncommitted hFOB and OM-treated cells and triggered by AM treatment (**Figure 3.12**), demonstrating that Scara5 is crucial during adipogenesis regardless of the cell model used or the species. It was hence investigated whether Scara5 and pmaxGFP plasmids transfection impaired hFOB ALP activity. Transfection through Lipofectamine 2000® proved successful, although fluorescent signal was lower in hFOB Scara5-transfected compared to hFOB pmaxGFP-transfected (**Figure 3.14**). The reason lies in the plasmids used for transfection: pmaxGFP originates from the Copepod *Pontellina sp*., whereas EGFP is an engineered form of GFP. As pmaxGFP manufacturer Amaxa™ (Lonza, Slough, UK) states, pmaxGFP transfected cells fluoresce more than EGFP transfected ones [261]. Both pmaxGFP and Scara5 -transfected cells treated with OM underwent ALP assay (**Figure 3.15 A**); Scara5 transfection diminished the ALP activity of hFOB, thus proving that even in a human model of MSCs-like cell Scara5 has a negative impact on osteogenesis (**Figure 3.16 A**). Although GapmeRs were used to silence Scara5, RT-qPCR showed that the knockdown was not successful. However, ALP activity was increased in those cells that receive the GapmeRs 2 (**Figure 3.15 B, Figure 3.16 B**). It can be hypothesised that the transfection of GapmeRs itself had an effect on ALP activity, as the pNP concentrations did not increase for OM treated cells but decreased for CM cells, thereby increasing the OM/CM fold change.

Be that as it may, despite hFOB cells being revealed as a valid model to study Scara5 overexpression-related differentiation, the time points required to achieve a complete osteogenic and adipogenic differentiation are too long to be sustained by a transient overexpression. Thus, murine BMSCs were used to investigate the molecular mechanism behind Scara5 activity for the remainder of the thesis (see **Chapter 5**).

In conclusion, this chapter outlined the role of Scara5 during BMSCs differentiation towards osteoblasts and adipocytes; when properly stimulated, Scara5-deficiency cells proved to be more prone to differentiate to osteoblasts at the expenses of adipocytes. Scara5 can be therefore considered as a crucial factor in determining BMSCs' fate (**Figure 3.17**). Following the examination of the role of Scara5 in osteoblasts and adipocytes *in vitro*, the next chapter will discuss the phenotypic effect of Scara5 absence *in vivo* in relation to bone/fat-related diseases, i.e. osteoporosis and diabetes.

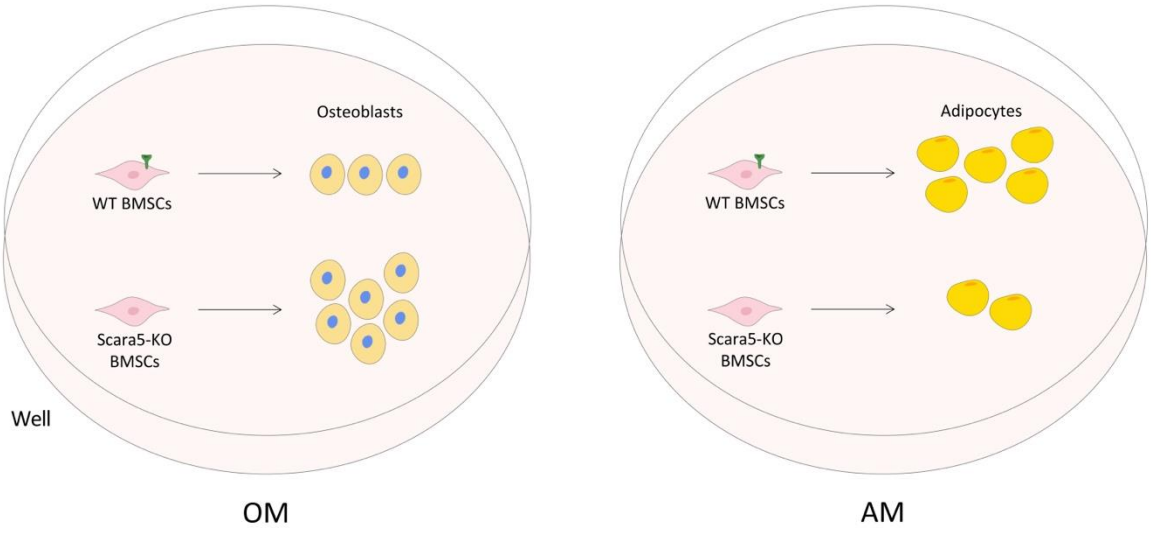


Figure 3.17 Scara5 is a key factor in BMSCs fate. It was hypothesised that Scara5 plays a role in BMSCs differentiation; it was therefore assessed that osteogenic stimuli induced BMSCs differentiation to osteoblasts more in the Scara5 null cells than in the WT ones. Oppositely, the absence of Scara5 severely impaired adipogenic differentiation of BMSCs AM-treated.

Chapter 4: Scara5 controls bone and fat deposition *in vivo*

4.1 Introduction

Experiments from the previous chapter showed Scara5's involvement in both osteogenesis and adipogenesis of murine BMSCs and MSCs-like hFOB 1.19. It remains unknown whether the differentiation ability of MSCs observed *in vitro* reflects *in vivo* differential bone and adipose tissue deposition between WT and Scara5 deficient mice.

Scara5 has been associated to adipogenesis *in vitro* [165], but no Scara5 deficient murine models have been generated to deepen understanding of this aspect. The only Scara5-deficient mice produced so far have been employed by Ojala *et al.* to study Scara5's role in autoimmune diseases that affect the interstitial connective tissue [178]. Since Scara5 was found highly expressed by fibroblasts, Scara5 null fibroblasts presented a reduced endocytic potential; their malfunction was pointed out as an underlying cause of some autoimmune diseases characterised by organs' lymphocytic infiltrations. This study described Scara5-KO mice as phenotypically normal mice, with no significant differences in terms of body and organs' weight except for the testis, where a defect in mouse fertility was observed [178].

Under physiological conditions, MSCs differentiate towards osteoblasts and adipocytes in response to defined stimuli. The onset of bone loss-related pathologies, such as osteoporosis and diabetes, is linked with MSCs reduced ability to become osteoblasts, favouring adipogenic differentiation. Consequently, the bone remodelling process (bone resorption/bone formation) is unbalanced, leading to more bone resorbed and less bone formed [262, 263]. At the same time, age-related osteoporosis has been linked to increased bone marrow adiposity [251, 263].

In this chapter, the phenotypic characterisation of C57BL/6J Scara5-KO mice will be outlined, thus determining how bone mass and fat deposition are affected by Scara5 deficiency *in vivo*. Furthermore, calvarial assay will be used to assess whether bone formation is altered in Scara5-null mice; ovariectomy-induced osteoporosis and Streptozotocin-induced diabetes will provide an insight on Scara5 involvement in bone/metabolic diseases.

4.2 Scara5 deficiency increases bone mass and decreases fat deposition *in vivo*

As presented in the previous chapter, Scara5 deficiency impaired BMSCs ability to differentiate towards adipocytes but not to osteoblasts *in vitro*. It was therefore investigated whether Scara5-KO mice presented with more bone and less fat than WT mice; micro-computed tomography (μCT) was used to determine bone structure, and mice total body and inguinal fat (iFAT) weights were evaluated to assess *in vivo* fat deposition.

4.2.1 C57BL/6J mice backcrossing to generate Scara5-WT and -KO colonies

Scara5 was knocked out by replacing a 228 base pairs (bp) region with a Scara5 targeting vector, as depicted in **Figure 4.1 A**. By removing Exons 7-9, the extracellular collagenous domain could no longer be codified and Scara5 thus lost its ligand-binding ability. Scara5-KO 129/Sv (agouti) embryonic cells were selected and electroporated into C57BL/6J blastocysts. The deriving male chimeras were mated with C57BL/6J females as the first step of the backcrossing process. Coat colour markers were used to determine whether the Scara5-KO embryonic cells contributed to the germ layer of the pups. In black coloured mice, the germ layer derived from the C57BL/6J cells, while in agouti mice the germ layer derived from the embryonic cells. Agouti mice were therefore heterozygous (HET) for the mutation. Scara5-HET mice were mated with C57BL/6J WT mice for 9 generations. Ear clips genotyping was performed throughout and allowed to select for HET mice. 9^{th} generation HET mice were finally bred to generate WT, HET, and Scara5-KO mice (**Figure 4.1 B**). WT and Scara5-KO mice were subsequently used to set up homozygous WT and Scara5-KO colonies.

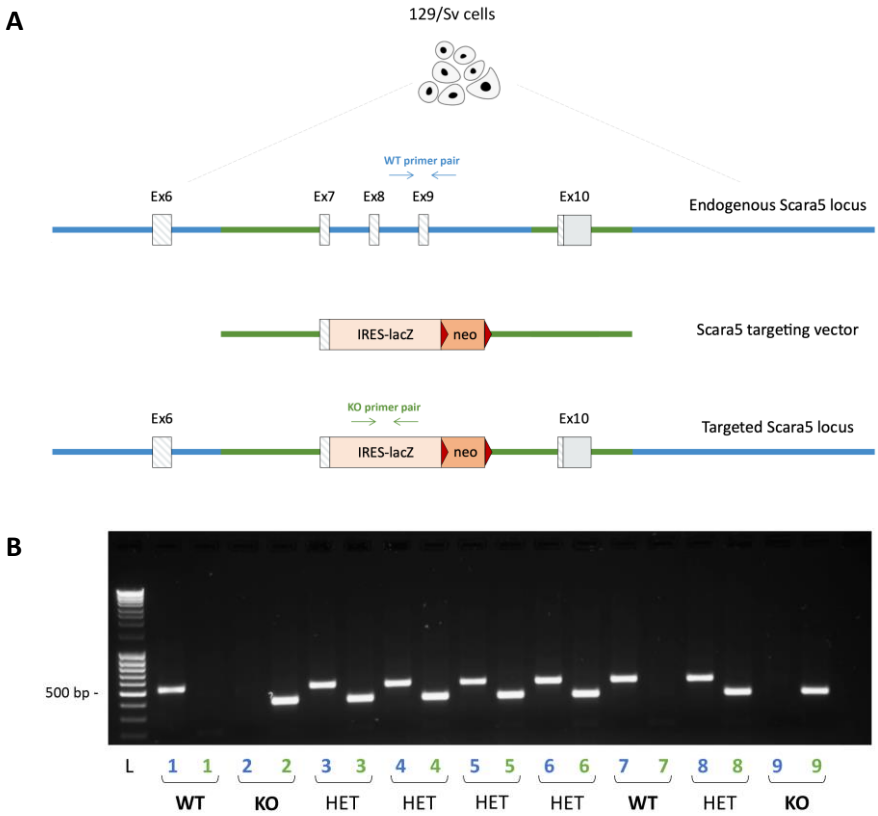


Figure 4.1 Mice backcrossing and genotyping allows to generate Scara5-WT and -KO offspring. Scara5 knockout was generated by homologous recombination, replacing Exons 7-9 with the reporter cassette IRES-lacZ and the neomycin gene for positive selection comprised between two loxP sites (red triangles). Scara5 targeting vector (≈ 11 kilobase) was subsequently electroporated into 129/Sv embryonic cells and neomycin-resistant cells were selected and injected in a C57BL/6J blastocyst (**A**). 9th generation heterozygous (HET) mice were bred to generate WT and Scara5-KO homozygous mice, which were genotyped 2 to 3 weeks after birth; WT primers (blue) amplified a region of 534 bp between exons 7-9, whereas KO primers (green) amplified a region of 400 bp within Scara5 targeting vector in a 2% (w/v) agarose gel. Product's amplification size determined by employing an 80-10,000 bp ladder (L) (**B**).

4.2.2 µCT analysis displays increased bone mass in female but not in male mice

11 weeks old WT and Scara5-KO mice tibiae were scanned for trabecular bone using µCT. As shown by reconstructed 3D images, the difference between WT and Scara5 deficient mice is appreciable for females' tibiae only (**Figure 4.2 A**). As confirmed by bone parameters analysis (**Figure 4.2 B**), females WT and KO tibiae significantly differed in terms of percentage of bone volume/total volume (% BV/TV). % BV/TV accounted for 9.040 ± 1.065% (mean ± SD) for WT females, while was equal to 10.686 ± 1.577% for Scara5-KO females. Trabecular thickness

(Tb/Th) was 0.043 ± 0.003 mm (mean ± SD) in WT tibiae and 0.045 ± 0.002 in Scara5-KO ones; however, the difference revealed not statistically significant (p = 0.0531). Trabecular separation and number (Tb/Sp, Tb/N) were not different between Scara5-WT and -KO murine tibiae. By contrast, no significant difference between WT and Scara5-null mice was found for any of the bone parameters in males.

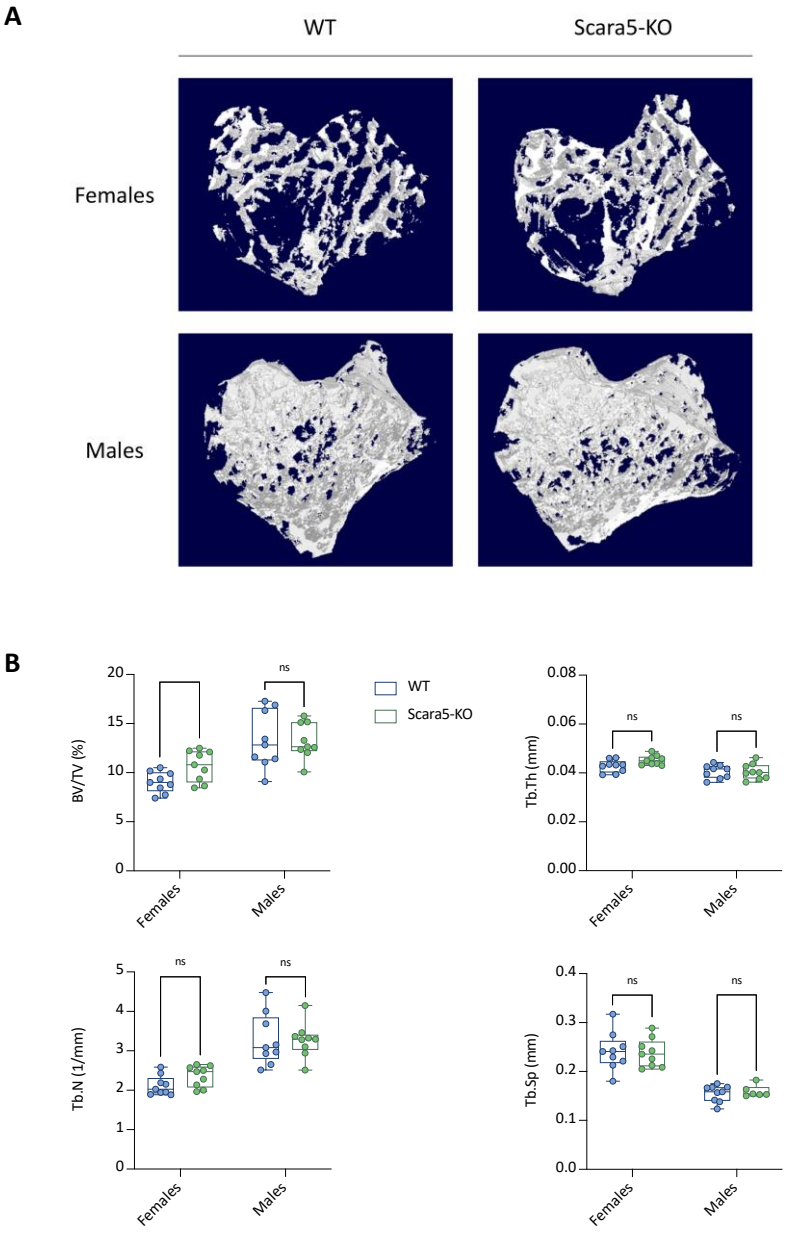


Figure 4.2 Scara5 deficient females, but not males, show increased tibiae bone mass. Representative μCT images of 11 weeks old WT and Scara5-KO mice tibiae (cross section view of trabecular bone) (**A**). Quantification of bone parameters, i.e. bone volume/total volume (BV/TV), trabecular thickness (Tb.Th), trabecular number (Tb.N), and trabecular separation (Tb.Sp) of WT and Scara5 deficient mice

(females n=9, males n=9) (**B**). Data are depicted as box plots and Mann-Whitney U test was used to determine the degree of significance (^{ns} $p > 0.05$, * $p \leq 0.05$).

Secondary bone parameters, i.e. bone surface/bone volume (BS/BV) and bone surface/total volume (BS/TV), are reported in **Table 4.1**. However, no statistically significant differences were observed between WT and Scara5-deficient tibiae, neither for females nor for males.

Table 4.1 Bone parameters of WT and Scara5-KO 11-weeks old mice. Additional bone parameters, i.e. bone surface/bone volume (BS/BV) and bone surface/total volume (BS/TV) of WT and Scara5-KO mice. Data are presented as mean ± SD (females n=10, males n=9).

Bone parameters	Females		Males	
	WT	Scara5-KO	WT	Scara5-KO
BS/BV (mm^{-1})	113.971 ± 5.507	108.625 ± 6.909	118.633 ± 9.793	119.111 ± 9.832
BS/TV (mm^{-1})	10.078 ± 1.097	11.181 ± 1.257	15.640 ± 2.824	15.681 ± 1.983

4.2.3 Inguinal fat measurements show a difference between WT and Scara5-KO mice

11 weeks old mice were sacrificed and their total body weight was measured. Subcutaneous inguinal fat pads were removed and weighed in order to determine any difference in terms of fat deposition. As shown in **Figure 4.3**, mice total body weight statistically differed between WT and Scara5-KO males (mean ± SD, 29.938 ± 1.693 g vs 27.470 ± 1.444 g), but not females (top left graph). However, iFAT weight was different between WT and Scara5-KO mice in both males and females (top right graph). iFAT weight was significantly higher in WT mice (mean ± SD, females 0.249 ± 0.050 g, males 0.264 ± 0.053 g) than in Scara5-KO ones (females 0.203 ± 0.031 g, males 0.184 ± 0.039 g). Furthermore, iFAT weight was expressed as a percentage of total body weight for each mouse. As depicted in the bottom left graph of **Figure 4.3**, WT female and male mice showed higher iFAT deposition than Scara5-KO mice. In particular, iFAT accounted for 1.144 ± 0.204% (mean ± SD) of total body weight of WT females and 0.940 ± 0.139% for Scara5-null females. A similar finding was observed in the male mice; the percentage of iFAT weight/total body weight was equal to 0.866 ± 0.152% (mean ± SD) for WT males and 0.669 ± 0.136% for Scara5-KO males.

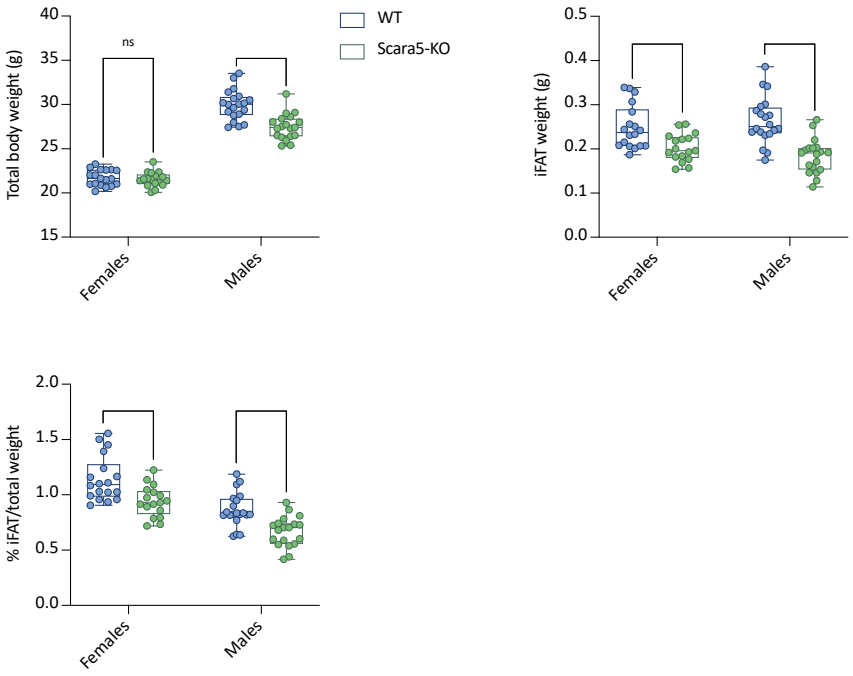


Figure 4.3 Inguinal fat pad weight is higher in WT than in Scara5-KO mice. 11 weeks old mice were weighted (top left) and their inguinal fat (iFAT) pads were collected; iFAT weight (top right) was subsequently related to the mice total body weight (bottom left) (females WT n=18, Scara5-KO n=17; males WT n=20, Scara5-KO n=19). Data are depicted as box plots and Mann-Whitney U test was used to determine the degree of significance (^{ns} $p > 0.05$, ** $p < 0.01$, **** $p < 0.0001$).

iFAT pads were also processed for histology to assess whether Scara5 deficiency impacted on adipocyte size and/or numbers. iFAT pads were embedded in paraffin and 4 μm sections were stained with Hematoxylin and Eosin (H&E) solution. The various histology processes used strip the sections of their lipid content therefore adipocytes were determined by their 'adipocyte ghost'. As depicted in **Figure 4.4 A**, adipocyte ghosts showed similar characteristics between WT and Scara5-KO mice fat pads. However, it is noticeable that females' adipocyte ghosts were bigger than males' ghosts. These aspects were confirmed by adipocytic parameters (i.e. WT adipocyte diameter, adipocyte number) analysis (**Figure 4.4 B**). Indeed, despite a non-significant difference between WT and Scara5-KO, WT females' adipocyte ghosts were bigger than WT males' ones (mean ± SD, 109.027 ± 31.793 μm vs 82.851 ± 9.790 μm). Consistently, due to the big size of females' adipocyte ghosts, the total number of adipocytes was lower in females' fat pads than in males' fat pads (mean ± SD, 270.810 ± 42.399 μm vs 351.476 ± 36.707 μm). Scara5-KO iFAT histology showed analogous results:

adipocyte ghosts' diameter was bigger in females' fat pads, while ghosts' number was higher in males' fat pads.

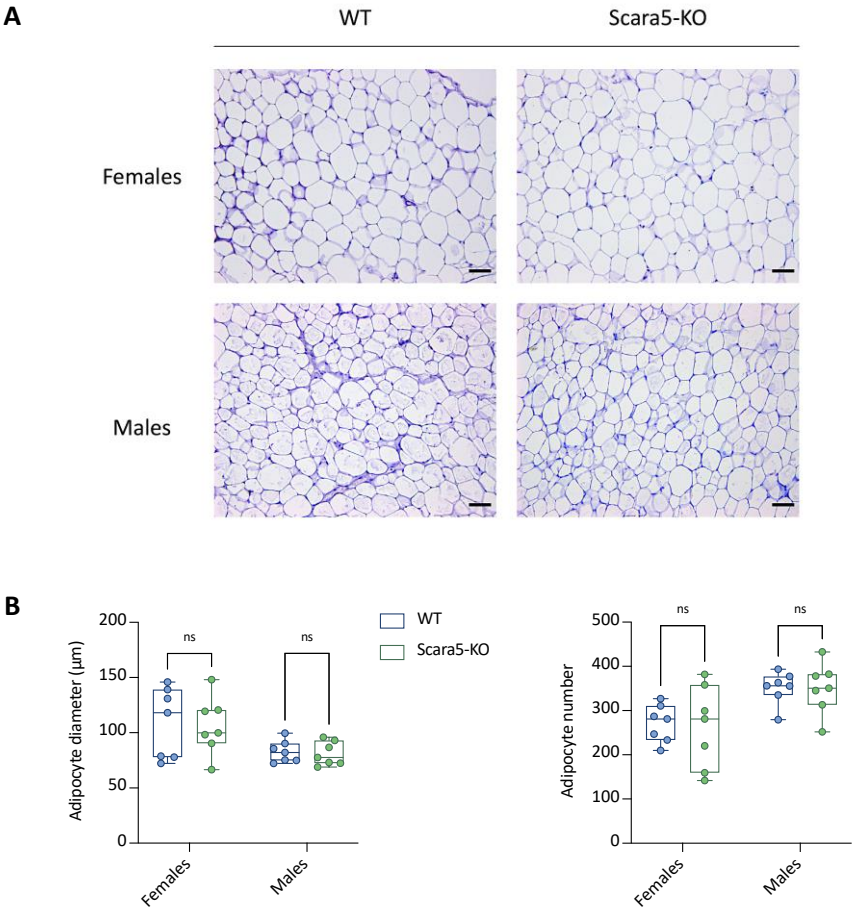


Figure 4.4 Inguinal fat pad histology shows no difference between Scara5-WT and -KO mice adipocyte size and number. Representative pictures of 4 µm Scara5-WT/-KO iFAT stained with H&E (20x bright field, 50 µm scale bar) (**A**). ImageJ *Adiposoft* macro was used to measure the diameter and the number of WT and Scara5 null adipocyte ghosts (**B**). Data are shown as box plots (n=7/group). Mann-Whitney U test was used to determine the degree of significance (^{ns} $p > 0.05$).

4.3 *In vivo* bone formation differs between WT and Scara5-KO mice

As above shown, Scara5-WT and -KO mice phenotype was characterised in terms of bone and fat deposition. Low dose lipopolysaccharide (LPS) injected over the calvaria has been used in the laboratory as a way to induce bone formation in response to low level inflammation. Next, the ability of LPS to induce bone formation in WT and Scara5-deficient mice was assessed using 5-7 weeks old male mice.

4.3.1 LPS at 0.25 mg/kg represents the optimal dose to generate a bone formation model

To determine whether bone formation occurred differently between WT and Scara5-KO mice, LPS or PBS were subcutaneously injected over the mice calvaria; at 7 and 14 days after the injection, bone-labelling Calcein was administered intraperitoneally, and the experiment was concluded after 16 days (**Figure 4.5 A**). Initially, two different concentrations of LPS were used (0.25 and 1.25 mg/kg) to determine the appropriate concentration to inject. As shown in **Figure 4.5 B**, two days after LPS injections mice lost some weight; however, 1.25 mg/kg proved to be damaging for the mice both in terms of weight (≈1.25 g were lost by each mouse in 2 days) and calvarial injury (skin broken around the injection site, **Figure 4.5 C**). Consequently, 1.25 mg/kg LPS-injected mice were sacrificed 3 days post-injection and 0.25 mg/kg was selected as the concentration to be used to perform the calvarial injection assay. Body weight increased over the dose-optimisation experiment (**Figure 4.5 B**), for both 0.25 mg/kg LPS- and PBS-injected mice. Following the dose optimisation, the experiment was performed on WT and Scara5-KO mice to determine if there was any difference in bone formation. Increasing body weight indicated a good health state of PBS/LPS-injected WT and Scara5-KO mice, despite the calvarial and intraperitoneal injections (**Figure 4.5 C, D**).

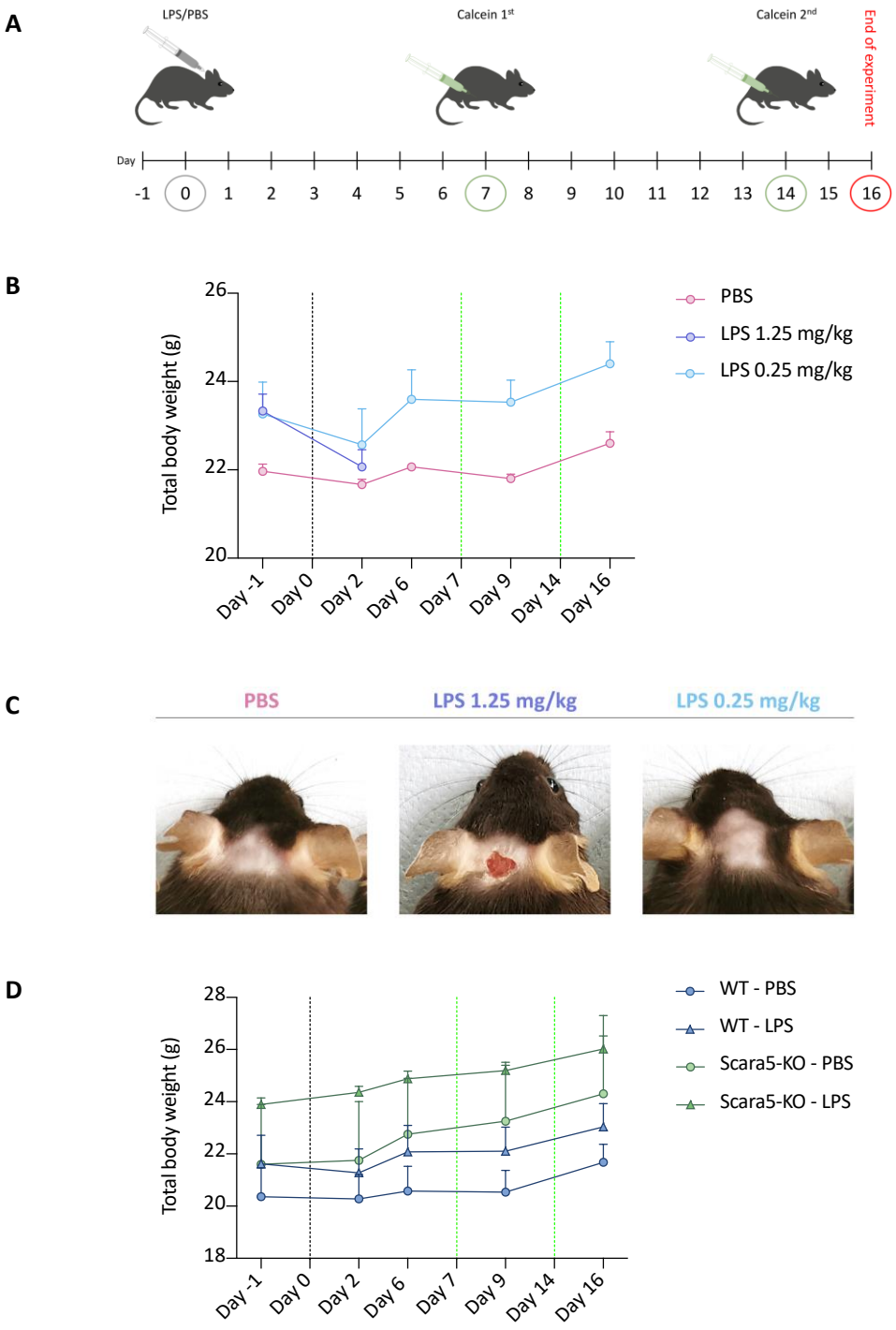


Figure 4.5 0.25 mg/kg LPS calvarial injection does not have harmful effects on mice health status. Diagram on calvarial assay's time course after LPS/PBS calvaria injection (grey circle); bone labelling Calcein was injected intraperitoneally after 7 and 14 days (green circles) and the experiment was concluded after 16 days (red circle) (**A**). PBS/LPS (1.25 and 0.25 mg/kg) calvaria injection effect on WT mice body weight is shown as mean ± SD (n=3/group); black and green dotted lines indicate PBS/LPS injection and Calcein injections, respectively (**B**). Representative photographs of PBS/LPS injected mice and the injection's effect on their calvaria 3 (LPS 1.25 mg/kg) or 16 days (PBS, LPS 0.25 mg/kg) post-

calvarial injection (**C**). PBS and 0.25 mg/kg LPS calvarial injection effect on both WT and Scara5-KO mice body weight is shown as mean ± SD (WT PBS n=5, LPS n=5; Scara5-KO PBS n=2, LPS n=5) (**D**).

4.3.2 Calvarial assay shows that Scara5-KO mice make more bone than WT counterparts

5-7 weeks old male mice were subcutaneously injected with either PBS or 0.25 mg/kg LPS over their calvaria. After 7 days, the first Calcein injection was performed; as shown in **Figure 4.6 A**, the first bone's layer was Calcein-labelled (Calcein 1st). 14 days post PBS/LPS injection, the second Calcein injection labelled a new bone layer (Calcein 2nd). The distance between the two layers was subsequently measured. **Figure 4.6 B** depicts the distance measurements, indicating that PBS injected Scara5-deficient mice presented a greater mineral apposition rate (MAR) than WT mice (mean ± SD, 0.793 ± 0.300 μm/day vs 0.433 ± 0.066 μm/day). LPS-stimulated bone growth was statistically more in Scara5-KO than in WT mice (mean ± SD, 1.190 ± 0.198 μm/day vs 0.728 ± 0.177 μm/day). Unfortunately, due to the low number of PBS-injected Scara5-KO mice (n=2), it was not possible to determine statistical significance and this aspect of the experiment is being repeated (**Figure 4.6 B**, graph on the left).

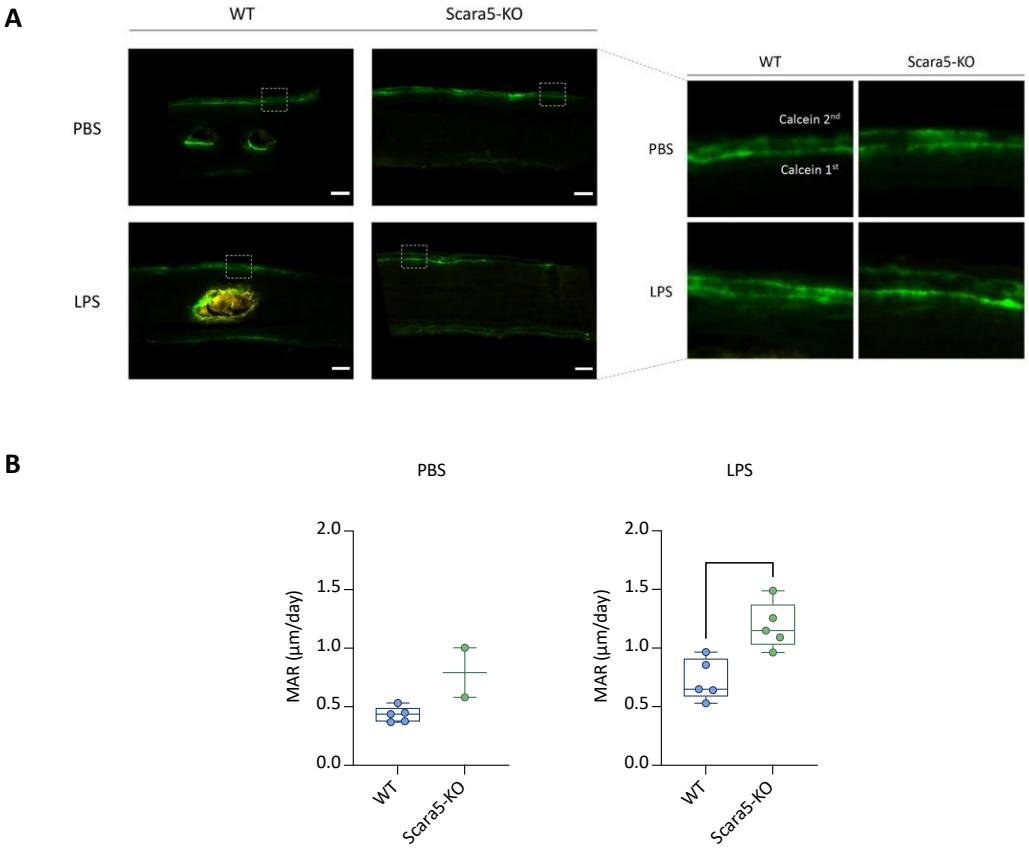


Figure 4.6 Plastic embedded calvaria display distinct bone growth between Scara5-WT and -KO mice.

Representative images and related zooming of bone-labelled layers of WT and Scara5-deficient calvaria (50 μm scale bar) (**A**). Measurement of calvaria MAR of WT (PBS/LPS n=5) and Scara5-KO (PBS n=2; LPS n=5) mice are represented as box plots; Mann-Whitney U test was used to determine the degree of significance (* $p \leq 0.05$).

4.4 Ovariectomy-induced osteoporosis causes bone mass reduction in both WT and Scara5 null female mice

It is well established that menopause increases bone loss and fragility fracture risk in >50 years old women, contributing to osteoporosis [264]. Bone loss can be achieved in female mice by ovariectomy (OVX), in order to study how different genetic and environmental conditions impact on bone loss-related osteoporosis [265].

Adult WT and Scara5-KO female mice were ovariectomised to determine whether Scara5 deficiency protects mice from ovariectomy-induced bone loss.

4.4.1 Tibiae μCT reveals bone mass reduction in both WT and Scara5-KO mice

8 weeks old female mice underwent ovariectomy or SHAM surgery and were sacrificed at 20 weeks old, to define bone structure of tibiae. As shown in **Figure 4.7 A**, OVX mice lost bone mass if compared to SHAM. In agreement with earlier findings, WT SHAM mice presented with less bone than Scara5-KO SHAM mice, and at 20 weeks of age this difference was greater than that observed in the 11 weeks old female mice (**Figure 4.2**). 3D-reconstructed images observations were confirmed by bone parameters analysis, as depicted in **Figure 4.7 B**. Indeed, BV/TV percentage was equal to 10.839 ± 1.411 (mean ± SD) for WT SHAM tibiae and to 15.582 ± 2.424 for Scara5-KO ones. Tb.N was also higher in Scara5-KO than in WT tibiae (mean ± SD, 3.160 ± 0.502 vs 2.306 ± 0.325). Be that as it may, all bone parameters decreased in response to OVX, in both WT and Scara5-KO mice. For example, WT OVX lost a mean value of 4.7% of BV/TV compared to SHAM mice; Scara5-KO OVX mice lost 7.2% of BV/TV compared to SHAM, whilst Tb.Sp increased by 0.091 mm and 0.097 mm in WT and Scara5-null OVX bones compared to SHAM bones.

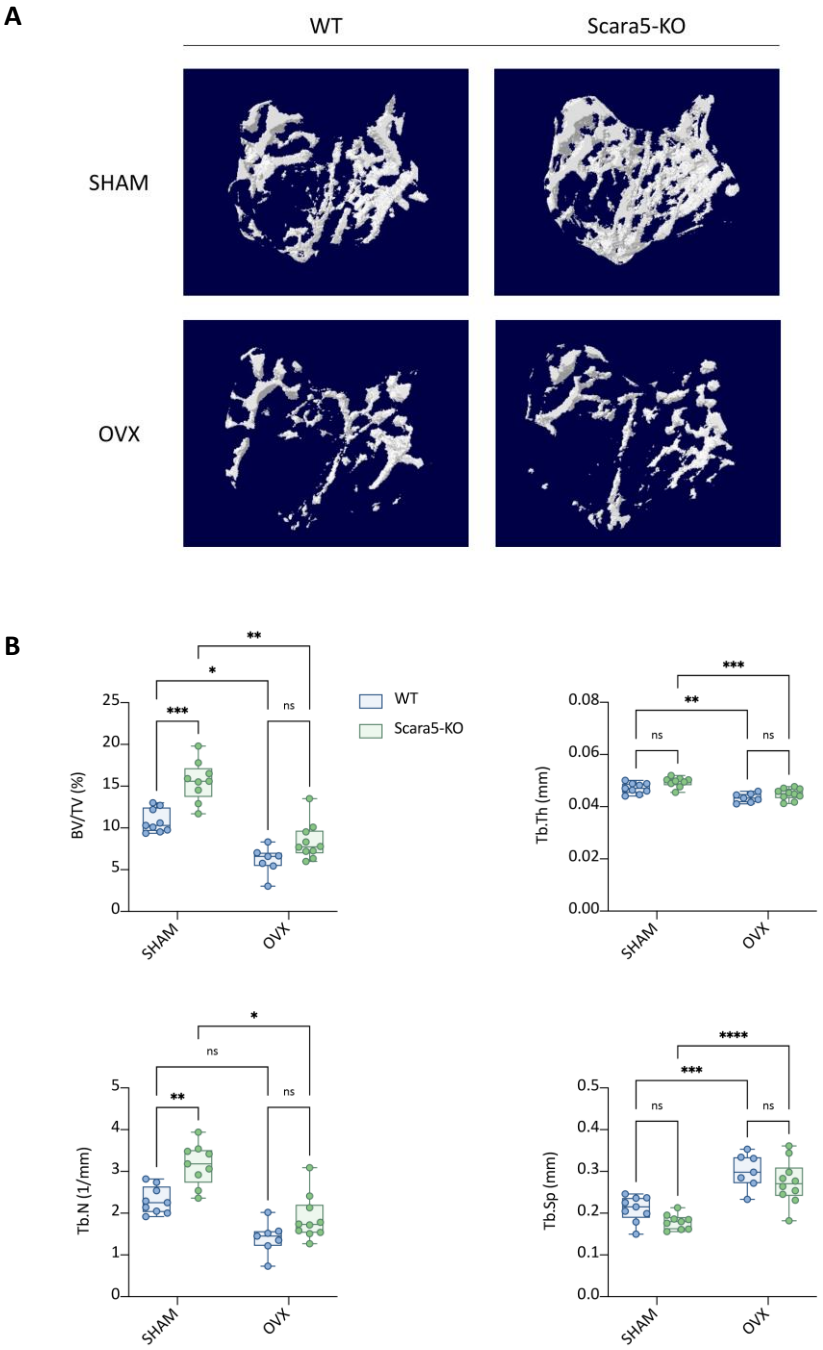


Figure 4.7 Tibiae bone mass decreases in response to ovariectomy-induced osteoporosis. Representative μCT images of 20 weeks old SHAM and ovariectomised (OVX) WT and Scara5-KO murine tibiae (cross section view of trabecular bone) (**A**). Quantification of bone parameters, i.e. bone volume/total volume (BV/TV), trabecular thickness (Tb.Th), trabecular number (Tb.N), and trabecular separation (Tb.Sp) of WT and Scara5 deficient mice (SHAM n=9; WT OVX n=7, Scara5-KO OVX n=10) (**B**). Data are depicted as box plots and two-way ANOVA with Tukey's post-hoc test was used to determine the degree of significance (^{ns} $p > 0.05$, * $p \leq 0.05$, ** $p < 0.01$, *** $p < 0.001$, **** $p < 0.0001$).

Secondary bone parameters are listed in **Table 4.2**. BS/BV was significantly lower in Scara5-KO SHAM than in WT SHAM tibiae and increased in Scara5-KO OVX tibiae only. Oppositely, BS/TV was lower in WT SHAM than in Scara5-KO SHAM bones; however, BS/TV diminished in response to OVX, in both WT and Scara5-deficient mice.

Table 4.2 Bone parameters of SHAM and OVX WT and Scara5-KO female mice. Additional bone parameters, i.e. bone surface/bone volume (BS/BV) and bone surface/total volume (BS/TV) of SHAM and OVX WT and Scara5-KO mice (SHAM n=9; WT OVX n=7, Scara5-KO OVX n=10). Data are presented as mean ± SD and two-way ANOVA with Tukey's post-hoc test was employed to determine the degree of significance. Asterisks were used to compare WT and Scara5-KO within a group (SHAM/OVX), whereas circles refer to WT or Scara5-KO comparison between groups (*/° $p \leq 0.05$).

Bone parameters	SHAM		OVX	
	WT	Scara5-KO	WT	Scara5-KO
BS/BV (mm^{-1})	97.922 ± 4.558	89.438 ± 4.426*	105.414 ± 5.877	104.611 ± 6.758°
BS/TV (mm^{-1})	10.628 ± 1.504	13.907 ± 2.016*	6.450 ± 1.841°	8.714 ± 2.245°

4.4.2 Osmium tetroxide staining shows no difference in bone marrow adipose tissue

Bone marrow adipose tissue (BMAT) exists as regulated (rBMAT) and constitutive (cBMAT), depending on its location and development within the bone. cBMAT is located within the yellow bone marrow of distal tibiae and caudal vertebrae, whereas rBMAT is situated in the red marrow of tibia proximal to the fibula junction, femur, and axial skeleton [266].

Osmium tetroxide (OsO_4) was used to stain tibiae's BMAT. Decalcified and stained tibiae underwent μCT analysis to determine the percentage of BMAT on bone volume. As depicted in **Figure 4.8 A**, 3D images did not show a difference in cBMAT/rBMAT staining between Scara5-WT and -KO tibiae. Indeed, quantification of BMAT (%) showed no statistical difference between SHAM/OVX WT and Scara5-null tibiae (**Figure 4.8 B**). Nevertheless, significant differences in terms of BMAT (both cBMAT and rBMAT) deposition were shown between SHAM and OVX tibiae. WT and Scara5-KO OVX tibiae displayed a BMAT/BV increase by 18.7% and 17.3%, respectively when compared to SHAM bones.

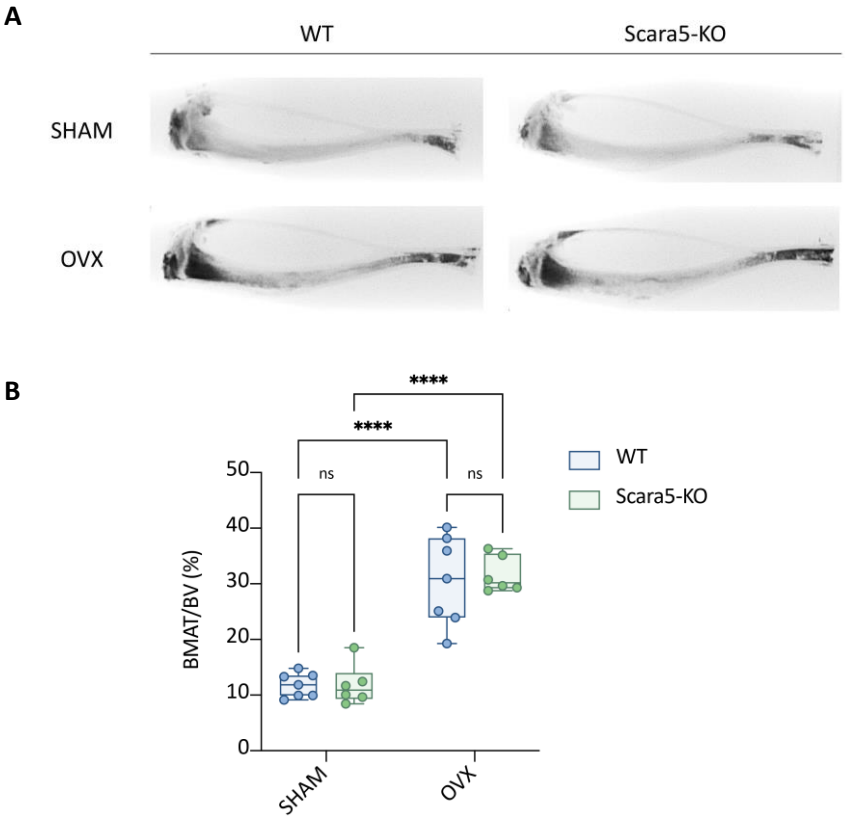


Figure 4.8 BMAT deposition does not change in response to Scara5 deficiency. Representative μCT images of 20 weeks old SHAM and ovariectomised (OVX) WT and Scara5-KO murine tibiae BMAT stained with osmium tetroxide (**A**). Quantification of bone marrow adipose tissue on bone volume (BMAT/BV of WT and Scara5 deficient mice (WT SHAM/OVX n=7; Scara5-KO SHAM/OVX n=6) (**B**). Data are presented as box plots and two-way ANOVA with Tukey's post-hoc test was used to determine the degree of significance (^{ns} $p > 0.05$, **** $p < 0.0001$).

4.5 Streptozotocin-induced diabetes impacted on bone/fat deposition of WT and Scara5 deficient mice

As well as osteoporosis, diabetes has been demonstrated to affect bone and fat homeostasis negatively [267]. As previously presented, OVX-induced osteoporosis showed that Scara5 absence did not prevent bone loss. It was therefore investigated whether the onset of Streptozotocin (Stz)-induced diabetes and its effect on bone and fat differed between Scara5-WT and -KO mice.

4.5.1 WT and Scara5-KO mice blood glucose equally increases in response to Stz treatment

As illustrated in **Figure 4.9 A**, 7 weeks old mice were intraperitoneally injected with a single high dose of Stz; after 13 days, 2 Linbit® pellets (insulin releaser) were implanted into the murine fat pads. The experiment was concluded after 40 days, when murine iFAT and tibiae were collected. As depicted in **Figure 4.9 B**, WT and Scara5 mice responded equally to both Stz and Linbit® implants and were considered diabetic if blood glucose levels exceeded 16.7 mmol/L [268]. In particular, Stz caused the increase of WT/Scara5-KO mice blood glucose concentrations from 9.557 ± 1.623/ 9.944 ± 0.938 mmol/L (mean ± SD) to 30.743 ± 4.399/ 30.844 ± 5.137 mmol/L after 12 days. As expected, Linbit® pellet implantation was followed by a drop in blood glucose levels, equal to 4.657 ± 1.700 mmol/L (mean ± SD) for WT mice and to 4.467 ± 1.534 mmol/L for Scara5-deficient mice. Nonetheless, a week after insulin pellets were implanted, mice blood glucose levels rose again above 16.7 mmol/L and until the end of the experiment. **Figure 4.9 C** shows how individual mice responded to both Stz injection and Linbit® pellets implantation. 12 days after the Stz injection, it was noticed that blood glucose of 3 WT and 5 Scara5-KO mice was above the glucometer limit (33.4 mmol/L). Furthermore, it is clear how after 28 days from Stz injection and 15 days after Linbit® implantation WT and Scara5-KO mice glucose levels increased, without however exceeding 33.4 mmol/L.

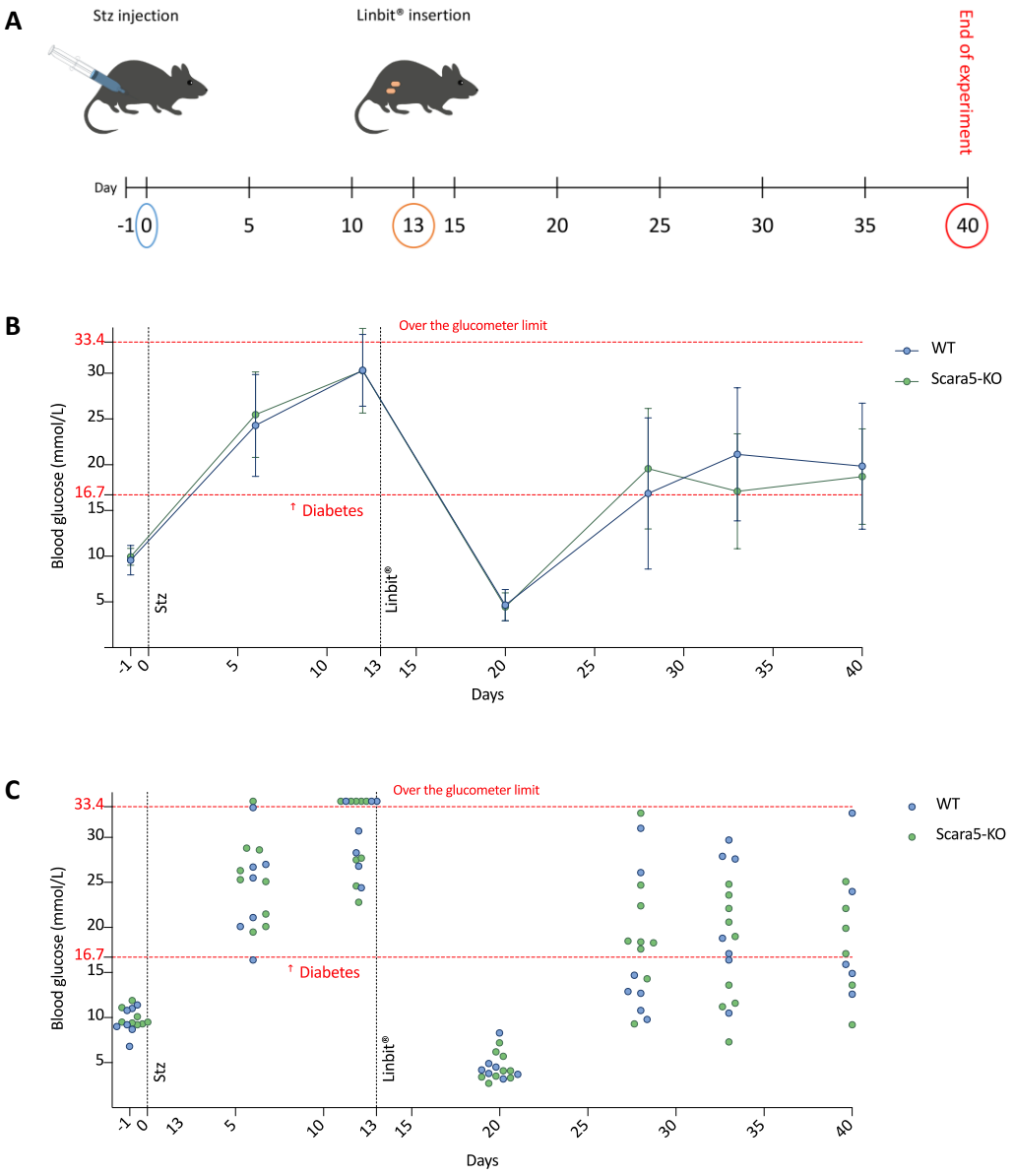


Figure 4.9 Mice blood glucose increases and decreases in response to Stz and Linbit®, respectively. Diagram on diabetes experiment's time course after Stz intraperitoneal injection (blue circle); Linbit® pellets were surgically inserted in the mice iFAT after 13 days (orange circle) and the experiment was concluded after 40 days (red circle) (**A**). Blood glucose was monitored weekly, and data are presented both in terms of mean ± SD (**B**) and as staggered single values (**C**) (WT n=7, Scara5-KO n=9).

4.5.2 Tibiae µCT shows bone mass reduction following Stz injection in both WT and Scara5 null mice

Healthy and diabetic 13 weeks old mice tibiae were analysed by µCT to assess whether diabetes impacted on bone structure and if this happened differently between WT and Scara5-null mice. As shown by **Figure 4.10 A**, Scara5-WT and -KO mice did not differ in terms

of bone structure, nor was any dissimilarity between healthy and diabetic mice particularly evident. Although WT and Scara5-null healthy mice were not different for any bone parameter considered (**Figure 4.10 B**), BV/TV was higher in healthy than in diabetic mice (mean ± SD, WT 20.845 ± 2.660 vs 15.793 ± 3.938; Scara5-KO 21.516 ± 2.140 vs 17.636 ± 2.771) (**Figure 4.10 C**). Healthy and diabetic animals' data could not be statistically compared as healthy mice did not undergo SHAM intraperitoneal injection nor SHAM surgery. Surprisingly, although diabetic WT and Scara5-KO mice displayed analogous bone structure, Tb.Th appeared the only trabecular bone parameter to be significantly different between WT and Scara5-KO tibiae (mean ± SD, 0.039 ± 0.002 vs 0.042 ± 0.002) (**Figure 4.10 C**).

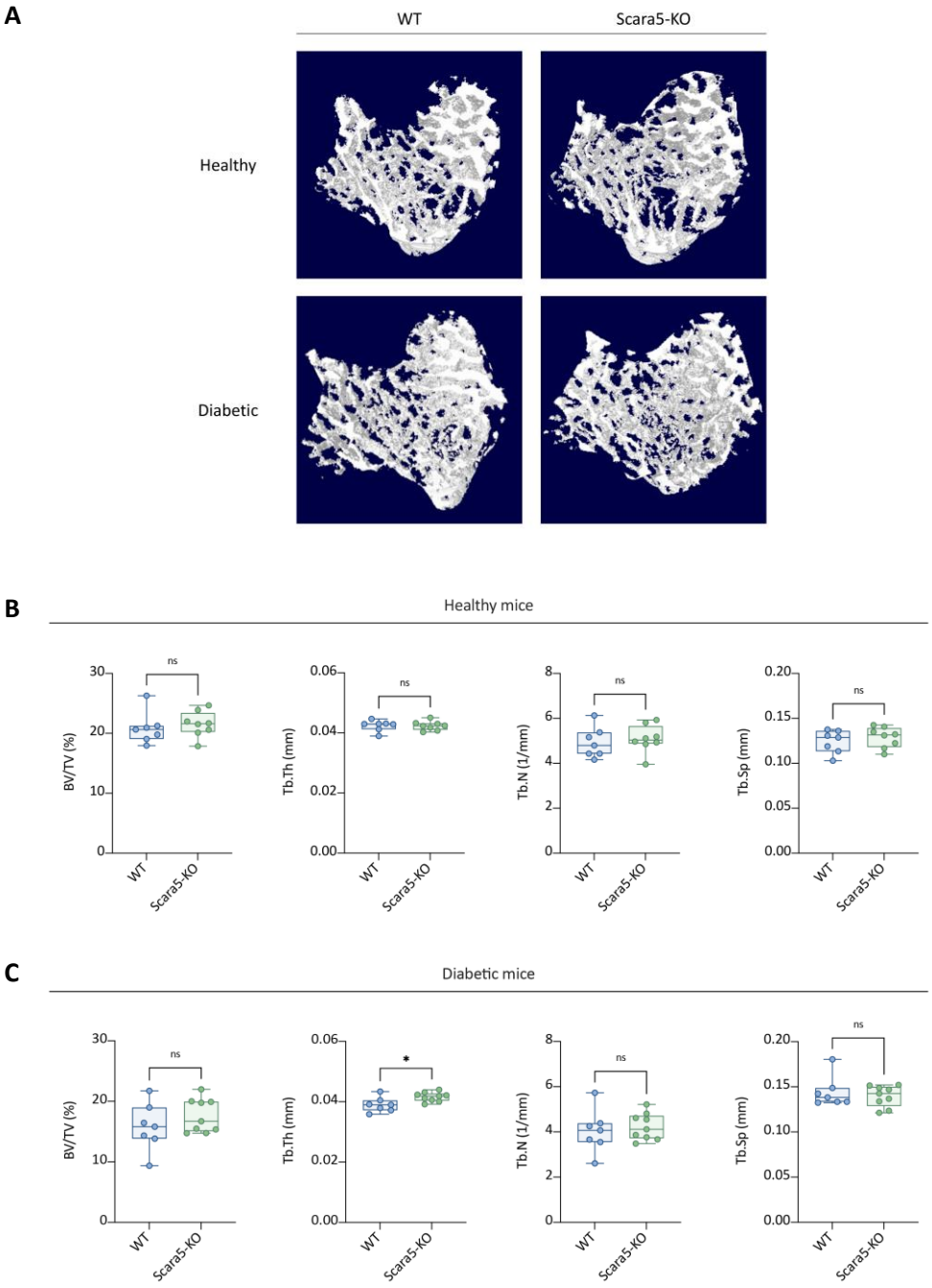


Figure 4.10 Stz-induced diabetes causes bone mass reduction. Representative µCT images of 13/14 weeks old male healthy and diabetic WT and Scara5-KO murine tibiae (cross section view of trabecular bone) (**A**). Quantification of bone parameters, i.e. bone volume/total volume (BV/TV), trabecular thickness (Tb.Th), trabecular number (Tb.N), and trabecular separation (Tb.Sp) of healthy WT and Scara5 deficient mice (WT n=7, Scara5-KO n=8) (**B**), and diabetic mice (WT n=7, Scara5-KO n=9) (**C**). Data are depicted as box plots and Mann-Whitney U test was used to determine the degree of significance (^{ns} $p > 0.05$, * $p \leq 0.05$).

Secondary bone parameters, i.e. bone surface/bone volume (BS/BV) and bone surface/total volume (BS/TV), are reported in **Table 4.3**. However, no statistically significant differences were observed between WT and Scara5-deficient tibiae, neither for healthy nor for diabetic mice.

Table 4.3 Additional bone parameters of control and diabetic Scara5-WT/-KO male mice. Additional bone parameters, i.e. bone surface/bone volume (BS/BV) and bone surface/total volume (BS/TV) of healthy and diabetic WT and Scara5-KO mice. Data are presented as mean ± SD (healthy WT n=7, Scara5-KO n=8; diabetic WT n=7, Scara5-KO n=9).

Bone parameters	Healthy		Diabetic	
	WT	Scara5-KO	WT	Scara5-KO
BS/BV (mm^{-1})	101.678 ± 6.205	101.820 ± 3.342	113.570 ± 6.560	105.412 ± 4.621
BS/TV (mm^{-1})	21.192 ± 2.911	21.920 ± 2.391	17.782 ± 3.954	18.510 ± 2.393

4.5.3 Stz-induced diabetes suppresses the fat deposition difference between WT and Scara5-KO mice

Stz-induced diabetes also impacted on mice fat deposition. As depicted in **Figure 4.11 A**, 13 weeks old WT and Scara5-KO males showed significant differences in terms of iFAT weight (mean ± SD, 0.360 ± 0.037 g vs 0.295 ± 0.024 g) and iFAT weight related to total body weight (1.206 ± 0.125% vs 0.997 ± 0.076%). Interestingly, diabetes induction caused the WT mice to lose iFAT whilst the Scara5-KO iFAT remained at a similar level to the healthy mice; hence the deposition differences were suppressed when diabetes was induced in WT and Scara5-deficient mice (**Figure 4.11 B**). What can be noticed is the fact that both body and iFAT weights, but not the percentage of iFAT weight on total body weight (% iFAT/total weight), were lower in diabetic mice than in healthy mice.

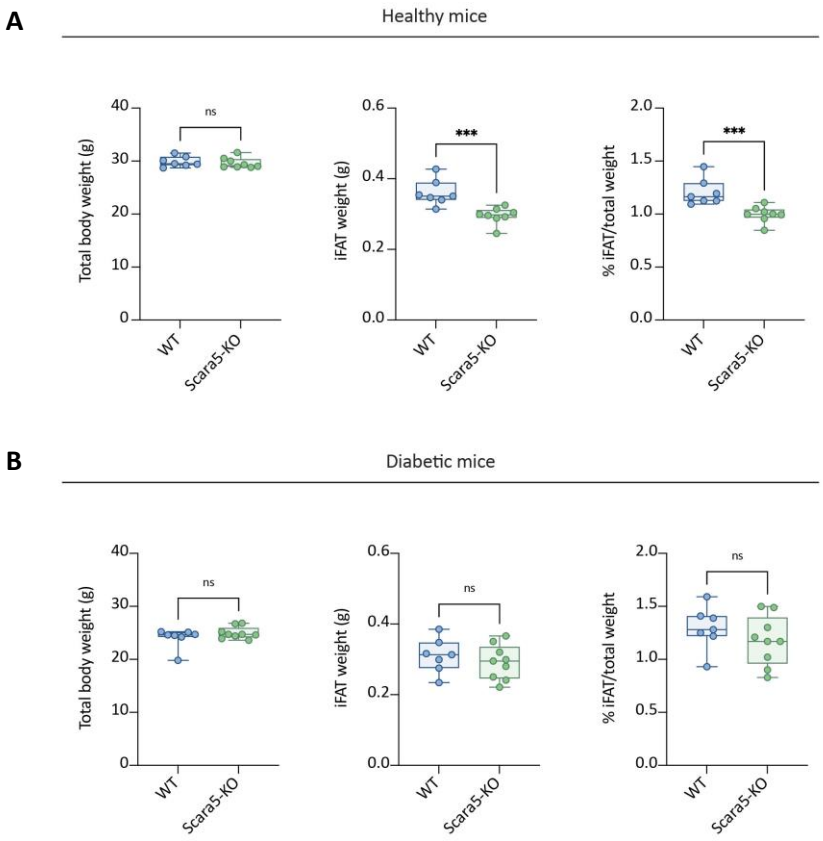


Figure 4.11 Fat deposition is no longer different when WT and Scara5-KO mice develop diabetes. 13/14 weeks old healthy (**A**) and diabetic (**B**) mice were weighted, as well as their inguinal fat (iFAT) pads. The iFAT weight was subsequently related to the total body weight (healthy WT n=7, Scara5-KO n=8; Diabetic WT n=7, Scara5-KO n=9). Data are depicted as box plots and Mann-Whitney U test was used to determine the degree of significance (^{ns} $p > 0.05$, *** $p < 0.001$).

4.6 Discussion

Until the last decade, Scara5 was described as a ferritin receptor and negative regulator of several types of cancers [213, 221]. Subsequently, Lee *et al.* firstly associated Scara5 with adipogenesis, pointing out a novel role of this receptor in MSCs differentiation [165]. As shown previously, WT and Scara5-KO murine BMSCs responded differently to osteogenic and adipogenic stimuli: Scara5-KO cells differentiated more into osteoblasts and less into adipocytes when treated with OM and AM, respectively. Consequently, the mouse phenotype was characterised to assess whether Scara5-KO models displayed a bone and/or a fat phenotype.

After being backcrossed for 9 generations, HET mice were used to generate homozygous WT and Scara5-KO colonies (**Figure 4.1**). The thorough backcrossing programme served to generate mice models with 99.99% C57BL/6J genetic background. This strain is often used to perform bone-related studies; in fact, C57BL/6J mice represents the inbreed strain with the lowest bone density [269]. Therefore, changes in bone mass are amplified, making this strain the most ideal for bone remodelling studies. Once generation 9 WT and Scara5-KO mice were obtained and aged for 11 weeks, their tibiae were μCT-analysed. The results showed more bone in Scara5-deficient tibiae than in WT tibiae; however, this was true for females only at this age (**Figure 4.2**). Surprisingly, WT and Scara5-null males' bones did not show any difference in terms of bone mass. Male mice displayed an increased bone mass if compared with females and this was also reported in Mun *et al.* study [270]. The male skeleton presents with a higher bone density than the female skeleton; Mun *et al.* demonstrated the existence of a sexual dimorphism in osteoclast formation, thereby attributing the females' lower bone mass to an increased osteoclast activity [270]. Also, Haffner-Luntzer *et al.* highlighted a difference between male and female mice fracture healing properties. In particular, male mice presented a higher tissue mineral density and a more rapid fracture healing, if compared with females, after bone fracture [271]. It can be hypothesised that Scara5 deficiency impacted just on females' bone density due to the intrinsic lower bone mass. Thus, the small bone mass increase in Scara5-KO tibiae could not be detected in male bones because of a bone sexual dimorphism.

Osteoblasts and adipocytes shared MSCs as common progenitors [122]. The low Scara5-null BMSCs' adipogenic potential outlined in the previous chapter was confirmed *in vivo*. It was indeed shown that Scara5-KO mice exhibit lower-weight inguinal fat pads in both males and females, even when iFAT weight was expressed as a percentage of total body weight. However, just males' total body weight was higher in WT than in Scara5-KO mice (**Figure 4.3**). These results indicated the strong impact that Scara5-deficiency had on fat deposition. Also, considering adipogenesis as the counterpart of osteogenesis, Scara5-KO mice presented less fat and consequently more bone. Although Scara5-null male mice did not show a clear bone phenotype, they displayed a strong fat phenotype, thereby supporting the data in the literature that describe Scara5 as an adipogenic marker [165]. Nonetheless, studies by Ojala *et al.* generated Scara5-KO mice models that did not show any difference in terms of body

weight compared to WT mice [178]; however, differences in testis were pointed out as affecting mice fertility. The phenotypic characterisation presented in the current chapter contradicts with the aforementioned; even so, the work from Ojala *et al.* only described the Scara5-null mice phenotype without showing any supporting data and they were not specifically looking for differences in fat and bone.

Although Scara5-deficient mice presented a reduced fat deposition, subcutaneous iFAT histology did not show any dissimilarity in terms of adipocyte size and/or number (**Figure 4.4**). In humans, adipocyte diameter varies from less than 20 to 300 μm, with women displaying higher body fat and fat deposits [272, 273]. Also, gluteal-femoral adipocytes are larger in woman than in men [17]. WT and Scara5-KO female mice, as well as human, displayed larger adipocytes than males; consequently, males' adipocytes outnumbered females' adipocytes. Hence, it can be concluded that the lower iFAT deposition in Scara5-KO compared to WT mice is not particularly due to smaller or fewer adipocytes. As previously shown, the reduced Scara5-KO BMSCs adipogenic potential *in vitro* can explain the overall reduction of fat deposition *in vivo*, indicating that these cells are disinclined to differentiate towards adipocytes.

Bone remodelling requires the coupled activities of osteoclasts and osteoblasts to remove and produce bone, respectively [40]. Inflammation has often been associated with bone loss because of osteoclasts' over-activation [274]. Nevertheless, pro-inflammatory cytokines (e.g. interleukin (IL)-1, IL 6, and tumour necrosis factor alpha – TNFα) released by fractured bones proved to be critical for tissue healing and regeneration, with inflammation being crucial in recruiting MSCs and inducing their proliferation and differentiation [275]. Moreover, Li *et al.* showed that ectopic new bone formation was linked to the activation of canonical/non-canonical Wnt signalling pathways in ankylosing spondylitis model *in vitro* [276]. It remains unclear whether the bone catalysis is followed by over-responsive osteogenesis when inflammation is triggered by unknown stimuli, or whether a common stimulus independently activates inflammatory response and MSCs differentiation [277]. A calvarial injection assay was performed to determine bone growth rate in terms of MAR in Scara5-WT and -KO mice; this assay has been developed to test how bone formation occurs *in vivo* in response to locally-administered agents [243]. LPS is a component of Gram-negative bacteria's outer membrane that stimulates immune response by activating monocytes and macrophages via Toll-like receptor 4 (TLR-4) [278]. It has been proved that LPS induces pro-inflammatory cytokines

secretion, therefore promoting osteoclastic bone resorption and inhibiting bone formation [279]. Additionally, Yu et al. performed a calvarial injection assay on C57Bl/6 mice using LPS to mimic bacteria-induced bone loss; the elevated concentration of LPS used (i.e. 25 mg/kg) provoked calvaria disruption because of osteoclasts' hyper-activation [280]. Until now, no published works highlighted the effect of low doses of LPS on bone formation, neither in humans nor in murine models. The current work showed that high levels of LPS (1.25 mg/kg) induced a disruptive inflammatory response in mice calvaria (**Figure 4.5**), in agreement with other studies. On the other hand, a lower dose of LPS (0.25 mg/kg) stimulated bone growth in both WT and Scara5-KO calvaria if compared with PBS-injected mice. Additionally, bone growth was much higher in Scara5-deficient than in WT calvaria, in both PBS and LPS injected mice (**Figure 4.6**). The contribution of inflammatory macrophages to bone physiology is well established; indeed, macrophages showed to influence osteoblasts differentiation both *in vitro* and *in vivo* [253, 281]. 100 ng/ml of LPS revealed to induce macrophage response in primary osteoblast cultures [281]; therefore, it can be speculated that low doses of LPS induced macrophages activation and a consequent mild inflammation that drove osteoblast-related bone growth. Although WT and Scara5-KO 11 weeks old male mice did not show any difference in terms of trabecular bone parameters (**Figure 4.2**), MAR analysis demonstrated a dissimilar speed at which osteoblasts-produced osteoid was mineralised in younger mice (5-7 weeks old). In this case, a high bone mineralisation did not reflect a higher bone density, although 5-7 weeks old tibiae were not μCT-analysed. Thus, it cannot be excluded that younger male mice would exhibit a higher bone mass in the aftermath of Scara5 deletion.

Bone loss and deterioration are often associated to age-related osteoporosis; this bone disorder is characterised by an unbalanced bone remodelling, favouring osteoclasts resorption activity over osteoblasts' bone formation [282]. Oestrogen plays a crucial role in bone metabolism: it acts on osteoclasts to inhibit bone resorption, as well as on osteoblasts and osteocytes to support bone formation [283]. Pre- and post-menopausal oestrogen-deficiency increases the expression of receptor activator of nuclear factor kappa beta (RANK) ligand (RANKL), than binds to RANK to activate osteoclasts [264]. Ovariectomy has been often performed on murine models to mimic osteoporotic-related bone loss. Hence, ovariectomy deprives female mice of oestrogen, therefore enhancing osteoclast activity [265]. Since Scara5-deficient tibiae displayed higher bone density than WT tibiae, it was initially hypothesised that

the absence of Scara5 could protect the mice from osteoporosis-related bone loss. The results showed that Scara5-WT and -KO mice lost their bone mass similarly, thus proving that Scara5-KO did not play any protective role towards bone health and integrity (**Figure 4.7**). However, 20 weeks old Scara5-KO mice still exhibited a higher bone mass than WT mice, confirming the results previously described, related to younger mice (11 weeks old). Considering that the absence of Scara5 proved to enhance MSCs differentiation into osteoblasts *in vitro* (see **Chapter 3**), as well as osteoblast activity and bone deposition *in vivo* (**Figure 4.6**), is not surprising that Scara5 deletion does not protect from osteoporosis-related bone loss. In fact, as previously stated, ovariectomy-induced osteoporosis hyper-activates osteoclasts without impacting on osteoblasts' activity directly [265]. Hence, the onset of osteoporosis increases the resorption of bone, while Scara5 deficiency impacted positively on osteoblast-driven bone deposition. In line with this, data from Dr Yi-Hsuan Lee PhD thesis showed that Scara5 expression did not affect osteoclast function in physiological conditions.

As expected, OVX induced BMAT accumulation in mice tibiae (**Figure 4.8**); various bone-related diseases, such as osteoporosis, have been associated with increased bone marrow adiposity in humans [284]. In murine models, ovariectomy causes both bone loss and BMAT expansion [285]. It is not surprising that one of the main causes of osteoporosis is the altered and preferential differentiation of MSCs to adipocytes, which explains why osteoporotic bones are characterised by an increased bone marrow adiposity [251]. OVX WT and Scara5-KO mice both displayed a similar increase of BMAT if compared to SHAM. By the same token, SHAM WT and Scara5-KO tibiae did not show different deposition of BMAT. Although Scara5-null mice exhibited less subcutaneous fat deposition than WT mice, MSCs differentiation to adipocytes seemed not to be affected within the bone marrow. However, it is important to underline that bone marrow adiposity is independent from visceral or subcutaneous fat deposition, as it displays a distinct metabolic function [286]. Furthermore, it remains unknown whether Scara5-WT and -KO younger mice present a different BMAT deposition, thus when MSCs are more active in terms of proliferation and differentiation.

As well as osteoporosis, diabetes also affects bone health and homeostasis. In particular, it has been shown that pancreatic β-cells disruption is strongly associated with increased osteoclasts' activity (via RANK/RANKL modulation), as well as osteoblasts' dysfunction (via Runt-related transcription factor 2 (RUNX2) and its target molecules' downregulation) [287]. In

addition, both RunX2 downregulation and upregulation of Wnt signalling pathway inhibitors (i.e. sclerostin and dickkopf-related protein 1) were described in mice with Stz-induced diabetes, therefore altering osteoblasts differentiation [288]. In the present work, age-matched healthy and diabetic mice were used to assess whether Scara5 deficiency would exert protection against diabetes onset and/or its related bone loss. Diabetes developed equally between WT and Scara5-KO mice after a single high dose of Stz (170 mg/kg) (**Figure 4.9**). Moreover, μCT analysis revealed decreased bone mass 40 days post Stz-injection (**Figure 4.10**); nonetheless, the bone mass reduction was analogous for both WT and Scara5-KO diabetic mice if compared with healthy mice. As above-discussed for osteoporosis, also diabetes-related bone loss can be linked to osteoclast over-activation [287], whereas Scara5 proved to exert a role on MSCs differentiation towards osteoblasts and adipocytes. For this experiment, healthy mice could not be used as controls as they did not receive a SHAM injection nor a SHAM surgery.

Although insulin resistance and obesity are clinical features of type 2 diabetes (T2D), it was recently reported that around 50% of type 1 diabetic patients are either obese or overweight [289]. However, there are no evidence proving that MSCs differentiation to adipocytes increases in type 1 diabetes (T1D) or T2D humans/murine models. Healthy WT and Scara5-null mice displayed a different fat phenotype, but this difference was suppressed by diabetes (**Figure 4.11**). It is not clear whether this is a consequence of diabetes or whether the insulin pellets' implantation within one of the fat pads vitiated the results (the "pelleted" fat pad appeared smaller than the contralateral one).

To summarise, this chapter showed how Scara5 deficiency impacted on mice bone and fat phenotype, stimulating bone formation and reducing subcutaneous fat accumulation. Bone-related pathologies developed independently of Scara5, meaning that it does not have any role in bone loss-related osteoporosis and diabetes. Nevertheless, these pathologies mostly impact on osteoclasts, provoking their hyper-activation and the consequent bone resorption, which proved to be comparable between WT and Scara5-KO mice (**Figure 4.12**).

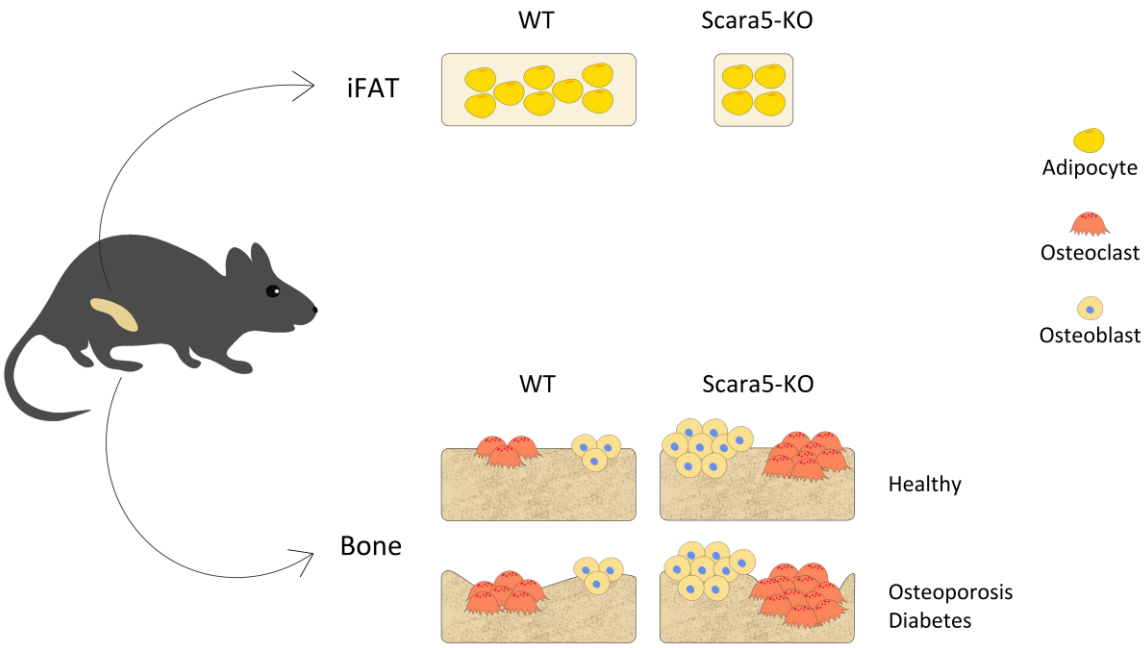


Figure 4.12 Scara5 absence increases bone and decreases fat deposition *in vivo*. Scara5-null mice presented a decreased bone fat deposition and an increased bone mass/bone formation if compared with WT mice. Osteoporosis and diabetes developed similarly between WT and Scara5-KO mice, triggering osteoclastic bone resorption upon their onset.

Chapter 5: Mechanistic investigation of Scara5 in MSCs commitment

5.1 Introduction

Throughout the years, a plethora of molecular pathways have been discovered to play a role in MSCs commitment and differentiation towards osteoblasts and adipocytes. Among them, one of the most studied is the canonical Wingless-related integration site (Wnt) signalling pathway. It has been shown that Wnt pathway exerts a fundamental role during MSCs commitment to early osteoblasts. Indeed, the deletion of β-catenin caused a shift in pre-osteoblasts differentiation, favouring adipogenesis over osteogenesis [290]. Canonical Wnt molecules (e.g. Wnt3a, Wnt10b) proved to stimulate osteoblast differentiation/proliferation and to inhibit osteoblast apoptosis, promoting bone formation [237]. As revealed in Chapter 3, Scara5 gene expression was not triggered by OM in mouse BMSCs. Sebastian *et al.* demonstrated that murine osteoblasts downregulate Scara5 expression in response to Wnt3a treatment [237]. It can therefore be assumed that Scara5 is not necessary during early/late stages of osteogenesis.

MSCs differentiation, as well as their survival and proliferation, is closely related to phosphatidylinositol-3-kinase (PI3K)-protein kinase B (AKT) pathway. Activated downstream protein mammalian target of rapamycin (mTOR), for example, promoted preadipocytes' adipogenesis; mTOR in fact upregulated the adipogenic transcriptional factors peroxisome proliferator activated receptor gamma (PPARγ) and CCAAT-enhancer-binding protein alpha (CEBPα) [291]. On the other hand, imatinib, a tyrosine kinase inhibitor used to treat acute myeloid leukaemia, proved to stimulate osteogenesis by inhibiting PI3K-AKT pathway [291]. While investigating Scara5 mechanism of action, Lee *et al.* determined that AKT activation was not affected by Scara5 downregulation in a preadipocyte cell line, nor by its overexpression in MSCs-like cells [165]. However, cancer-related studies linked Scara5-downregulation to PI3K/AKT activation [170, 222].

Scara5 is a ferritin receptor [213]; its overexpression increased intracellular iron and consequently reactive oxygen species levels in the oesophageal squamous cell carcinomas (ESCC) cell line [215]. Hence, it can be hypothesised that the absence of Scara5 perturbs the intracellular iron content. Iron is a crucial cofactor of several mitochondrial enzymes involved

in the citric acid cycle, directly controlling energy production [292]. Desferrioxamine (DFO)-related iron depletion proved to negatively affect the citric acid cycle, thereby decreasing ATP production via oxidative phosphorylation and promoting ATP production via glycolysis in the human lymphoblast cell line K-562 [148]. To date, it is still unknown whether Scara5-deficiency impacts on cellular metabolism.

This chapter will give insight into Scara5's mechanism of action in osteogenesis and adipogenesis, thus pointing at its role in maintaining iron homeostasis and metabolic balance.

5.2 Scara5 deficiency has minimal impact on Wnt signalling pathway

It is well established that BMSCs undergo osteogenic differentiation by activating RUNX2 and Wnt/β-catenin signalling (Wnt canonical signalling pathway) [290]. Since Scara5 deletion enhanced BMSCs' osteogenic potential, the Wnt signalling pathway was stimulated to determine whether its activation differed between WT and Scara5-KO BMSCs.

5.2.1 Lithium Chloride does not stimulate BMSCs osteogenesis

Lithium Chloride (LiCl) is able to activate canonical Wnt signalling by inhibiting glycogen synthetase kinase 3β (GSK3β), thereby stabilising free cytosolic β-catenin [293]. LiCl was shown to efficiently promote osteogenesis by activating Wnt/β-catenin pathway in human BMSCs [294], yet it did not influence the ALP activity of human exfoliated deciduous teeth-derived stem cells [295], so the exact effect on osteogenic differentiation is not clearly defined. WT and Scara5-KO BMSCs were treated with different concentrations of LiCl to assess whether osteogenesis could be promoted in primary murine cells; the concentrations of LiCl were selected according to the literature [294-296]. As depicted in **Figure 5.1**, pNP levels were measured after 3 days of treatment with LiCl; NaCl treatment was used as control to exclude effects related to Chloride; OM treatment was employed as the assay's positive control. LiCl suppressed ALP activity of BMSCs at all concentrations used, independently of Scara5 expression. NaCl also suppressed BMSCs' ALP activity, albeit not at the same level of LiCl. As expected, pNP levels elevated in Scara5-KO more than in WT BMSCs treated for 3 days in OM. These results would suggest that Scara5 may not play a role in Wnt signalling. However, as LiCl affects all canonical Wnt signalling and given the importance of the Wnt/β-catenin

pathway during osteogenesis, individual Wnt recombinant proteins were used to stimulate Wnt signalling in WT and Scara5-KO BMSCs.

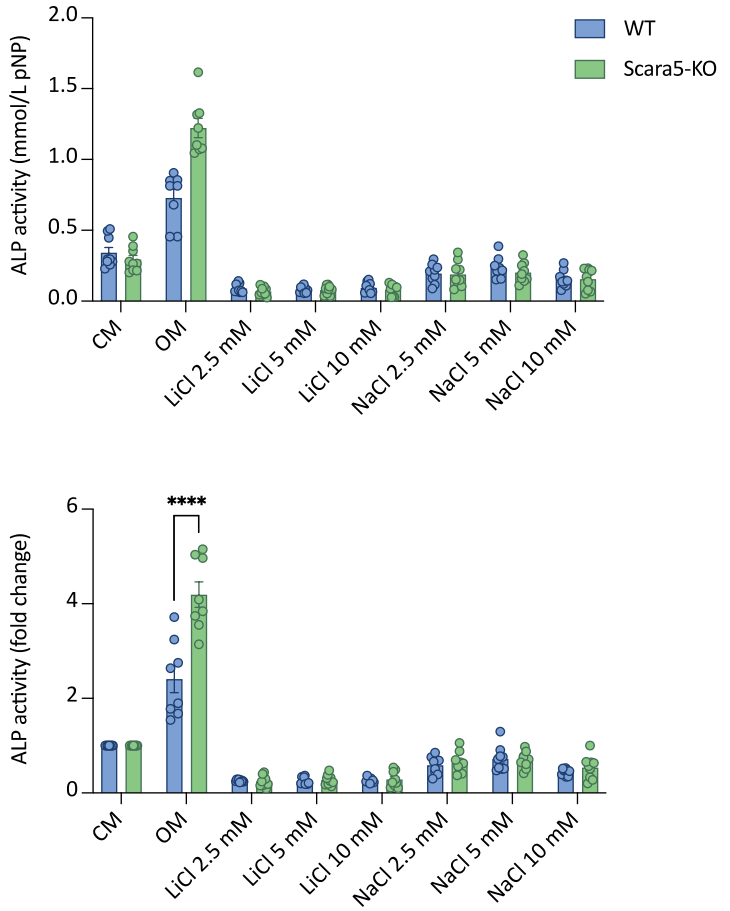


Figure 5.1 LiCl suppresses ALP activity of WT and Scara5-KO BMSCs. Different concentration of LiCl and NaCl were used to assess their impact on BMSCs ALP activity after 3 days of treatment. Data are presented as mean ± SEM (n=3, ≥2 technical replicates/n), both in terms of pNP concentration (top graph) and fold change (bottom graph). Two-way ANOVA with Šídák's post-hoc test was used to determine the degree of significance (**** $p < 0.0001$).

5.2.2 Wnt3a, but not Wnt5a nor Wnt10b, promotes osteogenesis of Scara5-null BMSCs more than WT counterparts

Wnt recombinant proteins were employed to assess whether they were able to promote osteogenesis of WT/Scara5-KO BMSCs and if it occurred differently between them. Different concentrations of Wnt3a (5-200 ng/ml) were tested; Wnt3a proved to increase pNP concentration of both WT and Scara5-KO BMSCs. ALP activity resulted significantly higher in Scara5-null BMSCs than in WT cells after 3 days-treatment of 10 ng/ml (fold change, mean ±

SEM, 1.531 ± 0.077 vs 1.177 ± 0.047), 100 ng/ml (2.753 ± 0.124 vs 1.811 ± 0.076), and 200 ng/ml (2.679 ± 0.099 vs 2.239 ± 0.174) Wnt3a (**Figure 5.2 A**). However, neither Wnt5a nor Wnt10b stimulated BMSCs osteogenesis; indeed, as shown in **Figure 5.2 B,** all Wnt5a's concentrations used suppressed ALP activity of BMSCs, independently of Scara5 expression. Similarly, Wnt10b treatment did not stimulate the ALP activity of WT and Scara5-KO BMSCs (**Figure 5.2 C**). Overall, Wnt3a was the only ligand that proved to stimulate differently WT and Scara5-KO BMSCs osteogenesis.

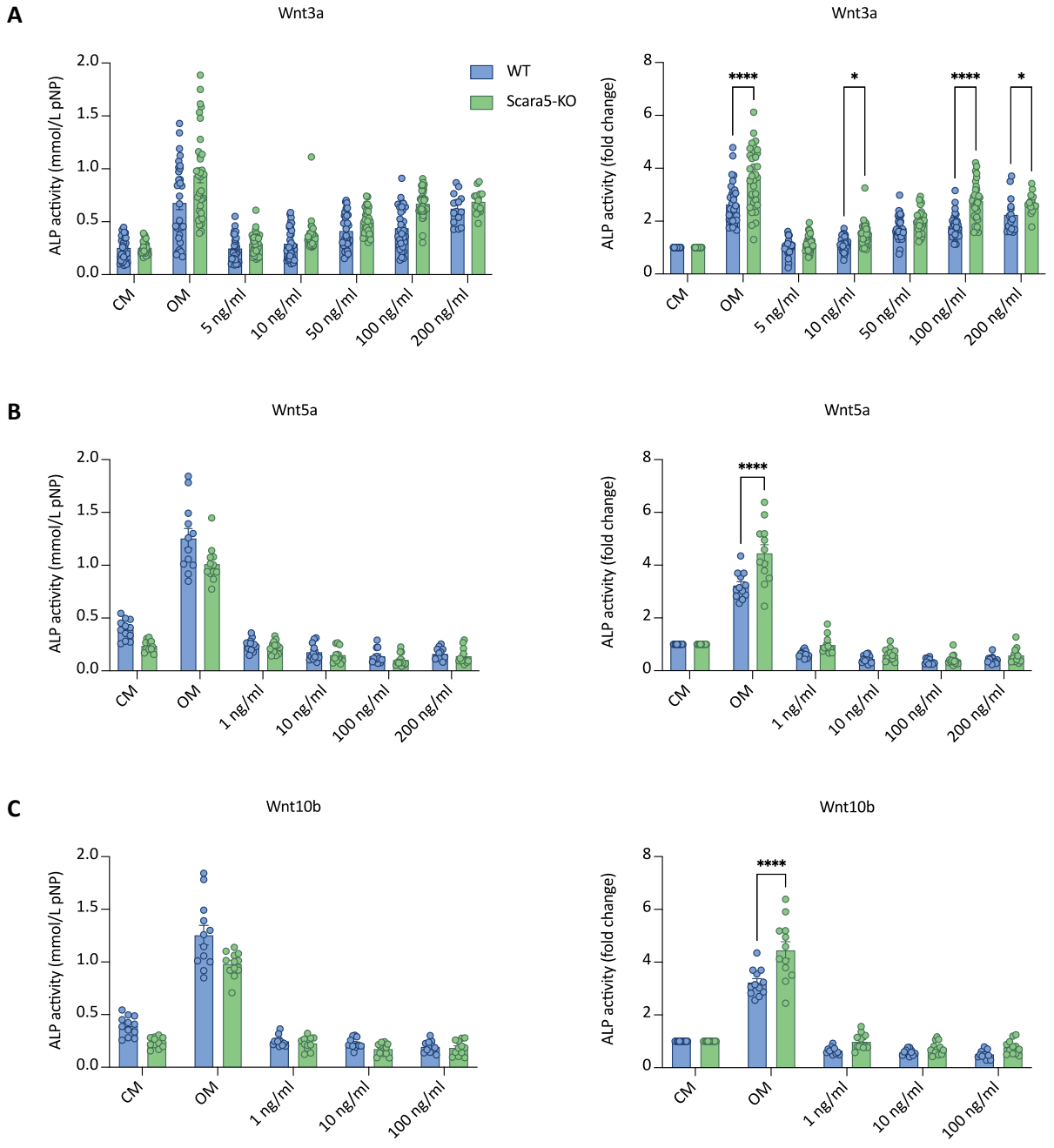


Figure 5.2 Wnt3a, but not Wnt5a nor Wnt10b, increases BMSCs' ALP activity. Various concentration

of Wnt recombinant proteins, i.e. Wnt3a (**A**), Wnt5a (**B**), and Wnt10b (**C**), were employed to test their effect of BMSCs ALP activity. Data are presented as mean ± SEM (n≥3, ≥3 technical replicates/n), both in terms of pNP concentration (on the left) and fold change (on the right). Two-way ANOVA with Šídák's post-hoc test was used to determine the degree of significance (* $p \leq 0.05$, **** $p < 0.0001$). OM treatment is included as a positive control for osteogenesis.

5.2.3 OM treatment does not stimulates Wnt signalling-related genes' expression in Scara5-WT and -KO BMSCs

To evaluate the ability of OM to activate the Wnt/β-catenin signalling pathway, BMSCs were treated for 2, 6, and 24 hours before being tested for Wnt-related genes' expression. Axin2 expression increased after 6 hours of OM treatment (mean ± SEM, WT 1.839 ± 0.347 vs Scara5-KO 2.240 ± 0.603) and marginally decreased over 24 hours (WT 1.564 ± 0.448 vs Scara5-KO 2.203 ± 0.690) (**Figure 5.3 A**). Despite Scara5-null cells expressed slightly higher levels of Axin2 compared to WT, the differences were not statistically significant. **Figure 5.3 B** depicts Dishevelled 3 (Dvl3) expression upon, which did significantly differ between WT and Scara5-KO cells after 24 hours of OM treatment (WT 1.210 ± 0.182 vs Scara5-KO 1.531 ± 0.116). Finally, Lef1 expression did not statistically differ between Scara5-WT and -KO (**Figure 5.3 C**).

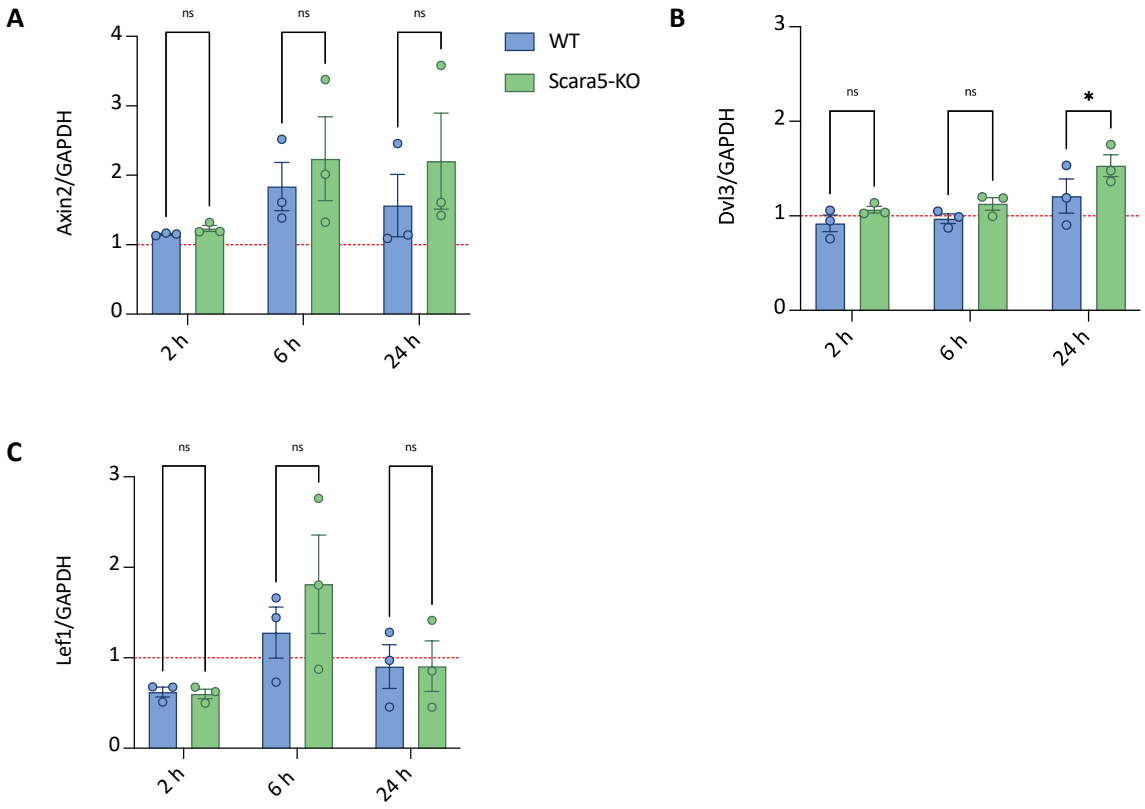


Figure 5.3 OM does not increase the expression of Wnt signalling related genes. WT and Scara5-null BMSCs were treated for 2, 6, and 24 hours with osteogenic medium and subsequently tested for the expression of Wnt-signalling-related genes (i.e. Axin2, Dvl3, and Lef1). $2^{-\Delta\Delta CT}$ method was applied and gene expression was normalised to GAPDH. Data are shown as mean ± SEM (n=3) in terms of fold change to their respective controls (red dotted line); two-way ANOVA with Tukey's post-hoc test was used to determine the degree of significance (^{ns} $p > 0.05$).

5.2.4 Wnt3a treatment increases Wnt signalling-related genes' expression in Scara5-WT and -KO BMSCs

OM treatment slightly stimulated Axin2, Dvl3, and Lef1 expression, therefore 100 ng/ml of Wnt3a recombinant protein were used to treat WT and Scara5-KO BMSCs; Wnt/β-catenin-related genes' expression was assessed after 2, 6, and 24 hours. Axin2 expression increased after Wnt3a treatment, particularly after 6 hours (mean ± SEM, WT 10.369 ± 4.475 vs Scara5-KO 13.069 ± 4.897); however, WT and Scara5-null BMSCs' Axin2 expression was not statistically different (**Figure 5.4 A**). No remarkable increases were detected in terms of Dvl3 expression (**Figure 5.4 B**). Finally, Lef1 expression rose after 2 and 6 hours of treatment (mean ± SEM 2 h WT 1.773 ± 0.249 vs Scara5-KO 1.947 ± 0.521; 6h WT 2.611 ± 0.937 vs Scara5-KO

2.840 ± 0.961), dropping dramatically after 24 hours (WT 1.063 ± 0.165 vs Scara5-KO 1.199 ± 0.060) (**Figure 5.4 C**). Due to the high variability, Lef1 expression was not statistically different between WT and Scara5-null BMSCs.

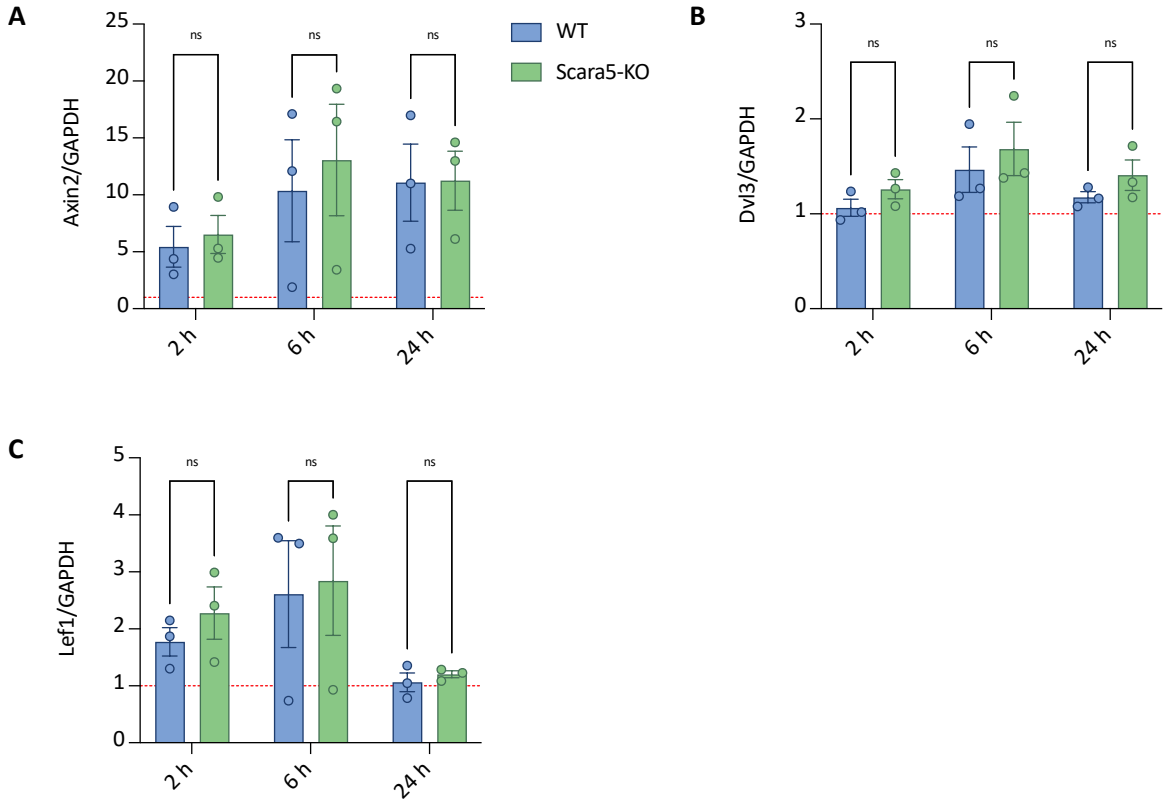


Figure 5.4 Wnt3a stimulates the expression of Wnt signalling genes equally between WT and Scara5-null BMSCs. BMSCs were treated with 100 ng/ml Wnt3a for 2, 6, and 24 hours. RT-qPCR was carried out to assess Axin2, Dvl3, and Lef1 expression of both WT and Scara5-KO BMSCs. $2^{-\Delta\Delta CT}$ method was applied and gene expression was normalised to GAPDH. Graphs' bars represent mean ± SEM (n=3) and data are presented as fold changes to their respective controls (red dotted line); Two-way ANOVA with Tukey's post-hoc test was used to determine the degree of significance (^{ns} $p > 0.05$).

5.2.5 β-catenin expression does not change in Wnt3a-treated Scara5-WT and -KO BMSCs

WT and Scara5-KO BMSCs were treated with 200 ng/ml Wnt3a for a maximum of 24 hours; cells were then lysed and total proteins were extracted. 10 μg of proteins underwent Western Blot (WB) analysis to determine whether total β-catenin expression increased differently between WT and Scara5-deficient cells. As displayed in **Figure 5.5 A**, representative blots showed almost no changes between controls (time 0, T0) and treatments. Indeed, Wnt3a treatment barely induced an increase of total β-catenin in both WT and Scara5-KO BMSCs,

with a maximum fold change of ≈1.5 (**Figure 5.5 B**). After 24 hours, β-catenin expression was comparable to the one of the untreated cells (mean ± SEM, WT 0.910 ± 0.020; Scara5-KO 0.977 ± 0.134). Overall, no differences could be highlighted between β-catenin expression of WT and Scara5-KO BMSCs.

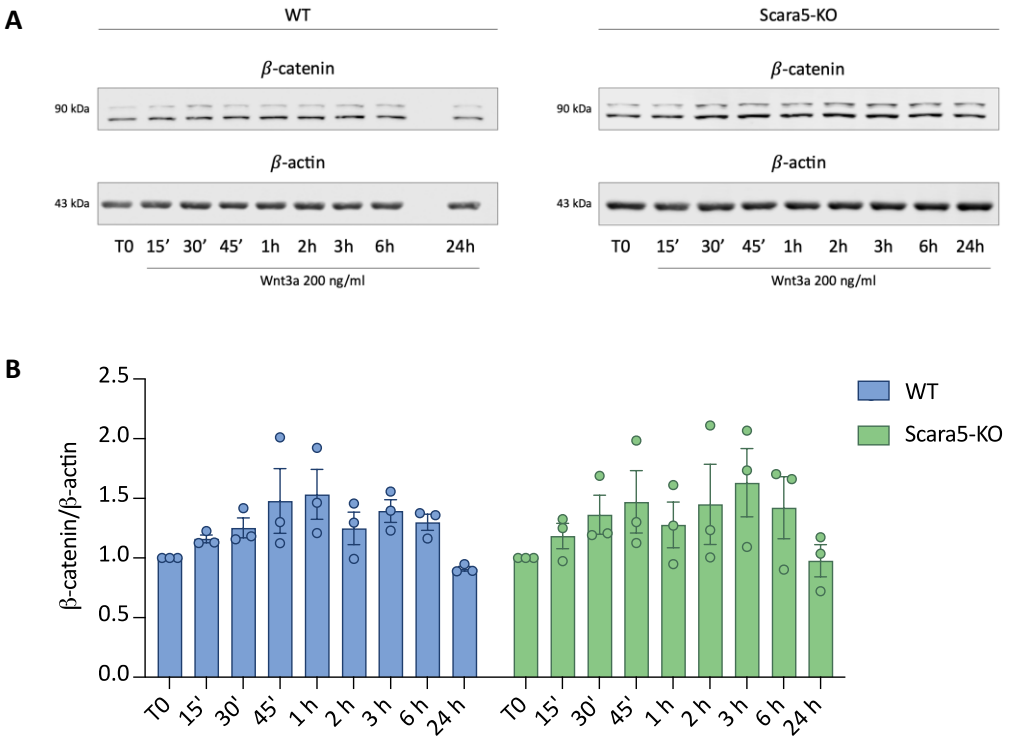


Figure 5.5 WT and Scara5-KO BMSCs respond similarly to Wnt3a treatment in terms of β-catenin expression. WT and Scara5-deficient BMSCs were treated with 200 ng/ml Wnt3a to determine β-catenin expression changes in 24 h by WB. Representative pictures of WB membranes; BMSCs were treated for different time points and lysed to extract the proteins. 10 μg of total protein were subjected to WB for the detection of β-catenin and β-actin (control) (**A**). Data are presented as mean ± SEM (n=3); Time 0 (T0) indicates the untreated cells (**B**).

5.3 Scara5 deficiency does not influence AKT-related pathways' function

As aforementioned, AKT signalling pathway plays a fundamental role in cell proliferation and differentiation [291]. To test whether Scara5 deficiency impacts on activation/phosphorylation of AKT and/or AKT-related pathways, an AKT phosphorylation array was employed. WT and Scara5-KO BMSCs were treated with either CM, OM, or AM (all serum-free) and lysed to obtain total proteins.

5.3.1 AKT-related proteins are differentially phosphorylated in WT and Scara5-KO BMSCs treated with osteogenic and adipogenic media

AKT signalling pathway controls cell proliferation, differentiation, and survival by interacting with other pathways, e.g. AMP-activated protein kinase (AMPK), human epidermal growth factor receptor/erythroblastic leukaemia viral oncogene B (HER/ErbB), hypoxia inducible factor 1 subunit alpha (HIF-1α), IGF-1, Janus kinase/signal transducer and activator of transcription (JAK/STAT), MAPK, mTOR, PI3K-AKT, TGF-β, and Wnt/β-Catenin pathway. Representative proteins of these signalling pathways were included in the phosphorylation array used (array map, **Figure 5.6**).

Every antibody is spotted in duplicate vertically	1	**POS**	**POS**	**NEG**	**NEG**	AKT (P-S473)	AMPKα (P-T172)	BAD (P-S112)	4E-BP1 (P-T36)
	2								
	3	ERK1 (P-T202/y204) ERK2 (P-Y185/Y187)	GSK3α (P-S21)	GSK3β (P-S9)	mTOR (P-S2448)	P27 (P-T198)	P53 (P-S15)	P70S6K (P-T421/S424)	PDK1 (P-S241)
	4								
	5	PRAS40 (P-T246)	PTEN (P-S380)	RAF-1 (P-S301)	RPS6 (P-S235/236	RSK1 (P-S380)	RSK2 (P-S386)	**NEG**	**POS**
	6								

Figure 5.6 AKT phosphorylation array map. RayBio® C-Series AKT Pathway Phosphorylation Array C1 was employed to determine whether the phosphorylation of AKT-related protein changed between WT and Scara5-KO BMSCs OM/AM-treated. Positive and negative controls are indicated as POS and NEG.

AKT phosphorylation array membranes were incubated with 200 μg of proteins extracted from CM (control)- and OM-treated BMSCs (**Figure 5.7 A**). Despite the heatmap showing some interesting changes in terms of pixel density, especially in the bottom part of the graph (**Figure 5.7 B**), just four proteins were considered upregulated after 20 minutes of OM treatment, with fold changes equal to or above 2 (**Figure 5.7 C**). Among the selected 4 proteins, the expression of RAF-1 (Raf-1 proto-oncogene, serine/threonine kinase) was similar between WT and Scara5-KO cells (fold change, 3.5 vs 3.8); on the other hand, Phosphatase and Tensin Homolog (PTEN) expression was higher in WT than in Scara5-KO BMSCs (fold change, 6.1 vs 3.6), whilst RPS6 (Ribosomal protein S6) and RSK1 (Ribosomal S6 Kinase 1) expression was higher in Scara5-null than in WT cells (4.0 and 11.5 vs 2.7 and 6.0).

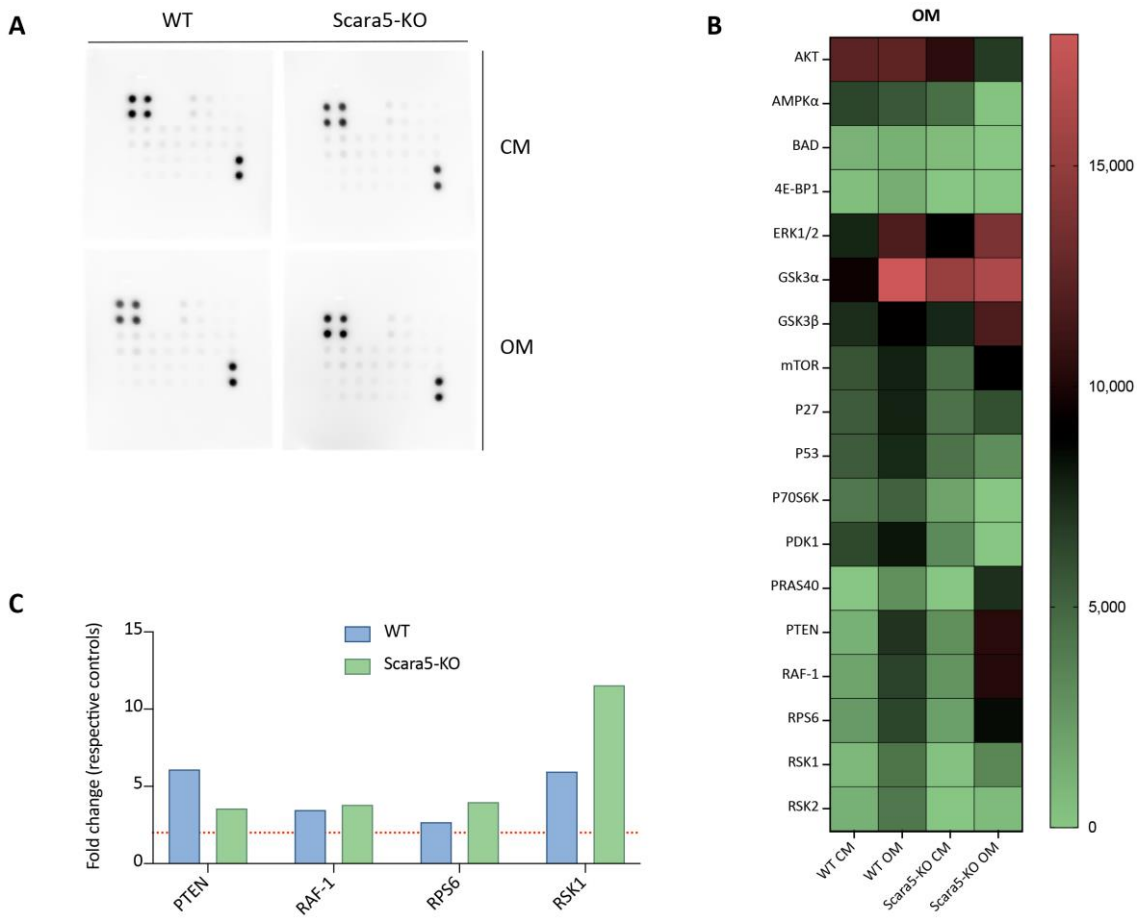


Figure 5.7 OM treatment induces AKT-related proteins upregulation more in Scara5-KO than in WT BMSCs. WT and Scara5-KO BMSCs were treated with osteogenic medium for 20 minutes; the membranes were incubated with 200 μg of proteins and ultimately visualised to quantify the dot density (**A**). Data are represented in terms of pixel density (0-18,000) in form of heat map (**B**). Selected proteins were upregulated in response to OM treatment; data are presented as fold change to the respective controls. Only fold changes above 2 (red dotted line) were considered and included in the graph (**C**).

Alongside the osteogenic treatment, BMSCs were also treated with AM to detect AKT-related proteins' phosphorylation and whether this was affected by Scara5 deficiency. 20 minutes of AM treatment increased the phosphorylation levels of several proteins (**Figures 5.8 A, Figure 5.8 B**); the bottom half of the heatmap graph shows how AM increased the protein phosphorylation more in WT than in Scara5-KO BMSCs (**Figure 5.8 B**). However, just 5 proteins were upregulated by AM treatment, with fold changes equal to/above 2 (**Figure 5.8 C**). Except for P70S6K (fold change, WT 2.4 vs Scara5-KO 1.8), the other proteins (i.e. PTEN,

RAF-1, RPS6, and RSK1) were phosphorylated far more in WT than in Scara5-KO cells, indicating that Scara5-KO BMSCs did not respond to AM at the same extent of WT BMSCs.

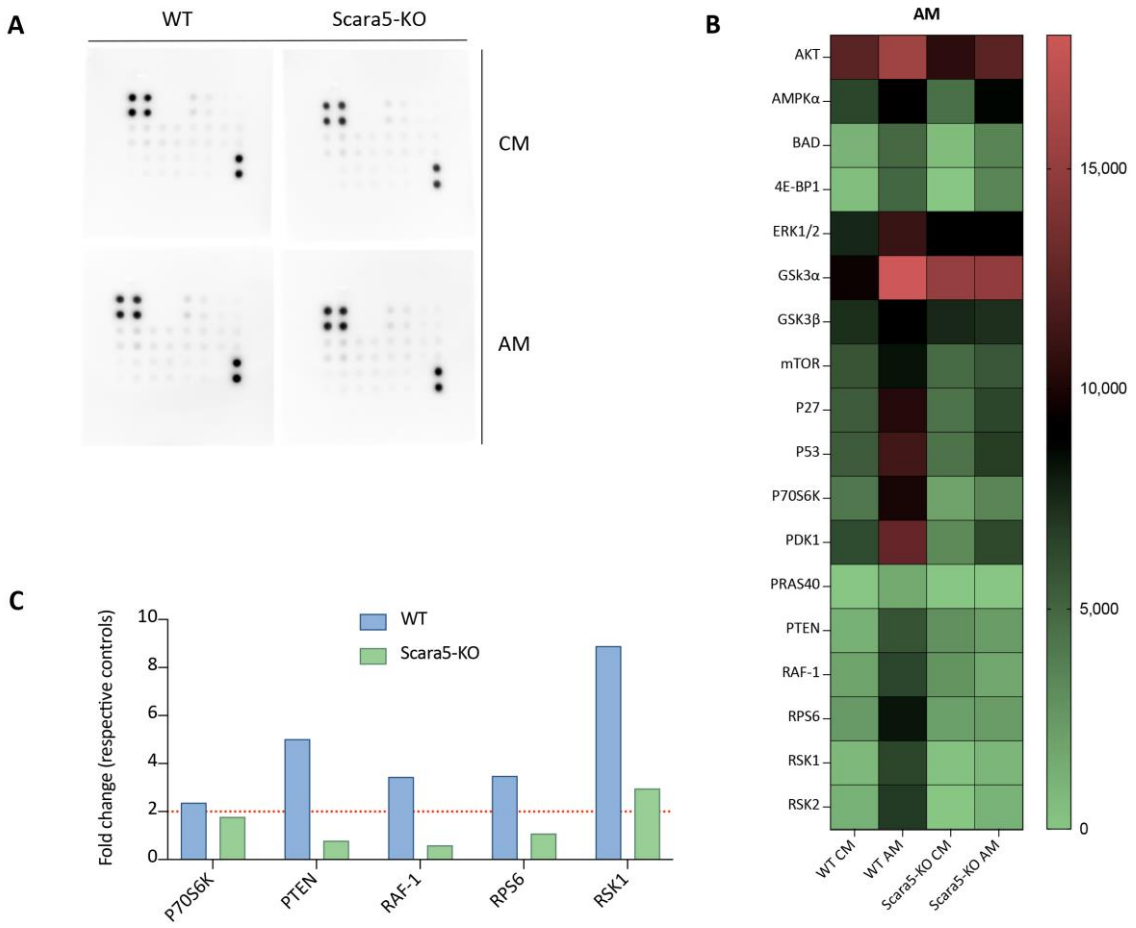


Figure 5.8 AM treatment induces AKT-related proteins upregulation more in WT than in Scara5-KO BMSCs. WT and Scara5-KO BMSCs were subjected to AM treatment for 20 minutes; 200 μg of proteins were used for the experiment, at the end of which black dots were visualised and quantified (**A**). Data are represented as pixel density (0-18,000) and depicted as heat map (**B**). AM treatment induced the upregulation of selected proteins; data are shown as fold change to the respective controls. Only fold changes above 2 (red dotted line) were included in the graph (**C**).

5.3.2 Scara5 does not play a role in AKT-related pathways, as confirmed by WB analysis

The AKT phosphorylation array showed some intriguing results, especially concerning BMSCs treated with AM. Indeed, some proteins were upregulated in WT more than in Scara5-null BMSCs in response to adipogenic stimuli. In order to validate these results, two proteins were selected (i.e. RPS6 and RSK1). WT and Scara5-KO BMSCs were treated with serum-free AM and the proteins were obtained from cell lysates before being subjected to WB analysis. As

depicted in **Figure 5.9 A**, phosphorylated RPS6 and RSK1 (pRPS6 and pRSK1) levels were similarly expressed by WT and Scara5-KO BMSCs. Quantification graphs shown in **Figure 5.9 B** outline a comparable response of WT and Scara5-KO cells to AM, being the protein levels of pRPS6 (on the left) and pRSK1 (on the right) very similar. Although the phosphorylation array showed encouraging results, neither pRPS6 nor pRSK1 proteins were upregulated after adipogenic stimulation. In particular, pRPS6 levels gradually diminished after 5 minutes of treatment (**Figure 5.9 B**, left), while pRSK1 levels steadily fluctuated over the experimental time points (**Figure 5.9 B**, right). Be that as it may, no significant differences emerged between Scara5-WT and -KO cells in terms of phosphorylated protein expression.

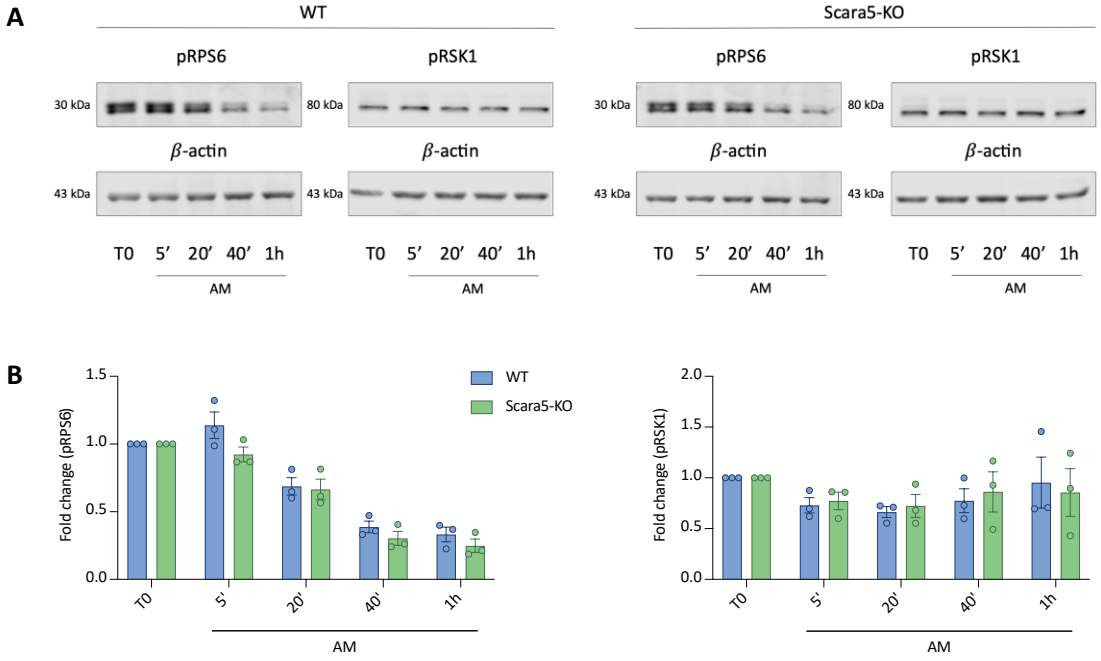


Figure 5.9 WT and Scara5-KO BMSCs express similar levels of phosphorylated RPS6 and RSK1 once treated with AM. BMSCs were AM-treated for different time points before being lysed to extract the proteins; representative pictures of 10 μg of proteins analysed by WB employing anti-mouse antibodies. β-actin was used for data normalisation (**A**). Data are depicted as mean ± SEM (n=3); Time 0 (T0) indicates the untreated cells (**B**).

5.4 Scara5 deficiency impacts on cell metabolism

Li and colleagues first associated Scara5 and ferritin in 2009; they demonstrated that mouse kidneys' capsule expressed high levels of Scara5 and that this receptor was responsible for serum ferritin endocytosis and the consequent iron delivery [213]. To determine whether Scara5

deficiency impacts on iron content, iron concentration was evaluated in murine organs. Furthermore, due to the central role of iron as a metabolic cofactor, WT and Scara5-KO BMSCs were tested for metabolic gene expression, as well as for their mitochondrial activity.

5.4.1 Scara5-KO murine kidneys display reduced iron content

WT and Scara5-deficient mice organs, i.e. testis and kidneys, were processed in order to quantify the iron content. Scara5 was indeed found abundantly expressed in testis [172] and in the renal capsule of mice [213]. As depicted in **Figure 5.10**, WT testis presented with more iron than Scara5-KO counterparts (mean ± SD, 0.144 ± 0.020 μmol/mg vs 0.112 ± 0.039 μmol/mg); however, the difference was not statistically significant. In the kidney, iron content was significantly higher in WT than in Scara5-KO murine models (mean ± SD, 1.252 ± 0.149 μmol/mg vs 1.044 ± 0.116 μmol/mg), thus suggesting a mild iron deficiency in Scara5-null mice.

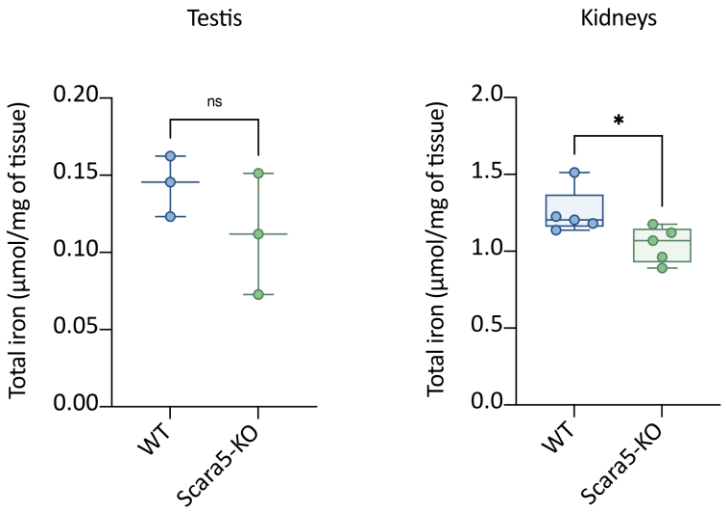


Figure 5.10 Iron content differs between Scara5-WT and -KO mice's kidneys, but not testis. 20 mg of tissue of 3 weeks old mice were digested to quantify their iron content. Data are presented as box plots (testis n=3, kidneys n=5); Mann-Whitney U test was used to determine the degree of significance (^{ns} $p > 0.05$, * $p \leq 0.05$). Iron quantification was partially performed by Dr Justin Bradley (School of Chemistry, University of East Anglia, Norwich, UK).

5.4.2 Metabolic gene expression differs between AM-treated WT and Scara5-KO BMSCs

Cells are usually provided with energy by two main metabolic pathways: glycolysis and oxidative phosphorylation (OXPHOS) [297]. Glucose is the main energy source for osteoblast proliferation and differentiation; the aerobic/anaerobic ATP production is indeed sufficient to support osteogenesis [159]. WT and Scara5-KO BMSCs were treated with OM for 7 days before being tested for the expression of glycolysis-related genes hexokinase 2 (HK2) and pyruvate kinase (PKM). 7 days of OM treatment was previously shown to be sufficient to measure an increased osteogenic gene expression (i.e. Alpl, OCN **Figure 3.5**). As displayed in **Figure 5.11**, HK2 expression slightly increased in response to osteogenic stimuli in both WT and Scara5-KO BMSCs, without significant differences. On the other hand, PKM expression did not rise when cells were treated with OM, neither in WT nor in Scara5-deficient BMSCs.

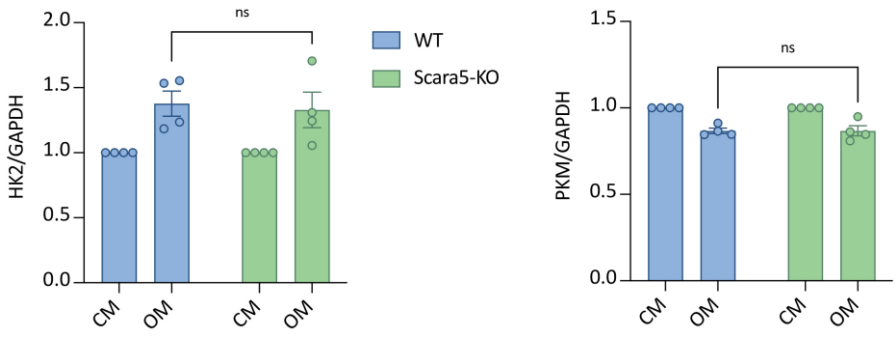


Figure 5.11 OM does not induce the expression of glycolysis-associated genes HK2 and PKM. 2.88 x 10^5 cells/well were seeded in a 6-well plate before being treated with OM for 7 days. RT-qPCR was carried out to assess HK2 and PKM expression of WT and Scara5-KO BMSCs. $2^{-\Delta\Delta CT}$ method was applied and gene expression was normalised to GAPDH. Graphs' bars are represented as mean ± SEM (n=4); unpaired two-tailed Student's t-test was used to determine the degree of significance (^{ns} $p > 0.05$).

In parallel with OM treatment, Scara5-WT and -KO BMSCs were also treated with AM for 7 days. Similarly to OM, 7 days of AM treatment was sufficient to induce the highest expression of both Adipoq and LEP in WT and Scara5-KO BMSCs (**Figure 3.8**). It has been proven that human adipose-derived stem cells consume more oxygen and increase their mitochondrial activity after 7 days of adipogenic induction [160]. The expression of lipid metabolism genes (i.e. fat specific protein 27 – Fsp27, hormone-sensitive lipase – Hsl, monoacylglycerol lipase – MGL), as well as bioenergetic genes (i.e. peroxisome proliferator activated receptor alpha – PPARα, uncoupling protein 3 – Ucp3) and glucose transporter 4

(Glut4) was evaluated. As depicted in **Figure 5.12**, except for MGL, WT BMSCs expressed higher levels of Fsp27 and Hsl if compared with Scara5-deficient cells. Similarly, PPARα, Ucp3 and Glut4 were poorly expressed by Scara5-KO cells. Altogether, these results indicated a strong impairment of metabolic genes' expression when Scara5-deficient BMSCs were exposed to adipogenic stimuli.

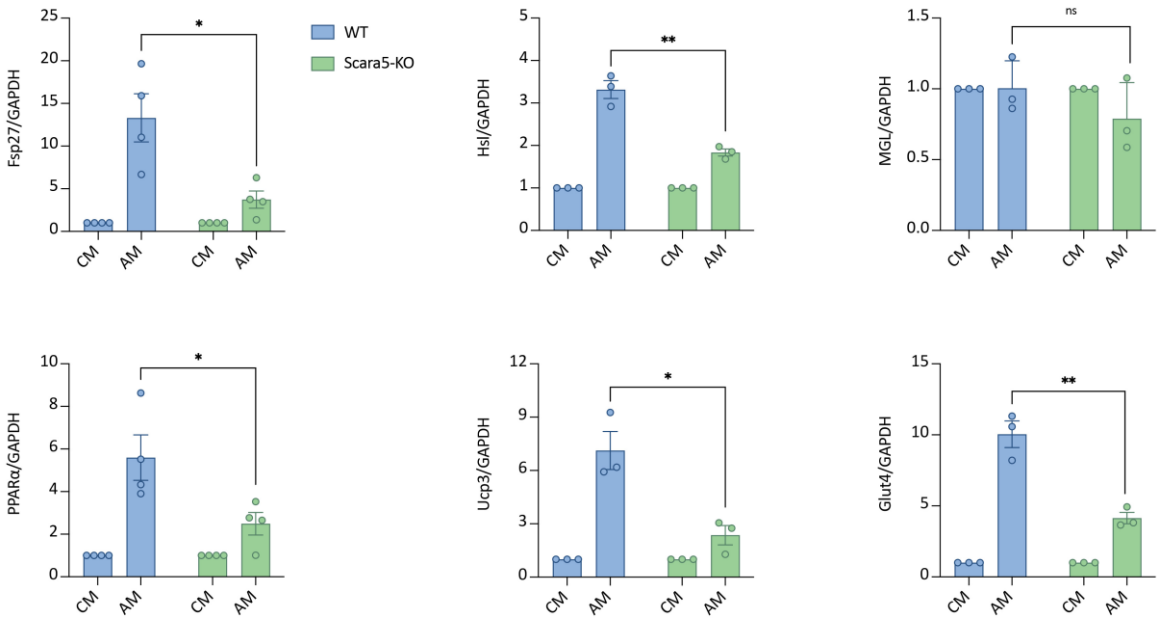


Figure 5.12 Metabolic genes are more expressed by AM-treated WT than Scara5-KO BMSCs. 2.88 x 10^5 cells/well were seeded in a 6-well plate before being treated with AM for 7 days. RT-qPCR was carried out to assess metabolic gene expression of WT and Scara5-KO BMSCs. $2^{-\Delta\Delta CT}$ method was applied and gene expression was normalised to GAPDH. Graphs' bars represent mean ± SEM (n≥3) and unpaired two-tailed Student's t-test was used to determine the degree of significance (^{ns} $p > 0.05$, * $p \leq 0.05$, ** $p < 0.01$).

5.4.3 Oxygen consumption rate differs between AM-treated WT and Scara5-KO BMSCs

Mitochondrial function was assessed in terms of oxygen consumption rate (OCR) using the well-established assay Cell Mito Stress Test kit; the aim was to determine whether the absence of Scara5, and the consequential iron deficiency, was linked to a reduced mitochondrial activity of BMSCs. WT and Scara5-KO were both maintained in CM and treated with AM. As shown in **Figure 5.13 A**, WT and Scara5-KO BMSCs kept in CM displayed a similar OCR; basal and maximal respiration were slightly higher in WT than in Scara5-null BMSCs, but not statistically significant differences emerged by data analysis. On the other hand, as

depicted in **Figure 5.13 B**, AM treatment impacted on the maximal respiration of WT and Scara5-KO BMSCs differently. Indeed, the injection of carbonyl cyanide-p-trifluoromethoxyphenylhydrazone (FCCP), an uncoupling agent that disrupts the mitochondrial membrane potential allowing the maximal consumption of oxygen, increased the OCR of WT but not of Scara5-KO BMSCs. In addition, although the basal respiration did not differ significantly between WT and Scara5-deficient cells, the maximal respiration proved to be significantly higher in WT than in Scara5-KO BMSCs (mean ± SEM, 89.533 ± 14.408 pmol/min per 1000 cells vs 54.400 ± 10.060 pmol/min per 1000 cells). Overall, these results highlighted a Scara5-KO-related mitochondrial dysfunction once cells were treated with AM.

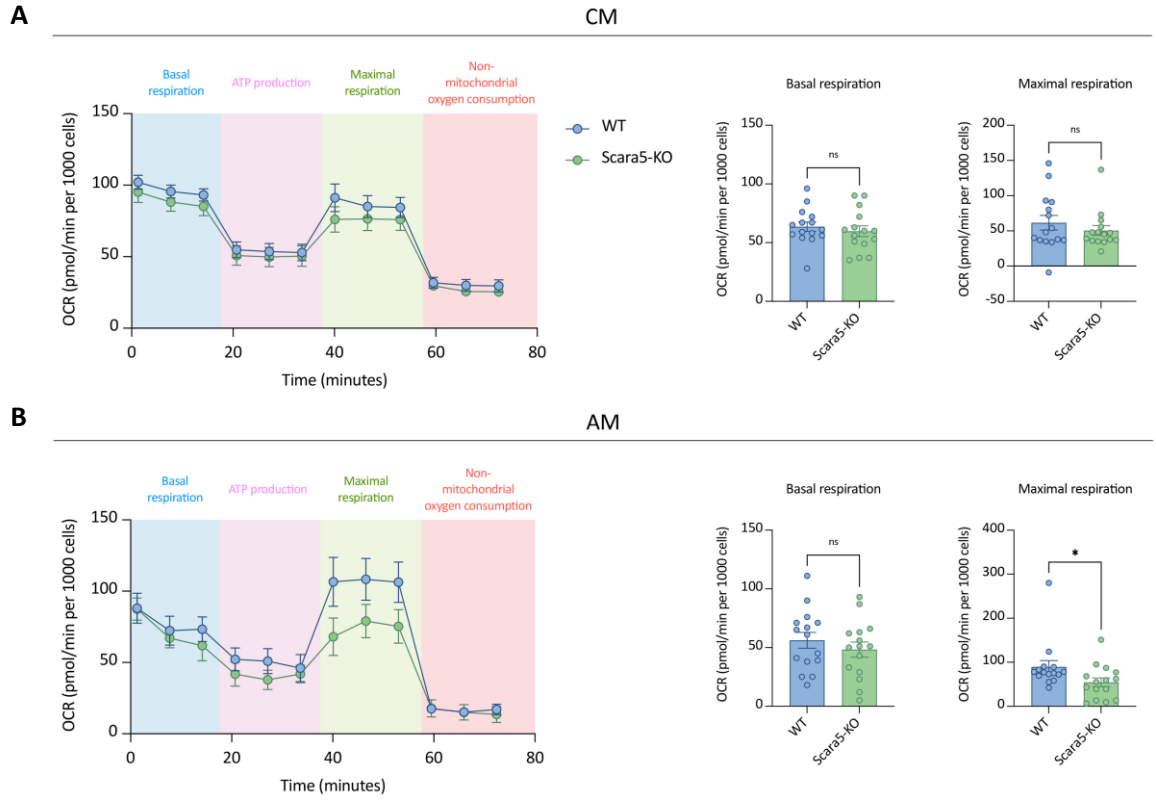


Figure 5.13 Scara5-null BMSCs exhibit a decreased OCR once AM-treated. Seahorse metabolic flux analysis of OCR in WT and Scara5-KO BMSCs treated with CM (**A**) and AM (**B**). Data on the left are depicted as kinetic profiles of different reactions, including basal respiration, ATP-linked respiration (following Oligomycin injection), maximal respiration (following FCCP injection), and non-mitochondrial respiration (following Rotenone and Antimycin A injection). Basal and maximal respiration are further represented as mean ± SEM (n=3, 5 technical replicates/n) on the right; Mann-Whitney U test was used to determine the degree of significance (^{ns} $p > 0.05$, * $p \leq 0.05$).

5.5 Discussion

MSCs differentiation into osteoblasts and adipocytes has been widely studied and debated. The osteo-adipogenic balance is crucial for bone homeostasis; indeed, bone-related pathologies, such as osteoporosis and osteopenia, are characterised by imbalanced osteoclast/osteoblast activity and an overall BMAT increase [122]. Over the years, multiple pathways and key transcription factors have been identified as implicated in the osteo-adipogenic differentiation. Among them, canonical Wnt signalling pathway, also known as Wnt/β-catenin signalling, exerts a crucial role in stimulating MSCs differentiation into osteoblasts and simultaneously inhibiting adipogenic differentiation [122]. When Wnt molecules bind to FZD and LRP5/6 coreceptors, the cytoplasmic phosphorylation of β-catenin is inhibited; therefore, unphosphorylated β-catenin translocates to the nucleus, binds to the TCF/LEF reporter, and regulates the expression of osteogenic target genes [28]. LiCl has shown to activate this pathway by inhibiting the activity of GSK3β, which is part of the cytoplasmic disruption complex. Hence, GSK3β inhibition activates Wnt/β-catenin signalling by increasing β-catenin concentration [293]. Tang *et al.* showed that LiCl promotes osteogenesis and inhibits adipogenesis of human BMSCs by regulating both Wnt and Hedgehog signalling pathways [294]. In addition, Yu and colleagues found that BMSCs derived from rats with steroid related osteonecrosis exhibited an abnormal osteo-adipogenic differentiation, which was attenuated by LiCl treatment and the consequent activation of β-catenin [296]. In this study, ALP activity was inhibited by LiCl in both WT and Scara5-KO BMSCs (**Figure 5.1**). Similarly, LiCl treatment of human stem cells isolated from exfoliated deciduous teeth did not impact on either ALP concentration or mineral deposition [295]. Furthermore, Zhu *et al.* work highlighted LiCl role in promoting human BMSCs proliferation by inhibiting GSK3β and activating Wnt/β-catenin pathway, without however stimulating cell osteogenesis [298]. Hence, LiCl does not represent a valid method to induce osteogenesis by activating Wnt/β-catenin signalling pathway.

Wnt molecules such as Wnt3a and Wnt10b have been demonstrated to bind to the ternary complex of FZD and LRP5/6 coreceptors and to activate the canonical pathway [122, 299]. On the other hand, Wnt5a has a role in the non-canonical Wnt signalling pathways (Wnt/Ca^{2+} and Wnt/PCP pathways) to promote adipogenesis via MAPK-independent pathway [300]. At the same time, Wnt5a deletion in mice calvaria osteoblasts impaired Wnt/β-catenin signalling by

reducing the expression of Lrp5/6 [301]. As a scavenger receptor, Scara5 is able to bind multiple targets and thus it was hypothesised that it may bind and internalise Wnt molecules. Consequently, Scara5 absence would favour Wnt molecules binding to FZD-Lrp5/Lrp6 and the pathway's activation. In the present work, BMSCs were treated with different concentrations of Wnt3a, Wnt5a, and Wnt10b (**Figure 5.2**). Wnt3a induced ALP activity of WT and Scara5-null cells, although the response was significantly higher in Scara5-KO cells, thus supporting the hypothesis that Scara5 deficiency increases Wnt3a availability for Wnt signalling activation. Neither Wnt5a nor Wnt10b stimulated WT/Scara5-KO BMSCs' ALP activity. It is not surprising that Wnt5a did not enhance BMSCs osteogenesis; indeed, as aforementioned, Wnt5a proved to favour adipogenesis at the expense of osteogenesis [300]. Regarding Wnt10b, it has always been positively associated with MSCs osteogenesis and bone regeneration [302-304]. Despite the lack of any published research indicating a direct impact of Wnt10b on cellular ALP concentration or activity, it remains unclear why Wnt10b did not stimulate murine BMSCs' ALP activity.

Osteogenesis is a convoluted process that requires the activation of multiple signalling pathways and transcription factors [122]. To induce osteogenic differentiation of MSCs, a cocktail of dexamethasone (Dex), ascorbic acid and β-glycerophosphate is often used. Among the other components, Dex upregulates four and a half LIM domains 2 (FHL2), which binds to β-catenin to facilitate its transport to the nucleus, thereby activating Wnt/β-catenin signalling. This action culminates with RUNX2 expression, essential for osteoblast differentiation and maturation [305]. Moreover, Dex can activate RUNX2 through β-catenin-like molecule TAZ and it can regulate its phosphorylation by increasing MAPK phosphatase expression [305]. It was therefore supposed that WT/Scara5-KO BMSCs could respond to both OM and Wnt ligands treatment by upregulating Wnt/β-catenin molecules. Axin2 is part of the cytoplasmic disruption complex and LRP signalosome [306], whereas Dvl3 plays a role in activating Wnt canonical signalling by phosphorylating LRP5/6, thus preventing cytoplasmic β-catenin degradation [307]. Additionally, Lef1 is part of the nuclear TCF/LEF reporter bound by β-catenin to mediate gene transcription [308]. RT-qPCR analysis, as well as Western blotting, showed no differences between WT and Scara5-KO BMSCs in terms of Wnt-related gene expression and β-catenin expression, respectively. Few published works have referred to Wnt3a recombinant protein treatment to activate Wnt signalling; in fact, MSCs osteogenesis

via Wnt/β-catenin signalling pathway was generally induced using Wnt3a conditioned medium produced by L-cells [136, 309]. One of the few works that use Wnt3a protein to activate Wnt pathway showed that HEK293T cells responded to 200 ng/ml of Wnt3a recombinant protein by increasing total β-catenin expression after 24 hours [310]. In the present work, 200 ng/ml did not induce β-catenin expression (**Figure 5.5**). It remains unknown whether a lower concentration of Wnt3a or a Wnt3a conditioned medium would have produced different results, although WT and Scara5-KO BMSCs treated with 100 ng/ml of Wnt3a expressed similar levels of Wnt-related genes.

Overall, Wnt3a treatment was able to increase ALP activity more in Scara5-null than in WT BMSCs; however, RT-qPCR and WB analysis did not confirm any difference between WT and Scara5-KO cells' expression of Wnt-related molecules. It can be assumed that the Wnt3a-stimulated ALP activity relies in the higher ability of Scara5-KO BMSCs to differentiate to osteoblasts instead of a hyper-activation of Wnt/β-catenin pathway. This can be confirmed by the fact that Wnt3a also proved to increase WT BMSCs' pNP concentration.

It is well established that AKT-related pathways play a role in cell proliferation and osteo-adipogenic differentiation of MSCs [291, 311]. For example, platelet-derived growth factor-BB (PDGF-BB) demonstrated to stimulate MSCs proliferation via PI3K/AKT and mTOR pathways activation; on the other hand, PDGF-BB binding to the PDGF receptor beta activated MEK and ERK1/2, which inhibited the expression of PPARγ and CEBPα, thereby blocking MSCs adipogenic differentiation [30]. This chapter showed that WT/Scara5-KO BMSCs responded to OM and AM treatments by phosphorylating several proteins included in the AKT phosphorylation array (**Figure 5.7**, **Figure 5.8**). Among the changes detected, OM stimulated the phosphorylation of RPS6 and RSK1 expression more in Scara5-KO than in WT BMSCs, whilst AM induced the phosphorylation of those proteins more in WT than in Scara5-KO BMSCs. RSK1 proved to phosphorylate RPS6 at S235/236 *in vitro/in vivo* though an mTOR-independent mechanism, inducing protein translation [312]. To date, MSCs osteogenesis has not been correlated with either RPS6 or RSK1 activation. On the contrary, RPS6 has been linked to the RPS6/ERK signalling cascade during adipogenesis; indeed, Ning *et al.* proved that quinine regulated adipogenesis in murine preadipocytes by activating ERK and consequently RPS6 [313]. Once a ligand such as insulin or growth factors binds to the tyrosine-kinase receptors, the activation of RAS and RAF induces a phosphorylation cascade which culminates

with the phosphorylation of MEK and ERK1/2. It has been shown that MEK/ERK signalling is extensively activated during adipogenesis of 3T3-L1 preadipocytes, mainly due to the insulin component of the adipogenic cocktail [119]. Activation of MEK/ERK pathway promoted adipogenesis by regulating PPARγ and C/EBPα expression [119]. The AKT phosphorylation array showed that AM stimulated the phosphorylation of RAF-1, RPS6, and RSK1, but not ERK 1/2, in WT more than Scara5-null cells (**Figure 5.8**); however, western blot analysis of three different biological samples did not confirm these results (**Figure 5.9**). It was therefore concluded that Scara5 deficiency did not impact on AKT-related signalling pathways.

Scara5 functions as a ferritin receptor; Yu *et al.* outlined Scara5 capacity to recognise and bind both light (L) and heavy (H) chains of ferritin through the cysteine rich domain (CRD) [167]. Indeed, the removal of the CRD abolished Scara5 ability to bind to L-/H-ferritin [167]. Serum ferritin mostly exists as L-ferritin and preferentially binds to Scara5, whereas H-ferritin binds to transferrin (Tf) receptor 1, TIM 2, and Scara5 [167, 214]. Iron can enter the cell as ferritin and as Tf, the main circulating form of iron, but Scara5 can only internalise iron in the form of ferritin. It can be speculated that the absence of Scara5 reduces the internalisation of L-ferritin, thus causing an intracellular mild iron deficiency (**Figure 5.14**). Oesophageal squamous cell carcinomas (ESCC) cells, as well as other cancer cell lines, expressed lower levels of Scara5. Liu and colleagues overexpressed Scara5 in ESCC cells, thus increasing intracellular iron levels and inducing ferroptosis, a regulated cell death mechanism dependent on iron [215]. Since Scara5 was found abundantly in the renal capsule, where it was described to bind and internalise L-ferritin [213], the present work analysed iron content in murine testis and kidneys. The results outlined a reduced iron content in Scara5-KO kidneys, thus highlighting a potential mild iron deficiency (**Figure 5.10**). Iron content of testis did not show a significant difference between WT and Scara5-KO mice; however, the concentration of iron in the testis was low and did not exceed 0.1 μmol/mg in testis and a greater number of samples may be needed, while iron content was equal to/above of 1 μmol/mg in murine kidneys.

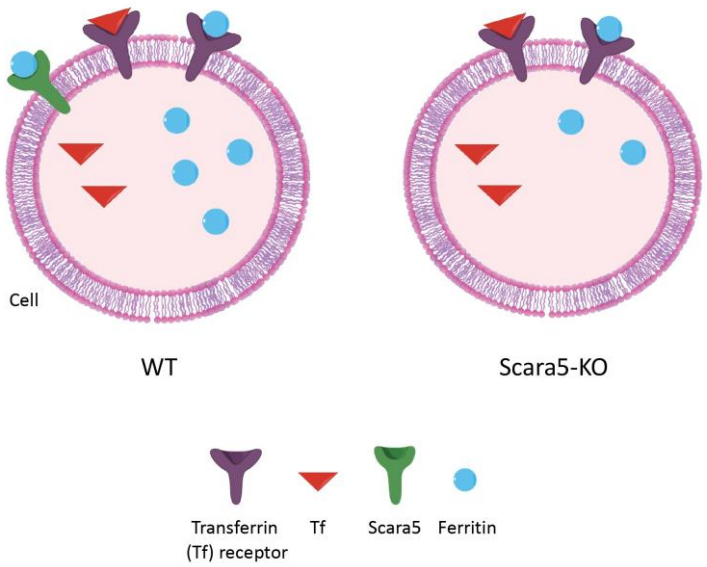


Figure 5.14 Mild iron deficiency hypothesis. Cells internalise iron in form of Tf and ferritin; Tf can be endocytosed via Tf receptor only, whilst ferritin can enter the cell via Tf receptor and Scara5, although it preferentially binds Scara5. It can therefore be hypothesised that Scara5-KO cells display a mild iron deficiency.

Iron serves as a cofactor for metabolic enzymes, the electron transport chain, and the synthesis of adenosine triphosphate (ATP), thereby contributing to energy metabolism. Perturbations in iron homeostasis reflect on cell metabolism; Oexle *et al.* firstly described the impact of iron perturbation on glycolysis, OXPHOS, and citric acid cycle [148]. DFO-induced iron deficiency diminished the activity of citric acid cycle enzymes in the human lymphoblast cell line K-562, thus causing a reduced formation of NADH. Low levels of NADH decreased mitochondrial ATP production and oxygen consumption (OXPHOS); consequently, glucose utilisation and lactate accumulation increased, thereby boosting ATP production through glycolysis [148]. Osteoblast differentiation and bone formation are strictly dependent on glycolysis to produce ATP; glucose represents a source of rapid energy production, ideal for cells that must respond quickly to bone fractures [158, 159]. In addition, Zhao *et al.* proved that low doses of DFO promoted ALP activity in human fetal osteoblast (hFOB 1.19), thus supporting the notion of a positive effect of mild iron deficiency on osteogenesis [163]. Nevertheless, WT and Scara5-KO BMSCs treated with OM for 7 days did not differ in the expression of glycolysis-related genes, i.e. HK2 and PKM (**Figure 5.11**). In contrast, the expression of OXPHOS/fatty acid oxidation (FAO)-related genes (i.e. Glut4, Fsp27, Hsl, MGL, PPARα) was much higher in WT than in Scara5-KO BMSCs treated with AM (**Figure 5.12**).

Tencerova *et al.* showed that murine BMSCs treated with adipogenic cocktail expressed the aforementioned genes as a consequence of the metabolic swich from glycolysis to OXPHOS [156]. Indeed, mitochondrial activity analysis revealed that committed adipocytic progenitor's energy production was mainly dependent on OXPHOS [156]. In the present work, the Mito stress test was employed to measure the mitochondrial respiration of AM-treated BMSCs. Scara5-null cells did not respond to the FCCP injection as much as WT BMSCs (**Figure 5.13**); the uncoupler FCCP mimics a physiological energy demand, thereby stimulating the respiratory chain to work at maximum capacity and to rapidly oxidate sugars, fats, and amino acids. Maximal respiration was statistically different between WT and Scara5-KO cells (**Figure 5.13**), consequently proving that Scara5 absence perturbs the metabolic state of BMSCs, possibly due to the mild iron deficiency (**Figure 5.15**). This is not surprising, since other cell models linked the intracellular iron deficiency showed reduced mitochondrial activity. For example, DFO treatment caused a metabolic shift to glycolysis in human induced pluripotent stem cell-derived cardiomyocytes [314]; in particular, Seahorse analysis highlighted a reduced mitochondrial respiratory activity in response to FCCP, corroborating the detrimental effect of iron deficiency on mitochondrial function [314]. Similarly, Fujisawa *et al.* demonstrated that increasing concentrations of DFO suppressed HeLa cells proliferation and reduced OCR [315].

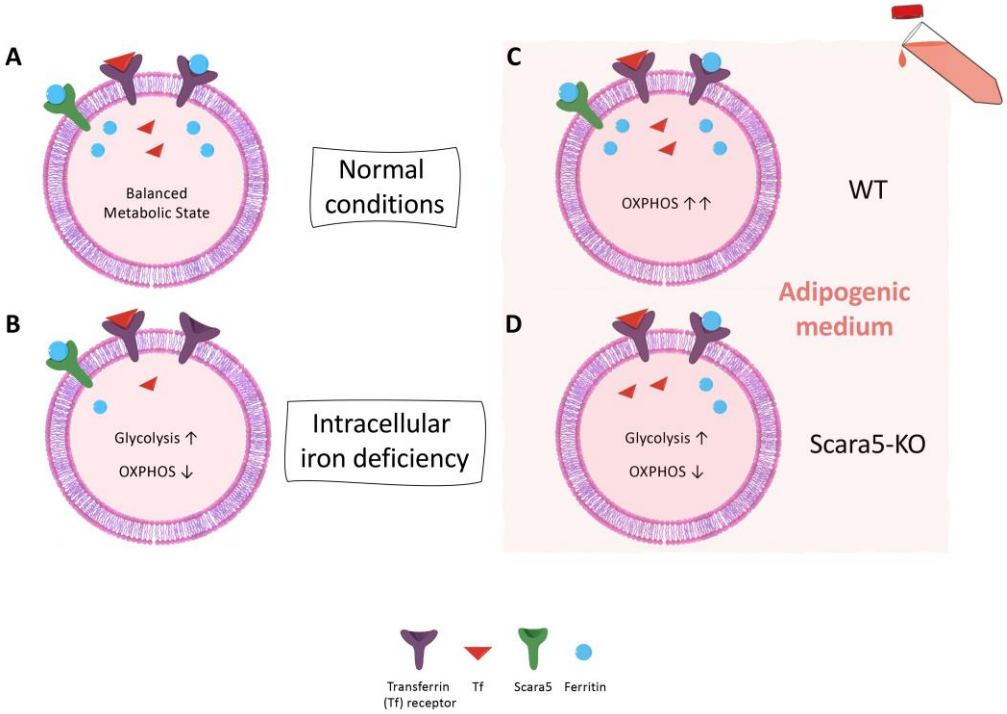


Figure 5.15 Scara5 hypothetic mechanism of action. In normal conditions, the cell is in a balanced

metabolic state (**A**). Intracellular iron deficiency perturbs the metabolic state, thereby inducing the cell to rely on glycolysis instead of OXPHOS for energy production (**B**). In the presence of adipogenic stimuli, WT BMSCs produce energy through OXPHOS to differentiate into adipocytes (**C**). The absence of Scara5, and the consequent iron deficiency, impairs the cell ability to produce ATP via OXPHOS and to properly differentiate into adipocytes (**D**).

To sum up, this chapter provided insights into the mechanism by which Scara5 deficiency alters cellular differentiation potential, exploring the osteo-adipogenic pathways as well as cellular metabolism. Scara5 deficiency did not affect known osteogenesis- or adipogenesis-related pathways (i.e. canonical Wnt signalling and AKT-related pathways). Scara5 works as a ferritin receptor, therefore regulating intracellular iron content; in fact, Scara5 absence impacted on iron content of murine kidneys. Due to the crucial role of iron as a co-factor for most mitochondrial enzymes, iron deficiency proven to undermine preadipocyte cells adipogenic differentiation in Suzuki and colleagues work [164]. Consistently, Scara5-null BMSCs mitochondrial activity resulted impaired in the presence of adipogenic stimuli. Taken together, the findings presented related Scara5 deficiency to a mild iron deficiency, which can be considered as a cause of the perturbation of the cellular metabolic functions. Alongside work undertaken on BMSCs and other cell types, iron deficiency has been shown to impact negatively on breast cancer cell growth and proliferation [316]. Since Scara5 deletion was linked to a reduced fat deposition and a mild iron deficiency, the next chapter will investigate whether the pathogenesis of breast cancer in a murine model where tumour cells are injected into the mammary fat pad differs between WT and Scara5-KO mice.

Chapter 6: Scara5 deficiency influences breast cancer pathogenesis

6.1 Introduction

In recent years, Scara5 has been closely associated with several types of cancer. Yan and colleagues ascertained Scara5 downregulation in 11 human cancer cell lines such as, inter alia, glioma cells (i.e. U251, U87), breast carcinoma cells (i.e. MDA-MB-231, MDA-MB-435s), and prostate cancer cells DU145 [221]. In work by You *et al.*, the human breast cancer (BrCa) cell line ZR-75-30 expressed low levels of Scara5; following Scara5 overexpression, these cells showed a reduced proliferation, migration, and metastatic potential [170]. Moreover, Scara5 was reported as downregulated in human breast cancer tissues, while normally expressed in the para-cancerous ones; its down-regulation was associated with greater tumour's size, higher histological grade, and ability to metastasise to lymph nodes [170].

The BrCa tumour microenvironment (TME) consists of local factors, cancer cells, immune cells, and stromal cells; TME is crucial for BrCa cells proliferation and response to therapies [317]. As part of the TME's stromal cells, adipocytes play a fundamental role in BrCa progression. Indeed, adipocytes' release of immunomodulatory factors and free-fatty acids can fuel cell proliferation, thereby influencing the fate of cancer development [318]. Furthermore, dysfunctional obese adipose tissue proved to secrete high levels of anti- and pro-inflammatory cytokines; the derived cytokine storm has been described as responsible for initiation and progression of BrCa [319]. Tumour development is intimately connected with iron metabolism. It is well recognised that tumour cells require a certain amount of iron for their proliferation and survival, since the DNA replication process is strictly dependent on iron, as well as numerous metabolic pathways [320]. In addition, Zhang *et al.* demonstrated that DFO-induced iron deficiency reduced BrCa growth in mouse models by impairing the hepcidin–ferroportin signalling [321].

Adipose tissue represents the ideal energy resource; in fact, its free fatty acids can be used by cancer cells as metabolites and the iron released by iron-enriched cells (e.g. macrophages) can support their proliferation [318]. The previous chapters shown that Scara5-deficiency impairs fat deposition in mice together with iron content. This chapter will highlight the

importance of WT and Scara5-KO mice's genetic background on BrCa development, considering iron as the key element.

6.2 BRPKp110-based BrCa develops similarly between WT and Scara5-KO mice

Murine BRPKp110 breast cancer cells were firstly generated by mechanical dissociation of C57BL/6 L-Stop-L-*KRas*^{G12D}*p53*$^{flx/flx}$L-Stop-L-*Myristoylated p110α*–GFP/+ primary breast tumour mass, which resembles a poorly metastatic luminal A-like BrCa [322, 323]. BRPKp110 were employed in the present work to be orthotopically injected into the fat pad and therefore to generate tumour masses that were subsequently analysed to determine whether the Scara5 TME has a role in BrCa pathogenesis.

6.2.1 Tumour volume does not differ between Scara5-WT and -KO mice after 21 days

WT and Scara5-KO mice underwent surgery for the orthotopic injection of BRPKp110 tumour cells into the left inguinal fat pad. As displayed in **Figure 6.1 A**, tumours developed after 10 days and their volume was periodically measured to monitor their growth. After 10, 14, 16, and 18 days post-injection, WT mice presented significant bigger tumours if compared with Scara5-KO mice (**Figure 6.1 B**). At the end of the experiment, after 21 days from cells' injection, the multilobate tumours were excised and measured by a digital caliper (**Figure 6.1 C**). Tumour volume did not differ between WT and Scara5-KO mice (mean ± SD, 736.111 ± 313.230 mm^3 vs 754.464 ± 400.113 mm^3), as well as tumour weight (0.564 ± 0.112 g vs 0.613 ± 0.268 g), indicating that Scara5 absence did not influence the last stages of BRPKp110-based BrCa development.

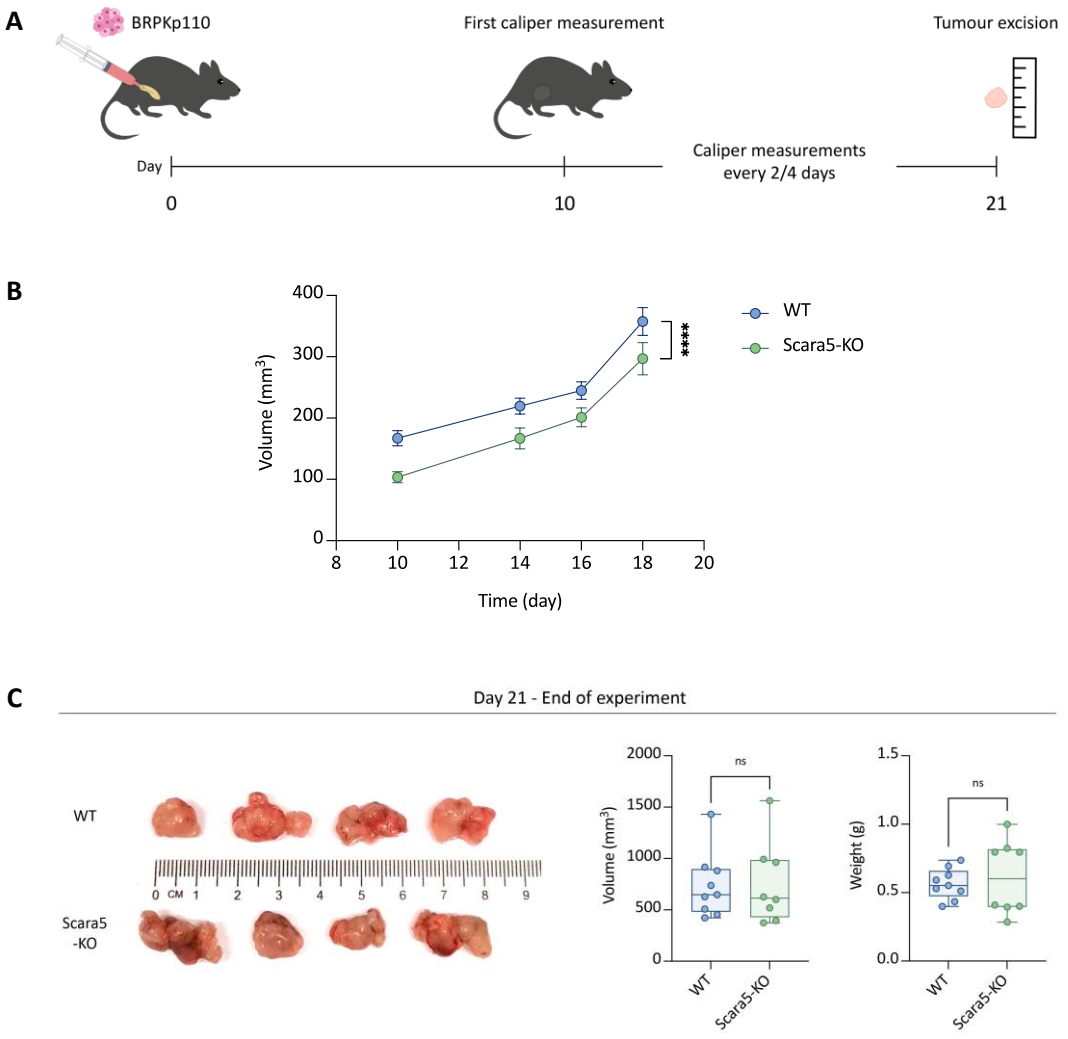


Figure 6.1 BRPKp110-based BrCa growth does not differ between WT and Scara5-KO mice. Timeline of BrCa experiment; 5 x 10^5 BRPKp110 cells were orthotopically injected into the left mammary fat pad and the tumours' volume was periodically measured from day 10 to day 21, when the tumour was excised and measured (**A**). External caliper measurements of live mice's tumours; data are presented as regression lines (WT n=9, Scara5-KO n=8) and simple linear regression analysis was used to determine the degree of significance (**** $p < 0.0001$) (**B**). Representative image of WT and Scara5-KO tumours; tumours' volume and weight were determined 21 days post-BRPKp110 injection and shown as box plots (WT n=9, Scara5-KO n=8); Mann-Whitney U test was used to determine the degree of significance (^{ns} $p > 0.05$) (**C**).

6.2.2 Tumour cell morphology, but not inflammatory marker expression, show a different pattern between WT and Scara5-null mice

As a response to cancer development, immune myeloid and lymphoid cells (e.g. macrophages, T cells) infiltrate the tumour [324]. Therefore, the tumours excised from WT and Scara5-KO mice did not contain breast cancer cells only; H&E staining indeed showed diverse types of cells within the cancerous masses, as depicted in **Figure 6.2 A**. While WT tumour cells appeared to follow a diagonal organisational pattern, Scara5-KO tumour cells seemed haphazardly positioned, lacking any semblance of order. In addition, Scara5-KO mice's tumours were invaded by a few adipocytes (**Figure 6.2 A**). Nevertheless, the expression of the most common inflammatory markers proved similar between WT and Scara5-KO mice's tumours (**Figure 6.2 B**), suggesting that cytokine expression was independent of mouse genetic background, thus independent of Scara5 deficiency.

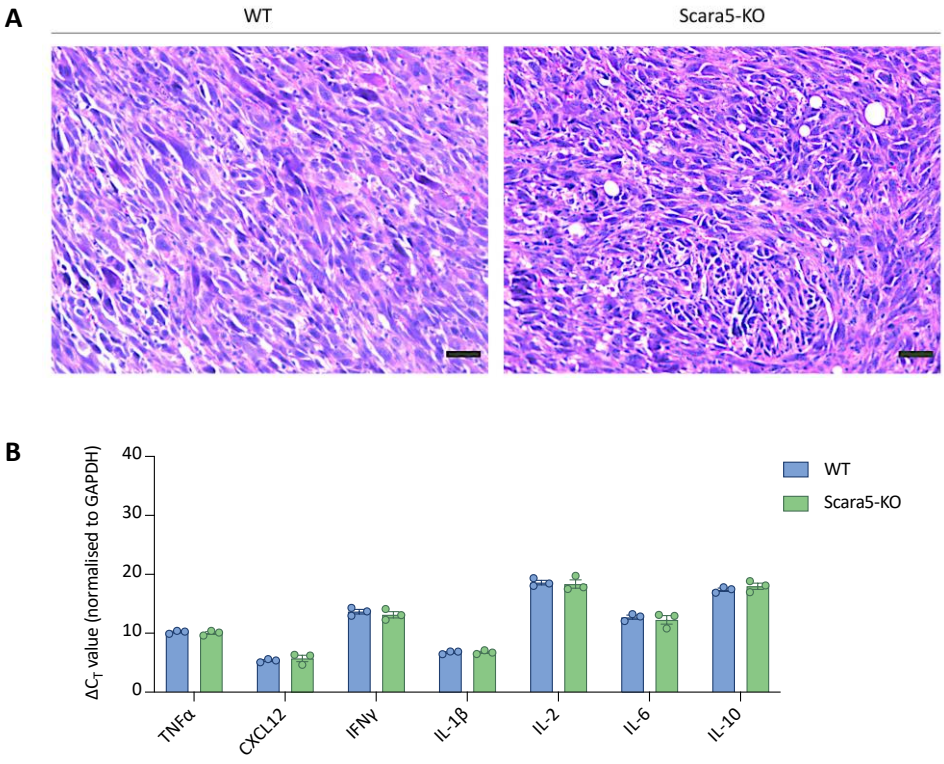


Figure 6.2 H&E staining, but not inflammatory genes' expression, reveals slight differences between WT and Scara5-KO tumours. Representative images of H&E-stained WT and Scara5-KO BRPKp110-based tumours (20x bright field, 50 μm scale bar) (n=4); white "bubbles" indicate adipocytes' ghosts (**A**). WT and Scara5-KO tumours were digested to obtain RNA and inflammatory markers' expression was assessed by RT-qPCR. $2^{-\Delta\Delta CT}$ method was applied and gene expression was normalised to GAPDH;

data are depicted as mean ± SEM (n=3) (**B**).

6.3 Scara5 expression is downregulated in murine BrCa cell lines

As previously stated in this chapter, Scara5 has been described as downregulated in various tumour cell lines [221]; due to the results obtained from the BrCa experiment, Scara5 expression was evaluated in BRPKp110 cells. As depicted in **Figure 6.3**, the osteoblast cell line 2T3 was used as control, since it expressed high levels of Scara5; on the other hand, BRPKp110 expressed lower levels of Scara5. Scara5 gene expression was therefore assessed in other murine BrCa cell lines, i.e. PyMT-BO5, E0771, and 4T1; among them, PyMT-BO5 and E0771 cells expressed the lowest levels of Scara5, equal to or below 0.02 (mean, fold change).

PyMT-BO5 is a primary mammary tumour cell line obtained by culturing a mechanically dissociated primary breast tumour mass spontaneously arisen at day 120 in a C57BL/6 background MMTV-PyMT mouse; the tumour cells are able to generate a tumour that resembles an antioestrogen-sensitive luminal B BrCa [325]. Hence, WT and Scara5-null BrCa models were generated using PyMT-BO5 cells.

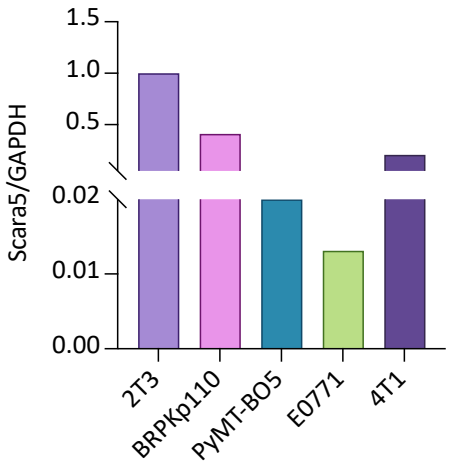


Figure 6.3 BrCa cell lines express low levels of Scara5. BrCa cell lines were analysed via RT-qPCR for Scara5-expression. $2^{-\Delta\Delta CT}$ method was applied and Scara5 expression was normalised to GAPDH; data of a single experiment are presented as mean, in terms of fold change; 2T3 cells were used as endogenous control.

6.4 PyMT-BO5-based BrCa develops differently between WT and Scara5-KO mice

PyMT-BO5 cells were orthotopically injected into the fat pad of adult WT and Scara5-KO mice; since PyMT-BO5 represents a more aggressive BrCa cell line [326], the experiment was carried out for 15 days only, at the end of which tumours were excised and analysed.

6.4.1 Scara5-KO mice develop smaller tumours than WT mice after 15 days

PyMT-BO5 cells were orthotopically injected into WT and Scara5-KO's fat pad. **Figure 6.4 A** illustrates the time course of the experiment; tumours were externally measured twice from day 10 and the mice were sacrificed 15 days post-BO5 injection, when the cancerous masses were excised. The experiment was repeated twice, using 18 WT female mice and 15 Scara5-KO females in total. During the first experiment, due to the small size of the tumours, their volumes measured 10 and 13 days post-injection were not precise and one animal/group was thought not to have developed any mass. In addition, WT and Scara5-KO mice's tumours were comparable in terms of volume (**Figure 6.4 B**). In contrast, the second experiment showed that both 10 and 13 days after BO5 injection WT mice develop bigger tumours than Scara5-KO counterparts (mean ± SD, day 10 WT 164.110 ± 44.460 mm^3, Scara5-KO 103.728 ± 44.231 mm^3; day 13 WT 235.540 ± 41.543 mm^3, Scara5-KO 186.527 ± 35.670 mm^3) (**Figure 6.4 B**). When tumours were excised, solely the first experiment showed that WT females presented significantly larger tumour volumes than Scara5-KO counterpart (1st experiment – mean ± SD, 237.886 ± 114.694 mm^3 vs 121.472 ± 52.840 ± mm^3; 2nd experiment, 1038.016 ± 650.939 ± mm^3 vs 510.121 ± 161.357 mm^3). Furthermore, although the tumour weight did not differ between WT and Scara5-null mice in the 1st experiment, the 2nd experiment proved that tumour weight was greater in WT than in Scara5-KO mice (mean ± SD, 0.760 ± 0.270 g vs 0.537 ± 0.082 g) (**Figure 6.4 C**). As depicted in **Figure 6.4 C**, it is also noticeable that BO5 cells develop smaller and single masses in the 1st experiment, while they formed multilobate tumours in the 2nd experiment.

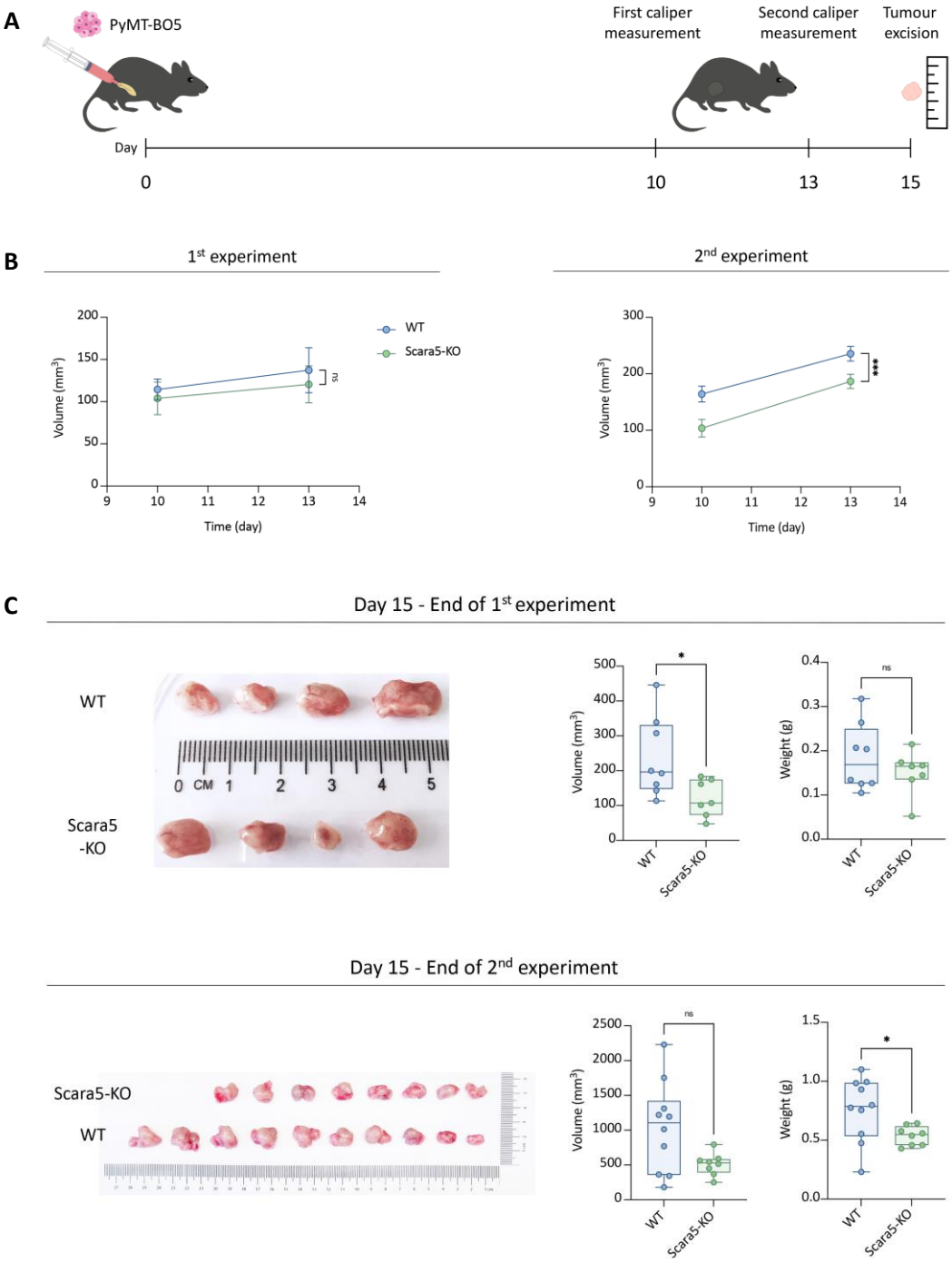


Figure 6.4 PyMT-BO5-based BrCa growth differs between WT and Scara5-KO mice. Timeline of BrCa experiment; 1 x 10^5 BRPKp110 cells were orthotopically injected into the left mammary fat pad and the tumours' volume was determined twice from day 10 to day 15, when the tumour was excised and measured (**A**). External caliper measurements of tumours in live mice; 2 experiments' data are presented as regression lines (1st experiment WT n=7, Scara5-KO n=6; 2nd experiment WT n=10, Scara5-KO n=8); simple linear regression analysis was used to determine the degree of significance (ns $p > 0.05$, *** $p < 0.001$) (**B**). Representative images of WT and Scara5-KO tumours from both 1st and 2nd experiment; tumours' volume and weight were assessed 15 days post-PyMT-BO5 injection and

depicted as box plots (1st experiment WT n=8, Scara5-KO n=7; 2nd experiment WT n=10, Scara5-KO n=8). Mann-Whitney U test assessed the degree of significance (ns $p > 0.05$, * $p \leq 0.05$) (**C**).

6.4.2 Tumour cell morphology and inflammatory marker expression exhibit similar patterns between WT and Scara5-null mice

After their excision, WT and Scara5-KO mice's tumours were stained with H&E to highlight any difference in terms of cell morphology. As shown in **Figure 6.5 A**, stained tissues were similar in terms of organisational pattern; adipocytes equally infiltrated WT and Scara5 BO5 masses. Moreover, the expression of inflammatory markers was analogous between WT and Scara5-KO tumours, proving that the cytokine expression was not affected by Scara5 absence (**Figure 6.5 B**).

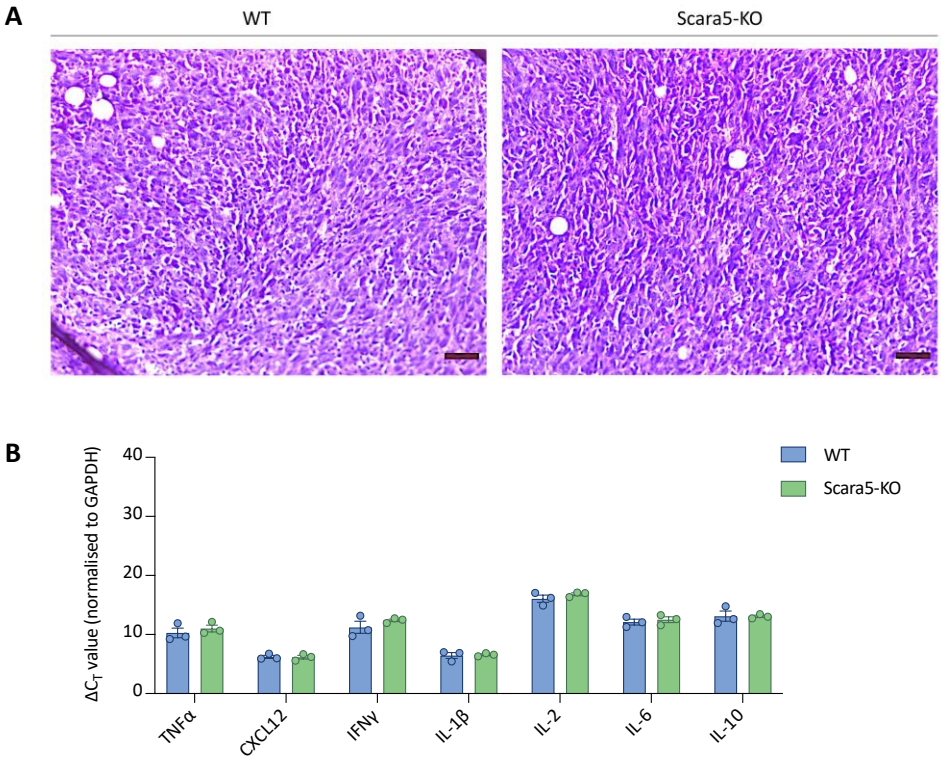


Figure 6.5 Scara5-WT and -KO tumours display similar H&E staining and inflammatory markers' expression. H&E-stained WT and Scara5-KO BO5-based tumours (20x bright field, 50 μm scale bar); the images are representative of two experiments performed independently (N=2). White "bubbles" indicate adipocytes' ghosts (**A**). WT and Scara5-KO tumours underwent RT-qPCR analysis for inflammatory markers' expression. $2^{-\Delta\Delta CT}$ method was applied and gene expression was normalised to GAPDH; data are depicted as mean ± SEM (n=3) (**B**).

6.5 Scara5 deficiency impacts on adipose tissue-BO5 cells crosstalk

Since PyMT-BO5 were injected into the fat pad of WT and Scara5-KO mice, the crosstalk between cancer cells and adipose tissue was favoured, hence increasing tumour growth [327]. To mimic BO5-fat crosstalk *in vitro*, murine iFAT was fragmented and incubated in serum-free CM for 24 hours; in parallel, WT and Scara5-KO iFAT fragments were also added to serum-free CM in the presence of PyMT-BO5 cells (**Figure 6.6**). The obtained WT and Scara5-KO supernatants (Sn) were used on BO5 cells, to test their effect on cell adhesion and proliferation.

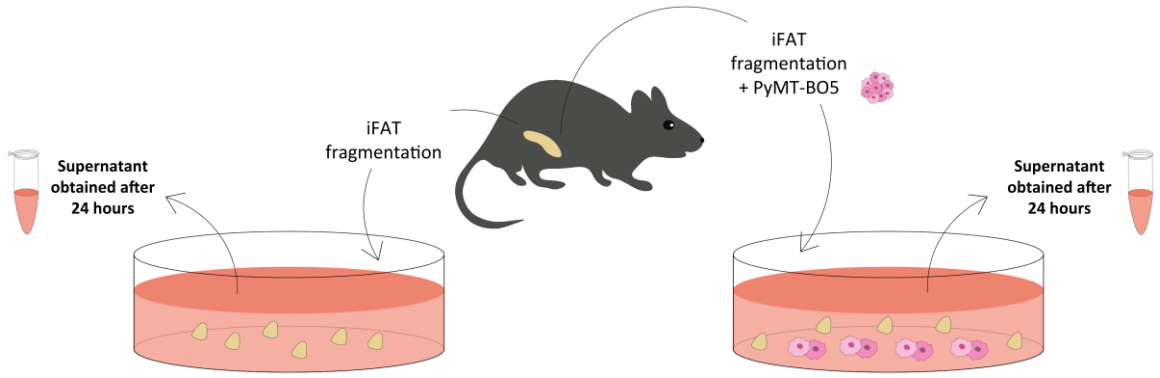


Figure 6.6 WT and Scara5-KO iFAT pads are processed to obtain supernatant. iFAT pads from WT and Scara5-KO mice were fragmented and included in FBS-free CM with or without cultivated BO5 cells. Supernatants were collected after 24 hours, centrifuged, and filtered before being used for subsequent experiments.

6.5.1 WT and Scara5-KO iFAT supernatants equally influence BO5 cell adhesion

Cell adhesion is a critical part of malignant transformation and cancer progression [328]. WT and Scara5-KO Sn were added to PyMT-BO5 cells for 45 minutes, at the end of which cells were stained with crystal violet. The analysis of the percentage of area occupied by adhered cells revealed that WT and Scara5-KO iFAT Sn adhesion was comparable with the control treatment (FBS-free CM) (**Figure 6.7 A**). Indeed, while FBS-free CM occupied 21.960 ± 1.180% (mean ± SEM) of the total area available, WT and Scara5-KO filled 23.547 ± 2.052% and 26.076 ± 1.520% of the area, respectively. However, the differences between WT and Scara5-KO Sn's effect were not statistically significant. An analogous effect was obtained by treating BO5 cells

with the Sn obtained from the iFAT and BO5 co-culture (**Figure 6.7 B**). Thus, Sn's influence on BO5 cells adhesion was independent of Scara5.

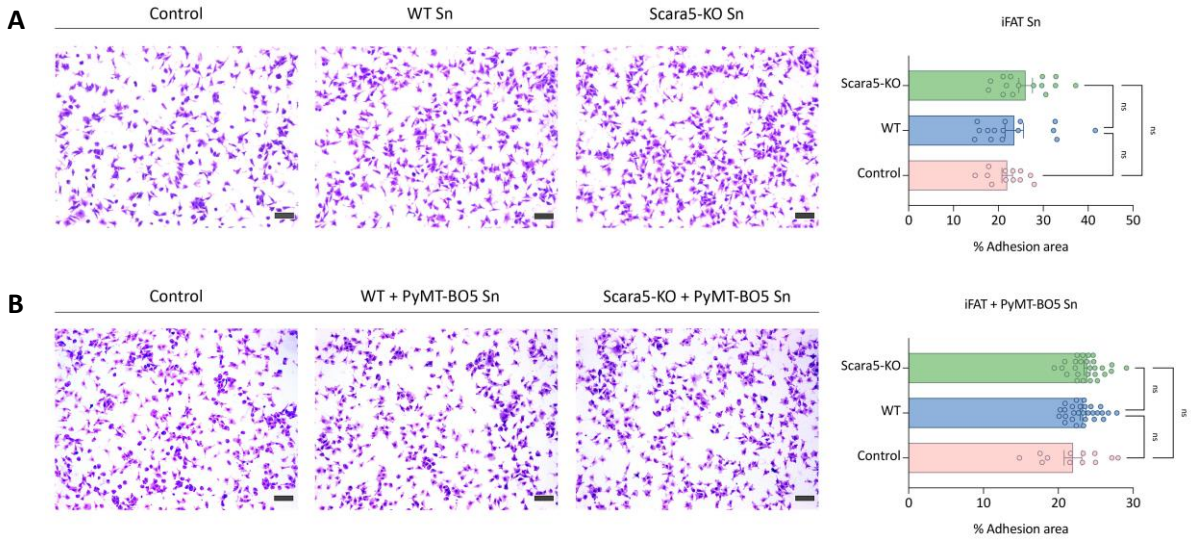


Figure 6.7 BO5 cell adhesion is not influenced by WT/Scara5-KO iFAT supernatants. Representative images of crystal violet-stained BO5 cells, treated with FBS-free CM (control), WT and Scara5-KO iFAT supernatant (Sn) (10x bright field, 100 μm scale bar); graph's bars depict mean ± SEM (n=5, >3 technical replicates/n) (**A**). Representative images of crystal violet-stained BO5 cells, treated with WT and Scara5-KO iFAT and BO5 cells Sn; FBS-free CM was used as control and data are represented as mean ± SEM (n=5) (**B**). One-way ANOVA test with Tukey's post hoc analysis was used to determine the degree of significance (^{ns} $p > 0.05$).

6.5.2 WT and Scara5-KO iFAT supernatants differently stimulate BO5 cell proliferation

As well as cell adhesion, PyMT-BO5 cell proliferation was determined after cells were treated with either iFAT Sn or iFAT-BO5 co-culture Sn. As displayed in **Figure 6.8 A**, both WT and Scara5-deficient iFAT Sn promoted BO5 proliferation after 1 and 3 days; however, WT iFAT Sn increased BO5 cells' proliferation more than Scara5-KO counterpart after 3 days only (mean ± SEM, 149.383 ± 3.488% vs 123.766 ± 6.774%). Similarly, the Sn obtained by co-culturing iFAT fragments and PyMT-BO5 cells stimulated BO5 proliferation after both 1 and 3 days (**Figure 6.8 B**). In particular, after 3 days, BO5 cells proliferated significantly more once cells were treated with WT than with Scara5-null Sn (mean ± SEM, 170.148 ± 11.754% vs 128.372 ± 5.557). Overall, Sn effect on cancer cell proliferation seemed to be influenced by Scara5 deficiency.

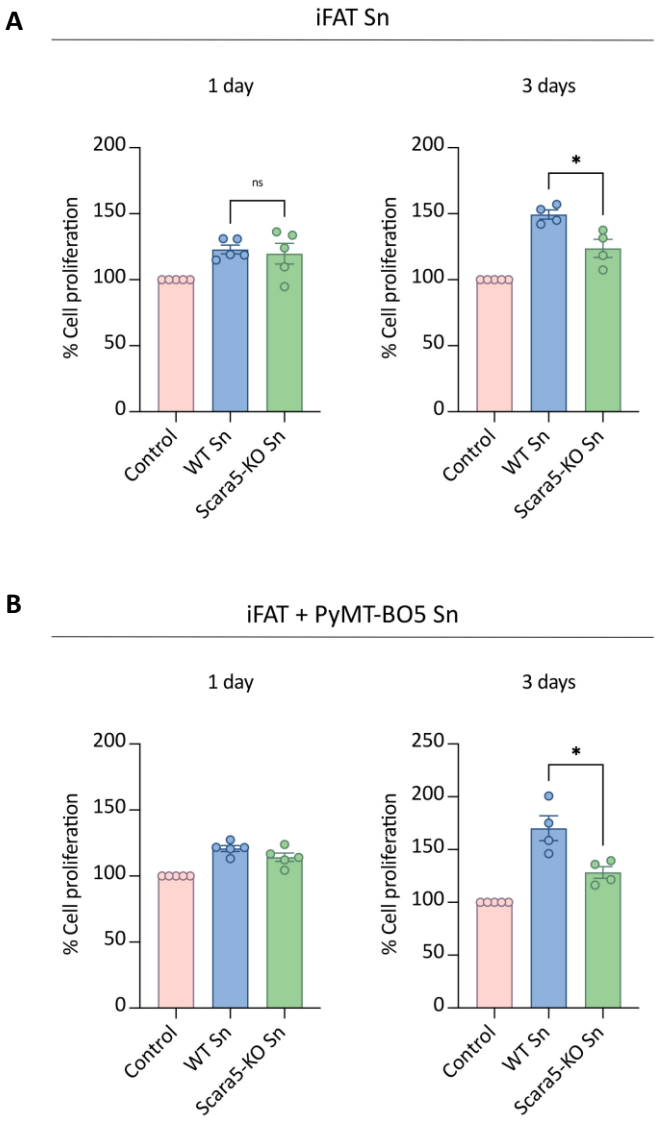


Figure 6.8 BO5 cell proliferation is stimulated more by WT than Scara5-KO iFAT/iFAT and BO5 supernatants. BO5 cells were treated with WT/Scara5-KO iFAT Sn (**A**) or iFAT and BO5 Sn (**B**), and their proliferation was assessed by MTT assay after 1 and 3 days. Data are depicted as mean ± SEM (n≥4) and FBS-free CM was used as control; unpaired two-tailed Student's t-test was used to determine the degree of significance (* $p \leq 0.05$) (**B**).

6.6 Iron as a key factor for Scara5-WT/-KO BrCa pathogenesis

As aforementioned, iron can be released by iron-enriched cells present in the adipose tissue, such as macrophages and lymphocytes; this element is fundamental for BrCa cells duplication and proliferation [318]. Due to the primary role of Scara5 as a ferritin receptor, iron content was measured in WT/Scara5-KO mice's tumours and the contralateral fat pad (not injected with BO5 cells).

6.6.1 DFO impairs the effect of WT more than Scara5-KO iFAT supernatant on BO5 cell proliferation

WT iFAT and iFAT-BO5 co-culture Sn proved to stimulate BO5 cells proliferation more than the Scara5-KO counterparts. Due to the established role of iron as a tumour growth stimulant, different concentrations of the iron chelator DFO were added to WT and Scara5-KO Sn to determine whether iron played a role in the proliferation of BO5. As displayed in **Figure 6.9 A**, 90-300 μM DFO had a considerable impact on BO5 proliferation, diminishing the initial stimulation of WT iFAT Sn. Specifically, 90 μM of DFO significantly diminished cell proliferation by 24%, 180 μM by 37%, and 300 μM by 73%. On the other hand, Scara5-KO iFAT Sn did not impact on cancer cells' proliferation; 300 μM was the only concentration of DFO that decreased the proliferation of BO5 cells by 21%. WT and Scara5-null iFAT and BO5 Sn showed similar results (**Figure 6.9 B**); however, only the highest concentration of DFO significantly reduced the proliferation of cells treated with WT Sn (mean ± SEM, Sn 161.434 ± 5.404%, Sn + 300 μM DFO 95.186 ± 5.257%). Even Scara5-KO Sn effect was affected by 300 μM DFO, but not significantly (mean ± SEM, Sn 127.432 ± 9.954%, Sn + 300 μM DFO 91.826 ± 3.858%). It can therefore be concluded that BO5 cell proliferation was more affected by DFO addition to WT Sn.

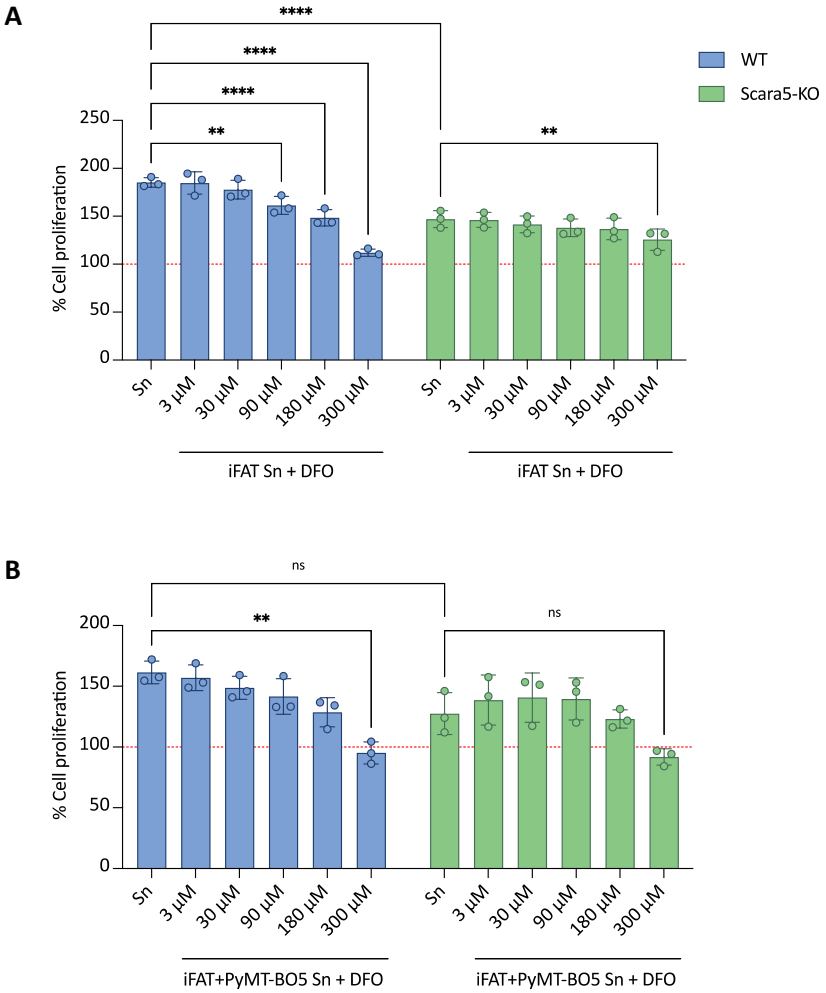


Figure 6.9 DFO undermines BO5 cells' proliferation once added to iFAT supernatants. MTT assay was performed on BO5 cells after 3 days of treatment with WT and Scara5-KO iFAT (**A**) and iFAT and BO5 cells' supernatants (Sn) (**B**) with or without DFO. Data are depicted as mean ± SEM (n=3) and expressed as percentage of the control, represented by BO5 treated with FBS-free CM (graphs' red lines). Two-way ANOVA with Tukey's post-hoc test was used to determine the degree of significance (^{ns} $p > 0.05$, ** $p < 0.01$, **** $p < 0.0001$).

6.6.2 WT and Scara5-KO tumours display different iron content

As above-mentioned, BO5 cells were injected into WT and Scara5-KO mammary iFAT. **Figure 6.10 A** shows that iron content was much lower in Scara5-KO than in WT tumours, as indicated by Potassium Ferrocyanide (blue) staining. As depicted in **Figure 6.10 B**, iron content was determined in the contralateral iFAT (the right fat pad, contralateral to the one injected with BO5 cells), as well as in tumours. The results showed that the WT contralateral fat pads contained slightly higher concentrations of iron than Scara5-KO counterparts (mean ± SD,

0.648 ± 0.221 μmol/mg vs 0.563 ± 0.239 μmol/mg); however, the difference was not statistically significant. On the other hand, Scara5-deficient tumours displayed a significantly lower content of iron if compared with WT tumours (mean ± SD, 0.651 ± 0.030 μmol/mg vs 0.731 ± 0.013 μmol/mg). Overall, Scara5-KO tumours presented with less iron than WT tumours, both histologically and chemically.

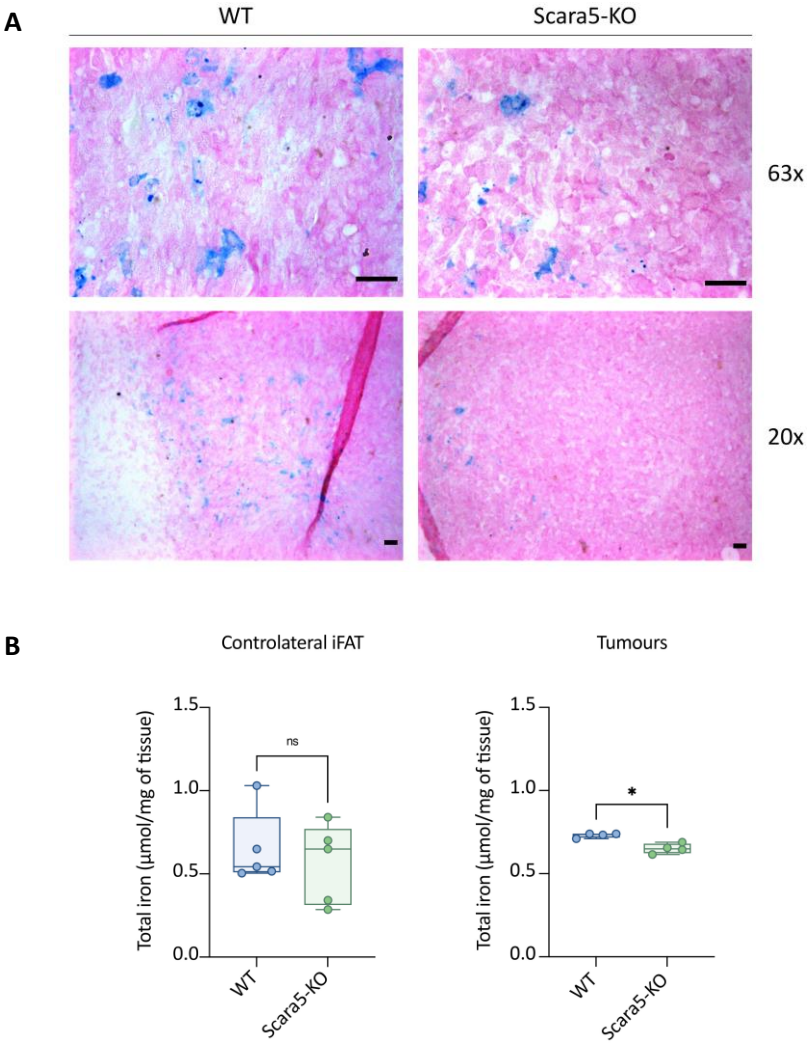


Figure 6.10 Scara5-KO mice's tumours display low levels of iron. Potassium Ferrocyanide (blue, iron) and Nuclear Red Thiazin (pink, background) stained tumours (63x/20x bright field, 25 μm scale bar); the images are representative of two experiments performed independently (N=2) (**A**). Iron quantification of WT/Scara5-KO contralateral iFAT pad and tumours (n≥4); data are depicted as box plots and Mann-Whitney U test was used to determine the degree of significance (^{ns} $p > 0.05$, * $p \leq 0.05$). Iron quantification was partially performed by Dr Justin Bradley (School of Chemistry, University of East Anglia, Norwich, UK) (**B**).

6.7. Discussion

Breast cancer (BrCa) stands as the most diagnosed cancer worldwide and significantly contributes to cancer-related mortality in women [329]. Adipose tissue proved to be critical for the development of BrCa; the adipocytic release of active molecules (e.g. adipokines, hormones, inflammatory factors) and free fatty acids indeed contributes to cancer development and growth [318, 330]. Throughout the years, many murine models of BrCa have been developed to understand the mechanisms by which BrCa develops, grow, and metastasise [329]. Nowadays, orthotopic injection of cancer cells into the mice mammary fat pads (inguinal fat pads) are used to generate BrCa models that better reproduce the disease location and the presence of the appropriate stomal compartment [331]. In 2014, Rutkowski *et al.* developed a mouse BrCa model in which the mammary ductal epithelium was characterised by ablation of p53 and the expression of the oncogenic K-ras [322]. These mutational events culminated in the formation of tumour masses that were mechanically dissociated to originate BRPKp110 cells, a poorly metastatic luminal A-like BrCa cell type [322, 323]. BRPKp110 cells themselves can be injected orthotopically into the mouse mammary fat pad to generate mouse BrCa models [332, 333]. Due to the strong crosstalk between adipose tissue cells and BrCa cells, and the reduced fat deposition associated with Scara5 deficiency, BRPKp110 cells were injected into WT and Scara5-KO mammary fat pad. Scara5 was described as downregulated in breast cancer tissues and cell lines; its overexpression in ZR-75-30 cell line suppressed cancer cell proliferation, migration, invasion, and favoured cell apoptosis by decreasing the phosphorylation levels of AKT, STAT3, and ERK1/2 [170]. In the present work, it was determined whether the Scara5-WT/-KO environment influenced BrCa growth. Scara5 deficiency indeed impacted on the tumour initiation, but 21 days after cell injection WT and Scara5-KO tumours were comparable in terms of volume and weight (**Figure 6.1**). Inflammatory cells that infiltrate the tumour regulates its growth, invasion, and metastasis; macrophages, stromal cells, and tumour cells, as well as dendritic cells and neutrophils, secrete cytokines in order to either contrast or support tumour cell proliferation [334, 335]. BRPKp110-based tumour masses developed in WT and Scara5-KO mice expressed similar levels of tumour promoting cytokines (i.e. TNFα, C-X-C motif chemokine ligand 12 – CXCL12, IFNγ, IL-1β, IL-2, IL-6, IL-10) (**Figure 6.2**). Analysis of tumour morphology revealed structural differences between WT and Scara5-KO tumours. However, these dissimilarities may reflect

a particular area of the section considered instead of indicating a real difference in terms of immune cell infiltration, as supported by the cytokine panel expression. Hence, the growth of BRPKp110-based tumours was not influenced by Scara5 deficiency after 21 days. It remains unknown whether a shorter experiment would have shown a different tumour growth in WT and Scara5-null mice, also considering that BRPKp110 tumours appeared multilobate when excised, indicating an excessive growth within the mice peritoneum.

As reported in You *et al.* study, three different BrCa cell lines displayed a downregulation of Scara5 (ZR-75-30, MCF-7, and MDA-MB-231 cells) [170]. Among them, ZR-75-30 cell line (luminal B subtype of BrCa) expressed the lowest levels of Scara5 and was therefore used to investigate the role of Scara5 in cancer growth and metastatic potential *in vitro* [170]. Similarly, murine cell lines of BrCa were herein analysed for Scara5 expression; both PyMT-BO5 and EO771, luminal B and triple negative subtype of BrCa, respectively, showed to express the lowest levels of Scara5 when compared to osteoblastic 2T3 cells expression (**Figure 6.3**). PyMT-BO5 cells were further selected to be orthotopically injected into mice's mammary fat pad because of their rapid growth and their ability to metastasise to bone. However, no bone metastasis was detected in this work, probably because the experiment was carried out for 15 days only. Two separate experiments involving almost 20 mice/group in total revealed smaller tumours in Scara5-KO than in WT mice, thus suggesting that Scara5-KO mice background did not support the tumour growth as much as WT counterpart (**Figure 6.4**). However, just the second experiment revealed overall bigger and multilobate tumours, with volumes similar to the ones reported in the literature [333]. In addition, tumour morphology analysis showed that tumour infiltration happened similarly between WT and Scara5-KO tumours, as also suggested by cytokine expression (**Figure 6.5**). Taken together, these data imply that the WT/Scara5-KO environment played a crucial role in supporting the tumour growth. To date, Scara5 expression and its role have been investigated in breast cancer cell lines and human breast cancer tissues; all studies described Scara5 as downregulated in tumour cells/tissues, being therefore responsible for an increased proliferation, invasion, and migration of cancer cells [170, 336]. However, Scara5 importance in the environment surrounding the tumour, such as the adipose tissue, has never been investigated.

As aforementioned, adipose tissue plays a fundamental role in supporting BrCa cells proliferation. Obesity at the time of diagnosis, for example, is associated with a higher risk of

total mortality and morbidity [226]. Indeed, obese adipocytes release pro-inflammatory cytokines (e.g. TNFα, IL-6) that have been linked to poor survival rate of BrCa patients [226]. Moreover, Picon-Ruiz *et al.* work showed that a co-culture of adipocytes and BrCa cells induced immature adipocytes to secrete a plethora of pro-inflammatory cytokines (i.e. IL-6, IL-8, IFNγ-inducible protein 10, chemokine ligand (CCL) 2, CCL5) *in vitro* [319]. The release of pro-inflammatory cytokines also increased both tumour-initiating and metastatic potential of MDA-MB-231 cells *in vivo*, when BrCa cells were orthotopically injected into the mammary fat pad of Balb/c nude mice [319]. To better understand the importance of the mouse background in tumour development, the iFAT and PyMT-BO5 cells crosstalk was mimicked by producing WT and Scara5-KO iFAT Sn *in vitro*, which was used to determine its effect on PyMT-BO5 cells' proliferation and adhesion. The results showed that cell proliferation, but not adhesion, was stimulated by WT Sn more than Scara5-KO Sn (**Figure 6.7**, **Figure 6.8**), in line with the different tumour growth observed *in vivo*. The work of Jablonka and colleagues already demonstrated that human adipose tissue Sn can stimulate BrCa cell proliferation [337]. They showed that the proliferation of MCF-7 cells (luminal A BrCa subtype), but not MDA-MB-231 cells (triple negative BrCa subtype), was boosted by human primary preadipocytes Sn treatment for 3 days [337]. Similarly, D'Esposito *et al.* found that human adipocytes Sn promoted MCF-7 and MDA-MB-231 cells proliferation by releasing factors such as CCL5, IL-8, and insulin-like growth factor (IGF)-1 [338]. Hence, the present work implies that Scara5-KO mice developed smaller tumours because the fat did not represent the most ideal environment for cancer cells to grow. It can be speculated that WT/Scara5-KO adipose tissue released different amounts of cytokines, although other secreted key factors can enhance BrCa cells proliferation and support the tumour growth (e.g. chemokines, growth factors, extracellular vesicles) [339].

The previous chapter showed that Scara5-KO mice presented with a mild iron deficiency. Iron is crucially important for rapidly dividing cancer cells, especially considering that iron is a co-factor for many enzymes that regulate DNA synthesis [340]. Thus, perturbations in iron homeostasis characterise BrCa malignancy and progression; in fact, several *in vivo* studies demonstrated that iron-rich diets, or subcutaneous injections of iron, induce BrCa growth [341]. As a support for the iron involvement in cancer cell proliferation, DFO was added to WT and Scara5-KO iFAT Sn; the results showed that DFO reduced the stimulatory effect of WT more

than Scara5-null Sn on BO5 cell proliferation (**Figure 6.9**), thereby implying that WT Sn contained higher concentrations of iron. Indeed, tumours developed in WT mice revealed higher concentrations of iron if compared with the Scara5-deficient counterparts (**Figure 6.10**). According to Zhang *et al.* studies, the orthotopic injection of 4T1 cells (triple negative BrCa subtype) into the mice mammary fat pad of Balb/c, and the consequent tumour growth, was affected by iron availability [321]. Mice subjected to an iron-deficient diet developed smaller tumours than the mice that received an intraperitoneal injection of iron-dextran [321]. Furthermore, *in vitro* studies using MCF-7 BrCa cells underscored the DFO ability to reduce the proliferation of cancer cells [342, 343]. Be that as it may, Scara5-KO environment resulted less favourable for BrCa cells growth, probably due to the intrinsic mild iron deficiency. In line with Marques *et al.* work, BrCa epithelial cells exhibit an "iron utilisation phenotype", characterised by an elevated hepcidin (negative regulator of iron export) and Tf receptor expression. On the other hand, stromal inflammatory cells that infiltrate the tumours (e.g. macrophages, neutrophils, and lymphocytes) display an "iron donor phenotype", with a consequent increase in ferroportin (the sole iron exporter) and ferritin expression [341]. One possible explanation for Scara5 downregulation in BrCa cells (**Figure 6.3**) is their iron utilisation phenotype, as these cells do not require iron storage in form of ferritin, but they tend to use iron to rapidly proliferate [340]. However, if the constitutive deletion of Scara5 impact on intracellular levels of ferritin, tumour infiltrating cells will not provide adequate amount of iron to cancer cells, subsequently reducing their proliferation. It remains unknown which type of cells infiltrated the tumours developed in WT and Scara5-KO mice; nonetheless, it can be hypothesised these cells are mostly macrophages, due to their renowned role as tumour infiltrating cells. In addition, macrophages favour the onset of a pro-tumour environment by releasing ferritin into the stroma, which can be used by cancer cells as fuel for their growth [344].

In summary, the findings of this chapter indicate that the absence of Scara5 creates an unfavourable environment for BrCa cells growth, thus suggesting that Scara5 plays a role in BrCa pathogenesis. Scara5 is a ferritin receptor, and its deletion was related to an intracellular mild iron deficiency. Liu *et al.* recently demonstrated that Scara5 overexpression induced ferroptosis (i.e. a form of programmed cell death dependent on iron) in ESCC cells due to their uptake of high levels of ferritin. Scara5-null mice exhibited a reduced fat deposition and

smaller tumours when PyMT-BO5 cells were injected into the fat pad. However, it remains uncertain whether the smaller tumour growth in Scara5-KO mice compared with WT mice was due to the smaller size of the iFAT pad, the iron levels of infiltrating cells, or a combination of these factors. Overall, these results suggest that Scara5-deficient environment does not support BrCa proliferation to the same extent of WT counterpart because the low levels of iron do not provide sufficient fuel for the growth of these cells (**Figure 6.11**).

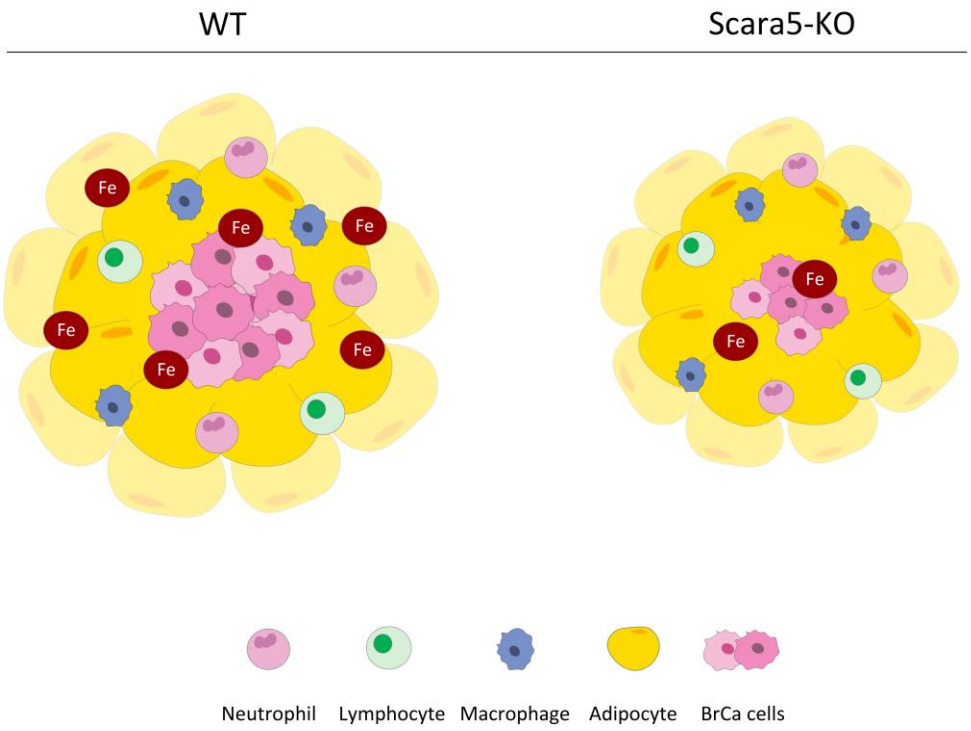


Figure 6.11 Scara5 deficiency impinges on the fat-BrCa crosstalk. The crosstalk between BrCa cells and iFAT of Scara5-KO mice is impaired as a possible consequence of the mild iron (Fe) deficiency and the iFAT pad size. Tumour infiltrating cells, such as neutrophils, lymphocytes, and macrophages, did not provide cancer cells with adequate levels of iron when Scara5 was missing, therefore reducing BrCa growth.

Chapter 7: Concluding Discussion

7.1 Discussion

Osteoporosis and the associated bone fragility affect millions of people worldwide, placing itself as one of the major health concerns among elderly people. In the UK, over 3 million people have osteoporosis leading to over 300,000 fragility fractures per year [345]. Several known risk factors impact on bone mass and strength causing osteoporosis, e.g. ageing, diet and body weight, genetic predisposition, menopausal state, certain medications, alcohol intake, and co-morbidities including diabetes. Similarly, costly health metabolic disorders as, inter alia, obesity and type 2 diabetes (T2D), represent a serious problem worldwide [346]. Obesity, for example, stands as one of the major health concerns of industrialised countries. According to World Health Organisation (WHO) 2021 report, the incidence of overweight (body mass index – BMI greater than or equal to 25 kg/m^2) and obesity (BMI greater than or equal to 30 kg/m^2) tripled between 1975 and 2016, including more than 30 million of 5 years old children [347]. An elevated BMI concomitantly increases the risk of T2D; indeed, overweight or obese people often present with insulin resistance. It is hypothesised that nonesterified fatty acids release from obese adipocytes negatively impacts on β-cells insulin secretion and favour insulin resistance. The combination of insulin resistance and an impaired function of pancreatic β-cells may favour prediabetes and T2D onset [348].

It is well recognised that bone loss-related diseases, as well as diabetes and obesity, impinge on MSCs differentiation towards osteoblasts. MSCs propensity to differentiate into adipocytes at the expenses of osteoblasts ultimately increases body and bone marrow adiposity, as a result of the suppression of critical osteogenic pathways activity, i.e. Wnt and BMP signalling pathways [263]. A significant number of key factors have been identified so far as regulators of MSCs lineage differentiation, thus playing a role in maintaining or disturbing the osteo-adipogenesis balance [249]. Among them, Scara5 recently emerged as a potential marker of adipogenesis, stimulating preadipocytes and multipotent cells adipogenic differentiation [165]. However, the role of Scara5 expression and function during MSCs differentiation and the osteoblast-adipocyte tug-of-war remains elusive.

The present work focused on understanding Scara5 role in MSCs lineage differentiation also by considering and linking together all roles of Scara5 identified so far. Hence, in this work, Scara5 is presented for the first time as a central receptor for MSCs osteo-adipogenic differentiation, iron homeostasis, and BrCa development.

The main findings of this work can be summarised as follows:

- Scara5 determines MSCs fate towards adipocytes at the expenses of osteoblasts.
- Scara5 deficiency impinges on iron homeostasis.
- Scara5 deficiency impacts on adipose tissue-BrCa crosstalk.

7.1.1 Scara5 determines MSCs fate towards adipocytes at the expenses of osteoblasts

In 2017, Lee and colleagues showed that preadipocytes and MSCs-like cells increased their ability to differentiate towards adipocytes upon Scara5 overexpression [165]. Consistent with their published data, work in this thesis showed that murine BMSCs with a constitutive Scara5-KO did not differentiate into adipocytes at the same extent as Scara5-WT cells. In addition, as BMSCs are the common precursor of both bone and fat cells, Scara5-KO BMSCs displayed a marked increase in osteogenic differentiation if compared with the WT counterparts. Scara5 expression increased in the presence of adipogenic stimuli only, thereby suggesting that Scara5 is necessary during the early stages of adipogenesis. Similarly to murine BMSCs, hFOB 1.19 expressed Scara5 when cultured in AM but not in OM; hFOB ALP activity decreased when Scara5 was overexpressed. Furthermore, the ability of WT and Scara5-KO BMSCs to differentiate into osteoblasts and adipocytes *in vitro* was reflected in the *in vivo* bone and fat phenotype. Scara5-KO mice indeed showed an increased bone mass and a decreased fat adiposity when compared with WT mice. Nevertheless, bone-affecting pathologies, such as oestrogen deficiency-induced osteoporosis and Streptozotocin-induced diabetes, developed independently of Scara5 expression, indicating that Scara5 deficiency does not stimulate osteoblast activity by reducing osteoclastic bone resorption, which is the main event that characterises these disorders [282, 287].

Beside Scara5, other SRs class A members have been reported as affecting bone homeostasis. In particular, MSR1 deletion in murine models increased mice bone mass because of impaired osteoclastic activity. Osteoclasts and macrophages share a common

myeloid precursor; it was observed that MSR1 deficiency altered osteoclast development, thus diminishing osteoclast number. Nonetheless, osteoblast number and activity and adipocyte number did not differ between MSR1-WT and -KO mice [216]. More recently, Chen *et al.* identified Scara3 as a regulator of MSCs differentiation fate to osteoblasts and adipocytes. Conversely to Scara5, Scara3 expression decreased during adipogenesis and increased during osteogenesis. In line with this, Scara3 overexpression promoted osteogenesis at the expenses of adipogenesis and its deletion enhanced murine BMSCs adipogenesis instead of osteogenesis. *In vivo* experiments showed that Scara3 overexpression supported bone formation and reduced bone loss and the accumulation of BMAT in aged and OVX mice, respectively [218]. Moreover, Scara3 stimulated bone formation via Forkhead Box O1 (FoxO1), which was reported to regulate and support osteoblast differentiation by binding to RUNX2 [349, 350]; FoxO1 expression increased upon Scara3 overexpression [218]. Be that as it may, the past years identified both Scara5 and Scara3 as potential regulators of MSCs fate switch between osteoblasts and adipocytes. It cannot be excluded that a connection between these two SRs can further control the MSCs differentiation. For example, does a concurrent Scara5 and Scara3-KO ablate the enhanced osteogenesis *in vitro*/*in vivo*?

The osteo-adipogenesis of MSCs is controlled by several factors and signalling pathways [122]. Wnt canonical pathway was the main pathway considered in the investigation of WT and Scara5-KO BMSCs differentiation. The results presented in this thesis showed that Wnt/β-catenin signalling was marginally affected by Scara5 deficiency, increasing the ALP activity of KO cells when stimulated with Wnt3a recombinant protein. It was hypothesised that this happened as a consequence of an intrinsic higher ability of Scara5-KO BMSCs to differentiate into osteoblasts, since Wnt3a enhanced ALP activity of WT BMSCs as well. However, Wnt signalling is just one of the pathways involved in MSCs osteo-adipogenesis. FAK/ERK signalling pathway, for example, promotes osteogenesis and suppresses adipogenesis of human MSCs [220, 351]. Suppression of the FAK/ERK signalling pathway by Scara5 overexpression induced preadipocyte differentiation to adipocytes [165]. However, it remains unknown whether Scara5 knockdown would enhance MSCs-like cells osteogenic differentiation via FAK/ERK signalling. Although the present work did not investigate FAK/ERK signalling pathway directly, it highlighted the predisposition of murine Scara5-KO BMSCs to differentiate into osteoblasts if compared with the WT counterparts.

Some limitations are inevitably associated with the aforementioned results; firstly, the population of primary cells used (i.e. BMSCs) is highly heterogeneous, thus posing some problems in carrying out some experiments. Indeed, despite several attempts, Alizarin Red S (ARS) and Oil Red O (ORO) staining protocols were successfully performed just once in technical triplicates. Although the use of a multipotent cell line was considered to overcome the "heterogeneity" problem (i.e. hFOB 1.19), the time required to complete both osteogenesis and adipogenesis differentiation was not compatible with a transient overexpression/knockdown of Scara5. Secondly, the role of Scara5 on osteoclast activity was not investigated in this thesis. Nonetheless, previous work carried out in the lab revealed that Scara5 expression had no impact on osteoclast function (Dr Yi-Hsuan Lee PhD thesis). Scara5 and MSR1 share a similar structure, being the most similar members of SRs class A; since MSR1 expression enhanced mouse bone mass by decreasing osteoclast number and activity, it could be assumed that Scara5 effect on bone mass *in vivo* depended on a reduced bone resorption. However, the calvarial injection experiment performed *in vivo* showed a more pronounced osteoblast-driven bone mineralisation in Scara5-KO than in WT mice. In addition, Scara5-KO mice displayed reduced fat deposition, indicating that Scara5 holds the balance of power during BMSCs commitment towards osteoblasts and adipocytes. Also, oestrogen deficiency-induced osteoporosis, an osteoclast-driven disease, proved to develop equally between WT and Scara5-KO mice. Despite the need of further confirmation, the results here presented, supported by Dr Lee data (Dr Yi-Hsuan Lee PhD thesis), suggest that Scara5 expression does not impact upon osteoclast bone resorption, in neither physiological nor pathological states.

7.1.2 Scara5 deficiency impinges on iron homeostasis

Scara5 proved to support and promote adipogenesis *in vitro* [165]; the findings presented in this thesis highlighted Scara5 role in BMSCs commitment, thus demonstrating its involvement in adipogenesis and osteogenesis both *in vitro* and *in vivo*. Different signalling pathways were explored (i.e. Wnt/β-catenin, AKT related pathways), without however proving a direct effect of Scara5 on their functions. Hence, Scara5 role as a ferritin receptor was investigated and linked to BMSCs commitment. Scara5 was identified as being able to bind both L- and H-subunits of ferritin, with a preference for L-ferritin binding [167, 213]. So far, this ferritin receptor

role has been reported in both kidney [213] and retinal cells [214]. Although ferritin is mainly known to store iron intracellularly, serum ferritin can play an important role in iron homeostasis. In fact, one molecule of ferritin can hold up to 4500 iron atoms that can be delivered and used according to the cellular needs [208]. Iron plays a crucial role in cellular metabolism, being the core of electron transporting chain proteins and one of the most important cofactors of enzymes involved in the production of ATP [205]. It was initially hypothesised that WT and Scara5-KO murine kidneys would display different concentrations of iron and, indeed, Scara5-KO kidneys presented with reduced iron levels, suggesting that the absence of Scara5 diminishes the amount of iron internalised by the cells. Due to the low levels of iron detectable in other tissues, it remains elusive whether other organs with a stromal component internalise less iron in the absence of Scara5.

Adipogenesis, as widely discussed in the previous chapters, is an energy demanding process that requires a switch from glycolysis to OXPHOS to produce a high number of ATP molecules [156]. It was reported that a mild iron deficiency impacted negatively on cell differentiation and on the mitochondrial respiratory chain complexes. In particular, iron deficiency negatively impacts on OXPHOS by decreasing the activity of mitochondrial respiratory chain complexes I and II [352]. Dysfunctional mitochondria cannot provide adequate energy for adipocyte differentiation, as well as lipid metabolism, oxidative capacity, and thermogenesis, thus contributing to the onset of metabolic diseases [353]. Mitochondria activity has been well described in BAT more than WAT, since brown adipocytes present with abundant mitochondria necessary to convert energy into heat in a process known as nonshivering thermogenesis [67, 79]. Iron deficiency has a detrimental effect on BAT thermogenesis, reducing the energy expenditure via mitochondrial OXPHOS [352]. Although less described, WAT mitochondria activity plays an important role during adipogenesis, lipolysis, lipogenesis, and fatty acid oxidation (also called β-oxidation). During adipogenesis, preadipocytes promote mitochondrial biogenesis [354]. Accordingly, preadipocytes expression of mitochondrial proteins and mitochondrial number increased drastically within four days of adipogenic induction [355]. In addition, oxygen consumption rate tended to rise throughout adipocyte differentiation, thus proving the importance of mitochondria activation in supporting adipogenesis and the elevated energy requirements [356].

The findings presented in this thesis highlighted reduced mitochondrial activity of BMSCs treated with adipogenic medium (AM) for 7 days. It was therefore concluded that the absence of Scara5 caused a mild iron deficiency within mouse BMSCs. This is considered a mild iron deficiency because iron can still enter the cell as Tf or ferritin via Tf receptor, the main iron transporter. However, circulating serum ferritin is mainly composed by L-subunits and it is unable to bind Tf receptor, thus preferring Scara5 [208, 212, 213]. A mild iron deficiency did not represent a problem for uncommitted BMSCs, which normally rely on glycolysis for ATP production [152], but was a problem for differentiating BMSCs, which required more energy to commit to adipocytes and a glycolysis-OXPHOS switch. Ferritin uptake has been reported as an essential step for adipogenic differentiation of preadipocytes [164]. Ferritin autophagy, a process named ferritinophagy, is prominently activated in the early phases of adipocytic differentiation. Hence, ferritin undergoes lysosomal degradation and the released iron can be used by mitochondria for energy production [164].

Although the data discussed complement the published literature in underscoring Scara5 impact on iron homeostasis and adipogenesis, a main limitation can be mentioned. Only WT and Scara5-KO mouse testis and kidneys have been analysed for their iron content. The number of WT and Scara5-null testis samples quantified was not sufficient to highlight any statistically significant difference and the low iron concentration in testis may impact on detection by the ferene-based iron assay. Hence, further work would help understanding whether these differences in iron content can be observed in other tissues/cells, including the bone marrow and BMSCs.

7.1.3 Scara5 deficiency impacts on adipose tissue-breast cancer crosstalk

Scara5-KO mice presented with more bone mass and less fat deposition if compared with WT counterparts, as a result of BMSCs propensity to differentiate into osteoblasts at the expenses of adipocytes. These results placed Scara5 as a negative regulator of osteogenesis and a stimulator of BMSCs adipogenesis, thus suggesting that its overexpression could increase overall adiposity. Excess adiposity represents a risk factor for obesity-associated metabolic disorders, such as T2D, but also for BrCa [357]. Many published works associate obesity with BrCa [358]; breast tissue is mainly composed of WAT that, when obese, promotes immune cells

infiltration and stimulates macrophage release of inflammatory cytokines and chemokines. This results in the setting of a TME that support cancer cell migration and invasion [358, 359].

Be that as it may, Scara5 expression is usually downregulated in cancer [221]. Among the types of cancer considered in the past years, Scara5 was found downregulated in human BrCa samples and in BrCa cell lines [170]. BrCa is a heterogeneous type of cancer that originates from the milk ducts-lining epithelial cells. Different BrCa subtypes have been identified so far according to ER, PR, and HER expression, which determines the incidence risk factor, the treatment response, risk of progression, and preferential sites of metastasis [360]. Adipose tissue plays a fundamental role in the development of BrCa, representing the main component of the TME; BrCa cells induce lipolysis of adipose tissue, thereby provoking the release of adipokines, proteases, hormones, as well as FFAs, the fuel source for cancer cells. Indeed, via β-oxidation, FFAs are converted into mitochondrial Acetyl-CoA, which ultimately enters the TCA cycle to produce NADH that will serve for ATP generation through OXPHOS [149]. Similarly, BrCa cells require a considerable amount of iron to survive, proliferate and migrate, being that iron is a central element of many enzymes involved in DNA synthesis and mitochondrial activity [320]. BrCa cells often upregulate TfR to increase iron uptake and store it in form of ferritin [361-363]. It can be speculated that cancer cells upregulate TfR and downregulate Scara5 as a defensive mechanism. In fact, although iron is needed for tumour growth, the concurrent expression of Scara5 and TfR could lead to excessive iron delivery within the cell. Iron overload increases ROS production and lipid peroxidation, often causing cell death by ferroptosis [215].

Scara5-WT and -KO mice were used to generate a luminal B-type BrCa. BrCa cells developed smaller tumours in Scara5-null than in WT mice, demonstrating that the distinct environments (i.e. WT and Scara5-KO mammary fat pads) provided different support for BO5 growth. Indeed, supernatant (Sn) obtained by culturing WT and Scara5-KO fat pads stimulated BrCa cells growth differently. Scara5-KO Sn did not support BrCa cells proliferation to the same extent as the WT counterpart, likely due to the reduced iron content. It was also demonstrated that the tumours developed in Scara5-KO mice presented with lower concentrations of iron, thus suggesting that BO5 cells did not grow as much, at least in part, because the Scara5-KO environment was not providing them with enough iron. As aforementioned, iron plays a pivotal role in metabolism and mitochondrial activity

independently of the cell type considered [205, 364]. Iron uptake from the surrounding environment can support the proliferation of BrCa cells, which mostly rely upon OXPHOS for energy production [365]. If the Scara5-null adipose tissue that surrounds the BrCa is poor in iron, cancer cells will not be able to internalise enough iron. This action will inevitably lead to the development of smaller tumours in Scara5-KO mice. Iron chelation is considered a potential therapeutic approach for the treatment of BrCa. Indeed, the reduction of intracellular iron levels has been shown to inhibit DNA synthesis, to promote cancer cell apoptosis, as well as to sensitise BrCa to chemotherapeutic drugs [366, 367]. Additionally, *in vivo* studies showed that triple negative BrCa cells developed smaller tumour in mice treated with DFO than in mice that underwent an iron-rich diet [321].

In summation, as depicted in **Figure 7.1**, this thesis presented Scara5 as a regulator of MSCs fate, thus highlighting that Scara5 deficiency promoted osteogenesis of progenitor cells as a consequence of a mild iron deficiency, which impaired cellular mitochondrial activity and adipogenic differentiation. Furthermore, reduced iron levels and fat deposition resulted in a defective crosstalk between adipose tissue and BrCa cells, culminating in smaller tumours development.

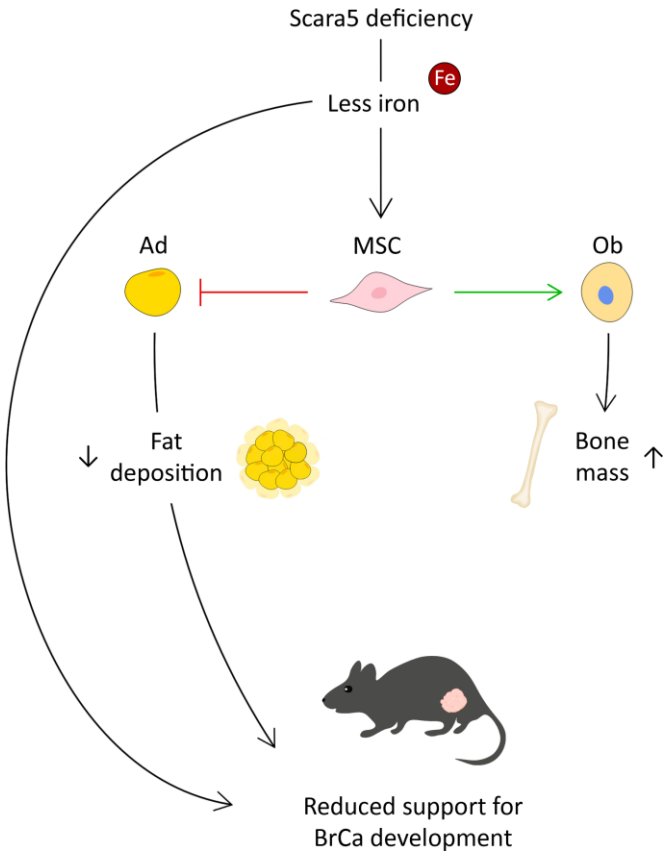


Figure 7.1 Hypothetic mechanism of Scara5 role in adipogenesis and BrCa-fat crosstalk. The absence of Scara5, together with the reduced iron internalisation, determined BMSCs fate differentiation towards osteoblasts (Ob) at the expense of adipocytes (Ad), thus increasing bone mass and diminishing the deposition of fat. By diminishing fat deposition, Scara5 deficiency and the consequent iron deficiency reduced the support for BrCa growth, both *in vitro* and *in vivo*.

7.2 Future Directions

The findings presented in this thesis pointed to Scara5 as a multifaceted receptor with interconnected roles. This study also paves the way to new investigations, that could strengthen the results obtained and uncover new functions of Scara5.

Scara5-deficiency impaired both adipogenesis of BMSCs *in vitro* and fat deposition *in vivo*. However, this study considered Scara5 effect on fat in normal conditions or upon the development of disorders that do not affect adipose tissue directly, i.e. osteoporosis and T1D. Scara5-KO mice could therefore undergo a high fat diet, in order to determine whether the absence of Scara5 exerts a protective role on fat deposition. Furthermore, the high fat diet, was reported as an effective tool to develop T2D in murine models [368]. A single high dose of

Stz favoured the onset of diabetes that resembled T1D more than T2D in WT and Scara5-KO mice, but T1D has not been related to bone loss and weight gain as much as T2D. Preliminary studies conducted in the lab by Dr Adel Ersek using C57BL/6J mice on the high fat diet failed to demonstrate an increase in glucose levels; hence this approach was not used as it would require further optimisation if needed in the future.

Wnt signalling and AKT-related pathways were investigated in the presence and the absence of Scara5, without however showing any significant relation with Scara5. It cannot be excluded that other pathways involved in MSCs osteo-adipogenesis are affected by Scara5 expression. BMP/Smad signalling, for example, is often described as a key pathway in MSCs differentiation towards osteoblasts. On the other hand, BMP/p38/MAPK pathway stimulates adipogenic differentiation of MSCs [122]. Scara5 role could therefore be explored in relation to these pathways, the balance of which can be decisive in determining MSC differentiation fate [122]. Similarly, Scara5 expression could be explored during the activation of Hh signalling, which stimulates adipogenesis of MSCs via Gli activation and osteogenesis by activating BMP/Smad signalling pathway [147]. Omics approaches would give more insights on Scara5 molecular function. Transcriptomics techniques, such as RNA sequencing (RNA-Seq), would determine Scara5 deficiency impact on gene expression, thus highlighting the most important differences between WT and Scara5-KO BMSCs. Similarly, mass spectrometry-based proteomics could help identifying other proteins that interact with Scara5, thereby improving the understanding of Scara5 expression in differentiating BMSCs.

This thesis showed that Scara5-KO BMSCs displayed impaired mitochondrial activity if compared with WT BMSCs during adipogenic differentiation. Since adipogenesis is an energy demanding process, the number of mitochondria increases to meet the needs of differentiating MSCs [151]. The use of mitochondria probes (e.g. MitoTracker green, nonyl acridine orange) could assess and highlight any differences between WT and Scara5-null BMSCs mitochondria mass, in both uncommitted and differentiating cells. Furthermore, it would be necessary to determine whether mitochondrial activity is impaired in differentiating Scara5-KO BMSCs due to a mild iron deficiency. Iron could be detected by using fluorescent indicators, where fluorescence is quenched by the iron present in the sample and measured by flow cytometry. In addition, it remains elusive whether Scara5-deficient BMSCs rely more

on glycolysis than WT cells, especially during osteogenic differentiation, and this could be investigated further by employing the Seahorse Glycolysis Stress Kit.

Regarding BrCa, it emerged that Scara5 deficiency and the related reduction of iron content and fat adiposity impaired the crosstalk between BrCa and adipose tissue, thus reducing the tumour growth in Scara5-KO mice. It would be interesting to investigate whether the genetic manipulation of Scara5 in BrCa cells would impact differently on tumour development. Here, Scara5 expression and the impact on BrCa development was evaluated in the BrCa environment (i.e. mammary fat pad). What would happen if Scara5 was downregulated or overexpressed in the BrCa cells that were injected into the fat pad? Moreover, it is still unknown which cells released iron for BrCa cells within the adipose tissue of WT and Scara5-KO mice. Macrophages are the most abundant iron donor cells of the adipose tissue [369, 370]; hence, macrophage staining could determine whether these are the main cells that orchestrate BrCa-fat crosstalk in the Scara5-WT/KO murine models.

In conclusion, this work provides new insights about Scara5 as a potential target for developing new therapies to contrast body fat deposition and, in turn, BrCa development by reducing intracellular iron levels. New studies will be necessary to evaluate human BrCa paracancerous tissues to assess whether Scara5 expression on the TME affects BrCa development in humans. Furthermore, a thorough analysis of Scara5 genomic sequence in cancerous and paracancerous tissues would help understanding whether Scara5 mutations, such as single nucleotide polymorphisms (SNPs), predispose some patients to the development of BrCa, or dictate the severity of disease.

Chapter 8: Bibliography

1. Datta, H.K., W.F. Ng, J.A. Walker, S.P. Tuck, and S.S. Varanasi, *The cell biology of bone metabolism.* Journal of Clinical Pathology, 2008. 61(5): p. 577-587.
2. Hadjidakis, D.J. and Androulakis, II, *Bone remodeling.* Ann N Y Acad Sci, 2006. 1092: p. 385-96.
3. Breeland, G., M.A. Sinkler, and R.G. Menezes, *Embryology, Bone Ossification*, in *StatPearls*. 2023, StatPearls Publishing LLC: Treasure Island (FL) ineligible companies.
4. Percival, C.J. and J.T. Richtsmeier, *Angiogenesis and intramembranous osteogenesis.* Dev Dyn, 2013. 242(8): p. 909-22.
5. Galea, G.L., M.R. Zein, S. Allen, and P. Francis-West, *Making and shaping endochondral and intramembranous bones.* Developmental Dynamics, 2021. 250(3): p. 414-449.
6. Ortega, N., D.J. Behonick, and Z. Werb, *Matrix remodeling during endochondral ossification.* Trends Cell Biol, 2004. 14(2): p. 86-93.
7. Li, J. and S. Dong, *The Signaling Pathways Involved in Chondrocyte Differentiation and Hypertrophic Differentiation.* Stem Cells International, 2016. 2016: p. 2470351.
8. Aghajanian, P. and S. Mohan, *The art of building bone: emerging role of chondrocyte-to-osteoblast transdifferentiation in endochondral ossification.* Bone Research, 2018. 6(1): p. 19.
9. Wolff, L.I. and C. Hartmann, *A Second Career for Chondrocytes—Transformation into Osteoblasts.* Current Osteoporosis Reports, 2019. 17(3): p. 129-137.
10. Feng, X. and J.M. McDonald, *Disorders of bone remodeling.* Annu Rev Pathol, 2011. 6: p. 121-45.
11. Wu, B., Z. Fu, X. Wang, P. Zhou, Q. Yang*, et al.*, *A narrative review of diabetic bone disease: Characteristics, pathogenesis, and treatment.* Frontiers in Endocrinology, 2022. 13.
12. Mizoguchi, T. and N. Ono, *The diverse origin of bone-forming osteoblasts.* J Bone Miner Res, 2021. 36(8): p. 1432-1447.
13. Blair, H.C., Q.C. Larrouture, Y. Li, H. Lin, D. Beer-Stoltz*, et al.*, *Osteoblast Differentiation and Bone Matrix Formation In Vivo and In Vitro.* Tissue Eng Part B Rev, 2017. 23(3): p. 268-280.
14. Florencio-Silva, R., G.R. Sasso, E. Sasso-Cerri, M.J. Simões, and P.S. Cerri, *Biology of Bone Tissue: Structure, Function, and Factors That Influence Bone Cells.* Biomed Res Int, 2015. 2015: p. 421746.
15. Yeniyol, S. and J.L. Ricci, *Alkaline phosphatase levels of murine pre-osteoblastic cells on anodized and annealed titanium surfaces.* Eur Oral Res, 2018. 52(1): p. 12-19.

16. Prins, H.J., A.K. Braat, D. Gawlitta, W.J. Dhert, D.A. Egan*, et al.*, *In vitro induction of alkaline phosphatase levels predicts in vivo bone forming capacity of human bone marrow stromal cells.* Stem Cell Res, 2014. 12(2): p. 428-40.
17. Termine, J.D., H.K. Kleinman, S.W. Whitson, K.M. Conn, M.L. McGarvey*, et al.*, *Osteonectin, a bone-specific protein linking mineral to collagen.* Cell, 1981. 26(1 Pt 1): p. 99-105.
18. Rosset, E.M. and A.D. Bradshaw, *SPARC/osteonectin in mineralized tissue.* Matrix Biol, 2016. 52-54: p. 78-87.
19. Moser, S.C. and B.C.J. van der Eerden, *Osteocalcin-A Versatile Bone-Derived Hormone.* Front Endocrinol (Lausanne), 2018. 9: p. 794.
20. Morinobu, M., M. Ishijima, S.R. Rittling, K. Tsuji, H. Yamamoto*, et al.*, *Osteopontin Expression in Osteoblasts and Osteocytes During Bone Formation Under Mechanical Stress in the Calvarial Suture In Vivo.* Journal of Bone and Mineral Research, 2003. 18(9): p. 1706-1715.
21. Dallas, S.L. and L.F. Bonewald, *Dynamics of the transition from osteoblast to osteocyte.* Ann N Y Acad Sci, 2010. 1192: p. 437-43.
22. Gaur, T., C.J. Lengner, H. Hovhannisyan, R.A. Bhat, P.V.N. Bodine*, et al.*, *Canonical WNT Signaling Promotes Osteogenesis by Directly Stimulating Runx2 Gene Expression.* Journal of Biological Chemistry, 2005. 280(39): p. 33132-33140.
23. Komori, T., H. Yagi, S. Nomura, A. Yamaguchi, K. Sasaki*, et al.*, *Targeted disruption of Cbfa1 results in a complete lack of bone formation owing to maturational arrest of osteoblasts.* Cell, 1997. 89(5): p. 755-64.
24. Komori, T., *Regulation of Proliferation, Differentiation and Functions of Osteoblasts by Runx2.* Int J Mol Sci, 2019. 20(7).
25. Nakashima, K., X. Zhou, G. Kunkel, Z. Zhang, J.M. Deng*, et al.*, *The novel zinc finger-containing transcription factor osterix is required for osteoblast differentiation and bone formation.* Cell, 2002. 108(1): p. 17-29.
26. Mbalaviele, G., S. Sheikh, J.P. Stains, V.S. Salazar, S.L. Cheng*, et al.*, *Beta-catenin and BMP-2 synergize to promote osteoblast differentiation and new bone formation.* J Cell Biochem, 2005. 94(2): p. 403-18.
27. Mason, J.J. and B.O. Williams, *SOST and DKK: Antagonists of LRP Family Signaling as Targets for Treating Bone Disease.* J Osteoporos, 2010. 2010.
28. Holdsworth, G., S.J. Roberts, and H.Z. Ke, *Novel actions of sclerostin on bone.* J Mol Endocrinol, 2019. 62(2): p. R167-R185.
29. Khosla, S., J.J. Westendorf, and M.J. Oursler, *Building bone to reverse osteoporosis and repair fractures.* The Journal of Clinical Investigation, 2008. 118(2): p. 421-428.
30. Holmen, S.L., C.R. Zylstra, A. Mukherjee, R.E. Sigler, M.C. Faugere*, et al.*, *Essential role of beta-catenin in postnatal bone acquisition.* J Biol Chem, 2005. 280(22): p. 21162-8.
31. Song, B., K.D. Estrada, and K.M. Lyons, *Smad signaling in skeletal development and regeneration.* Cytokine Growth Factor Rev, 2009. 20(5-6): p. 379-88.

32. Amarasekara, D.S., S. Kim, and J. Rho, *Regulation of Osteoblast Differentiation by Cytokine Networks.* International Journal of Molecular Sciences, 2021. 22(6): p. 2851.
33. Phimphilai, M., Z. Zhao, H. Boules, H. Roca, and R.T. Franceschi, *BMP Signaling Is Required for RUNX2-Dependent Induction of the Osteoblast Phenotype.* Journal of Bone and Mineral Research, 2006. 21(4): p. 637-646.
34. Feng, X. and S.L. Teitelbaum, *Osteoclasts: New Insights.* Bone Res, 2013. 1(1): p. 11-26.
35. Tencerova, M. and M. Kassem, *The Bone Marrow-Derived Stromal Cells: Commitment and Regulation of Adipogenesis.* Front Endocrinol (Lausanne), 2016. 7: p. 127.
36. Borciani, G., G. Montalbano, N. Baldini, G. Cerqueni, C. Vitale-Brovarone*, et al.*, *Co-Culture Systems of Osteoblasts and Osteoclasts: Simulating in Vitro Bone Remodeling in Regenerative Approaches.* Acta Biomater, 2020.
37. Kenkre, J.S. and J. Bassett, *The bone remodelling cycle.* Ann Clin Biochem, 2018. 55(3): p. 308-327.
38. Raggatt, L.J. and N.C. Partridge, *Cellular and Molecular Mechanisms of Bone Remodeling*.* Journal of Biological Chemistry, 2010. 285(33): p. 25103-25108.
39. Henriksen, K., J. Bollerslev, V. Everts, and M.A. Karsdal, *Osteoclast Activity and Subtypes as a Function of Physiology and Pathology—Implications for Future Treatments of Osteoporosis.* Endocrine Reviews, 2011. 32(1): p. 31-63.
40. Matsuo, K. and N. Irie, *Osteoclast–osteoblast communication.* Archives of Biochemistry and Biophysics, 2008. 473(2): p. 201-209.
41. Sims, N.A. and T.J. Martin, *Osteoclasts Provide Coupling Signals to Osteoblast Lineage Cells Through Multiple Mechanisms.* Annu Rev Physiol, 2020. 82: p. 507-529.
42. Zaidi, M., D. Lizneva, and T. Yuen, *The role of PDGF-BB in the bone-vascular relationship during aging.* J Clin Invest, 2021. 131(20).
43. Ivanova, M.M., J. Dao, N. Kasaci, A. Friedman, L. Noll*, et al.*, *Wnt signaling pathway inhibitors, sclerostin and DKK-1, correlate with pain and bone pathology in patients with Gaucher disease.* Front Endocrinol (Lausanne), 2022. 13: p. 1029130.
44. Boyce, B.F., E. Rosenberg, A.E. de Papp, and L.T. Duong, *The osteoclast, bone remodelling and treatment of metabolic bone disease.* Eur J Clin Invest, 2012. 42(12): p. 1332-41.
45. Föger-Samwald, U., P. Dovjak, U. Azizi-Semrad, K. Kerschan-Schindl, and P. Pietschmann, *Osteoporosis: Pathophysiology and therapeutic options.* Excli j, 2020. 19: p. 1017-1037.
46. Seitz, S., M. Priemel, J. Zustin, F.T. Beil, J. Semler*, et al.*, *Paget's Disease of Bone: Histologic Analysis of 754 Patients.* Journal of Bone and Mineral Research, 2009. 24(1): p. 62-69.
47. Cheng, C., K. Wentworth, and D.M. Shoback, *New Frontiers in Osteoporosis Therapy.* Annual Review of Medicine, Vol 71, 2020, 2020. 71: p. 277-288.

48. Nih Consensus Development Panel on Osteoporosis Prevention, D. and Therapy, *Osteoporosis prevention, diagnosis, and therapy.* JAMA, 2001. 285(6): p. 785-95.
49. Jackuliak, P. and J. Payer, *Osteoporosis, Fractures, and Diabetes.* International Journal of Endocrinology, 2014.
50. Hernlund, E., A. Svedbom, M. Ivergard, J. Compston, C. Cooper*, et al.*, *Osteoporosis in the European Union: medical management, epidemiology and economic burden. A report prepared in collaboration with the International Osteoporosis Foundation (IOF) and the European Federation of Pharmaceutical Industry Associations (EFPIA).* Arch Osteoporos, 2013. 8: p. 136.
51. Jiang, N. and W. Xia, *Assessment of bone quality in patients with diabetes mellitus.* Osteoporos Int, 2018. 29(8): p. 1721-1736.
52. Moayyeri, A., A. Soltani, N.K. Tabari, M. Sadatsafavi, A. Hossein-neghad*, et al.*, *Discordance in diagnosis of osteoporosis using spine and hip bone densitometry.* BMC Endocrine Disorders, 2005. 5(1): p. 3.
53. Dhaliwal, R., D. Cibula, C. Ghosh, R.S. Weinstock, and A.M. Moses, *Bone quality assessment in type 2 diabetes mellitus.* Osteoporos Int, 2014. 25(7): p. 1969-73.
54. Saeedi, P., I. Petersohn, P. Salpea, B. Malanda, S. Karuranga*, et al.*, *Global and regional diabetes prevalence estimates for 2019 and projections for 2030 and 2045: Results from the International Diabetes Federation Diabetes Atlas, 9th edition.* Diabetes Research and Clinical Practice, 2019. 157.
55. Conte, C., R. Bouillon, and N. Napoli, *Diabetes and bone*. 2020. p. 941-969.
56. Walsh, J.S. and T. Vilaca, *Obesity, Type 2 Diabetes and Bone in Adults.* Calcif Tissue Int, 2017. 100(5): p. 528-535.
57. Bouillon, R., *Diabetic bone disease.* Calcified Tissue International, 1991. 49(3): p. 155-160.
58. Poiana, C. and C. Capatina, *OSTEOPOROSIS AND FRACTURE RISK IN PATIENTS WITH TYPE 2 DIABETES MELLITUS.* Acta endocrinologica (Bucharest, Romania : 2005), 2019. 15(2): p. 231-236.
59. Silva, B.C. and J.P. Bilezikian, *Trabecular bone score: perspectives of an imaging technology coming of age.* Arq Bras Endocrinol Metabol, 2014. 58(5): p. 493-503.
60. Katayama, Y., T. Akatsu, M. Yamamoto, N. Kugai, and N. Nagata, *Role of nonenzymatic glycosylation of type I collagen in diabetic osteopenia.* J Bone Miner Res, 1996. 11(7): p. 931-7.
61. Lu, J., J. Liu, L. Li, Y. Lan, and Y. Liang, *Cytokines in type 1 diabetes: mechanisms of action and immunotherapeutic targets.* Clin Transl Immunology, 2020. 9(3): p. e1122.
62. Richard, A.J., U. White, C.M. Elks, and J.M. Stephens, *Adipose Tissue: Physiology to Metabolic Dysfunction*, in *Endotext*, K.R. Feingold, et al., Editors. 2000-2020, MDText.com, Inc.: South Dartmouth (MA).

63. Parra-Peralbo, E., A. Talamillo, and R. Barrio, *Origin and Development of the Adipose Tissue, a Key Organ in Physiology and Disease.* Frontiers in Cell and Developmental Biology, 2021. 9.
64. Tang, W., D. Zeve, J.M. Suh, D. Bosnakovski, M. Kyba*, et al.*, *White fat progenitor cells reside in the adipose vasculature.* Science, 2008. 322(5901): p. 583-6.
65. Rodeheffer, M.S., K. Birsoy, and J.M. Friedman, *Identification of white adipocyte progenitor cells in vivo.* Cell, 2008. 135(2): p. 240-9.
66. Corvera, S., *Cellular Heterogeneity in Adipose Tissues.* Annu Rev Physiol, 2021. 83: p. 257-278.
67. Unamuno, X., G. Frühbeck, and V. Catalán, *Adipose Tissue*, in *Encyclopedia of Endocrine Diseases (Second Edition)*, I. Huhtaniemi and L. Martini, Editors. 2019, Academic Press: Oxford. p. 370-384.
68. White, U. and E. Ravussin, *Dynamics of adipose tissue turnover in human metabolic health and disease.* Diabetologia, 2019. 62(1): p. 17-23.
69. Arner, P. and M. Rydén, *Human white adipose tissue: A highly dynamic metabolic organ.* Journal of Internal Medicine, 2022. 291(5): p. 611-621.
70. Ghaben, A.L. and P.E. Scherer, *Adipogenesis and metabolic health.* Nature Reviews Molecular Cell Biology, 2019. 20(4): p. 242-258.
71. He, N., M. Liu, and Y. Wu, *Adipose tissue and hematopoiesis: Friend or foe?* Journal of Clinical Laboratory Analysis, 2023. 37(6): p. e24872.
72. Park, A., W.K. Kim, and K.H. Bae, *Distinction of white, beige and brown adipocytes derived from mesenchymal stem cells.* World J Stem Cells, 2014. 6(1): p. 33-42.
73. Arner, E., P.O. Westermark, K.L. Spalding, T. Britton, M. Rydén*, et al.*, *Adipocyte turnover: relevance to human adipose tissue morphology.* Diabetes, 2010. 59(1): p. 105-9.
74. Longo, M., F. Zatterale, J. Naderi, L. Parrillo, P. Formisano*, et al.*, *Adipose Tissue Dysfunction as Determinant of Obesity-Associated Metabolic Complications.* Int J Mol Sci, 2019. 20(9).
75. Lettner, A. and M. Roden, *Ectopic fat and insulin resistance.* Curr Diab Rep, 2008. 8(3): p. 185-91.
76. Unger, R.H., *Lipid overload and overflow: metabolic trauma and the metabolic syndrome.* Trends Endocrinol Metab, 2003. 14(9): p. 398-403.
77. Farooqi, I.S. and S. O'Rahilly, *Leptin: a pivotal regulator of human energy homeostasis.* Am J Clin Nutr, 2009. 89(3): p. 980s-984s.
78. Mittendorfer, B., *Origins of metabolic complications in obesity: adipose tissue and free fatty acid trafficking.* Curr Opin Clin Nutr Metab Care, 2011. 14(6): p. 535-41.
79. Cinti, S., *White, brown, beige and pink: A rainbow in the adipose organ.* Current Opinion in Endocrine and Metabolic Research, 2019. 4: p. 29-36.
80. Fedorenko, A., P.V. Lishko, and Y. Kirichok, *Mechanism of fatty-acid-dependent UCP1 uncoupling in brown fat mitochondria.* Cell, 2012. 151(2): p. 400-13.

81. Wang, S., M.H. Pan, W.L. Hung, Y.C. Tung, and C.T. Ho, *From white to beige adipocytes: therapeutic potential of dietary molecules against obesity and their molecular mechanisms.* Food Funct, 2019. 10(3): p. 1263-1279.
82. Morroni, M., A. Giordano, M.C. Zingaretti, R. Boiani, R. De Matteis*, et al.*, *Reversible transdifferentiation of secretory epithelial cells into adipocytes in the mammary gland.* Proceedings of the National Academy of Sciences, 2004. 101(48): p. 16801-16806.
83. Giordano, A., A. Smorlesi, A. Frontini, G. Barbatelli, and S. Cinti, *White, brown and pink adipocytes: the extraordinary plasticity of the adipose organ.* Eur J Endocrinol, 2014. 170(5): p. R159-71.
84. Li, Q., Y. Wu, and N. Kang, *Marrow Adipose Tissue: Its Origin, Function, and Regulation in Bone Remodeling and Regeneration.* Stem Cells Int, 2018. 2018: p. 7098456.
85. Li, Y., Y. Meng, and X. Yu, *The Unique Metabolic Characteristics of Bone Marrow Adipose Tissue.* Front Endocrinol (Lausanne), 2019. 10: p. 69.
86. Krings, A., S. Rahman, S. Huang, Y. Lu, P.J. Czernik*, et al.*, *Bone marrow fat has brown adipose tissue characteristics, which are attenuated with aging and diabetes.* Bone, 2012. 50(2): p. 546-552.
87. Laharrague, P., D. Larrouy, A.-M. Fontanilles, N. Truel, A. Campfield*, et al.*, *High expression of leptin by human bone marrow adipocytes in primary culture.* The FASEB Journal, 1998. 12(9): p. 747-752.
88. Scheller, E.L., A.A. Burr, O.A. MacDougald, and W.P. Cawthorn, *Inside out: Bone marrow adipose tissue as a source of circulating adiponectin.* Adipocyte, 2016. 5(3): p. 251-269.
89. Sakers, A., M.K. De Siqueira, P. Seale, and C.J. Villanueva, *Adipose-tissue plasticity in health and disease.* Cell, 2022. 185(3): p. 419-446.
90. Villarroya, F., R. Cereijo, A. Gavaldà-Navarro, J. Villarroya, and M. Giralt, *Inflammation of brown/beige adipose tissues in obesity and metabolic disease.* Journal of Internal Medicine, 2018. 284(5): p. 492-504.
91. Fain, J.N., A.K. Madan, M.L. Hiler, P. Cheema, and S.W. Bahouth, *Comparison of the Release of Adipokines by Adipose Tissue, Adipose Tissue Matrix, and Adipocytes from Visceral and Subcutaneous Abdominal Adipose Tissues of Obese Humans.* Endocrinology, 2004. 145(5): p. 2273-2282.
92. Cawthorn, W.P., E.L. Scheller, B.S. Learman, S.D. Parlee, B.R. Simon*, et al.*, *Bone marrow adipose tissue is an endocrine organ that contributes to increased circulating adiponectin during caloric restriction.* Cell metabolism, 2014. 20(2): p. 368-375.
93. Luo, L. and M. Liu, *Adipose tissue in control of metabolism.* Journal of Endocrinology, 2016. 231(3): p. R77-R99.
94. Stern, J.H., J.M. Rutkowski, and P.E. Scherer, *Adiponectin, Leptin, and Fatty Acids in the Maintenance of Metabolic Homeostasis through Adipose Tissue Crosstalk.* Cell Metab, 2016. 23(5): p. 770-84.

95. Fu, Y., N. Luo, R.L. Klein, and W.T. Garvey, *Adiponectin promotes adipocyte differentiation, insulin sensitivity, and lipid accumulation.* Journal of Lipid Research, 2005. 46(7): p. 1369-1379.
96. Körner, A., M. Wabitsch, B. Seidel, P. Fischer-Posovszky, A. Berthold*, et al.*, *Adiponectin expression in humans is dependent on differentiation of adipocytes and down-regulated by humoral serum components of high molecular weight.* Biochem Biophys Res Commun, 2005. 337(2): p. 540-50.
97. Martínez-Sánchez, N., *There and Back Again: Leptin Actions in White Adipose Tissue.* Int J Mol Sci, 2020. 21(17).
98. Malmström, R., M.R. Taskinen, S.L. Karonen, and H. Yki-JÄrvinen, *Insulin increases plasma leptin concentrations in normal subjects and patients with NIDDM.* Diabetologia, 1996. 39(8): p. 993-996.
99. Saladin, R., P. De Vos, M. Guerre-Millot, A. Leturque, J. Girard*, et al.*, *Transient increase in obese gene expression after food intake or insulin administration.* Nature, 1995. 377(6549): p. 527-528.
100. Müller, G., J. Ertl, M. Gerl, and G. Preibisch, *Leptin Impairs Metabolic Actions of Insulin in Isolated Rat Adipocytes*.* Journal of Biological Chemistry, 1997. 272(16): p. 10585-10593.
101. Seufert, J., T.J. Kieffer, C.A. Leech, G.G. Holz, W. Moritz*, et al.*, *Leptin suppression of insulin secretion and gene expression in human pancreatic islets: implications for the development of adipogenic diabetes mellitus.* J Clin Endocrinol Metab, 1999. 84(2): p. 670-6.
102. Laubner, K., T.J. Kieffer, N.T. Lam, X. Niu, F. Jakob*, et al.*, *Inhibition of Preproinsulin Gene Expression by Leptin Induction of Suppressor of Cytokine Signaling 3 in Pancreatic β-Cells.* Diabetes, 2005. 54(12): p. 3410-3417.
103. Thomas, T., F. Gori, S. Khosla, M.D. Jensen, B. Burguera*, et al.*, *Leptin Acts on Human Marrow Stromal Cells to Enhance Differentiation to Osteoblasts and to Inhibit Differentiation to Adipocytes*.* Endocrinology, 1999. 140(4): p. 1630-1638.
104. Coelho, M., T. Oliveira, and R. Fernandes, *Biochemistry of adipose tissue: an endocrine organ.* Arch Med Sci, 2013. 9(2): p. 191-200.
105. Astapova, O. and T. Leff, *Adiponectin and PPARγ: cooperative and interdependent actions of two key regulators of metabolism.* Vitam Horm, 2012. 90: p. 143-62.
106. Rosen, E.D., C.J. Walkey, P. Puigserver, and B.M. Spiegelman, *Transcriptional regulation of adipogenesis.* Genes Dev, 2000. 14(11): p. 1293-307.
107. Aprile, M., M.R. Ambrosio, V. D'Esposito, F. Beguinot, P. Formisano*, et al.*, *PPARG in Human Adipogenesis: Differential Contribution of Canonical Transcripts and Dominant Negative Isoforms.* PPAR Res, 2014. 2014: p. 537865.
108. Hernandez-Quiles, M., M.F. Broekema, and E. Kalkhoven, *PPARgamma in Metabolism, Immunity, and Cancer: Unified and Diverse Mechanisms of Action.* Frontiers in Endocrinology, 2021. 12.

109. Koutnikova, H., T. Cock, M. Watanabe, S. Houten, M. Champy*, et al.*, *Compensation by the muscle limits the metabolic consequences of lipodystrophy in PPAR gamma hypomorphic mice.* PNAS, 2003. 100: p. 14457-14462.
110. Tamori, Y., J. Masugi, N. Nishino, and M. Kasuga, *Role of Peroxisome Proliferator-Activated Receptor-γ in Maintenance of the Characteristics of Mature 3T3-L1 Adipocytes.* Diabetes, 2002. 51(7): p. 2045-2055.
111. Imai, T., R. Takakuwa, S. Marchand, E. Dentz, J.-M. Bornert*, et al.*, *Peroxisome proliferator-activated receptor γ is required in mature white and brown adipocytes for their survival in the mouse.* Proceedings of the National Academy of Sciences, 2004. 101(13): p. 4543-4547.
112. Madsen, M.S., R. Siersbæk, M. Boergesen, R. Nielsen, and S. Mandrup, *Peroxisome proliferator-activated receptor γ and C/EBPα synergistically activate key metabolic adipocyte genes by assisted loading.* Mol Cell Biol, 2014. 34(6): p. 939-54.
113. Ambele, M.A., P. Dhanraj, R. Giles, and M.S. Pepper, *Adipogenesis: A Complex Interplay of Multiple Molecular Determinants and Pathways.* Int J Mol Sci, 2020. 21(12).
114. Zhang, H., J. Nøohr, C.H. Jensen, R.K. Petersen, E. Bachmann*, et al.*, *Insulin-like growth factor-1/insulin bypasses Pref-1/FA1-mediated inhibition of adipocyte differentiation.* J Biol Chem, 2003. 278(23): p. 20906-14.
115. Boucher, J., M.A. Mori, K.Y. Lee, G. Smyth, C.W. Liew*, et al.*, *Impaired thermogenesis and adipose tissue development in mice with fat-specific disruption of insulin and IGF-1 signalling.* Nature Communications, 2012. 3(1): p. 902.
116. Choi, S.M., D.F. Tucker, D.N. Gross, R.M. Easton, L.M. DiPilato*, et al.*, *Insulin regulates adipocyte lipolysis via an Akt-independent signaling pathway.* Mol Cell Biol, 2010. 30(21): p. 5009-20.
117. Savova, M.S., L.V. Mihaylova, D. Tews, M. Wabitsch, and M.I. Georgiev, *Targeting PI3K/AKT signaling pathway in obesity.* Biomedicine & Pharmacotherapy, 2023. 159: p. 114244.
118. Wen, X., B. Zhang, B. Wu, H. Xiao, Z. Li*, et al.*, *Signaling pathways in obesity: mechanisms and therapeutic interventions.* Signal Transduction and Targeted Therapy, 2022. 7(1): p. 298.
119. Prusty, D., B.-H. Park, K.E. Davis, and S.R. Farmer, *Activation of MEK/ERK Signaling Promotes Adipogenesis by Enhancing Peroxisome Proliferator-activated Receptor γ (PPARγ) and C/EBPα Gene Expression during the Differentiation of 3T3-L1 Preadipocytes *.* Journal of Biological Chemistry, 2002. 277(48): p. 46226-46232.
120. Huang, X., G. Liu, J. Guo, and Z. Su, *The PI3K/AKT pathway in obesity and type 2 diabetes.* Int J Biol Sci, 2018. 14(11): p. 1483-1496.
121. Smas, C.M., L. Chen, L. Zhao, M.J. Latasa, and H.S. Sul, *Transcriptional repression of pref-1 by glucocorticoids promotes 3T3-L1 adipocyte differentiation.* J Biol Chem, 1999. 274(18): p. 12632-41.

122. Chen, Q., P. Shou, C. Zheng, M. Jiang, G. Cao*, et al.*, *Fate decision of mesenchymal stem cells: adipocytes or osteoblasts?* Cell Death & Differentiation, 2016. 23(7): p. 1128-1139.
123. Schipani, E. and H.M. Kronenberg, *Adult mesenchymal stem cells*, in *StemBook*. 2008, Harvard Stem Cell Institute: Cambridge (MA).
124. Prockop, D.J., *Marrow Stromal Cells as Stem Cells for Nonhematopoietic Tissues.* Science, 1997. 276(5309): p. 71-74.
125. Caplan, A.I., *Mesenchymal stem cells.* Journal of Orthopaedic Research, 1991. 9(5): p. 641-650.
126. Caplan, A.I., *Mesenchymal Stem Cells: Time to Change the Name!* STEM CELLS Translational Medicine, 2017. 6(6): p. 1445-1451.
127. Via, A.G., A. Frizziero, and F. Oliva, *Biological properties of mesenchymal Stem Cells from different sources.* Muscles, ligaments and tendons journal, 2012. 2(3): p. 154-162.
128. Dominici, M., K. Le Blanc, I. Mueller, I. Slaper-Cortenbach, F. Marini*, et al.*, *Minimal criteria for defining multipotent mesenchymal stromal cells. The International Society for Cellular Therapy position statement.* Cytotherapy, 2006. 8(4): p. 315-7.
129. Margiana, R., A. Markov, A.O. Zekiy, M.U. Hamza, K.A. Al-Dabbagh*, et al.*, *Clinical application of mesenchymal stem cell in regenerative medicine: a narrative review.* Stem Cell Research & Therapy, 2022. 13(1): p. 366.
130. Jones, D.L. and A.J. Wagers, *No place like home: anatomy and function of the stem cell niche.* Nature Reviews Molecular Cell Biology, 2008. 9(1): p. 11-21.
131. Sbierski-Kind, J., N. Mroz, and A.B. Molofsky, *Perivascular stromal cells: Directors of tissue immune niches.* Immunol Rev, 2021. 302(1): p. 10-31.
132. Hass, R., C. Kasper, S. Böhm, and R. Jacobs, *Different populations and sources of human mesenchymal stem cells (MSC): A comparison of adult and neonatal tissue-derived MSC.* Cell Communication and Signaling, 2011. 9(1): p. 12.
133. Xu, L. and G. Li, *Circulating mesenchymal stem cells and their clinical implications.* Journal of Orthopaedic Translation, 2014. 2(1): p. 1-7.
134. zur Nieden, N.I., G. Kempka, D.E. Rancourt, and H.-J. Ahr, *Induction of chondro-, osteo- and adipogenesis in embryonic stem cells by bone morphogenetic protein-2: Effect of cofactors on differentiating lineages.* BMC Developmental Biology, 2005. 5(1): p. 1.
135. Bennett, C.N., H. Ouyang, Y.L. Ma, Q. Zeng, I. Gerin*, et al.*, *Wnt10b increases postnatal bone formation by enhancing osteoblast differentiation.* J Bone Miner Res, 2007. 22(12): p. 1924-32.
136. Boland, G.M., G. Perkins, D.J. Hall, and R.S. Tuan, *Wnt 3a promotes proliferation and suppresses osteogenic differentiation of adult human mesenchymal stem cells.* Journal of Cellular Biochemistry, 2004. 93(6): p. 1210-1230.
137. Kim, J.-A., H.-K. Choi, T.-M. Kim, S.-H. Leem, and I.-H. Oh, *Regulation of mesenchymal stromal cells through fine tuning of canonical Wnt signaling.* Stem Cell Research, 2015. 14(3): p. 356-368.

138. Ross, S.E., N. Hemati, K.A. Longo, C.N. Bennett, P.C. Lucas*, et al.*, *Inhibition of Adipogenesis by Wnt Signaling.* Science, 2000. 289(5481): p. 950-953.
139. de Winter, T.J.J. and R. Nusse, *Running Against the Wnt: How Wnt/β-Catenin Suppresses Adipogenesis.* Frontiers in Cell and Developmental Biology, 2021. 9.
140. Kopan, R., *Notch signaling.* Cold Spring Harb Perspect Biol, 2012. 4(10).
141. Baron, M., *An overview of the Notch signalling pathway.* Seminars in Cell & Developmental Biology, 2003. 14(2): p. 113-119.
142. Ross, D.A., P.K. Rao, and T. Kadesch, *Dual roles for the Notch target gene Hes-1 in the differentiation of 3T3-L1 preadipocytes.* Mol Cell Biol, 2004. 24(8): p. 3505-13.
143. Song, B.Q., Y. Chi, X. Li, W.J. Du, Z.B. Han*, et al.*, *Inhibition of Notch Signaling Promotes the Adipogenic Differentiation of Mesenchymal Stem Cells Through Autophagy Activation and PTEN-PI3K/AKT/mTOR Pathway.* Cell Physiol Biochem, 2015. 36(5): p. 1991-2002.
144. Shimizu, T., T. Tanaka, T. Iso, H. Matsui, Y. Ooyama*, et al.*, *Notch signaling pathway enhances bone morphogenetic protein 2 (BMP2) responsiveness of Msx2 gene to induce osteogenic differentiation and mineralization of vascular smooth muscle cells.* J Biol Chem, 2011. 286(21): p. 19138-48.
145. Deng, Z.L., K.A. Sharff, N. Tang, W.X. Song, J. Luo*, et al.*, *Regulation of osteogenic differentiation during skeletal development.* Front Biosci, 2008. 13: p. 2001-21.
146. Fontaine, C., W. Cousin, M. Plaisant, C. Dani, and P. Peraldi, *Hedgehog signaling alters adipocyte maturation of human mesenchymal stem cells.* Stem Cells, 2008. 26(4): p. 1037-46.
147. Spinella-Jaegle, S., G. Rawadi, S. Kawai, S. Gallea, C. Faucheu*, et al.*, *Sonic hedgehog increases the commitment of pluripotent mesenchymal cells into the osteoblastic lineage and abolishes adipocytic differentiation.* J Cell Sci, 2001. 114(Pt 11): p. 2085-94.
148. Oexle, H., E. Gnaiger, and G. Weiss, *Iron-dependent changes in cellular energy metabolism: influence on citric acid cycle and oxidative phosphorylation.* Biochim Biophys Acta, 1999. 1413(3): p. 99-107.
149. Bonora, M., S. Patergnani, A. Rimessi, E. De Marchi, J.M. Suski*, et al.*, *ATP synthesis and storage.* Purinergic Signal, 2012. 8(3): p. 343-57.
150. Cooper, G., *The Mechanism of Oxidative Phosphorylation.* The Cell: A Molecular Approach. 2nd edition. Sunderland (MA): Sinauer Associates, 2000.
151. Yan, W., S. Diao, and Z. Fan, *The role and mechanism of mitochondrial functions and energy metabolism in the function regulation of the mesenchymal stem cells.* Stem Cell Research & Therapy, 2021. 12(1): p. 140.
152. Rafalski, V.A., E. Mancini, and A. Brunet, *Energy metabolism and energy-sensing pathways in mammalian embryonic and adult stem cell fate.* J Cell Sci, 2012. 125(Pt 23): p. 5597-608.
153. Zhang, Y., G. Marsboom, P.T. Toth, and J. Rehman, *Mitochondrial Respiration Regulates Adipogenic Differentiation of Human Mesenchymal Stem Cells.* PLOS ONE, 2013. 8(10): p. e77077.

154. Hsu, Y.-C., Y.-T. Wu, T.-H. Yu, and Y.-H. Wei, *Mitochondria in mesenchymal stem cell biology and cell therapy: From cellular differentiation to mitochondrial transfer.* Seminars in Cell & Developmental Biology, 2016. 52: p. 119-131.
155. Pierce, J.L., D.L. Begun, J.J. Westendorf, and M.E. McGee-Lawrence, *Defining osteoblast and adipocyte lineages in the bone marrow.* Bone, 2019. 118: p. 2-7.
156. Tencerova, M., E. Rendina-Ruedy, D. Neess, N. Færgeman, F. Figeac*, et al.*, *Metabolic programming determines the lineage-differentiation fate of murine bone marrow stromal progenitor cells.* Bone Research, 2019. 7(1): p. 35.
157. Wellen, K.E., G. Hatzivassiliou, U.M. Sachdeva, T.V. Bui, J.R. Cross*, et al.*, *ATP-citrate lyase links cellular metabolism to histone acetylation.* Science, 2009. 324(5930): p. 1076-80.
158. Lee, W.C., A.R. Guntur, F. Long, and C.J. Rosen, *Energy Metabolism of the Osteoblast: Implications for Osteoporosis.* Endocr Rev, 2017. 38(3): p. 255-266.
159. Fujihara, C., T. Nantakeeratipat, and S. Murakami, *Energy Metabolism in Osteogenic Differentiation and Reprogramming: A Possible Future Strategy for Periodontal Regeneration.* Frontiers in Dental Medicine, 2022. 3.
160. Drehmer, D.L., A.M. de Aguiar, A.P. Brandt, L. Petiz, S.M.S.C. Cadena*, et al.*, *Metabolic switches during the first steps of adipogenic stem cells differentiation.* Stem Cell Research, 2016. 17(2): p. 413-421.
161. Li, Q., Z. Gao, Y. Chen, and M.X. Guan, *The role of mitochondria in osteogenic, adipogenic and chondrogenic differentiation of mesenchymal stem cells.* Protein Cell, 2017. 8(6): p. 439-445.
162. Fujisawa, K., T. Takami, S. Okada, K. Hara, T. Matsumoto*, et al.*, *Analysis of Metabolomic Changes in Mesenchymal Stem Cells on Treatment with Desferrioxamine as a Hypoxia Mimetic Compared with Hypoxic Conditions.* Stem Cells, 2018. 36(8): p. 1226-1236.
163. Zhao, G.-y., L.-p. Zhao, Y.-f. He, G.-F. Li, C. Gao*, et al.*, *A Comparison of the Biological Activities of Human Osteoblast hFOB1.19 Between Iron Excess and Iron Deficiency.* Biological Trace Element Research, 2012. 150(1): p. 487-495.
164. Suzuki, T., T. Komatsu, H. Shibata, A. Tanioka, D. Vargas*, et al.*, *Crucial role of iron in epigenetic rewriting during adipocyte differentiation mediated by JMJD1A and TET2 activity.* Nucleic Acids Research, 2023. 51(12): p. 6120-6142.
165. Lee, H., Y.J. Lee, H. Choi, J.W. Seok, B.K. Yoon*, et al.*, *SCARA5 plays a critical role in the commitment of mesenchymal stem cells to adipogenesis.* Sci Rep, 2017. 7(1): p. 14833.
166. Whelan, F.J., C.J. Meehan, G.B. Golding, B.J. McConkey, and D.M. Bowdish, *The evolution of the class A scavenger receptors.* BMC Evol Biol, 2012. 12: p. 227.
167. Yu, B., C. Cheng, Y. Wu, L. Guo, D. Kong*, et al.*, *Interactions of ferritin with scavenger receptor class A members.* Journal of Biological Chemistry, 2020. 295(46): p. 15727-15741.
168. Fang, Y., F. Wu, G. Shang, and C. Yin, *SCARA5 in bone marrow stromal cell-derived exosomes inhibits colorectal cancer progression by inactivating the PI3K/Akt pathway.* Genomics, 2023. 115(4): p. 110636.

169. Huang, J., C. Lv, B. Zhao, Z. Ji, and Z. Gao, *SCARA5 inhibits oral squamous cell carcinoma via inactivating the STAT3 and PI3K/AKT signaling pathways.* Open Med (Wars), 2023. 18(1): p. 20230627.
170. You, K., F. Su, L. Liu, X. Lv, J. Zhang*, et al.*, *SCARA5 plays a critical role in the progression and metastasis of breast cancer by inactivating the ERK1/2, STAT3, and AKT signaling pathways.* Molecular and Cellular Biochemistry, 2017. 435(1-2): p. 47-58.
171. PrabhuDas, M.R., C.L. Baldwin, P.L. Bollyky, D.M.E. Bowdish, K. Drickamer*, et al.*, *A Consensus Definitive Classification of Scavenger Receptors and Their Roles in Health and Disease.* J Immunol, 2017. 198(10): p. 3775-3789.
172. Jiang, Y., P. Oliver, K.E. Davies, and N. Platt, *Identification and characterization of murine SCARA5, a novel class A scavenger receptor that is expressed by populations of epithelial cells.* J Biol Chem, 2006. 281(17): p. 11834-45.
173. Dunne, D.W., D. Resnick, J. Greenberg, M. Krieger, and K.A. Joiner, *The type I macrophage scavenger receptor binds to gram-positive bacteria and recognizes lipoteichoic acid.* Proc Natl Acad Sci U S A, 1994. 91(5): p. 1863-7.
174. Taban, Q., P.T. Mumtaz, K.Z. Masoodi, E. Haq, and S.M. Ahmad, *Scavenger receptors in host defense: from functional aspects to mode of action.* Cell Communication and Signaling, 2022. 20(1): p. 2.
175. Cheng, C., E. Zheng, B. Yu, Z. Zhang, Y. Wang*, et al.*, *Recognition of lipoproteins by scavenger receptor class A members.* Journal of Biological Chemistry, 2021. 297(2).
176. Moore, K.J. and M.W. Freeman, *Scavenger Receptors in Atherosclerosis.* Arteriosclerosis, Thrombosis, and Vascular Biology, 2006. 26(8): p. 1702-1711.
177. Swystun, L.L., K. Ogiwara, J.D. Lai, J.R.M. Ojala, O. Rawley*, et al.*, *The scavenger receptor SCARA5 is an endocytic receptor for von Willebrand factor expressed by littoral cells in the human spleen.* J Thromb Haemost, 2019. 17(8): p. 1384-1396.
178. Ojala, J.R., T. Pikkarainen, G. Elmberger, and K. Tryggvason, *Progressive reactive lymphoid connective tissue disease and development of autoantibodies in scavenger receptor A5-deficient mice.* Am J Pathol, 2013. 182(5): p. 1681-95.
179. Uffelmann, E., Q.Q. Huang, N.S. Munung, J. de Vries, Y. Okada*, et al.*, *Genome-wide association studies.* Nature Reviews Methods Primers, 2021. 1(1): p. 59.
180. Gouveia, C., E. Gibbons, N. Dehghani, J. Eapen, R. Guerreiro*, et al.*, *Genome-wide association of polygenic risk extremes for Alzheimer's disease in the UK Biobank.* Sci Rep, 2022. 12(1): p. 8404.
181. Sanchez-Roige, S., P. Fontanillas, S.L. Elson, J.C. Gray, H. de Wit*, et al.*, *Genome-Wide Association Studies of Impulsive Personality Traits (BIS-11 and UPPS-P) and Drug Experimentation in up to 22,861 Adult Research Participants Identify Loci in the CACNA1I and CADM2 genes.* J Neurosci, 2019. 39(13): p. 2562-2572.
182. Emilsson, V., M. Ilkov, J.R. Lamb, N. Finkel, E.F. Gudmundsson*, et al.*, *Co-regulatory networks of human serum proteins link genetics to disease.* Science, 2018. 361(6404): p. 769-773.

183. Gudjonsson, A., V. Gudmundsdottir, G.T. Axelsson, E.F. Gudmundsson, B.G. Jonsson*, et al.*, *A genome-wide association study of serum proteins reveals shared loci with common diseases.* Nat Commun, 2022. 13(1): p. 480.
184. Kichaev, G., G. Bhatia, P.R. Loh, S. Gazal, K. Burch*, et al.*, *Leveraging Polygenic Functional Enrichment to Improve GWAS Power.* Am J Hum Genet, 2019. 104(1): p. 65-75.
185. Yengo, L., S. Vedantam, E. Marouli, J. Sidorenko, E. Bartell*, et al.*, *A saturated map of common genetic variants associated with human height.* Nature, 2022. 610(7933): p. 704-712.
186. Cosentino, J., B. Behsaz, B. Alipanahi, Z.R. McCaw, D. Hill*, et al.*, *Inference of chronic obstructive pulmonary disease with deep learning on raw spirograms identifies new genetic loci and improves risk models.* Nat Genet, 2023. 55(5): p. 787-795.
187. Nardone, G.G., B. Spedicati, M.P. Concas, A. Santin, A. Morgan*, et al.*, *Identifying missing pieces in color vision defects: a genome-wide association study in Silk Road populations.* Front Genet, 2023. 14: p. 1161696.
188. Zhang, Q., R.E. Marioni, M.R. Robinson, J. Higham, D. Sproul*, et al.*, *Genotype effects contribute to variation in longitudinal methylome patterns in older people.* Genome Med, 2018. 10(1): p. 75.
189. Sakaue, S., M. Kanai, Y. Tanigawa, J. Karjalainen, M. Kurki*, et al.*, *A cross-population atlas of genetic associations for 220 human phenotypes.* Nat Genet, 2021. 53(10): p. 1415-1424.
190. Sabater-Lleal, M., J.E. Huffman, P.S. de Vries, J. Marten, M.A. Mastrangelo*, et al.*, *Genome-Wide Association Transethnic Meta-Analyses Identifies Novel Associations Regulating Coagulation Factor VIII and von Willebrand Factor Plasma Levels.* Circulation, 2019. 139(5): p. 620-635.
191. Temprano-Sagrera, G., C.M. Sitlani, W.P. Bone, M. Martin-Bornez, B.F. Voight*, et al.*, *Multi-phenotype analyses of hemostatic traits with cardiovascular events reveal novel genetic associations.* J Thromb Haemost, 2022. 20(6): p. 1331-1349.
192. Sun, B.B., J.C. Maranville, J.E. Peters, D. Stacey, J.R. Staley*, et al.*, *Genomic atlas of the human plasma proteome.* Nature, 2018. 558(7708): p. 73-79.
193. Surapaneni, A., P. Schlosser, L. Zhou, C. Liu, N. Chatterjee*, et al.*, *Identification of 969 protein quantitative trait loci in an African American population with kidney disease attributed to hypertension.* Kidney Int, 2022. 102(5): p. 1167-1177.
194. Pietzner, M., E. Wheeler, J. Carrasco-Zanini, A. Cortes, M. Koprulu*, et al.*, *Mapping the proteo-genomic convergence of human diseases.* Science, 2021. 374(6569): p. eabj1541.
195. Low, S.K., S. Chung, A. Takahashi, H. Zembutsu, T. Mushiroda*, et al.*, *Genome-wide association study of chemotherapeutic agent-induced severe neutropenia/leucopenia for patients in Biobank Japan.* Cancer Sci, 2013. 104(8): p. 1074-82.

196. Thareja, G., A. Belkadi, M. Arnold, O.M.E. Albagha, J. Graumann*, et al.*, *Differences and commonalities in the genetic architecture of protein quantitative trait loci in European and Arab populations.* Hum Mol Genet, 2023. 32(6): p. 907-916.
197. Bhatt, I.S., N. Wilson, R. Dias, and A. Torkamani, *A genome-wide association study of tinnitus reveals shared genetic links to neuropsychiatric disorders.* Sci Rep, 2022. 12(1): p. 22511.
198. Wells, H.R.R., F.N.Z. Abidin, M.B. Freidin, F.M.K. Williams, and S.J. Dawson, *Genome-wide association study suggests that variation at the RCOR1 locus is associated with tinnitus in UK Biobank.* Sci Rep, 2021. 11(1): p. 6470.
199. van Loon, J., A. Dehghan, T. Weihong, S. Trompet, W.L. McArdle*, et al.*, *Genome-wide association studies identify genetic loci for low von Willebrand factor levels.* Eur J Hum Genet, 2016. 24(7): p. 1035-40.
200. *Expression Atlas*. [01/2024]; Available from: https://www.ebi.ac.uk/gxa/home.
201. Wang, D., B. Eraslan, T. Wieland, B. Hallström, T. Hopf*, et al. A deep proteome and transcriptome abundance atlas of 29 healthy human tissues*. Molecular systems biology, 2019. 15, e8503 DOI: 10.15252/msb.20188503.
202. *Scara5_Homo sapiens (Expression Atlas)*. [01/2024]; Available from: https://www.ebi.ac.uk/gxa/genes/ensg00000168079?bs=%7B%22homo%20sapiens%22%3A%5B%22ORGANISM_PART%22%5D%7D&ds=%7B%22kingdom%22%3A%5B%22animals%22%5D%7D#baseline.
203. Huttlin, E.L., M.P. Jedrychowski, J.E. Elias, T. Goswami, R. Rad*, et al.*, *A tissue-specific atlas of mouse protein phosphorylation and expression.* Cell, 2010. 143(7): p. 1174-1189.
204. *Scara5_Mus musculus (Expression Atlas)*. [01/2024]; Available from: https://www.ebi.ac.uk/gxa/genes/ensmusg00000022032?bs=%7B%22mus%20musculus%22%3A%5B%22ORGANISM_PART%22%5D%7D&ds=%7B%22kingdom%22%3A%5B%22animals%22%5D%7D#baseline.
205. Ginzburg, Y.Z., *Hepcidin-ferroportin axis in health and disease.* Vitam Horm, 2019. 110: p. 17-45.
206. Ganz, T. and E. Nemeth, *The hepcidin-ferroportin system as a therapeutic target in anemias and iron overload disorders.* Hematology Am Soc Hematol Educ Program, 2011. 2011: p. 538-42.
207. Soldin, O.P., L.H. Bierbower, J.J. Choi, J.J. Choi, S. Thompson-Hoffman*, et al.*, *Serum iron, ferritin, transferrin, total iron binding capacity, hs-CRP, LDL cholesterol and magnesium in children; new reference intervals using the Dade Dimension Clinical Chemistry System.* Clin Chim Acta, 2004. 342(1-2): p. 211-7.
208. Wang, W., M.A. Knovich, L.G. Coffman, F.M. Torti, and S.V. Torti, *Serum ferritin: Past, present and future.* Biochim Biophys Acta, 2010. 1800(8): p. 760-9.
209. Kotla, N.K., P. Dutta, S. Parimi, and N.K. Das, *The Role of Ferritin in Health and Disease: Recent Advances and Understandings.* Metabolites, 2022. 12(7).
210. Knovich, M.A., J.A. Storey, L.G. Coffman, S.V. Torti, and F.M. Torti, *Ferritin for the clinician.* Blood Rev, 2009. 23(3): p. 95-104.

211. Chen, T.T., L. Li, D.H. Chung, C.D. Allen, S.V. Torti*, et al.*, *TIM-2 is expressed on B cells and in liver and kidney and is a receptor for H-ferritin endocytosis.* J Exp Med, 2005. 202(7): p. 955-65.
212. Li, L., C.J. Fang, J.C. Ryan, E.C. Niemi, J.A. Lebrón*, et al.*, *Binding and uptake of H-ferritin are mediated by human transferrin receptor-1.* Proc Natl Acad Sci U S A, 2010. 107(8): p. 3505-10.
213. Li, J.Y., N. Paragas, R.M. Ned, A. Qiu, M. Viltard*, et al.*, *Scara5 Is a Ferritin Receptor Mediating Non-Transferrin Iron Delivery.* Developmental Cell, 2009. 16(1): p. 35-46.
214. Mendes-Jorge, L., D. Ramos, A. Valença, M. López-Luppo, V.M.R. Pires*, et al.*, *L-ferritin binding to scara5: a new iron traffic pathway potentially implicated in retinopathy.* PloS one, 2014. 9(9): p. e106974-e106974.
215. Liu, Y., R. Xiong, T. Xiao, L. Xiong, J. Wu*, et al.*, *SCARA5 induced ferroptosis to effect ESCC proliferation and metastasis by combining with Ferritin light chain.* BMC Cancer, 2022. 22(1): p. 1304.
216. Lin, Y.L., W.J.S. de Villiers, B. Garvy, S.R. Post, T.R. Nagy*, et al.*, *The effect of class a scavenger receptor deficiency in bone.* J Biol Chem, 2007. 282(7): p. 4653-4660.
217. Yao, Y., X. Cai, F. Ren, Y. Ye, F. Wang*, et al.*, *The Macrophage-Osteoclast Axis in Osteoimmunity and Osteo-Related Diseases.* Front Immunol, 2021. 12: p. 664871.
218. Chen, P., B. Hu, L.Q. Xie, T.J. Jiang, Z.Y. Xia*, et al.*, *Scara3 regulates bone marrow mesenchymal stem cell fate switch between osteoblasts and adipocytes by promoting Foxo1.* Cell Prolif, 2021. 54(8): p. e13095.
219. Huang, J., D.L. Zheng, F.S. Qin, N. Cheng, H. Chen*, et al.*, *Genetic and epigenetic silencing of SCARA5 may contribute to human hepatocellular carcinoma by activating FAK signaling.* J Clin Invest, 2010. 120(1): p. 223-41.
220. Salasznyk, R.M., R.F. Klees, W.A. Williams, A. Boskey, and G.E. Plopper, *Focal adhesion kinase signaling pathways regulate the osteogenic differentiation of human mesenchymal stem cells.* Experimental cell research, 2007. 313(1): p. 22-37.
221. Yan, N., S. Zhang, Y. Yang, L. Cheng, C. Li*, et al.*, *Therapeutic upregulation of Class A scavenger receptor member 5 inhibits tumor growth and metastasis.* Cancer Sci, 2012. 103(9): p. 1631-9.
222. Wang, J., S. Wang, L. Chen, and J. Tan, *SCARA5 suppresses the proliferation and migration, and promotes the apoptosis of human retinoblastoma cells by inhibiting the PI3K/AKT pathway.* Mol Med Rep, 2021. 23(3).
223. Arnold, M., E. Morgan, H. Rumgay, A. Mafra, D. Singh*, et al.*, *Current and future burden of breast cancer: Global statistics for 2020 and 2040.* Breast, 2022. 66: p. 15-23.
224. Orrantia-Borunda, E., P. Anchondo-Nuñez, L.E. Acuña-Aguilar, F.O. Gómez-Valles, and C.A. Ramírez-Valdespino, *Subtypes of Breast Cancer*, in *Breast Cancer*, H.N. Mayrovitz, Editor. 2022, Exon Publications: Brisbane (AU).

225. Kothari, C., C. Diorio, and F. Durocher, *The Importance of Breast Adipose Tissue in Breast Cancer.* Int J Mol Sci, 2020. 21(16).
226. Brock, C.K., K.L. Hebert, M. Artiles, M.K. Wright, T. Cheng*, et al.*, *A Role for Adipocytes and Adipose Stem Cells in the Breast Tumor Microenvironment and Regenerative Medicine.* Front Physiol, 2021. 12: p. 751239.
227. Bhaskaran, K., I. Douglas, H. Forbes, I. dos-Santos-Silva, D.A. Leon*, et al.*, *Body-mass index and risk of 22 specific cancers: a population-based cohort study of 5·24 million UK adults.* Lancet, 2014. 384(9945): p. 755-65.
228. Wu, Q., B. Li, Z. Li, J. Li, S. Sun*, et al.*, *Cancer-associated adipocytes: key players in breast cancer progression.* Journal of Hematology & Oncology, 2019. 12(1): p. 95.
229. Huang, X., J. Cao, and X. Zu, *Tumor-associated macrophages: An important player in breast cancer progression.* Thorac Cancer, 2022. 13(3): p. 269-276.
230. Núñez-Ruiz, A., F. Sánchez-Brena, C. López-Pacheco, N.A. Acevedo-Domínguez, and G. Soldevila, *Obesity modulates the immune macroenvironment associated with breast cancer development.* PLoS One, 2022. 17(4): p. e0266827.
231. Kolb, R. and W. Zhang, *Obesity and Breast Cancer: A Case of Inflamed Adipose Tissue.* Cancers (Basel), 2020. 12(6).
232. Sul, J.H., B. Han, C. Ye, T. Choi, and E. Eskin, *Effectively Identifying eQTLs from Multiple Tissues by Combining Mixed Model and Meta-analytic Approaches.* PLOS Genetics, 2013. 9(6): p. e1003491.
233. Huang, S., L. Xu, Y. Sun, T. Wu, K. Wang*, et al.*, *An improved protocol for isolation and culture of mesenchymal stem cells from mouse bone marrow.* J Orthop Translat, 2015. 3(1): p. 26-33.
234. Marozin, S., B. Simon-Nobbe, S. Irausek, L.W.K. Chung, and G. Lepperdinger, *Kinship of conditionally immortalized cells derived from fetal bone to human bone-derived mesenchymal stroma cells.* Scientific Reports, 2021. 11(1): p. 10933.
235. Kim, B.-Y., H.-Y. Yoon, S.-I. Yun, E.-R. Woo, N.-K. Song*, et al.*, *In Vitro and In Vivo Inhibition of Glucocorticoid-induced Osteoporosis by the Hexane Extract of Poncirus trifoliata.* Phytotherapy Research, 2011. 25(7): p. 1000-1010.
236. Tang, D.-Z., W. Hou, Q. Zhou, M. Zhang, J. Holz*, et al.*, *Osthole stimulates osteoblast differentiation and bone formation by activation of β-catenin–BMP signaling.* Journal of Bone and Mineral Research, 2010. 25(6): p. 1234-1245.
237. Sebastian, A., N.R. Hum, D.K. Murugesh, S. Hatsell, A.N. Economides*, et al.*, *Wnt co-receptors Lrp5 and Lrp6 differentially mediate Wnt3a signaling in osteoblasts.* PLoS One, 2017. 12(11): p. e0188264.
238. Dayton, T.L., V. Gocheva, K.M. Miller, A. Bhutkar, C.A. Lewis*, et al.*, *Isoform-specific deletion of PKM2 constrains tumor initiation in a mouse model of soft tissue sarcoma.* Cancer & Metabolism, 2018. 6(1): p. 6.
239. Gurley, J.M., B.A. Griesel, and A.L. Olson, *Increased Skeletal Muscle GLUT4 Expression in Obese Mice After Voluntary Wheel Running Exercise Is Posttranscriptional.* Diabetes, 2016. 65(10): p. 2911-9.

240. Manna, P.R., J. Cohen-Tannoudji, R. Counis, C.W. Garner, I. Huhtaniemi*, et al.*, *Mechanisms of action of hormone-sensitive lipase in mouse Leydig cells: its role in the regulation of the steroidogenic acute regulatory protein.* J Biol Chem, 2013. 288(12): p. 8505-8518.
241. Scheller, E.L., N. Troiano, J.N. Vanhoutan, M.A. Bouxsein, J.A. Fretz*, et al.*, *Use of osmium tetroxide staining with microcomputerized tomography to visualize and quantify bone marrow adipose tissue in vivo.* Methods Enzymol, 2014. 537: p. 123-39.
242. Galarraga, M., J. Campión, A. Muñoz-Barrutia, N. Boqué, H. Moreno*, et al.*, *Adiposoft: automated software for the analysis of white adipose tissue cellularity in histological sections.* Journal of Lipid Research, 2012. 53(12): p. 2791-2796.
243. McGregor, N.E., I.J. Poulton, E.C. Walker, and N.A. Sims, *Testing Bone Formation Induction by Calvarial Injection Assay in vivo.* Bio-protocol, 2020. 10(6): p. e3560.
244. Deeds, M.C., J.M. Anderson, A.S. Armstrong, D.A. Gastineau, H.J. Hiddinga*, et al.*, *Single dose streptozotocin-induced diabetes: considerations for study design in islet transplantation models.* Lab Anim, 2011. 45(3): p. 131-40.
245. Ullah, I., R.B. Subbarao, and G.J. Rho, *Human mesenchymal stem cells - current trends and future prospective.* Biosci Rep, 2015. 35(2).
246. Zhu, H., Z.K. Guo, X.X. Jiang, H. Li, X.Y. Wang*, et al.*, *A protocol for isolation and culture of mesenchymal stem cells from mouse compact bone.* Nat Protoc, 2010. 5(3): p. 550-60.
247. Yen, M.-L., C.-C. Chien, I.-M. Chiu, H.-I. Huang, Y.-C. Chen*, et al.*, *Multilineage Differentiation and Characterization of the Human Fetal Osteoblastic 1.19 Cell Line: A Possible In Vitro Model of Human Mesenchymal Progenitors.* Stem cells (Dayton, Ohio), 2007. 25: p. 125-31.
248. Lim, K.R.Q. and T. Yokota, *Invention and Early History of Gapmers.* Methods Mol Biol, 2020. 2176: p. 3-19.
249. Zhang, Y., D. Khan, J. Delling, and E. Tobiasch, *Mechanisms Underlying the Osteo- and Adipo-Differentiation of Human Mesenchymal Stem Cells.* TheScientificWorldJournal, 2012. 2012: p. 793823.
250. Pavathuparambil Abdul Manaph, N., K.N. Sivanathan, J. Nitschke, X.-F. Zhou, P.T. Coates*, et al.*, *An overview on small molecule-induced differentiation of mesenchymal stem cells into beta cells for diabetic therapy.* Stem Cell Research & Therapy, 2019. 10(1): p. 293.
251. Hu, L.F., C. Yin, F. Zhao, A. Ali, J.H. Ma*, et al.*, *Mesenchymal Stem Cells: Cell Fate Decision to Osteoblast or Adipocyte and Application in Osteoporosis Treatment.* International Journal of Molecular Sciences, 2018. 19(2).
252. Moerman, E.J., K. Teng, D.A. Lipschitz, and B. Lecka-Czernik, *Aging activates adipogenic and suppresses osteogenic programs in mesenchymal marrow stroma/stem cells: the role of PPAR-gamma2 transcription factor and TGF-beta/BMP signaling pathways.* Aging Cell, 2004. 3(6): p. 379-89.

253. Nicolaidou, V., M.M. Wong, A.N. Redpath, A. Ersek, D.F. Baban*, et al.*, *Monocytes induce STAT3 activation in human mesenchymal stem cells to promote osteoblast formation.* PLoS One, 2012. 7(7): p. e39871.
254. Guihard, P., Y. Danger, B. Brounais, E. David, R. Brion*, et al.*, *Induction of osteogenesis in mesenchymal stem cells by activated monocytes/macrophages depends on oncostatin M signaling.* Stem Cells, 2012. 30(4): p. 762-72.
255. Thomas, S. and B.G. Jaganathan, *Signaling network regulating osteogenesis in mesenchymal stem cells.* J Cell Commun Signal, 2022. 16(1): p. 47-61.
256. Xu, L., Y. Liu, Y. Sun, B. Wang, Y. Xiong*, et al.*, *Tissue source determines the differentiation potentials of mesenchymal stem cells: a comparative study of human mesenchymal stem cells from bone marrow and adipose tissue.* Stem Cell Res Ther, 2017. 8(1): p. 275.
257. Coelho, M.J. and M.H. Fernandes, *Human bone cell cultures in biocompatibility testing. Part II: effect of ascorbic acid, beta-glycerophosphate and dexamethasone on osteoblastic differentiation.* Biomaterials, 2000. 21(11): p. 1095-102.
258. Huang, W., S. Yang, J. Shao, and Y.-P. Li, *Signaling and transcriptional regulation in osteoblast commitment and differentiation.* FBL, 2007. 12(8): p. 3068-3092.
259. Ahmad, B., C.J. Serpell, I.L. Fong, and E.H. Wong, *Molecular Mechanisms of Adipogenesis: The Anti-adipogenic Role of AMP-Activated Protein Kinase.* Frontiers in Molecular Biosciences, 2020. 7.
260. Martella, E., C. Bellotti, B. Dozza, S. Perrone, D. Donati*, et al.*, *Secreted adiponectin as a marker to evaluate in vitro the adipogenic differentiation of human mesenchymal stromal cells.* Cytotherapy, 2014. 16(11): p. 1476-1485.
261. News, A. *Introducing maxGFP*. 22 May 2023]; Available from: https://www.researchgate.net/file.PostFileLoader.html?id=54e394c5d767a6d54c8b4615&assetKey=AS%3A273704561381376%401442267660878&psig=AOvVaw134vKCqMn-FLLBZd5Mhqoa&ust=1684841444030413/.
262. Phetfong, J., T. Sanvoranart, K. Nartprayut, N. Nimsanor, K. Seenprachawong*, et al.*, *Osteoporosis: the current status of mesenchymal stem cell-based therapy.* Cell Mol Biol Lett, 2016. 21: p. 12.
263. Picke, A.-K., G. Campbell, N. Napoli, L.C. Hofbauer, and M. Rauner, *Update on the impact of type 2 diabetes mellitus on bone metabolism and material properties.* Endocrine Connections, 2019. 8(3): p. R55-R70.
264. *Management of osteoporosis in postmenopausal women: the 2021 position statement of The North American Menopause Society.* Menopause, 2021. 28(9): p. 973-997.
265. Bouxsein, M.L., K.S. Myers, K.L. Shultz, L.R. Donahue, C.J. Rosen*, et al.*, *Ovariectomy-Induced Bone Loss Varies Among Inbred Strains of Mice.* Journal of Bone and Mineral Research, 2005. 20(7): p. 1085-1092.
266. Li, Z., J. Hardij, D.P. Bagchi, E.L. Scheller, and O.A. MacDougald, *Development, regulation, metabolism and function of bone marrow adipose tissues.* Bone, 2018. 110: p. 134-140.

267. Murray, C.E. and C.M. Coleman, *Impact of Diabetes Mellitus on Bone Health.* Int J Mol Sci, 2019. 20(19).
268. Furman, B.L., *Streptozotocin-Induced Diabetic Models in Mice and Rats.* Current Protocols, 2021. 1(4): p. e78.
269. Beamer, W.G., L.R. Donahue, C.J. Rosen, and D.J. Baylink, *Genetic variability in adult bone density among inbred strains of mice.* Bone, 1996. 18(5): p. 397-403.
270. Mun, S.H., S. Jastrzebski, J. Kalinowski, S. Zeng, B. Oh*, et al.*, *Sexual Dimorphism in Differentiating Osteoclast Precursors Demonstrates Enhanced Inflammatory Pathway Activation in Female Cells.* Journal of Bone and Mineral Research, 2021. 36(6): p. 1104-1116.
271. Haffner-Luntzer, M., V. Fischer, and A. Ignatius, *Differences in Fracture Healing Between Female and Male C57BL/6J Mice.* Frontiers in Physiology, 2021. 12.
272. Stenkula, K.G. and C. Erlanson-Albertsson, *Adipose cell size: importance in health and disease.* Am J Physiol Regul Integr Comp Physiol, 2018. 315(2): p. R284-r295.
273. Karastergiou, K., S.R. Smith, A.S. Greenberg, and S.K. Fried, *Sex differences in human adipose tissues - the biology of pear shape.* Biol Sex Differ, 2012. 3(1): p. 13.
274. Adamopoulos, I.E., *Inflammation in bone physiology and pathology.* Curr Opin Rheumatol, 2018. 30(1): p. 59-64.
275. Mountziaris, P.M. and A.G. Mikos, *Modulation of the inflammatory response for enhanced bone tissue regeneration.* Tissue Eng Part B Rev, 2008. 14(2): p. 179-86.
276. Li, X., J. Wang, Z. Zhan, S. Li, Z. Zheng*, et al.*, *Inflammation Intensity–Dependent Expression of Osteoinductive Wnt Proteins Is Critical for Ectopic New Bone Formation in Ankylosing Spondylitis.* Arthritis & Rheumatology, 2018. 70(7): p. 1056-1070.
277. Collison, J., *Low-level inflammation promotes bone growth.* Nature Reviews Rheumatology, 2018. 14(5): p. 249-249.
278. Meng, F. and C.A. Lowell, *Lipopolysaccharide (LPS)-induced macrophage activation and signal transduction in the absence of Src-family kinases Hck, Fgr, and Lyn.* J Exp Med, 1997. 185(9): p. 1661-70.
279. Wu, X., K. Zhao, X. Fang, F. Lu, W. Zhang*, et al.*, *Inhibition of Lipopolysaccharide-Induced Inflammatory Bone Loss by Saikosaponin D is Associated with Regulation of the RANKL/RANK Pathway.* Drug Des Devel Ther, 2021. 15: p. 4741-4757.
280. Yu, W., L. Zhong, L. Yao, Y. Wei, T. Gui*, et al.*, *Bone marrow adipogenic lineage precursors promote osteoclastogenesis in bone remodeling and pathologic bone loss.* The Journal of Clinical Investigation, 2021. 131(2).
281. Chang, M.K., L.-J. Raggatt, K.A. Alexander, J.S. Kuliwaba, N.L. Fazzalari*, et al.*, *Osteal Tissue Macrophages Are Intercalated throughout Human and Mouse Bone Lining Tissues and Regulate Osteoblast Function In Vitro and In Vivo1.* The Journal of Immunology, 2008. 181(2): p. 1232-1244.

282. Pouresmaeili, F., B. Kamalidehghan, M. Kamarehei, and Y.M. Goh, *A comprehensive overview on osteoporosis and its risk factors.* Ther Clin Risk Manag, 2018. 14: p. 2029-2049.
283. Inoue, S., K. Fujikawa, M. Matsuki-Fukushima, and M. Nakamura, *Effect of ovariectomy induced osteoporosis on metaphysis and diaphysis repair process.* Injury, 2021. 52(6): p. 1300-1309.
284. Muruganandan, S., R. Govindarajan, and C.J. Sinal, *Bone Marrow Adipose Tissue and Skeletal Health.* Curr Osteoporos Rep, 2018. 16(4): p. 434-442.
285. Li, Z. and O.A. MacDougald, *Preclinical models for investigating how bone marrow adipocytes influence bone and hematopoietic cellularity.* Best Pract Res Clin Endocrinol Metab, 2021. 35(4): p. 101547.
286. Di Iorgi, N., A.O. Mo, K. Grimm, T.A. Wren, F. Dorey*, et al.*, *Bone acquisition in healthy young females is reciprocally related to marrow adiposity.* J Clin Endocrinol Metab, 2010. 95(6): p. 2977-82.
287. Kalaitzoglou, E., I. Popescu, R.C. Bunn, J.L. Fowlkes, and K.M. Thrailkill, *Effects of Type 1 Diabetes on Osteoblasts, Osteocytes, and Osteoclasts.* Curr Osteoporos Rep, 2016. 14(6): p. 310-319.
288. Hie, M., N. Iitsuka, T. Otsuka, and I. Tsukamoto, *Insulin-dependent diabetes mellitus decreases osteoblastogenesis associated with the inhibition of Wnt signaling through increased expression of Sost and Dkk1 and inhibition of Akt activation.* Int J Mol Med, 2011. 28(3): p. 455-62.
289. Mottalib, A., M. Kasetty, J.Y. Mar, T. Elseaidy, S. Ashrafzadeh*, et al.*, *Weight Management in Patients with Type 1 Diabetes and Obesity.* Curr Diab Rep, 2017. 17(10): p. 92.
290. Song, L., M. Liu, N. Ono, F.R. Bringhurst, H.M. Kronenberg*, et al.*, *Loss of wnt/β-catenin signaling causes cell fate shift of preosteoblasts from osteoblasts to adipocytes.* J Bone Miner Res, 2012. 27(11): p. 2344-58.
291. Chen, J., R. Crawford, C. Chen, and Y. Xiao, *The key regulatory roles of the PI3K/Akt signaling pathway in the functionalities of mesenchymal stem cells and applications in tissue regeneration.* Tissue Eng Part B Rev, 2013. 19(6): p. 516-28.
292. Wyart, E., M.Y. Hsu, R. Sartori, E. Mina, V. Rausch*, et al.*, *Iron supplementation is sufficient to rescue skeletal muscle mass and function in cancer cachexia.* EMBO reports, 2022. 23(4): p. e53746.
293. Galli, C., M. Piemontese, S. Lumetti, E. Manfredi, G.M. Macaluso*, et al.*, *GSK3b-inhibitor lithium chloride enhances activation of Wnt canonical signaling and osteoblast differentiation on hydrophilic titanium surfaces.* Clin Oral Implants Res, 2013. 24(8): p. 921-7.
294. Tang, L., Y. Chen, F. Pei, and H. Zhang, *Lithium Chloride Modulates Adipogenesis and Osteogenesis of Human Bone Marrow-Derived Mesenchymal Stem Cells.* Cell Physiol Biochem, 2015. 37(1): p. 143-52.

295. Rattanawarawipa, P., P. Pavasant, T. Osathanon, and W. Sukarawan, *Effect of lithium chloride on cell proliferation and osteogenic differentiation in stem cells from human exfoliated deciduous teeth.* Tissue Cell, 2016. 48(5): p. 425-31.
296. Yu, Z., L. Fan, J. Li, Z. Ge, X. Dang*, et al.*, *Lithium chloride attenuates the abnormal osteogenic/adipogenic differentiation of bone marrow-derived mesenchymal stem cells obtained from rats with steroid-related osteonecrosis by activating the β-catenin pathway.* Int J Mol Med, 2015. 36(5): p. 1264-72.
297. Wang, Z., D. Guan, S. Wang, L.Y.A. Chai, S. Xu*, et al.*, *Glycolysis and Oxidative Phosphorylation Play Critical Roles in Natural Killer Cell Receptor-Mediated Natural Killer Cell Functions.* Front Immunol, 2020. 11: p. 202.
298. Zhu, Z., J. Yin, J. Guan, B. Hu, X. Niu*, et al.*, *Lithium stimulates human bone marrow derived mesenchymal stem cell proliferation through GSK-3β-dependent β-catenin/Wnt pathway activation.* Febs j, 2014. 281(23): p. 5371-89.
299. Cawthorn, W.P., A.J. Bree, Y. Yao, B. Du, N. Hemati*, et al.*, *Wnt6, Wnt10a and Wnt10b inhibit adipogenesis and stimulate osteoblastogenesis through a β-catenin-dependent mechanism.* Bone, 2012. 50(2): p. 477-89.
300. Tang, Q., C. Chen, Y. Zhang, M. Dai, Y. Jiang*, et al.*, *Wnt5a regulates the cell proliferation and adipogenesis via MAPK-independent pathway in early stage of obesity.* Cell Biol Int, 2018. 42(1): p. 63-74.
301. Okamoto, M., N. Udagawa, S. Uehara, K. Maeda, T. Yamashita*, et al.*, *Noncanonical Wnt5a enhances Wnt/β-catenin signaling during osteoblastogenesis.* Sci Rep, 2014. 4: p. 4493.
302. Hsu, M.N., K.L. Huang, F.J. Yu, P.L. Lai, A.V. Truong*, et al.*, *Coactivation of Endogenous Wnt10b and Foxc2 by CRISPR Activation Enhances BMSC Osteogenesis and Promotes Calvarial Bone Regeneration.* Mol Ther, 2020. 28(2): p. 441-451.
303. Huang, K., S. Cai, T. Fu, Q. Zhu, L. Liu*, et al.*, *Wnt10b regulates osteogenesis of adipose-derived stem cells through Wnt/β-catenin signalling pathway in osteoporosis.* Cell Proliferation, 2023. n/a(n/a): p. e13522.
304. Bennett, C.N., K.A. Longo, W.S. Wright, L.J. Suva, T.F. Lane*, et al.*, *Regulation of osteoblastogenesis and bone mass by Wnt10b.* Proceedings of the National Academy of Sciences, 2005. 102(9): p. 3324-3329.
305. Langenbach, F. and J. Handschel, *Effects of dexamethasone, ascorbic acid and β-glycerophosphate on the osteogenic differentiation of stem cells in vitro.* Stem Cell Research & Therapy, 2013. 4(5): p. 117.
306. Song, X., S. Wang, and L. Li, *New insights into the regulation of Axin function in canonical Wnt signaling pathway.* Protein Cell, 2014. 5(3): p. 186-93.
307. Sharma, M., I. Castro-Piedras, G.E. Simmons, Jr., and K. Pruitt, *Dishevelled: A masterful conductor of complex Wnt signals.* Cell Signal, 2018. 47: p. 52-64.
308. Kubota, T., T. Michigami, and K. Ozono, *Wnt signaling in bone metabolism.* J Bone Miner Metab, 2009. 27(3): p. 265-71.

309. Shang, Y.C., S.H. Wang, F. Xiong, C.P. Zhao, F.N. Peng*, et al.*, *Wnt3a signaling promotes proliferation, myogenic differentiation, and migration of rat bone marrow mesenchymal stem cells.* Acta Pharmacol Sin, 2007. 28(11): p. 1761-74.
310. Reischmann, P., J. Fiebeck, N. von der Weiden, and O. Müller, *Measured Effects of Wnt3a on Proliferation of HEK293T Cells Depend on the Applied Assay.* International Journal of Cell Biology, 2015. 2015: p. 928502.
311. Gharibi, B., M.S. Ghuman, and F.J. Hughes, *Akt- and Erk-mediated regulation of proliferation and differentiation during PDGFRβ-induced MSC self-renewal.* J Cell Mol Med, 2012. 16(11): p. 2789-801.
312. Roux, P.P., D. Shahbazian, H. Vu, M.K. Holz, M.S. Cohen*, et al.*, *RAS/ERK signaling promotes site-specific ribosomal protein S6 phosphorylation via RSK and stimulates cap-dependent translation.* J Biol Chem, 2007. 282(19): p. 14056-64.
313. Ning, X., J. He, X. Shi, and G. Yang, *Regulation of Adipogenesis by Quinine through the ERK/S6 Pathway.* Int J Mol Sci, 2016. 17(4): p. 504.
314. Johnson, B.B., J. Reinhold, T.L. Holmes, J.A. Moore, V. Cowell*, et al.*, *Modelling Metabolic Shifts during Cardiomyocyte Differentiation, Iron Deficiency and Transferrin Rescue Using Human Pluripotent Stem Cells.* Metabolites, 2022. 12(1): p. 9.
315. Fujisawa, K., T. Takami, T. Matsumoto, N. Yamamoto, T. Yamasaki*, et al.*, *An iron chelation-based combinatorial anticancer therapy comprising deferoxamine and a lactate excretion inhibitor inhibits the proliferation of cancer cells.* Cancer & Metabolism, 2022. 10(1): p. 8.
316. Manz, D.H., N.L. Blanchette, B.T. Paul, F.M. Torti, and S.V. Torti, *Iron and cancer: recent insights.* Ann N Y Acad Sci, 2016. 1368(1): p. 149-61.
317. Li, J.J., J.Y. Tsang, and G.M. Tse, *Tumor Microenvironment in Breast Cancer-Updates on Therapeutic Implications and Pathologic Assessment.* Cancers (Basel), 2021. 13(16).
318. Corrêa, L.H., R. Corrêa, C.M. Farinasso, L.P. de Sant'Ana Dourado, and K.G. Magalhães, *Adipocytes and Macrophages Interplay in the Orchestration of Tumor Microenvironment: New Implications in Cancer Progression.* Front Immunol, 2017. 8: p. 1129.
319. Picon-Ruiz, M., C. Pan, K. Drews-Elger, K. Jang, A.H. Besser*, et al.*, *Interactions between Adipocytes and Breast Cancer Cells Stimulate Cytokine Production and Drive Src/Sox2/miR-302b–Mediated Malignant Progression.* Cancer Research, 2016. 76(2): p. 491-504.
320. Pfeifhofer-Obermair, C., P. Tymoszuk, V. Petzer, G. Weiss, and M. Nairz, *Iron in the Tumor Microenvironment-Connecting the Dots.* Front Oncol, 2018. 8: p. 549.
321. Zhang, S., Y. Chen, W. Guo, L. Yuan, D. Zhang*, et al.*, *Disordered hepcidin-ferroportin signaling promotes breast cancer growth.* Cell Signal, 2014. 26(11): p. 2539-50.
322. Rutkowski, M.R., M.J. Allegrezza, N. Svoronos, A.J. Tesone, T.L. Stephen*, et al.*, *Initiation of metastatic breast carcinoma by targeting of the ductal epithelium*

with adenovirus-cre: a novel transgenic mouse model of breast cancer. J Vis Exp, 2014(85).

323. Allegrezza, M.J., M.R. Rutkowski, T.L. Stephen, N. Svoronos, A. Perales-Puchalt*, et al.*, *Trametinib Drives T-cell–Dependent Control of KRAS-Mutated Tumors by Inhibiting Pathological Myelopoiesis.* Cancer Research, 2016. 76(21): p. 6253-6265.
324. Bense, R.D., C. Sotiriou, M.J. Piccart-Gebhart, J. Haanen, M. van Vugt*, et al.*, *Relevance of Tumor-Infiltrating Immune Cell Composition and Functionality for Disease Outcome in Breast Cancer.* J Natl Cancer Inst, 2017. 109(1).
325. Christenson, J.L., K.T. Butterfield, N.S. Spoelstra, J.D. Norris, J.S. Josan*, et al.*, *MMTV-PyMT and Derived Met-1 Mouse Mammary Tumor Cells as Models for Studying the Role of the Androgen Receptor in Triple-Negative Breast Cancer Progression.* Horm Cancer, 2017. 8(2): p. 69-77.
326. Murali, B., Q. Ren, X. Luo, D.V. Faget, C. Wang*, et al.*, *Inhibition of the Stromal p38MAPK/MK2 Pathway Limits Breast Cancer Metastases and Chemotherapy-Induced Bone Loss.* Cancer Res, 2018. 78(19): p. 5618-5630.
327. Lengyel, E., L. Makowski, J. DiGiovanni, and M.G. Kolonin, *Cancer as a Matter of Fat: The Crosstalk between Adipose Tissue and Tumors.* Trends Cancer, 2018. 4(5): p. 374-384.
328. Hartmann, T.N., *Editorial: Metabolism and Cell Adhesion in Cancer.* Frontiers in Cell and Developmental Biology, 2022. 10.
329. Liu, C., P. Wu, A. Zhang, and X. Mao, *Advances in Rodent Models for Breast Cancer Formation, Progression, and Therapeutic Testing.* Frontiers in Oncology, 2021. 11.
330. Wu, Y., X. Li, Q. Li, C. Cheng, and L. Zheng, *Adipose tissue-to-breast cancer crosstalk: Comprehensive insights.* Biochimica et Biophysica Acta (BBA) - Reviews on Cancer, 2022. 1877(5): p. 188800.
331. Kocatürk, B. and H.H. Versteeg, *Orthotopic injection of breast cancer cells into the mammary fat pad of mice to study tumor growth.* J Vis Exp, 2015(96).
332. Buchta Rosean, C., R.R. Bostic, J.C.M. Ferey, T.-Y. Feng, F.N. Azar*, et al.*, *Preexisting Commensal Dysbiosis Is a Host-Intrinsic Regulator of Tissue Inflammation and Tumor Cell Dissemination in Hormone Receptor–Positive Breast Cancer.* Cancer Research, 2019. 79(14): p. 3662-3675.
333. McKee, A.M., B.M. Kirkup, M. Madgwick, W.J. Fowler, C.A. Price*, et al.*, *Antibiotic-induced disturbances of the gut microbiota result in accelerated breast tumor growth.* iScience, 2021. 24(9).
334. Coussens, L.M. and Z. Werb, *Inflammation and cancer.* Nature, 2002. 420(6917): p. 860-7.
335. Talmadge, J.E., M. Donkor, and E. Scholar, *Inflammatory cell infiltration of tumors: Jekyll or Hyde.* Cancer Metastasis Rev, 2007. 26(3-4): p. 373-400.
336. Ulker, D., Y.E. Ersoy, Z. Gucin, M. Muslumanoglu, and N. Buyru, *Downregulation of SCARA5 may contribute to breast cancer via promoter hypermethylation.* Gene, 2018. 673: p. 102-106.

337. Jablonka, A., J. Scheich, F. Jacobsen, T. Hirsch, M. Hagouan*, et al.*, *Influence of preadipocyte-conditioned medium on the proliferation and invasive potential of breast cancer cell lines in vitro.* Archives of Gynecology and Obstetrics, 2018. 298(6): p. 1159-1171.
338. D'Esposito, V., F. Passaretti, A. Hammarstedt, D. Liguoro, D. Terracciano*, et al.*, *Adipocyte-released insulin-like growth factor-1 is regulated by glucose and fatty acids and controls breast cancer cell growth in vitro.* Diabetologia, 2012. 55(10): p. 2811-2822.
339. Zahari, S., S.E. Syafruddin, and M.A. Mohtar, *Impact of the Cancer Cell Secretome in Driving Breast Cancer Progression.* Cancers (Basel), 2023. 15(9).
340. Brown, R.A.M., K.L. Richardson, T.D. Kabir, D. Trinder, R. Ganss*, et al.*, *Altered Iron Metabolism and Impact in Cancer Biology, Metastasis, and Immunology.* Front Oncol, 2020. 10: p. 476.
341. Marques, O., G. Porto, A. Rêma, F. Faria, A. Cruz Paula*, et al.*, *Local iron homeostasis in the breast ductal carcinoma microenvironment.* BMC Cancer, 2016. 16(1): p. 187.
342. Bajbouj, K., J. Shafarin, and M. Hamad, *High-Dose Deferoxamine Treatment Disrupts Intracellular Iron Homeostasis, Reduces Growth, and Induces Apoptosis in Metastatic and Nonmetastatic Breast Cancer Cell Lines.* Technology in Cancer Research & Treatment, 2018. 17: p. 1533033818764470.
343. Kuban-Jankowska, A., K.K. Sahu, M. Gorska-Ponikowska, J.A. Tuszynski, and M. Wozniak, *Inhibitory Activity of Iron Chelators ATA and DFO on MCF-7 Breast Cancer Cells and Phosphatases PTP1B and SHP2.* Anticancer Res, 2017. 37(9): p. 4799-4806.
344. DeRosa, A. and A. Leftin, *The Iron Curtain: Macrophages at the Interface of Systemic and Microenvironmental Iron Metabolism and Immune Response in Cancer.* Frontiers in Immunology, 2021. 12.
345. Avgerinou, C., I. Petersen, A. Clegg, R.M. West, D. Osborn*, et al.*, *Trends in incidence of recorded diagnosis of osteoporosis, osteopenia, and fragility fractures in people aged 50 years and above: retrospective cohort study using UK primary care data.* Osteoporos Int, 2023. 34(8): p. 1411-1427.
346. Ricci, S. and P. Cacialli, *Stem Cell Research Tools in Human Metabolic Disorders: An Overview.* Cells, 2021. 10(10).
347. (WHO), W.H.O. *Obesity and overweight*. 2021 [cited 2023 25/08]; Available from: https://www.who.int/news-room/fact-sheets/detail/obesity-and-overweight.
348. Al-Goblan, A.S., M.A. Al-Alfi, and M.Z. Khan, *Mechanism linking diabetes mellitus and obesity.* Diabetes Metab Syndr Obes, 2014. 7: p. 587-91.
349. Teixeira, C.C., Y. Liu, L.M. Thant, J. Pang, G. Palmer*, et al.*, *Foxo1, a Novel Regulator of Osteoblast Differentiation and Skeletogenesis *.* Journal of Biological Chemistry, 2010. 285(40): p. 31055-31065.

350. Ma, X., P. Su, C. Yin, X. Lin, X. Wang*, et al.*, *The Roles of FoxO Transcription Factors in Regulation of Bone Cells Function.* International Journal of Molecular Sciences, 2020. 21(3): p. 692.
351. Hu, J., H. Liao, Z. Ma, H. Chen, Z. Huang*, et al.*, *Focal Adhesion Kinase Signaling Mediated the Enhancement of Osteogenesis of Human Mesenchymal Stem Cells Induced by Extracorporeal Shockwave.* Sci Rep, 2016. 6: p. 20875.
352. Kim, S.L., S. Shin, and S.J. Yang, *Iron Homeostasis and Energy Metabolism in Obesity.* Clin Nutr Res, 2022. 11(4): p. 316-330.
353. Lee, J.H., A. Park, K.J. Oh, S.C. Lee, W.K. Kim*, et al.*, *The Role of Adipose Tissue Mitochondria: Regulation of Mitochondrial Function for the Treatment of Metabolic Diseases.* Int J Mol Sci, 2019. 20(19).
354. Rosen, E.D. and B.M. Spiegelman, *Molecular regulation of adipogenesis.* Annu Rev Cell Dev Biol, 2000. 16: p. 145-71.
355. Wilson-Fritch, L., A. Burkart, G. Bell, K. Mendelson, J. Leszyk*, et al.*, *Mitochondrial biogenesis and remodeling during adipogenesis and in response to the insulin sensitizer rosiglitazone.* Mol Cell Biol, 2003. 23(3): p. 1085-94.
356. Si, Y., S. Palani, A. Jayaraman, and K. Lee, *Effects of forced uncoupling protein 1 expression in 3T3-L1 cells on mitochondrial function and lipid metabolism.* Journal of Lipid Research, 2007. 48(4): p. 826-836.
357. Rodríguez, A., L. Méndez-Giménez, and G. Frühbeck, *Chapter 6 - Cross-Talk between Autophagy and Apoptosis in Adipose Tissue: Role of Ghrelin*, in *Autophagy: Cancer, Other Pathologies, Inflammation, Immunity, Infection, and Aging*, M.A. Hayat, Editor. 2015, Academic Press: Amsterdam. p. 121-131.
358. Devericks, E.N., M.S. Carson, L.E. McCullough, M.F. Coleman, and S.D. Hursting, *The obesity-breast cancer link: a multidisciplinary perspective.* Cancer Metastasis Rev, 2022. 41(3): p. 607-625.
359. Himbert, C., M. Delphan, D. Scherer, L.W. Bowers, S. Hursting*, et al.*, *Signals from the Adipose Microenvironment and the Obesity-Cancer Link-A Systematic Review.* Cancer Prev Res (Phila), 2017. 10(9): p. 494-506.
360. Polyak, K., *Heterogeneity in breast cancer.* J Clin Invest, 2011. 121(10): p. 3786-8.
361. Page Faulk, W., B.-L. Hsi, and P.J. Stevens, *TRANSFERRIN AND TRANSFERRIN RECEPTORS IN CARCINOMA OF THE BREAST.* The Lancet, 1980. 316(8191): p. 390-392.
362. Torti, S.V. and F.M. Torti, *Cellular iron metabolism in prognosis and therapy of breast cancer.* Crit Rev Oncog, 2013. 18(5): p. 435-48.
363. Guo, Q., L. Li, S. Hou, Z. Yuan, C. Li*, et al.*, *The Role of Iron in Cancer Progression.* Frontiers in Oncology, 2021. 11.
364. Duan, G., J. Li, Y. Duan, C. Zheng, Q. Guo*, et al.*, *Mitochondrial Iron Metabolism: The Crucial Actors in Diseases.* Molecules, 2023. 28(1): p. 29.
365. Evans, K.W., E. Yuca, S.S. Scott, M. Zhao, N. Paez Arango*, et al.*, *Oxidative Phosphorylation Is a Metabolic Vulnerability in Chemotherapy-Resistant Triple-Negative Breast Cancer.* Cancer Res, 2021. 81(21): p. 5572-5581.

366. Thompson, H.J., E.S. Neil, and J.N. McGinley, *Pre-Clinical Insights into the Iron and Breast Cancer Hypothesis.* Biomedicines, 2021. 9(11): p. 1652.
367. Islam, S., N. Hoque, N. Nasrin, M. Hossain, F. Rizwan*, et al.*, *Iron Overload and Breast Cancer: Iron Chelation as a Potential Therapeutic Approach.* Life, 2022. 12(7): p. 963.
368. Heydemann, A., *An Overview of Murine High Fat Diet as a Model for Type 2 Diabetes Mellitus.* Journal of Diabetes Research, 2016. 2016: p. 2902351.
369. Liang, W. and N. Ferrara, *Iron Metabolism in the Tumor Microenvironment: Contributions of Innate Immune Cells.* Frontiers in Immunology, 2021. 11.
370. Ganz, T., *Macrophages and Systemic Iron Homeostasis.* Journal of Innate Immunity, 2012. 4(5-6): p. 446-453.